VICTORIA UNIVERSITY OF WELLINGTON

MASTER'S THESIS

Finite-element Modelling of Haupapa/Tasman Glacier's Basal Sliding Events

Author:
Clarrie MACKLIN

Supervisors:
Dr. Huw HORGAN
Dr. Brian ANDERSON

A thesis submitted in fulfilment of the requirements for the degree of Master of Science in Geophysics

in the

Antarctic Research Centre
School of Geography, Environment, and Earth Sciences

November 7, 2019

Declaration of Authorship

I, Clarrie MACKLIN, declare that this thesis titled, "Finite-element Modelling of Haupapa/Tasman Glacier's Basal Sliding Events" and the work presented in it are my own. I confirm that:

- This work was done wholly or mainly while in candidature for a research degree at this University.
- Where any part of this thesis has previously been submitted for a degree or any other qualification at this University or any other institution, this has been clearly stated.
- Where I have consulted the published work of others, this is always clearly attributed.
- Where I have quoted from the work of others, the source is always given. With the exception of such quotations, this thesis is entirely my own work.
- I have acknowledged all main sources of help.
- Where the thesis is based on work done by myself jointly with others, I have made clear exactly what was done by others and what I have contributed myself.

Signed:

Date:

VICTORIA UNIVERSITY OF WELLINGTON

Abstract

Faculty of Science
School of Geography, Environment, and Earth Sciences

Master of Science

Finite-element Modelling of Haupapa/Tasman Glacier's Basal Sliding Events

by Clarrie MACKLIN

The rate of ice loss from glaciers and ice caps is a major source of uncertainty in predicting sea level rise out to 2100. Improving the predictive capability of ice flow models will, in part, require a more robust coupling of climate to long-term and short-term variability in glacial discharge. An ongoing concern is the role that surface melting and rainfall plays in accelerating glacier flow. Rapid drainage of surface water to the base of a glacier or ice sheet is thought to elevate basal water pressure, reduce basal friction, and thereby increases sliding speed. Here, we present several rain-induced speed-ups of Haupapa/Tasman Glacier, South Island, New Zealand, recorded by GNSS (Global Navigation Satellite System) instruments. Observed speed-up events involve large vertical offsets (up to 53 cm) and large horizontal accelerations of up to twenty-four times background velocity. Due to it's pronounced sliding events, Haupapa/Tasman Glacier offers a useful case study for investigating the processes that govern the sliding behaviour of large glaciers prone to increasing meltwater variability as a cause of enhanced mass loss in a warming climate. The observed correspondence of vertical displacement and horizontal acceleration in this study suggests that the rapid growth of water-filled cavities at the bed controls basal motion during speed-ups. However, sliding laws that relate changes in basal velocity to changes in water pressure do not account for cavity growth. To investigate the processes governing a typical speed-up event, we use a finite-element modelling approach combined with a commonly-used sliding law to recreate internal deformation and basal sliding of Haupapa/Tasman Glacier during rain-induced acceleration. In general, we find peak velocities can only be achieved when basal water pressure exceeds ice overburden and velocity at the glacier sides is allowed to exceed that observed by a GNSS unit situated near the margins. The sliding law requires a more complete treatment of cavity growth under rapid water pressure changes to better capture basal acceleration observed at Haupapa/Tasman Glacier.

Acknowledgements

Firstly, I thank my supervisors Huw and Brian for providing me with guidance through what has been an absolute trail-blazer of a year. I have felt welcomed and supported during my entire stint as a budding geophysics student deciding to take the plunge head-first into the world of glaciology. I must also thank Huw for inviting me to Haupapa/Tasman Glacier and thereby demonstrating that glaciers are more than just a series of matrices and error messages on my computer screen.

I extend my deepest gratitude to Eric and Trudy Westergaard for setting up the Rachael Westergaard Memorial Scholarship in Geophysics. I have been provided with sustenance, shelter, and above all, the privilege to spend my time learning about a subject that matters to me. Thanks to your support. Above all, I thank you for your warmness and genuine interest in supporting me on my learning path.

To the students and faculty of the Summer of Applied Geophysical Experience 2018 class, my heart goes out to you all. I know none of you understood my Kiwi banter, but I somehow manage to feel right at home in the middle of a New Mexico desert. A huge thanks, also, to the Geological Society of New Zealand for funding the trip.

To my Mum, my rock, my day one, I thank you. You have helped me see the light on more occasions than you know. Science is hard. Really hard. And when it got a little too hard for me to deal with you were always there.

To Dad a.k.a. Pappa bear, for checking in on me, for being a positive role model in my life, for always offering support and shelter, for your wisdom, for keeping my belly full and my time off full of fun, I thank you.

To Andy, my little brother who is both taller and bigger than me, I thank you for being there throughout the year. For being the funniest dude I know and always ready to play God of War.

To Dani, the best office mate anyone could hope for. Words can't do justice to the positive energy you bring when my coding get cloudy. I have thoroughly enjoyed going through the struggles of geophysical modelling together. Also, big thanks to you and your hubby for the edits. To Arran, a massive, massive, massive thanks for our discussions on subglacial drainage. The progress I made since having someone to talk about glaciers with was exponential. To Lauren, you have been a huge inspiration to me over the last year. Thank you for all your advice and edits. To Damian and Jiten, thank you for your unparalleled Geophysics chat and cricket banter. To Alec, thanks for being a top bloke over the years. I wish you the best for your future, mate. To Benji, thanks for the music yarns my man.

To Josie, a huge thanks for helping edit my work and for appreciating my terrible ice puns.

Lastly, a big shout out to the boyz: Aeron, Cameron, Kieren, Angus, Steven, Troy "Trigga" Coutts, Sam, Adam, Lachlan, Sharn, Zac, Ollie, and Gazza. Love you guys. I will be cracking a cold one with you lads as soon as I hand this beast in.

Contents

List of Figures

List of Tables

List of Abbreviations

IPCC	**I**ntergovernmental **P**anel on **C**limate **C**hange
GNSS	**G**lobal **N**avigation **S**atellite **S**ystem
DEM	**D**igital **E**levation **M**odel

Physical Constants

Gas Constant	$G = 8.314\,\mathrm{J\,K^{-1}\,mol^{-1}}$
Gravity Constant	$g = 9.81\,\mathrm{m\,s^{-1}}$
Ice Density	$\rho_i = 900\,\mathrm{kg\,m^{-3}}$

List of Symbols

a	Seasonal variability in surface velocity	$\mathrm{m\,yr^{-1}}$
a_s	Fractional area of cavity volume	$\mathrm{m^{-1}}$
A	Creep parameter in Glen's flow law	$\mathrm{MPa^{-3}\,yr^{-1}}$
A_s	Friction parameter for sliding in the absence of cavities	$\mathrm{MPa^{-3}\,yr^{-1}}$
B	Bed separation	m
C_b	Budd-type sliding law friction coefficient	$\mathrm{MPa^2\,m^{-3}\,yr^{-3}}$
C_{max}	Iken's bound parameter	
C_s	Coulomb-type sliding law friction coefficient	$\mathrm{MPa\,m^{-1/3}\,yr^{-1/3}}$
C_w	Weertman-type sliding law friction coefficient	$\mathrm{MPa\,m^{-1/3}\,yr^{-1/3}}$
h	Height of bed obstacles	m
n	Glen's flow law exponent	
N	Effective pressure	MPa
q	Post-peak exponent	
P_w	Water pressure	MPa
t_{peak}	Time for modelled water pressure to rise to peak P_w	hr
t_{rise}	Time for modelled water pressure to decay to background P_w	hr
T_{ice}	Ice Temperature	K
u_b	Sliding speed	$\mathrm{m\,yr^{-1}}$
u_{def}	Deformational velocity	$\mathrm{m\,yr^{-1}}$
u_{side}	Peak speed of glacier model boundaries	$\mathrm{m\,yr^{-1}}$
λ	Separation between bed obstacles	m
λ_L	Downstream obstacle separation	m
λ_T	Lateral obstacle separation	m
τ_b	Basal stress	MPa
$\boldsymbol{\tau}$	Deviatoric stress tensor	MPa
$\boldsymbol{\sigma}$	Stress tensor	MPa
σ_{nn}	Stress normal to glacier bed	MPa

For Mum & Dad

Chapter 1

Introduction

1.1 Glaciers and sea-level rise

The decline of glaciers and ice caps provided the largest source of meltwater contributing to sea level rise over the twentieth century (Church et al., 2013; Gregory et al., 2012). In addition, the rate of this meltwater contribution is likely to accelerate in the coming decades (Church et al., 2013). Combined global records of glacier mass balance, glacier surface elevation, and glacier terminus position, compiled by the World Glacier Monitoring Service (WGMS), demonstrate that current mass loss rates are unprecedented in the historical record (Zemp et al., 2015). However, models that predict the total glacial ice loss by the end of the century produce a wide range of sea level rise estimates. An ensemble of ice loss models presented in the fifth IPCC (Intergovernmental Panel on Climate Change) assessment suggested 0.04–0.26 m of sea level rise could be attributed to glaciers (Church et al., 2013). In terms of informing policy that responds to the impacts human activity has on sea-level rise – and thereby the impacts of sea-level rise on society – reducing this range of uncertainty is a crucial endeavour. Even if our current climate remained constant, 28–44% of the current global glacier volume would likely melt over a few centuries (Marzeion et al., 2018) (Figure 1.1). Considering global climate models are in consensus that global mean temperatures will increase out to 2100 (i.e. Collins et al. (2013)) and even for conservative scenarios in which anthropogenic emissions peak and decline, it is highly likely that accelerated glacier mass loss on a global scale will be observed over the coming decades.

Predicting the future behaviour of glaciers relies heavily on numerical models of ice melting and ice flow. However, not all of the processes leading to accelerated mass loss are well constrained or even implemented in predictive models (Vaughan et al., 2013). Large ensembles of glacier mass loss models are used in IPCC reports as a primary resource for assessing the likely rate of future glacier ice loss (Church et al., 2013). These models are typically calculated by surface mass balance – i.e. a glacier will grow or shrink depending on the balance between snowfall accumulation on a glacier during winter and the amount of surface melting during summer months (Cuffey and Paterson, 2010). The expected change in glacier volume can then be calculated by using a global distribution of glacier volume (e.g. Huss and

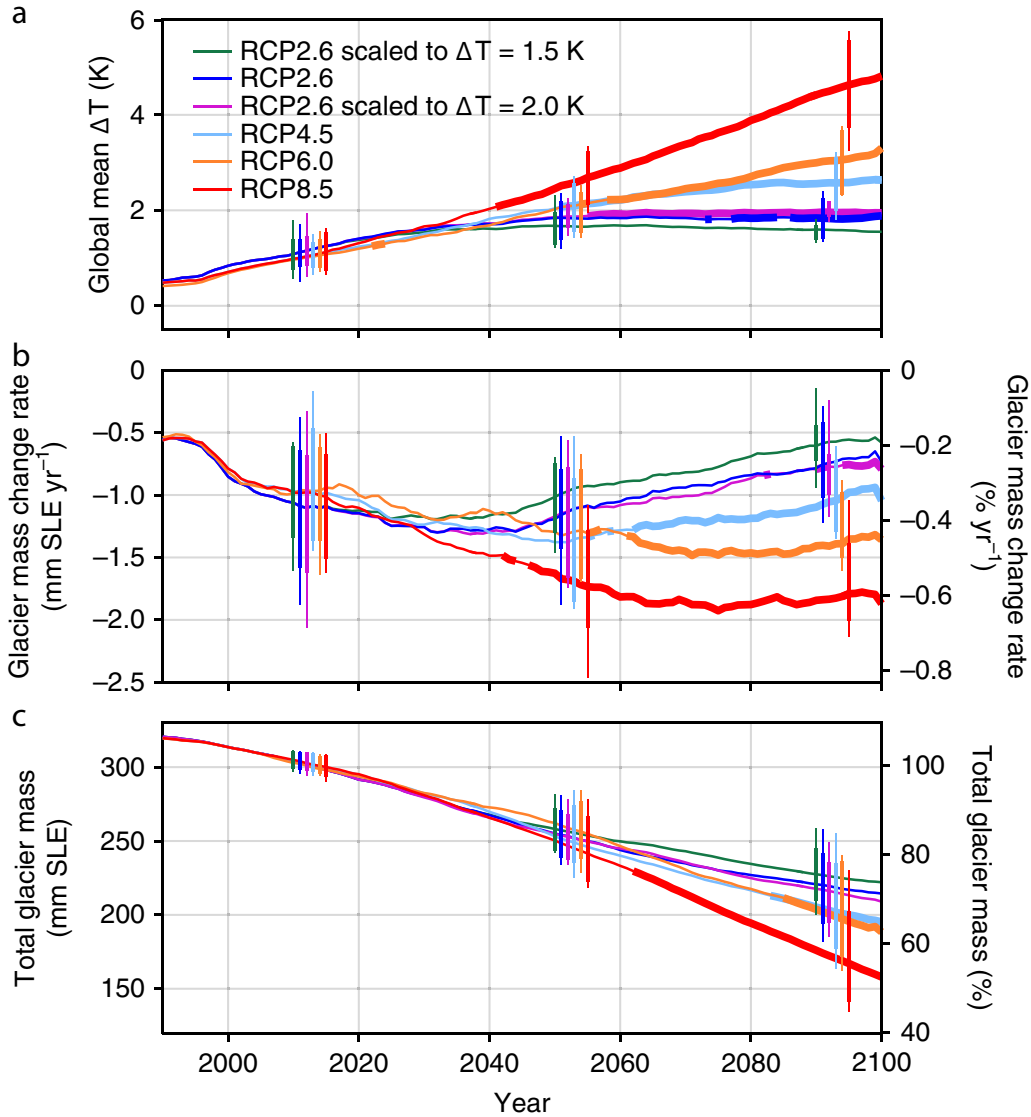

FIGURE 1.1: A model of projected global glacier mass loss out to 2100 from Marzeion et al. (2018). Modelling results show a range of possible global glacier loss outcomes from conservative (RCP 2.6) to continually increasing (RPC 8.5) emissions scenarios. An RPC, or Representative Concentration Pathway, is a scenario of greenhouse gas emissions used in climate models to test the sensitivity of global temperatures to greenhouse gas concentrations in the atmosphere. Marzeion et al. (2018) is the major reference for the sensitivity of assessing the glacier mass loss to either 1.5 °C or 2.0 °C of global mean temperature increase in the most recent IPCC report Hoegh-Guldberg et al. (2006). Marzeion et al. (2018) suggest that, ultimately, glacier mass loss is inevitable over the coming centuries; however, the rate at which it occurs is sensitive to the emissions and resulting change in mean global temperature

Farinotti, 2012) and the temperature and precipitation output of global climate models (Marzeion, Jarosch, and Hofer, 2012; Radić and Hock, 2011; Radić et al., 2014). However, surface mass balance may not be a complete measure of glacial mass loss. Recent estimates suggest that of Greenland's 1991–2015 total mass loss around 60% can be attributed to melting (which amounts to $\sim 0.47 \pm 0.23$ mm per year sea level equivalent) (Broeke et al., 2016; Flowers, 2018). This anomaly in mass loss is attributed to other processes occurring in response to warming, such as increased ice discharge into the ocean through accelerated ice flow in outlet glaciers (Broeke et al., 2009). Accelerations in ice flow supports the movement of ice to lower, warmer altitudes where melting is more prevalent (De Fleurian et al., 2018; Ridley et al., 2010). The deficit between ice loss through melting and the total observed ice loss has grown over the last few decades as Greenland continues experiencing a negative trend in ice volume per year (Flowers, 2018) (Figure 1.2). The risk of using a purely surface mass balance based model is to mispredict the true extent of glacial ice loss (Howat, Joughin, and Scambos, 2007; Solomon et al., 2007); hence assessing the impact of dynamic losses on glacial and ice sheet decline has become an increasingly significant topic of research (e.g Broeke et al. (2009), Enderlin et al. (2014), Flowers (2018), Kjeldsen et al. (2015), and Nienow et al. (2017)).

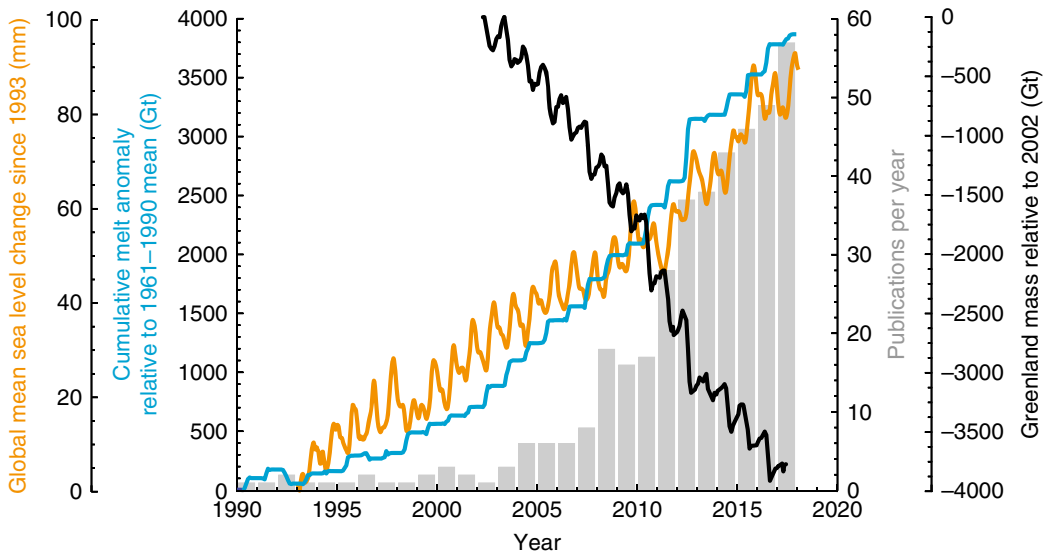

FIGURE 1.2: The increasing anomaly between calculated and observed ice mass loss from Greenland as depicted in Flowers et al. (2018). The mass loss in Greenland Ice Sheet has triggered a recent spike in the melting and dynamics of ice sheets and outlet glaciers. Figure from

Glaciers can respond to warming by several means that are often not fully implemented in glacier or ice sheet models that predict mass loss over the coming century (Bindschadler et al., 2013; Nienow et al., 2017; Rignot, 2009; Vaughan et al., 2013). Processes that can rapidly alter glacier flow usually involve some interaction with water, such as calving at marine-terminating glaciers, rainfall events, or instances of

rapid surface melting. For example, accelerated glacier flow has been linked to the submarine melting due to warming ocean currents (Rignot, Koppes, and Velicogna, 2010), the thinning and ungrounding of glacier fronts (Thomas, 2004), and drainage of surface meltwater to the glacier bed (Iken and Bindschadler, 1986; Zwally et al., 2002). These processes are a product of the climate a glacier is situated in, meaning that same global temperature increase causing enhanced surface melting can also trigger glacier mass loss. For instance, the warming of ocean waters has been suggested to enhance mass loss by increasing calving rates at marine-terminating glaciers in Greenland (Rignot, Koppes, and Velicogna, 2010). Additionally, increased variability in surface melting or heavy rainfall in rainfall events can result in more episodes of rapid surface water drainage to the glacier bed and induce glacier acceleration (Schoof, 2010; Vaughan et al., 2013).

This study is focused on the process of surface-water induced changes in ice motion – a process which potentially has an increasingly important role in deglaciation. Ice motion is most sensitive to water inputs when the variation in surface water reaching the bed of the glacier is high — i.e. a sudden increase in the rate of melting during the year or episodes of high rainfall rate have a greater effect on enhancing glacier velocity than simply increasing the average annual melting or rainfall (Schoof, 2010). This has implications on glacier mass loss in Greenland, for instance, where more frequent rain events and greater temperature variability are predicted in climate models (Schoof, 2010; Schuenemann and Cassano, 2010). The concern here is that if episodes of rapid surface water production become more common (i.e. from surface melting or rainfall) so would accelerate ice flow. Accelerated ice flow translates to an increasingly large volume of ice being able to reach the terminus (where ice is lost through calving or melt) each year. However, both the coupling of climate to ice dynamics and the interaction of subglacial water flow with basal sliding are often described as "poorly understood" (Andrews et al., 2018; Chu, 2013; Cowton et al., 2016; Howat, Joughin, and Scambos, 2007; Howat et al., 2008; Kamb et al., 1994; Nick et al., 2009; Schoof, 2005; Vallot et al., 2017). In terms of improving our predictive capability of how glaciers respond to their external environment, an outstanding question is: what mechanisms control the influence of basal water on ice motion?

Understanding the significance of changes in glacier motion induced by surface water largely relies on a combination of field observations and numerical modelling (Nienow et al., 2017). Originally, GPS (Global Positioning System) measurements of enhanced surface velocity in response to warm surface temperatures (i.e. above the melting point for ice) prompted the study of glacier sliding as facilitating mass loss (Bartholomew et al., 2010; Church et al., 2013; Zwally et al., 2002). Numerical models have since been developed to assess the impact of basal lubrication on sea-level rise, though their results do not always agree with each other (Church et al., 2013). Bindschadler et al. (2013) used an ensemble of Greenland Ice Sheet models to suggest an average contribution of 6.8 cm of sea level rise by 2100 due when a

sliding factor that increases basal velocity with time is implemented (where other processes that influence ice loss, such as mass balance, are held constant). However, some numerical models suggest that enhanced basal sliding will have only a subtle effect on the overall decline of global glacier mass compared to other processes. For instance, Nick et al. (2009)'s flowline models of large Greenland outlet glaciers, which include a parameter for enhancing basal sliding, can induce significant surface thinning, but stabilise after only 150 m of terminus retreat over five years. In contrast, Nick et al. (2009)'s model that focuses on the removal of stress against the terminus successfully reproduced a 12 km yr^{-1} retreat observed at Helheim Glacier. These examples of Greenlandic outlet glaciers provide insight into the sensitivity of glacier and ice sheet loss to various processes. However, both examples are limited in their treatment of glacial hydrology, opting for easily implementable, empirical coefficients to control sliding rate. These contradicting results, as well as the lack of physically-based treatments of basal sliding in numerical models, make it difficult to assess the importance of surface melting on basal sliding (and thereby glacial mass loss) in predictions of sea-level rise.

Recent interest has focused on better incorporating physical processes into glacial hydrology and ice flow models, shown by the significant increase in literature on Greenland glacial hydrology (Figure 1.2) and large intercomparison projects for subglacial hydrology models (De Fleurian et al., 2018; Flowers, 2018). Models which couple glacial hydrology to changes in ice dynamics, while still in their early stages, are being developed for assessing the response of ice flow to hydrological processes (De Fleurian et al., 2014; Gagliardini and Werder, 2018; Hewitt, 2013; Pimentel, Flowers, and Schoof, 2010). Working towards predicting future glacier dynamics relies on better incorporating the physical processes in our models to more confidently evaluate their impacts on sea-level rise (Nienow et al., 2017).

1.2 Observations of the effect of surface water production on ice motion

Neglecting the effects of surface-water induced sliding could mean that the total ice mass loss of land-terminating glaciers is not being correctly predicted. Significant changes in flow speed on daily and seasonal timescales are well documented for alpine glaciers (e.g. Copland, Sharp, and Nienow, 2003; Iken, 1972; Iken and Bindschadler, 1986; Jansson, 1995; Lliboutry, 1959; Lliboutry, 1965), and, more recently, in large outlet glaciers of the Greenland Ice Sheet (e.g. Bartholomew et al., 2012; Shepherd et al., 2009; Zwally et al., 2002). The acceleration of ice flow in both contexts is correlated to instances of enhanced surface melt or rainfall. Figure 1.3 shows the vertical displacement and horizontal velocity record of Unteraargletscher, Switzerland over a single melt season (the summer months when surface temperatures over part of a glacier are regularly above melting point) (Iken et al., 1983). These data demonstrate that over the summer months, as a response to the increased rate of surface

melt production, a general increase in surface velocity and surface elevation is observed. This longer-term increase in surface velocity is also inter-dispersed with several short-term peaks in velocity throughout the melt season, which are more than triple the velocity of the winter flow speed. Furthermore, these speed-up events are also accompanied by vertical uplift of the glacier where the maximum horizontal acceleration coincides with the maximum rate of uplift (Anderson, 2004; Cowton et al., 2016; Iken et al., 1983).

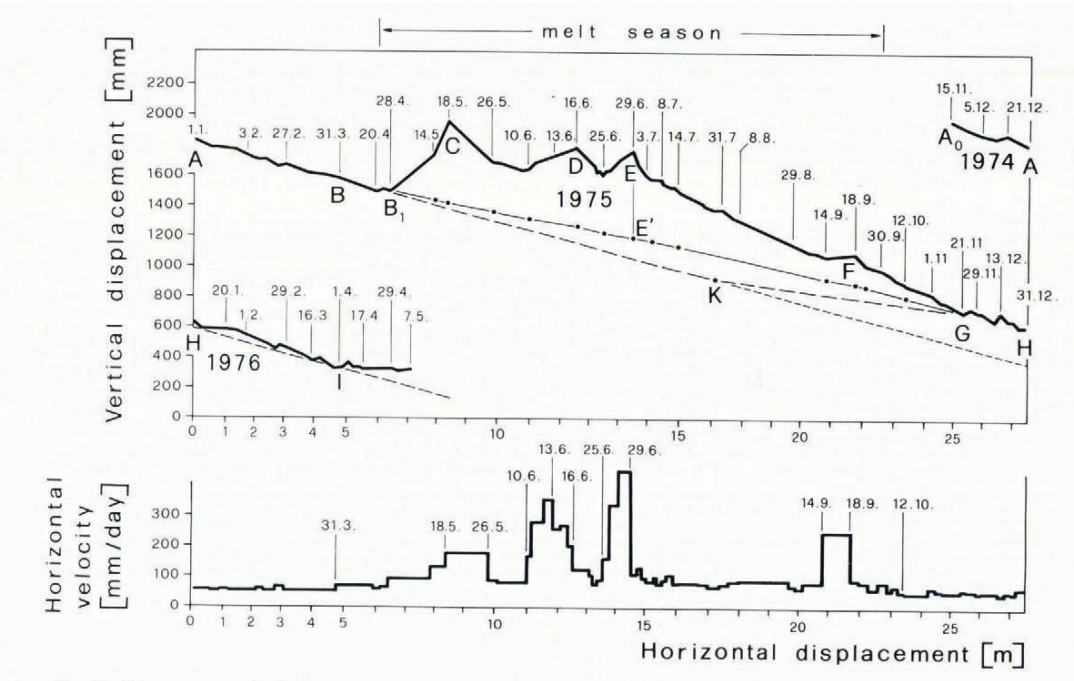

FIGURE 1.3: Glacial surface uplift associated with the onset of melt season. During melt season, the vertical displacement (top) initially increases quickly, remains elevated, but slowly decreases back to its original path. The same is true for horizontal velocity (bottom). However, both records also include several spikes in both vertical displacement and horizontal velocity referred to as "speed-up events". The surface position was measured by tracking features on the surface of the glacier using an automatic camera.

Explaining the size of significant velocity variations during melt season requires a description of how enhanced water flow beneath a glacier influences its sliding speed. The slip of basal ice over its underlying geology, deformation of subglacial sediments, and the viscous deformation of ice under gravity combine to produce observed surface motion (Cuffey and Paterson, 2010). Basal sliding is a component of the glacier's flow field that can undergo changes over short-timescales (see Section 2.2 for a more detailed discussion). Surface water drains to the base of the glacier and reduces friction by decreasing the area of contact between ice and the glacial bed. The weakening of basal friction in response to subglacial water flow is strongly dependent on water pressure (Clarke, 2005; Cuffey and Paterson, 2010). Subglacial water pressure is often measured by drilling boreholes or using naturally occurring vertical shafts in the glacier that connect to the base, where changes in water height

are a proxy for changes in basal water pressure (Iken, 1972; Iken and Bindschadler, 1986; Rada and Schoof, 2018). Iken and Bindschadler (1986) used measured surface velocity during the early melt season at Findelengletscher, Switzerland to validate the link between basal water pressure and sliding velocity (Flowers, 2011). Observations of increased water pressure have been correlated with instances of enhanced surface motion (Figure 1.4). Similar short-term and seasonal variation presented in Iken and Bindschadler's work has since been documented on both glaciers which are at the melting point through much of the year (*temperate* glaciers) (Hooke et al., 1989; Nienow et al., 2005; Raymond et al., 1995) and polar glaciers, which have mostly frozen beds and whose surface is below the melting point much of the year (polythermal glaciers) (Bingham, Nienow, and Sharp, 2003; Copland, Sharp, and Nienow, 2003; Jansson, 1995). Furthermore, velocity variation is observed in response to daily cycles of warming and cooling (Blake et al., 1994; Nienow et al., 2005; Raymond et al., 1995; Shepherd et al., 2009).

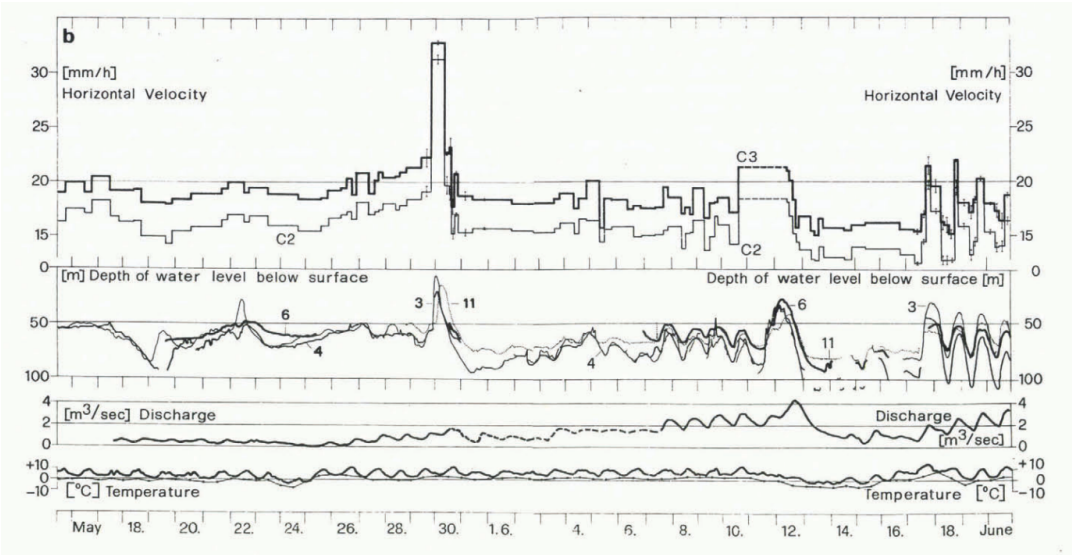

FIGURE 1.4: Observed variation of surface velocity due to changes in basal water pressure from Iken and Bindschadler (1986). The top plot depicts horizontal surface velocity with time, the plot beneath shows the depth of water in a borehole (where a higher water level corresponds to elevated basal water pressure. The conformity of surface velocity and borehole level suggests short-term speed-up events are linked to rapid increases in basal water pressure.

The link between atmospheric temperature and ice velocity has been suggested as a possible feedback mechanism that could greatly increase the rate that ice is delivered to the oceans due to enhanced sliding (Chu, 2013; Cowton et al., 2016; Zwally et al., 2002). Studies of large Greenland outlet glaciers, in particular, that demonstrate a surface velocity or borehole water pressure response to surface melting have been important for demonstrating the relationship of surface melting and glacial acceleration (Andrews et al., 2015; Bartholomaus, Anderson, and Anderson, 2008; Flowers, 2018; Zwally et al., 2002). However, inputs of surface melt-water during

melt season have been shown to result in both net increases of surface ice velocity (Bartholomew et al., 2010) or net decreases (Tedstone et al., 2015). Understanding this complexity relies on both how subglacial water flow evolves due to changing surface water inputs (see Section 1.4.2, 2.4.2) and how basal sliding responds to changes in water pressure (Section 1.3).

1.3 Basal Sliding

Explaining how glaciers accelerate over hourly to seasonal scales requires some relationship between changes in basal water pressure and sliding velocity. Such a relationship is typically described through a *sliding law*: an equation that links the amount of friction generated by glacial ice against its bed, the roughness and strength of the underlying geology, and the pressure of the water flowing beneath the ice. However, it is unclear whether a general sliding law exists (Cuffey and Paterson, 2010; Raymond and Harrison, 1988). While several sliding laws have been proposed and used for recreating glacier motion (Flowers, 2015), they are often inconsistent with observations of glacier velocity and water pressure over time Iken and Truffer (1997) and Raymond and Harrison (1988)(Section 1.4). Furthermore, in predicting the dynamical behaviour of ice sheet grounding zones over the coming century, considerably different glacial retreats are modelled depending on the choice of sliding law (Brondex, Gillet-Chaulet, and Gagliardini, 2019; Brondex et al., 2017; Gladstone et al., 2017). A major drawback to improving sliding laws is the fact that direct observations are scarce and hence the definition of sliding has come largely from theoretical arguments and surface measurement (see Chapter 2.5)(Cuffey and Paterson, 2010). Sliding law theory has provided insights into the mechanisms of glacier sliding, but recent observations of surface velocity and subglacial drainage demonstrate that the sliding relationship is complex and the processes represented in sliding laws may be incomplete — especially for rapid accelerations (Harper et al., 2007; Howat et al., 2008; Iken and Truffer, 1997; Sugiyama and Gudmundsson, 2004) (Section 1.4).

1.3.1 The sliding law

Models of ice flow rely on a sliding law to dictate how frictional stress at the base translates to sliding velocity (Raymond and Harrison, 1987; Stearns and Veen, 2018). For a glacier to slide at a steady velocity, there must be friction at the base to stop the ice from accelerating indefinitely. An issue here is that basal ice has almost no ability to apply shear stress against an underlying surface; glacial ice is assumed to apply negligible friction against a flat surface due to a water film that develops at the interface between ice and rock (Cuffey and Paterson, 2010). The apparent "frictional force" that balances the weight of the glacier must result from bumps that protrude from the bedrock which provide an obstacle to flow. In other words, resistance to basal ice flow is created by normal forces σ_{nn} opposing the ice flow where stresses

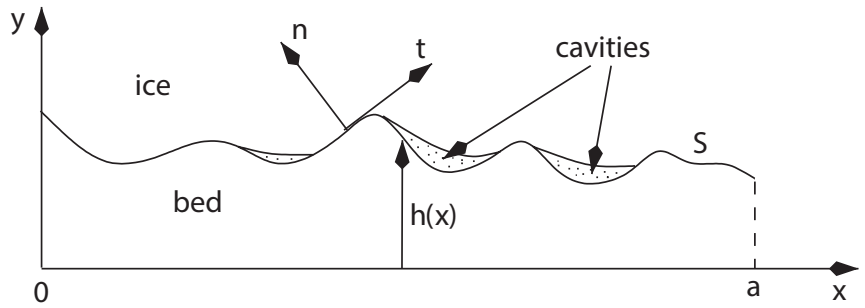

FIGURE 1.5: An idealised glacier bed from Schoof (2005). While in nature, glacier beds are likely to be rougher than this diagram, simplified bed geometries are useful for illustrating the mathematical descriptions of glacier sliding. $h(x)$ is the bed topography. Ice flows over bumps in the bed. Water at the base collects in cavities on the downstream side of bed obstacles. In this diagram, **n** and **t** are the normal and tangential vectors to the bed. Normal stresses σ_{nn} are forces normal to the bed, and shear stresses are tangential, but these are likely to be negligible for basal ice against bedrock.

parallel to the bed are unlikely to exist (see Figure 1.5). For an idealised bed, the total apparent frictional stress, referred to as the "basal stress" τ_b is given by the average of the normal stresses between two obstacle peaks (Figure 1.5):

$$\tau_b = \frac{1}{\lambda} \int_0^{\lambda} \sigma_{nn} h'(x) dx \tag{1.1}$$

where $h(x)$ is height of the bed topography, and λ is the average distance between obstacle peaks (Schoof, 2005). Following the proposition that ice is under a greater pressure on the upstream side of obstacles, Weertman (1957) defined a relationship of basal stress to the sliding velocity (see Section 2.5):

$$\tau_b = C_w u_b^{m-1} \tag{1.2}$$

where u_b is the sliding velocity,$m = 1/n$ is the inverse of Glen's flow law parameter, and C_w is a friction coefficient that depends on the bed roughness and the thermodynamic and mechanical properties of glacial ice (Cuffey and Paterson, 2010). The "Weertman-type" sliding law provides a first-order description of the physical processes causing glacial sliding and has had applications in predictive models of ice sheet evolution (e.g. Brondex et al., 2017; Pattyn et al., 2012; Ritz et al., 2015). However, such a formulation has no bearing in modelling the acceleration of ice flow over hourly to seasonal timescales because it does not include the effect of basal water pressure. Other sliding laws have since been developed that include the influence of subglacial water.

1.3.2 Basal sliding in the presence of elevated basal water pressure

A commonly applied sliding law is a Weertman-type law that is extended to account for variations in the sliding velocity, and while this broadly captures the relationship between water pressure and sliding speed observations, it demonstrates physical limitations. Basal water pressure influences sliding speed by changing the effective pressure of ice upon its rock N, given by the difference between ice overburden pressure P_i and basal water pressure P_w:

$$N = P_i - P_w \tag{1.3}$$

It is expected that under elevated water pressures, basal water is able to force open cavities in the lee-side of bedrock obstacles (where normal stresses are lower) (Figure 1.5)(Iken, 1981; Lliboutry, 1986; Lliboutry, 1959)(see Section 2.4.2, 2.5.1, 2.5.3 for a detailed description of cavity growth). Cavity growth reduces the area of ice-bed contact, and thereby reduces the effective roughness of the bed. Lower roughness causes friction to decrease and sliding speed to accelerate. Originally, the extended Weertman sliding law, or "Budd-type" sliding law, was formulated from laboratory experiments that indicated ice sliding velocity is strongly controlled by effective pressure at the rock–ice interface :

$$\tau_b = C_b u_b^m N^q \tag{1.4}$$

where C_b is some friction coefficient and q is a constant (Budd, Jenssen, and Smith, 1984; Budd, Keage, and Blundy, 1979; Cuffey and Paterson, 2010; Gladstone et al., 2017). This formula generally captures the overall relationship between effective pressure and sliding speed where $u_b \propto 1/N$. For instance, the surface velocity and basal water pressure data over a melt-season from Iken and Bindschadler (1986)(Figure 1.4) follows this inverse proportionality (Figure 1.6). Several studies have also applied a "Budd-type" sliding law to model observations over seasonal timescales (Bindschadler, 1983; Blake et al., 1994; Jansson, 1995); however, the constants q, m, and C_b have been shown to vary for certain glaciers between years or even over a single melt season (Hooke et al., 1989; Iken and Truffer, 1997). Furthermore, Raymond and Harrison (1987) noted that when attempting to model the surge behaviour of Variegated Glacier, Alaska that no general quantitative relationship between water pressure and sliding could be successfully attained using this sliding law to model spatial or temporal variations in sliding speed. Therefore, the "Budd-type" sliding law may have some use in providing an empirical fit to observations but is likely to be limited in its use in predictive models of glacier behaviour.

Resolving a general relationship between effective pressure and sliding velocity requires that the physical processes that control the influence of basal water upon ice motion are quantified by the sliding law. The Weertman- and Budd-type laws are known to be missing some of the processes involved in varying sliding speed

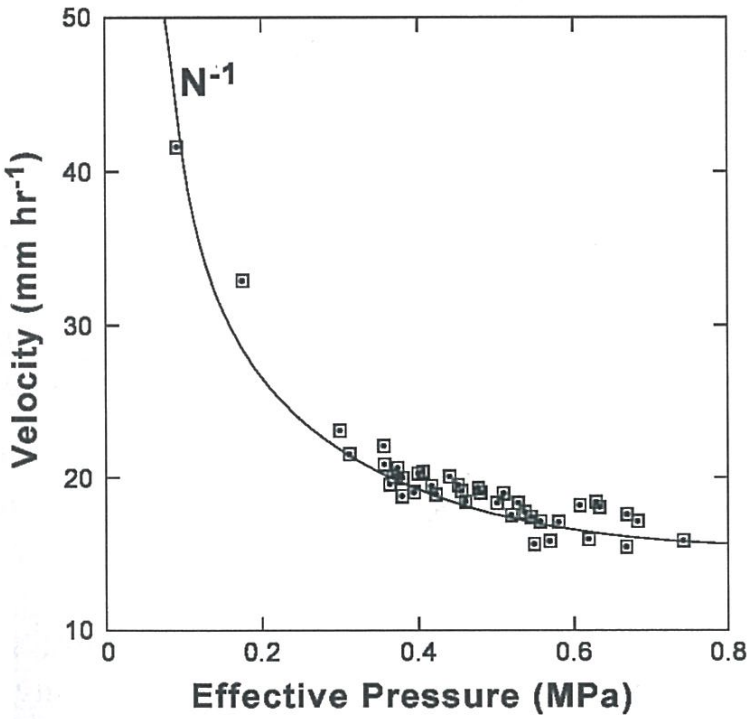

FIGURE 1.6: Surface velocity versus Effective pressure data from Unteraargletscher, Switzerland, during melt season of 1982 presented inIken and Bindschadler, 1986. In general, an inverse relationship between sliding speed and effective pressure holds. This figure is adapted from Cuffey and Paterson, 2010

on sub-hourly to seasonal timescales. Furthermore, Equations 1.2 & 1.4 are both unbounded: they imply that basal stress τ_b can increase to arbitrarily high values as u_b becomes very large, or $\tau_b \to 0$ as $N \to 0$ if $q > 0$ (Brondex et al., 2017). The following section illustrates how a more physically robust treatment of basal friction is introduced into the sliding law. Namely, the key development from the Weertman- and Budd-type sliding laws is that limits are placed on the basal stress based on the geometry of the glacier bed.

Sliding in the presence of cavities

An upper limit to basal stresses was derived for an idealised glacier bed by Iken (1981) who showed that basal stress is restricted by the maximum slope of bedrock obstacles (see Section 2.5.2 for a detailed explanation). One of the consequences of Iken's bound is that, if water pressures are high enough, the bed of the glacier is unable to supply basal stress that balances the flow of the glacier under gravity. This represents the case where large water pressures cause water-filled cavities to grow beyond the point of maximum slope (Gagliardini et al., 2007). A sliding law that obeys that upper limit for sliding velocity was derived by Schoof (2005) (referred to as the "Coulomb-type" sliding law). Originally derived for an arbitrary glacier bed

and linear ice rheology, Gagliardini et al. (2007) extended the sliding law to hold for non-linear rheology using a finite-element model:

$$\tau_b = \frac{C_s u_b^m}{(1 + (C_s/C_{max}N)^{1/m} u_b)^m} \tag{1.5}$$

where C_s is a friction coefficient, and C_{max} is the maximum slope of the bedrock topography (which also denotes the maximum value of τ_b/N)(Brondex et al., 2017). In the case of very high water pressures (i.e. $N \rightarrow 0$) where cavities are large and basal stress begins to decrease, limits on sliding velocity then are applied by stretching within the glacier or lateral shear against margin walls (Cuffey and Paterson, 2010). This sliding law has been applied in modelling ice flow in response to basal water pressure changes during surface lake drainage events (Pimentel and Flowers, 2011), glacial surges (Flowers et al., 2011; Jay-Allemand et al., 2011), ice margin dynamics (Hewitt, 2013), and spring speed-up events in mountain glaciers (De Fleurian et al., 2014).

The Coulomb-type sliding law is the most physically robust sliding law available in that it accounts for a hydrological process acting at the glacial base – i.e. a changing cavity size in response to elevated water pressure. However, the sliding law is not without its limitations. The derivation of the Coulomb-type sliding law relies on the assumption that acceleration at the glacier base is negligible, implying that cavity volume is steady at a given water pressure (Gagliardini et al., 2007; Schoof, 2005). However, this assumption is challenged by observations of rapid changes in glacier velocity in response to surface water inputs. Furthermore, observations of subglacial water pressure and glacial velocity demonstrate that the relationship between basal water pressure and sliding speed is not always consistent.

1.4 Inconsistencies in the basal water pressure - sliding speed relationship

The sliding laws in Equations 1.4 & 1.5 assume a constant relationship between basal water pressure and sliding speed; however, this assumption breaks down when surface water inputs vary on hourly to daily timescales. On these timescales, the physical rates of cavity growth and the evolution of the subglacial hydrological system become significant factors in how basal water influences ice motion. Furthermore, the effective pressure response at the bed (Equation 1.3) can vary depending on how water drainage beneath the glacier evolves.

1.4.1 The role of transient cavity growth on sliding speed

If basal water pressure varies at a greater rate than subglacial cavities can grow, a sliding response will occur that is not predictable using existing sliding laws. This may explain observations made by Sugiyama and Gudmundsson (2004) who demonstrated that greater flow speeds at Lauteraargletscher, Switzerland, result

when basal water pressure is increasing with time compared to when water pressure is decreasing with time (Figure 1.7). As increasing water pressure is associated with cavity growth, these results indicate that the physical expansion of cavities may temporarily enhance basal velocity (Cuffey and Paterson, 2010). The enhanced sliding response while cavities are growing was first demonstrated by Iken (1981), who used a finite-element model of ice flow over an idealised bed to demonstrate the greatest sliding response occurred during the moment a water pressure change was applied and decreased until a steady cavity size is achieved (see Section 2.5.3 for background theory). Once cavities adjust to a steady size, forces at the glacier bed are in balance and, theoretically, the sliding law should predict the sliding velocity based on the basal water pressure (Howat et al., 2008). On the timescale of surface water induced speed-up events, it appears that water pressures and cavity size may not always be in balance. Water pressure variations measured in the field appear to demonstrate that water pressure and cavity growth occur out of phase (Kamb, 1987). Moreover, peaks in borehole measured water pressures made by Sugiyama and Gudmundsson (2004) occurred prior to peak uplift. This raises the issue that sliding laws may not predict the true basal velocity during instances of high variability of surface water production which can cause significant fluctuations in basal water pressure (Cowton et al., 2016; Howat et al., 2008).

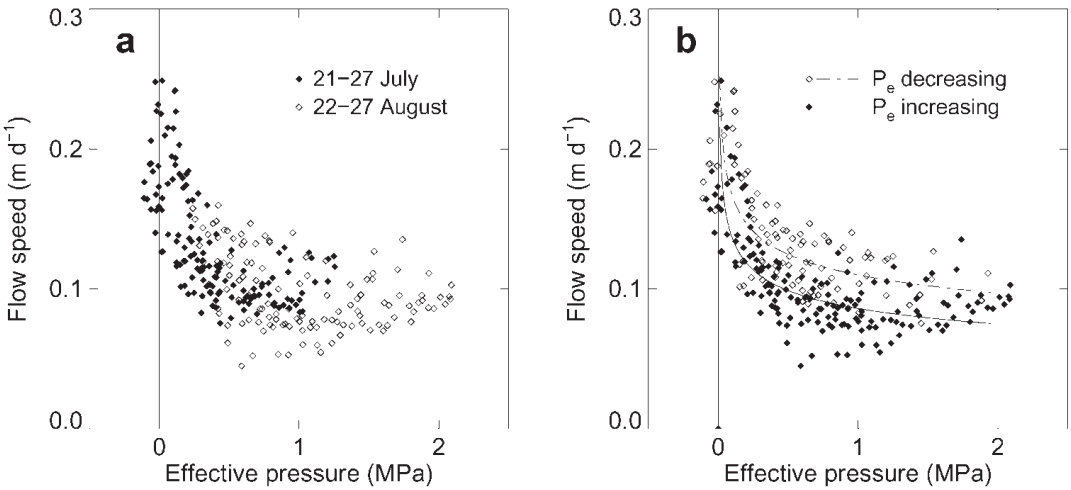

FIGURE 1.7: Observations from Sugiyama and Gudmundsson (2004) demonstrate that sliding speed has a different response depending on whether water pressure is increasing or decreasing. Horizontal surface speed versus Effective pressure data is grouped two time periods (left) and by water pressure increasing/decreasing phase (right)

Cavity growth is then thought to produce a significant effect on glacial acceleration over large scales. This lead Howat et al. (2008) to propose a transient sliding law that also varied depending on the fractional area of bed separation a_s:

$$\tau_b = f(u_b, N, a_s) \tag{1.6}$$

As basal cavities are assumed to be water-filled, changes in surface uplift associated

with enhanced surface water input or sliding rate are attributed to the change in water stored at the bed in the cavity volumes (Bartholomaus, Anderson, and Anderson, 2008; Iken et al., 1983). In accordance with the suggestions of Iken (1981), several field studies of glacier surface velocities during speed-up events demonstrate that horizontal and vertical velocities increase together during the initial phase of acceleration, but vertical velocity returns to zero over a much shorter timescale (Anderson, 2004; Cowton et al., 2016; Horgan et al., 2015; Iken et al., 1983). The transient effect of cavity growth on sliding speed is large during the initial accelerations as cavities are expanding rapidly, moderate when cavity size is has attained its maximum steady size and small when cavities are contracting (Cowton et al., 2016).

Measurements of cavity size based on surface observations suggest water pressure and cavity size do not always vary together. Cavity size is typically inferred from surface motion by measuring bed separation (Section 2.14). Bed separation is measured by removing vertical strain and the vertical component of sliding from the vertical velocity record (e.g. from GPS measurements). It is difficult to constrain water pressure from bed separation alone since any water pressure above the separation pressure will trigger cavity growth and any decrease in water pressure with time will trigger cavity collapse (Howat et al., 2008). The water pressure — basal separation relationship is not always observed to be consistent, the decay in surface elevation can occur over several days despite water pressure levels declining over a single day (Iken and Truffer, 1997; Iken and Bindschadler, 1986). Cavities close due to the deformation of ice under its weight (i.e. "creep" closure), which can take longer than subglacial water drainage develops to alleviate high water pressures (Anderson, 2004; Cuffey and Paterson, 2010). For instance, Anderson (2004) used a cavity growth model that calculated creep closure rates to account for the disparity between the timescales of basal water pressure decrease and surface elevation decay. In other studies, a lag between peak horizontal velocity and bed separation is observed, suggesting that as cavities grow and begin to approach a steady size, the temporary enhancement of sliding speed lessens (Horgan et al., 2015; Howat et al., 2008; Iken et al., 1983). This is consistent with the behaviour of sliding speed predicted by Iken (1981) and suggested by equation 1.6. The caveat of these studies is that Budd-type or Coulomb-type sliding laws do not capture the complete mechanics of transient glacier accelerations, and may underestimate the true rate of acceleration under rapidly changing water pressure.

1.4.2 The role of glacial hydrology on sliding speed

Because transient glacier accelerations are driven by rapid changes in basal water pressure, how water is conveyed along the basal boundary becomes important. Glacier motion can be accelerated, suppressed, or remain unaffected to inputs of surface water depending on the efficiency in which the subglacial drainage can convey basal water (Magnússon et al., 2010; Nienow et al., 2005; Sole et al., 2013; Tedstone et al., 2013)(see Section 2.4.2 for a more detailed discussion of subglacial drainage).

Pronounced speed-up events have been associated with poorly-developed or inefficient drainage systems, such as might be seen at the end of winter when water inputs are low and cavities are small and poorly connected (Iken and Bindschadler, 1986; Kamb, 1987). For instance, Figure 1.8 shows the surface motion response of an outlet glacier in Greenland to surface melting. As soon as positive temperatures begin to develop, surface water variability increases (which is also shown in Figure 1.3). Simultaneous increases in surface elevation and velocity are explained by increased water the rate of water entering the bed can be greater than the discharge capacity of the system, resulting in increasing water pressure and spikes in velocity (Bartholomaus, Anderson, and Anderson, 2008; Bartholomew et al., 2010; Schoof, 2010). The subsequent slowdown towards the end of the melt season is thought to be due to the development of more efficient drainage networks the evacuate basal water from the system (Bartholomaus, Anderson, and Anderson, 2008; Tedstone et al., 2015).

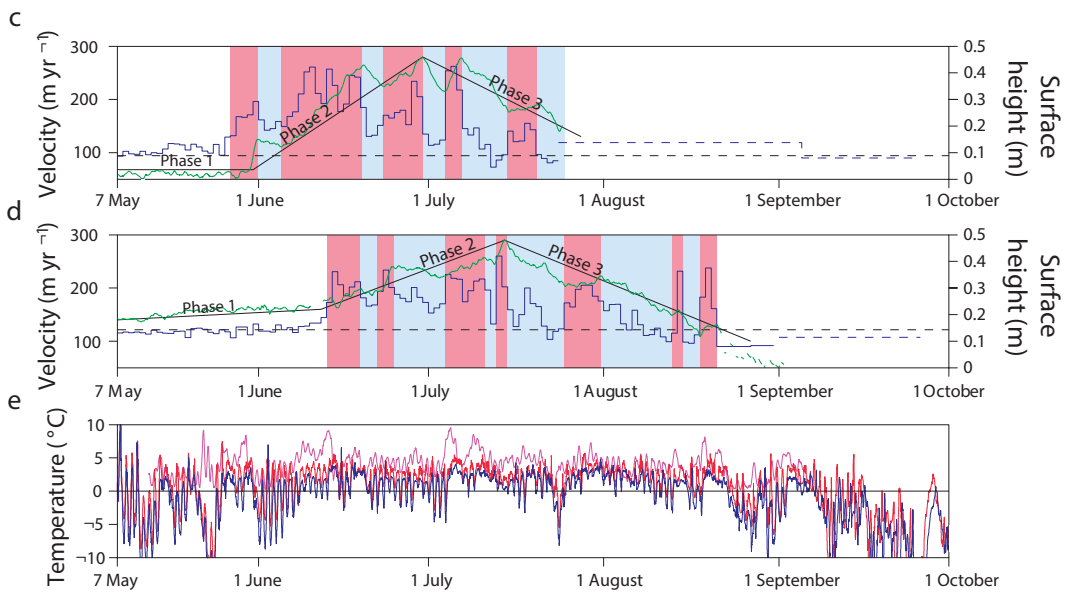

FIGURE 1.8: Seasonal evolution of the subglacial drainage system evident in GPS and surface temperature data from Bartholomew et al. (2010). GPS units installed on the ablation zone of a land-terminating glacier on the Western margin of the Greenland Ice Sheet show increasing velocity and uplift over the melt season. A longer-term uplift and horizontal velocity signal are superimposed with spikes in velocity (speed-ups). The patterns in surface velocity can be explained by an increase in meltwater overwhelming an inefficient drainage system (see Section 2.4.2). The sites are 795 m and 1063 m above sea level respectively

This seasonal evolution of the subglacial drainage system can help explain why, contrary to the predictions of sliding laws, glacial accelerations are not always linked to increases in water input or basal water pressure. Observations of Bench Glacier, Alaska provide an example of an alpine glacier that shows multiple responses to enhanced surface melt during early melt-season and precipitation (Fudge et al., 2009;

Harper et al., 2007). Figure 1.9 shows two phases of acceleration in response to rainfall events where the pressure-sliding relationship is not consistent. The second acceleration occurs for lower water pressures and ceases before water pressure reaches a maximum. Such complexity in the sliding behaviour of two tightly spaced events has been described by differences in the connectivity of the basal drainage system. Figure 1.10 shows two instances in which ice velocity at Bench Glacier increased without a decrease in effective pressure. Furthermore, the second phase of acceleration did not involve any significant change in local effective pressure. The first mode is thought to be associated with bed separation related to cavity growth and the second phase is resulting from a highly connected subglacial system in which a smaller region of the glacier bed is in contact with the bedrock.

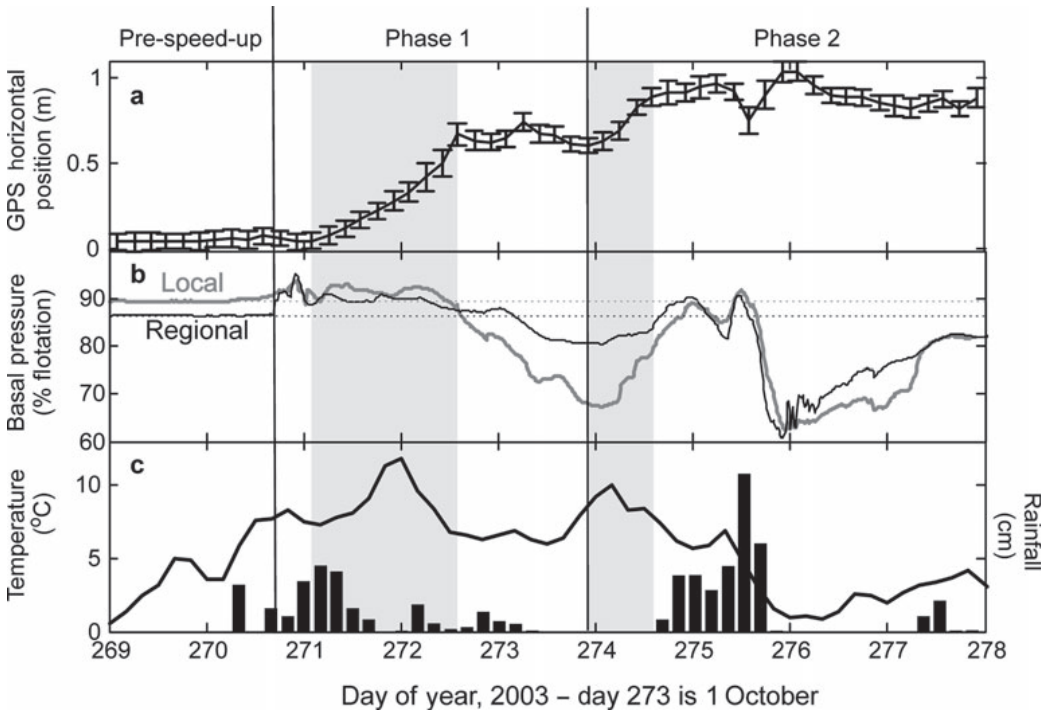

FIGURE 1.9: Inconsistent effective pressure and sliding speed relationship at bench Glacier, Alaska. Borehole observations of Bench Glacier, Alaska presented by Fudge et al. (2009) show that two markedly different phases of acceleration occur following large rainfall events

The full complexities of glacier motion in response to inputs in surface water may not be fully captured by existing sliding laws. In terms of improving assessments of surface water variability on glacier mass loss, the interaction between basal hydrology and sliding should be better constrained. In terms of testing known theory on how

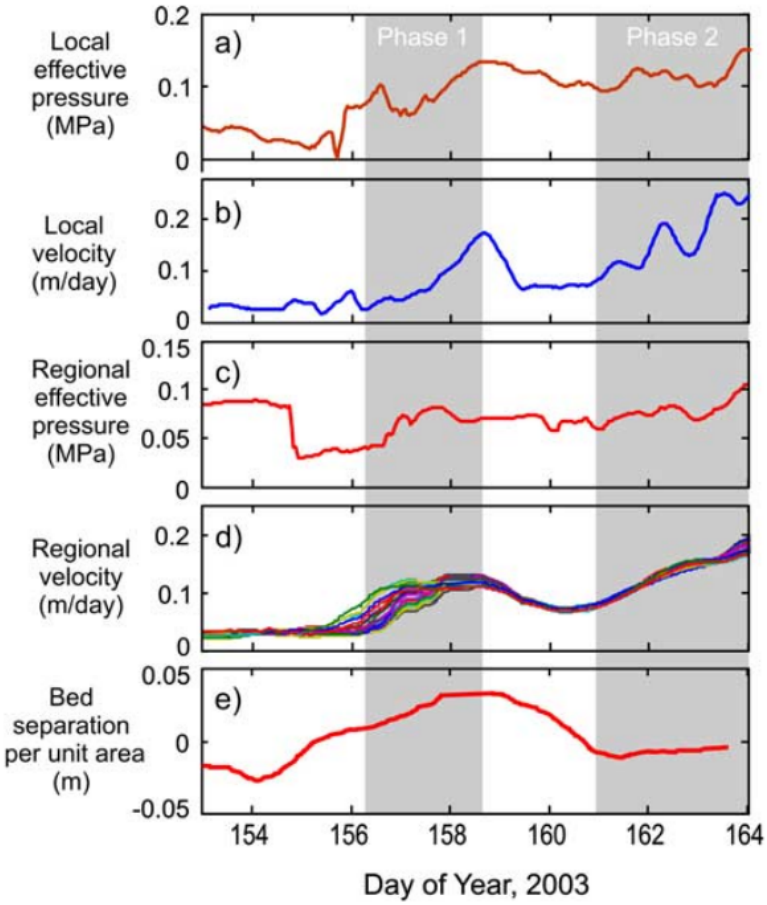

FIGURE 1.10: Two modes of glacier acceleration observed at Bench Glacier, Alaska from Harper et al. (2007). The first sliding event involves increased horizontal motion associated with bed separation due to cavity growth. The second sliding event shows little change in bed separation and is thought to be due to a change in connectivity in the subglacial drainage system.

1.5 Finite-element modelling of ice flow and basal hydrology

One widely used tool for modelling ice flow, and in some cases basal hydrology, is finite-element modelling. Recent interest has focused on the complex interactions between ice flow and basal hydrology that are difficult to observe directly, but can are recreated in models to better understand the importance of the potential feedbacks between surface melt, precipitation and enhanced mass loss due to increased ice discharge (e.g Hewitt, 2013). Gagliardini and Werder (2018), for instance, use Elmer/Ice shallow stream ice flow model coupled with a Glacial Drainage System (GlaDS) hydrology model to demonstrate the increasing sensitivity of ice flow to surface melt input. Their results indicate that a coupled hydrology and ice flow model results in a volume loss between 23–41% greater than a model based purely on mass balance alone.

An effective pressure dependent sliding law is essential for joining a model of basal hydrology to ice flow; however, sliding laws are not always consistent with

the basal hydrology models they respond to. Sliding laws assume a steady-state cavity size, but both the volume and growth rate of cavities influence the rate of sliding. In turn, the growth rate of cavities is controlled by the sliding velocity. Hewitt (2013) calls attention to the fact that a hydrological model where cavity volume is allowed to evolve freely negates the assumption underlying the Coulomb-type law that forces at the glacier base are in balance (Section 2.5.3). Howat et al. (2008), based on observations of horizontal velocity correlating strongly with vertical velocity attributed to cavity growth, argued for the need to include a cavity evolution term into the sliding law. Ultimately, sliding laws may only be applicable in regions where cavity volume is in a near-steady state condition, such as at a distance from subglacial channels or moulins (Cowton et al., 2016; Howat et al., 2008).

Models that provide treatment of both basal hydrology and ice sliding are still in their early stages and improvements could be made to the sliding law (Flowers, 2018; Hewitt, 2013). Field studies incorporated with numerical models may provide a useful avenue in which to constrain existing theory and demonstrate what processes are required in models to reproduce observations of accelerated glacier flow.

1.6 Haupapa/Tasman Glacier

Haupapa/Tasman Glacier resides in Aoraki/Mt Cook National Park, accumulating near the main divide of the Southern Alps. The glacier covers an area of $\sim$95 km^2 and contains $\sim$30% of New Zealand's perennial ice (Chinn, 2001). Several tributaries contribute to Haupapa/Tasman Glacier's flow field, most notably the Hochstetter Ice Fall which feeds the lower glacier (Figure 1.11). High erosion rates from the surrounding mountains keep the lowermost 10 km covered in rocky debris that exceeded 3 m thick in places, though the thickest parts are now gone (Kirkbride and Warren, 1999).

In recent decades, Haupapa/Tasman Glacier has undergone significant retreat and calving. In 1986, a proglacial lake began to develop from patches of surface melting, initiating a period of terminus retreat (Chinn, 1996). Since the lake formed, the terminus has retreated at an average rate of 180 ma^{-1} and by 2013 the lake covered an area of 6.7 km^2 (Chinn, 1996; Hart, 2014).

Haupapa/Tasman Glacier, New Zealand, has exhibited rapid accelerations over periods of $\sim$24 hours in response to episodes of heavy rainfall (Figure 1.11) (Horgan et al., 2015). Surface velocities of up to 15 times its background velocity (velocity measured as a linear regression of position over a 24-hour window) are reported in Horgan et al. (2015). Speed-up events of this size provide a strong basal sliding signal compared to the background velocity field. A sliding anomaly of this size is desirable for measuring the response of a glacier's motion to rapid changes in surface water input.

Haupapa/Tasman Glacier Site Map

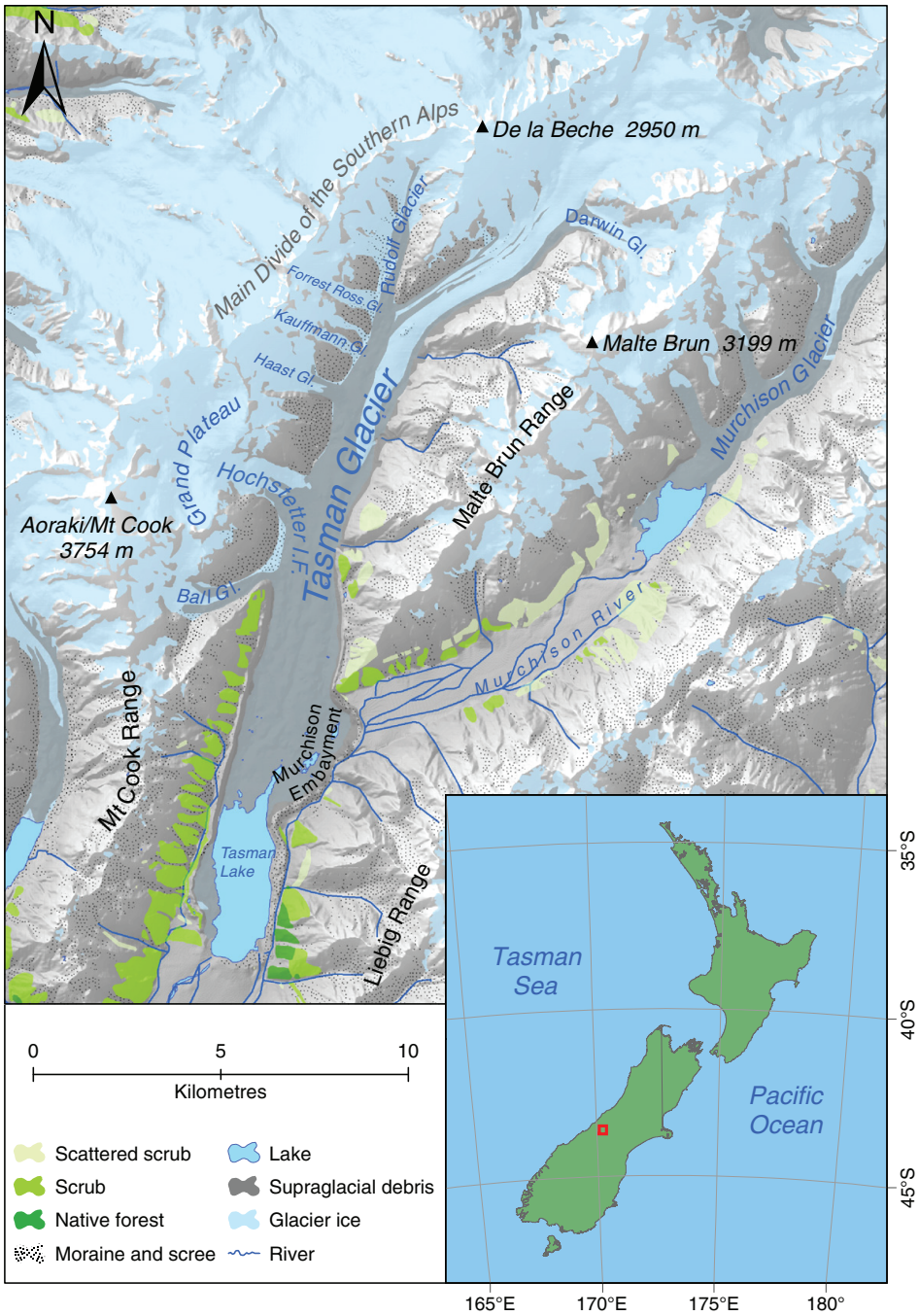

FIGURE 1.11: A map of Tasman Valley and surrounding Aoraki/Mt Cook National Park from Redpath et al. (2013). Several tributary glaciers flow into the main trunk of Haupapa/Tasman Glacier. Topographic data for this map is sourced from the LINZ NZTopo Database.

1.6.1 Rainfall events

Aoraki/Mt. Cook National Park receives high annual rainfall, up to $\sim$14 m yr^{-1}, and commonly experiences episodes of intense rainfall (Henderson and Thompson, 1999). High precipitation rates are largely attributed to the orographic effect caused by the Southern Alps which provide a high reaching ($\sim$ 2.5km) and extensive ($\sim$ 600km) barrier to prevailing westerly winds (Henderson and Thompson, 1999). While the western side of the Southern Alps generally receives a more consistent rainfall, large storm events that affect the entire divide often progress northeast from the passage of cold fronts from the south (Henderson and Thompson, 1999). The progression of storms is fast enough such that even within the largest basins draining the main divide, intense rain is onset within three hours (Henderson and Thompson, 1999). Rainfall during storms can then be considered as falling simultaneously across Haupapa/Tasman Glacier and surrounding valleys (Figure 1.11).

The main trunk of Haupapa/Tasman Glacier is part of a glacial complex that drains the area of the main divide covering Mt Cook and surrounding peaks into Tasman Valley (Figure 1.11). This provides a catchment area of $\sim$160 km^2 through which water is collected during rainfall events (Ministry for the Environment, 2010). Rainwater feeds into the glacier by landing directly the main trunk of Haupapa/Tasman Glacier, the surface of tributaries, and along valley walls that surround Tasman and its tributaries.

1.6.2 Haupapa/Tasman Glacier's bed

A limited number of studies have been conducted to investigate the thickness and geology of Haupapa/Tasman Glacier's bed. Seismic surveys in the early 1970's suggested thick ice of 535-725 m near the Ball Glacier confluence (Broadbent, 1973)(Figure 1.11). Gravity surveys conducted nearby suggested ice thicknesses of $\sim$ 600 m, suggesting an overdeepening in this region (Broadbent, 1974; Claridge, 1983; Nobes et al., 2010; Purdie et al., 2016). The ice thickness near the terminus has previously measured to be $\sim$200-220 m, which agrees well with lake bathymetry records (Broadbent, 1974; Claridge, 1983; Purdie et al., 2016).

The nature of the contact between basal ice and the glacial bed is not known, though limited observations suggest a till layer 100-200m thick near the terminus (Nobes et al., 2010). Thick till layers are observed in nearby glaciers, such as a 620 m thick till observed in seismic data from Lake Pukaki, to the south of the terminus (Kleffmann et al., 2010).

In lieu of reliable constraints of Haupapa/Tasman Glacier's bed, hard-bed sliding mechanics will be assumed to apply – as opposed to soft-bed mechanics which describes slip over subglacial till (Cuffey and Paterson, 2010). Hard-bed sliding is mathematically easier to implement that slip over a deformable bed. Furthermore, for water pressures close to flotation, hard bed sliding follows similar behaviour to

the plastic deformation of saturated til, and so the hard-bed approach may be appropriate despite a lack of constraint on the degree of sediment at the base of Haupapa/Tasman Glacier (Brondex et al., 2017; Pimentel, Flowers, and Schoof, 2010; Schoof, 2005, 2006).

1.6.3 Observations of glacier flow field

Large-scale observations of Haupapa/Tasman Glacier's surface velocity have typically relied on feature tracking from satellite imagery (Herman, Anderson, and Leprince, 2011; Kaab, 2002; Quincey and Glasser, 2009; Redpath et al., 2013). The rocky debris cover across Haupapa/Tasman Glacier creates distinct surface features that track the change in surface position. Cross-correlating two images of the glacier after some time interval shows where similar pixels have moved and hence velocity vectors can be derived. Quincey and Glasser (2009) describes three "flow units" that contribute the majority of ice flow into the Lower Haupapa/Tasman Glacier: the head of the Haupapa/Tasman Glacier, which drains snowfields of the main divide; the Rudolph glacier; and the Hochstetter Ice Fall, which drains the Grand Plateau and eastern flanks of Mt. Cook over a steep gradient change (Figure 1.11). Using two pairs of ASTER (Advanced Spaceborne Thermal Emission and Reflection Radiometer) images of Haupapa/Tasman Glacier's surface (2009-2010 and 2010-2011), Redpath et al. (2013) derived flow fields for the Haupapa/Tasman Glacier. They demonstrate that while Rudolph glacier provides a significant influx into the Upper Haupapa/Tasman Glacier, the main trunk is still the dominant velocity signal (Redpath et al., 2013). There is a significant discontinuity in the velocity field where the Hochstetter ice fall enters the main trunk (Figure 1.12). The Hochstetter Ice Fall has a large control on the velocity field of the Lower Haupapa/Tasman Glacier and provides a large degree of incoming flux. However, the ice flow is not divergent at Hochstetter confluence, so it is likely that the Upper Tasman also some control over the final flow at the lower part of the glacier (Redpath et al., 2013). Between 2009 and 2011, Redpath et al. (2013) demonstrated that ice surface-flow accelerated $\sim$25% at Rudolf Glacier confluence while the Upper Tasman and Hochstetter tributaries slowed significantly suggesting a more dynamic background field than previously thought (Herman, Anderson, and Leprince, 2011; Redpath et al., 2013)

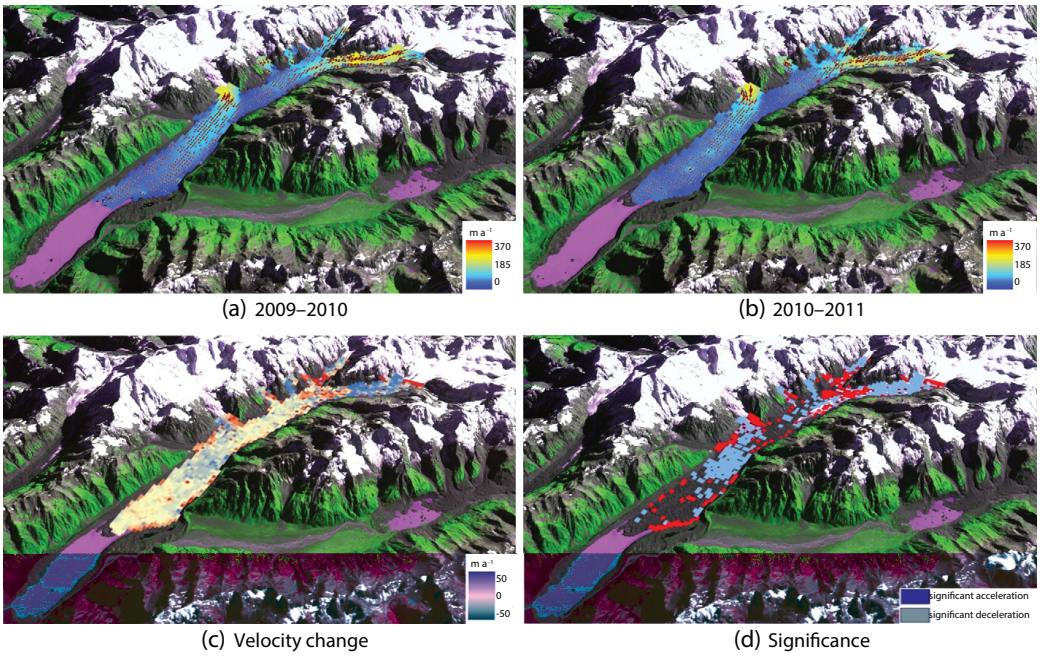

FIGURE 1.12: Observations of Haupapa/Tasman Glacier's flow field using satellite imagery. The displayed velocity fields are derived from ASTER imagery by Redpath et al. (2013). Plot c) shows the change in velocity of the glacier's flow field between 2009-2010 and 2010-2011

1.6.4 Surface observations of Haupapa/Tasman Glacier's speed-up events

Seventeen rapid speed-up events in response to high rainfall rates were recorded by several GNSS (Global Navigation Satellite System) instruments installed on Tasman Glacier between November 2012 and January 2015 (Horgan et al., 2015). Each peak in horizontal velocity is preceded by a period of elevated rainfall, which is thought to flood the subglacial drainage system and raise the basal water pressure (Figure 1.13). The basal water pressure near the glacier's terminus is approximated by the lake-level record. This record demonstrates that the maximum rate of change in lake-level with time correlates with the maximum bed separation rate and peak velocity (Figure 1.13). This finding suggests that a) the speed-ups are a water pressure driven process and b) that the sliding velocity is proportional to the rate at which water is added (or removed) from the system, not the total surface water input, which is in line with the conclusions of Iken and Bindschadler (1986), Schoof (2010), and Sugiyama and Gudmundsson (2004).

During speed-up events at Haupapa/Tasman Glacier, the vertical surface motion is interpreted to be the result of cavity growth under elevated water pressures (Horgan et al., 2015). Up to 56 ± 2 cm of vertical displacement is observed in Horgan et al.'s record; however, only $\sim$4 cm of vertical displacement can be attributed to vertical deformation of ice and the vertical component of the sliding velocity during speed-ups, the rest is thought to be due to bed separation (Horgan et al., 2015). Bed separation is the uplift of a glacier's base due to an increase in the average volume of water-filled cavity per area of glacier bed (Anderson, 2004; Iken et al., 1983). During speed-up events at Haupapa/Tasman Glacier, peaks in bed separation are coincident with the maximum rate of lake-level change and while the horizontal velocity is increasing rapidly (Figure 1.13). Horgan et al. (2015) interpret these speed-up events as occurring in two stages. The first stage involves an initial rapid increase in velocity as the addition of rain-water raises basal water pressure, triggering the growth of cavities. Secondly, sliding velocity plateaus at an elevated value until bed separation reaches its peak value. Peak bed separation marks the cessation of cavity growth, which is followed by a drop in horizontal velocity background levels while the surface remains elevated. Finally, the lake level and bed separation decay over several days as cavities close under viscous creep (Figure 1.13) (Cuffey and Paterson, 2010; Horgan et al., 2015).

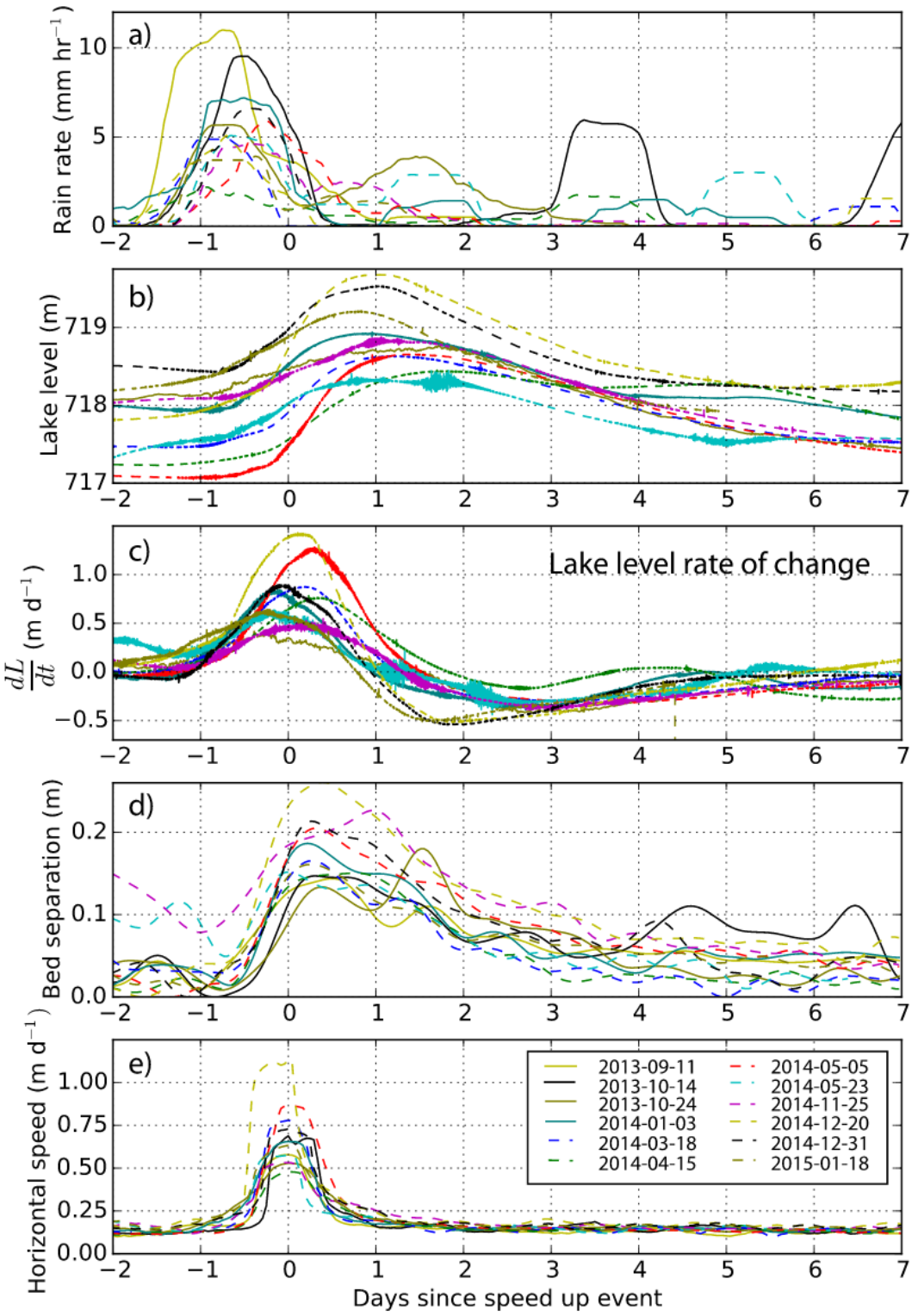

FIGURE 1.13: Speed-up observations of Haupapa/Tasman Glacier from Horgan et al. (2015). The records of rainfall, lake-level, and surface velocity provide an insight into the evolution of the processes inducing speed-up events. Plots from top to bottom are: of rain rate (mm hr^{-1}), lake level (m), rate of lake level change (m d^{-1}), bed separation (m), and horizontal speed (m d^{-1}). Measurements of horizontal and vertical motion were made by GPS instruments. The level of the proglacial lake indicates basal water pressure at the glacier sole.

Rainfall-Horizontal Velocity relationship

The rainfall–horizontal velocity at Haupapa/Tasman Glacier follows a power-law relationship (Figure 1.14), however, does not appear to display an upper bound. As rain-rate increases, the total sliding speed generally scales up, supporting the idea that a greater rate of water entering the subglacial drainage system translates into a greater effective pressure drop and hence faster sliding (Horgan et al., 2015). However, the factors that limit sliding speed don't appear to be present in the data; we would expect that if Coulomb-type sliding law applied to accelerated sliding at Haupapa/Tasman Glacier, then even if the base stopped providing basal stress under high water pressure, that friction against the valley walls or stretching within the ice would act to balance the glacier's driving stress (Cuffey and Paterson, 2010). Either that rainfall rates are not great enough to produce water pressures where cavitation is significant (or as effective pressure approaches zero)(Equation 1.3) or the rainfall rate is not a complete proxy for basal water pressures. Due to the bed separation and large water input rates observed, it is unlikely to be the former case (Horgan et al., 2015; Figure 1.13). It is more likely that there are additional processes in the hydrological system or controls outside of the basal environment that limit the total sliding velocity. Providing tests for what these processes and global controls might be could be achieved through a finite-element framework.

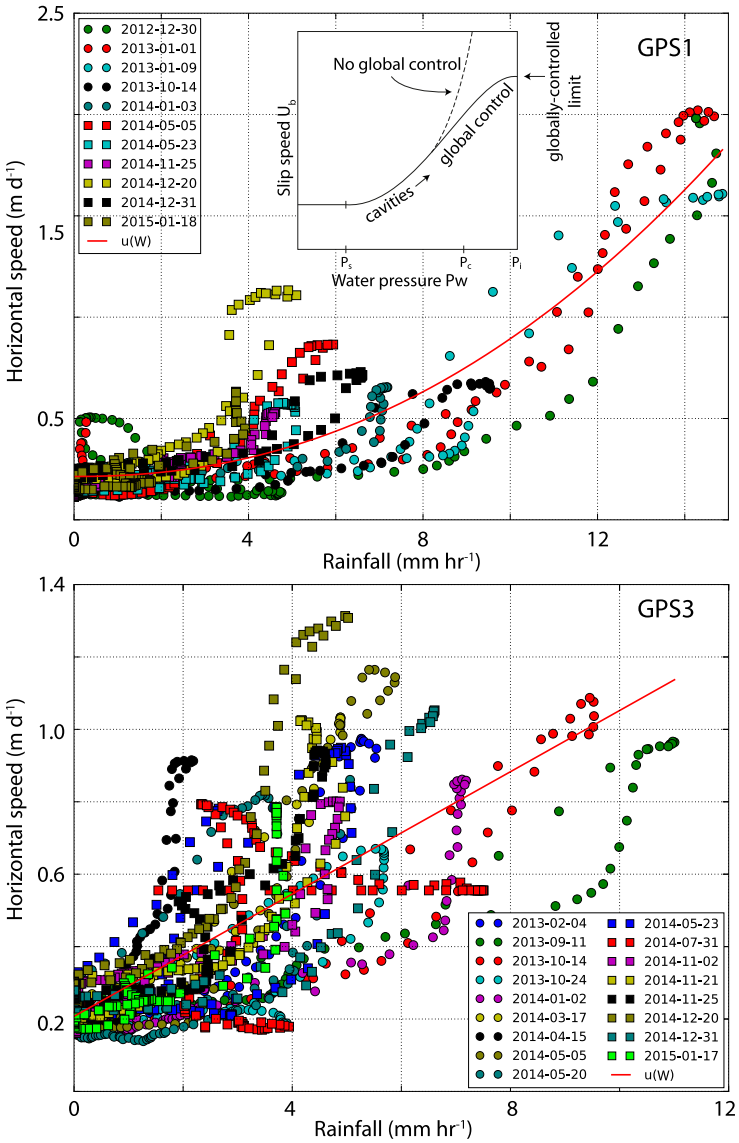

FIGURE 1.14: The relationship between rainfall rate and horizontal velocity for several speed-up events presented in Horgan et al. (2015). The lag between the rainfall-rates and horizontal velocity are accounted for by cross-correlating the two time series to find the time delay between peak rainfall and speed for each event. GPS1 is located within 500 m of the calving front and GPS3 is located 4.5 km upstream.

1.7 Research Questions

This study is motivated by the need to better constrain the impact of surface melting and rainfall on glacier motion. However, the physical processes underlying the interaction of subglacial water and basal sliding are not fully understood. Haupapa/Tasman Glacier undergoes significant accelerations from background velocity in response to rainfall, meaning it provides an excellent case study for studying the processes that lead to rapid sliding. This thesis aims to address the following questions:

1. *Is the relationship between horizontal and vertical displacement consistent across Haupapa/Tasman Glacier during speed-ups, or is spatial variability significant?* Using two GNSS (Global Navigation Satellite System) units, Horgan et al. (2015) argued that cavity growth has a significant influence on basal motion at Haupapa/Tasman Glacier during speed-ups. This influence inferred from the obsreved hysteresis between horizontal acceleration and bed separation. The extended GNSS network used in this study may help constrain whether the mechanisms driving speed-ups are consistent across Haupapa/Tasman Glacier or whether it is only significant near the centre-line.

2. *If cavity growth causes enhanced basal motion during rapid water input at Haupapa/-Tasman Glacier, what are the consequences of modelling speed-up events using a sliding law which assumes a steady-state cavity size?* Cavity growth and collapse is thought to be occurring during speed-ups at Haupapa/Tasman Glacier (Horgan et al., 2015); however, sliding laws do not include a treatment of cavity evolution. A finite-element model creates a space in which to recreate the processes of enhanced sliding and cavity growth in order to match horizontal and vertical GNSS records (Chapter 5). Whether the surface displacement recorded by GNSS units motion can be replicated or not will be informative on the relative importance of what processes both enhance and limit sliding velocity. Of particular interest are constraints on basal water pressure, which is not expected to exceed the weight of the overlying ice, and basal roughness, where it is unlikely for the height of bed obstacles to be greater than obstacle separation.

1.8 Summary

Here, the context of rapid acceleration as a poorly constrained process that leads to enhanced glacial mass loss is introduced. A better understanding of the interaction between surface water and basal friction is required, but sliding laws that represent this interaction are not currently able to describe the full complexity of how subglacial drainage affects ice motion. Rain-induced speed-up events at Haupapa/Tasman Glacier will be investigated in this study to observe surface motion

during rapid acceleration. Surface observations will provide constraints on a finite-element model used to assess the consequences of using a Coulomb-type law during speed-ups. The following chapter will discuss the theoretical background behind subglacial drainage and basal sliding that are used to explain accelerations in sliding speed.

Chapter 2

Background Theory

2.1 Glacial hydrology and the glacier bed

Clarifying how subglacial water interacts with basal ice to trigger accelerated sliding is made difficult by the fact that direct observations of the glacier bed during acceleration are rare (Clarke, 2005). Accordingly, sliding laws have largely been informed from surface observations and theoretical derivations using idealised glacier beds. Similarly, our understanding of the storage and flow of water beneath glaciers is informed primarily by observations outside the glacial interior (e.g. from changes in surface motion, discharge of rivers that drain glaciers etc.). While glacier beds have been instrumented and photographed in several studies (e.g Blake et al., 1994; Kamb and LaChapelle, 1964), it is far more convenient to document the behaviour of the glacier surface. Significant accelerations in surface displacement result from changes in subglacial drainage (Section 2.4.2) and/or glacier sliding (Section 2.2). Recording changes in surface motion provide constraints on the processes that involve the flow of water beneath the glacier and how ice slides across bedrock (Clarke, 2005; Cuffey and Paterson, 2010).

This chapter presents the existing theoretical models of basal water flow and ice sliding that have been used to model glacial hydrology and ice flow. Any numerical model attempting to capture rapid changes in glacier velocity necessarily includes some treatment of basal water flow and its effect on ice-bedrock friction. The flow of surface water into and beneath a glacier is a primary influence on hourly-seasonal velocity changes for land-terminating glaciers (e.g Gagliardini and Werder, 2018; Iken and Bindschadler, 1986; Nienow et al., 2005; Section 1.2). Hence, the interaction between water and basal ice is fundamental to basal sliding theory — i.e. the physics describing how ice slides at a steady speed over its bedrock, where the topography of a glacial bed has strong controls on sliding speed. This chapter will illustrate how steady sliding speed can be perturbed by changes in subglacial drainage which lead to speed-up events.

2.2 Glacier Flow Field

Nearly all glacier velocity observations are made at the surface. Because surface motion gives the combined motion of all movement within and beneath the glacier, the sliding velocity must be isolated from the internal glacier velocity (Figure 2.1). Movement within the glacier itself occurs as viscous deformation under the weight of the ice. Viscous deformation is the macroscale phenomena of dislocation creep which occurs on the scale of individual ice grains. Dislocation creep involves planes of ice crystals sliding past each other (Cuffey and Paterson, 2010). Glacier velocity increases from the bed to the surface due to the relative motion of these ice layers (Figure 2.1). The glacier itself also moves relative to its underlying geology by sliding across it (as in the "Warm Rigid Bed (Class 1)" example in Figure 2.1). If the glacier bed is made of weak sediments, the deformation of these sediments also provides some velocity downslope (as in the "Soft Bed (Class 3 & 4)" examples in Figure 2.1). Glacier beds can be considered either "hard" or "soft" depending on the strength and amount of subglacial sediments, where hard beds only undergo significant sliding and soft beds mostly experience sediment deformation with some sliding (Clarke, 2005). The total observed surface velocity is then a combination of these three components:

$$\vec{u}_{surf} = \int_{z_b}^{z_s} \left(\vec{u}_b + \vec{u}_{sed} + \vec{u}_{def} \right) dz \tag{2.1}$$

where $\vec{u}_{surf}$ is the surface velocity field, $\vec{u}_{def}$ is the deformation field of the glacial ice, $\vec{u}_b$ is the sliding velocity and $\vec{u}_{sed}$ is the deformation rate of the underlying geology.

For glaciers assumed to slide over hard beds, high sliding velocities and large speed-ups are observed in both temperate and polar environments (Copland, Sharp, and Nienow, 2003; Cuffey and Paterson, 2010; Howat et al., 2008; Iken and Bindschadler, 1986). Because temperature has a strong control on ice viscosity, glaciers in temperate environments tend to have faster deformation speed (Cuffey and Paterson, 2010). Warmer conditions also mean more well-lubricated beds throughout the year and so sliding makes up a greater proportion of the total surface velocity. In polar regions of high elevation, "Cold Rigid bed" glaciers (Figure 2.1) are found where most of the motion is due to deformation creep for glaciers sliding over a hard bed (Cuffey and Paterson, 2010). However, surface water inputs can still cause significant speed-ups by temporarily lubricating the bed (Copland, Sharp, and Nienow, 2003; Pelt et al., 2018). Variations in surface velocity over hourly-seasonal scales can typically not be described by changes in deformation rate due to warmer temperatures increasing ice viscosity. Either the temperature changes required to reproduce observed speed-ups are too large (i.e. the ice would melt the ice before it could achieve high enough viscosity) or observed surface temperature variation at the surface, especially for ice sheets and polar glaciers, can often too short-lived, and ice too poor a conductor of hear, to significantly warm the glacier interior to match observations surface velocity changes (Zwally et al., 2002). Hence, explaining observations

of rapid changes in a glacier's surface velocity can only be described by processes occurring at the base of the glacier (Clarke, 2005; Cuffey and Paterson, 2010).

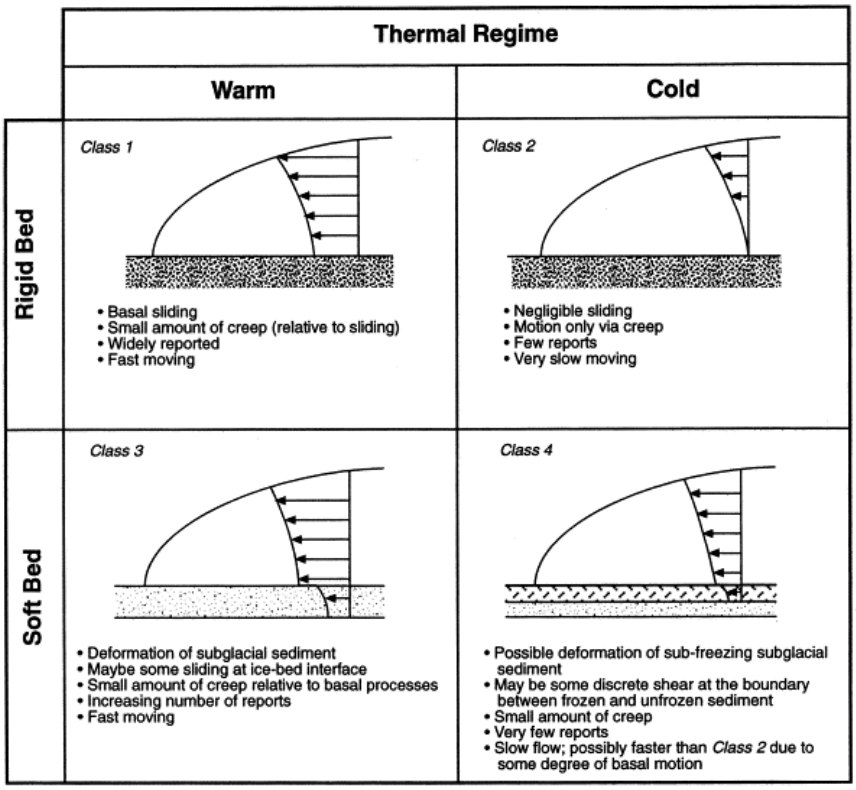

FIGURE 2.1: Components of a glacier's velocity field

2.3 Sources of rapid water inputs

Glacial acceleration over short timescales has been linked to the rate of surface water entering the glacier's subglacial drainage system (Kamb et al., 1994; Schoof, 2010). While there are several ways surface water can be sourced before being transported to the subglacial environment, the most commonly considered is surface melt (Flowers, 2018; Fountain and Walder, 1998).

2.3.1 Surface melt

Glaciers gain ice at the surface from the accumulation of snow and lose ice from ablation (processes that lead to ice loss). One of the main forms of ablation is melting at the surface. Surface meltwater is generated when there is a surplus of energy at the surface (from net surface radiation, latent heat, and sensible fluxes and internal heat transfer) and air temperatures at the melting point of ice (Cuffey and Paterson, 2010). Water that exits the glacier without refreezing results in mass loss and usually ends up either draining into river systems or channelled directly into oceans (for marine-terminating glaciers). The total meltwater run-off is not only an essential value in calculating the annual surface mass balance of a glacier but is also useful

in explaining enhanced glacier or ice sheet sliding (Bartholomew et al., 2010; Iken and Bindschadler, 1986; Van De Wal et al., 2008). Even in the Greenland Ice Sheet where ice is over a kilometre thick, surface melt production has been correlated to an increase in surface velocity recorded by GPS instruments (Zwally et al., 2002).

Melting at the surface is often the largest and most consistent source of water (Fountain and Walder, 1998). Surface melt mainly affects ice motion in a glacier's ablation zone. The lower elevation ablation zone is warmer and typically has exposed ice and glacial crevasses. Hence, melting is more intense and any water produced at the surface is readily able to drain to the base, meaning the response of basal motion is strongest. Whereas the opposite is true as you move into the accumulation zone where temperatures are generally cooler and water travels slowly through porous firn (Fountain and Walder, 1998).

2.3.2 Lake Drainage

The drainage of surface lakes along Greenland's margins induces significant velocity responses in outlet glaciers (Box and Ski, 2007; Das et al., 2008b; Stevens et al., 2015). Surface lakes form in areas with low surface slope where channels of surface melt converge on local low points (Cuffey and Paterson, 2010). Lakes can drain rapidly through fractures in the ice that propagate to the base, locally flooding the basal environment with large quantities of water (Das et al., 2008a). Das et al. (2008b) reported a Greenlandic surface lake that underwent an initially slow $\sim$ 16 hr drainage, before rapidly draining for $\sim$ 1.4 hr. During the $\sim$ 1.4 hr of drainage, a nearby GPS station experience an uplift of 1.2m and horizontal displacement of 0.8m.

2.3.3 Rainfall

Heavy rainfall and rapid surface melt produce similar effects upon basal water pressure and enhanced ice motion (Iken and Bindschadler, 1986). Studies linking basal water pressure to variations in surface velocity need to keep a record of both temperature (to infer melt rates) and precipitation to infer the trigger of speed-ups (Fudge et al., 2009; Hooke et al., 1989; Howat et al., 2008). Rainfall is typically more significant in temperate, alpine environments where precipitation falls as rain for a greater portion of the year and where mountain valleys provide an effective catchment. Though, large rainfall events are observed in Greenland Ice Sheet where, for example, large speed-up events that do not follow the seasonal trend in surface melt production can be explained by episodes of heavy rainfall (Sole et al., 2013).

2.4 Subglacial Hydrology

A glacier's sliding speed can be heavily influenced by the addition of water to the glacier's base (Cuffey and Paterson, 2010; Iken and Bindschadler, 1986). Greater water content at the base causes a decrease in the contact area between ice and bedrock.

A decrease in ice–bed contact area reduces basal friction by lowering the effective pressure of ice upon bedrock and allows faster sliding. However, the flow of water and sliding speed are both inextricably linked. Greater sliding speed can also open space and increase the connectivity of drainage pathways at the bed.

2.4.1 Routing surface water to the glacier bed

For water collected at the glacier surface to have any significant effect on basal friction, pathways through the ice must exist and accommodate large quantities of water to the glacier bed. Ice itself is virtually impermeable, meaning that water flow must be accommodated through cracks or tunnels in the glacier (Fountain and Walder, 1998). Crevasses are a common feature of glaciers that are thought to convey surface water into the glacier and, in some instances, to the glacial bed (Das et al., 2008a; Fountain and Walder, 1998; Stenborg, 1973). A crevasse forms due to tensile stresses in the ice and water pressure in a crevasse (if present) acting together overcome glacial ice's fracture toughness (a material property that represents the threshold elastic stress needed to induce fracture)(Veen, 1998). Fractures can also open during instances of basal acceleration that enhance tensile stresses within a glacier (Kamb and Engelhardt, 1987; Roux et al., 2010; Stevens et al., 2015). The steady size of fractures is sustained by a continual competition of flowing water causing melting and creep closure of ice (Röthlisberger, 1972). Fractures in glacial ice are thought to develop into a network of fractures that eventually converge at the glacier's base (Fountain and Walder, 1998; Figure 2.2).

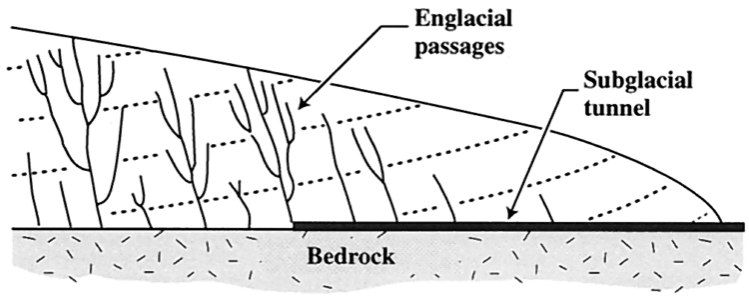

FIGURE 2.2: A figure of englacial networks from Fountain & Walder (1998). The dashed lines are lines of equal hydropotential in a glacier.

Surface water can also drain to the bed along the glacier's margins or into vertical shafts that connect directly to the glacier's base. Like englacial conduits, these vertical shafts, referred to as *moulins*, also develop from wall melting of fractures (Fountain and Walder, 1998). These differ from the englacial network in that they provide a much faster flow of water to the glacier's bed and transport water near-vertically from where it enters at the surface. Moulins provide a larger flux of water to a glacier's base but are generally more sparse than crevasse and fracture networks (Fountain and Walder, 1998).

2.4.2 Subglacial drainage systems

Basal friction is influenced by the subglacial water pressure (Section 1.3), which in turn depends on the rate of water entering the glacier bed and the efficiency this water can be drained (Kamb, 1987). The subglacial drainage system is essentially the "plumbing" of the glacier: a series of water channels hidden beneath the ice that convey water towards the glacier terminus. Exposed glacier beds provide an insight into the nature of subglacial drainage; these beds are typically comprised of undulating rock surfaces with interweaving channels between protruding rock obstacles (Walder and Hallet, 1979). Precipitates (materials left by the evaporation of fluid) left in these channels provide evidence of previous fluid flow in the area (Cuffey and Paterson, 2010; Iken and Bindschadler, 1986; Walder and Hallet, 1979). Active subglacial drainage systems are difficult to map out and are only occasionally accessed by tunnelling projects or borehole photography (Cuffey and Paterson, 2010; Kamb, Engelhardt, and Harrison, 1979; Kamb and LaChapelle, 1964). It is more common, and far more convenient, to infer changes in the subglacial drainage system based on the time it takes for surface water to drain from the surface, through the glacier, along the glacier bed, and out of the terminus (i.e. the "traverse time" of water through the glacier). Traverse time can be measured by adding a tracer material that is not created naturally in the region directly into the glacier where surface water drains to the bed (e.g. moulins) and measuring its concentration in glacial discharge at the other end (Iken and Bindschadler, 1986; Werder, Schuler, and Funk, 2010). This is typically achieved by using radioactive dyes, such as displayed in (Figure 2.3). The peak on the left ("Injection #2") shows that the dye inserted at the surface travels much faster during the first injection and the material also arrives over a shorter time. The second peak relates to slower drainage where the arrival of the material is across a broad range of times – suggesting a slower, meandering flow. In general, there are two observed modes of subglacial drainage: "fast" or "slow" type drainage.

Fast or "channelised" drainage

"Fast" drainage involves subglacial water being efficiently conveyed through a series of large channels that cover a relatively small part of the bed. In this model of drainage, subglacial channels form an arborescent (tree-like) network with a central trunk orientated down-glacier (Figure 2.4). Smaller channels converge on each other, becoming continually larger until they reach the central tunnel that eventually emerges at the terminus. Large channels are sometimes seen at the base of glaciers following large discharges of subglacial water (Figure 2.5). Hence, they are thought to provide the most efficient and direct transport of beneath a glacier. These channels are typically much larger than the smaller channels weaving between bedrock topography observed in deglaciated beds (Walder and Hallet, 1979).

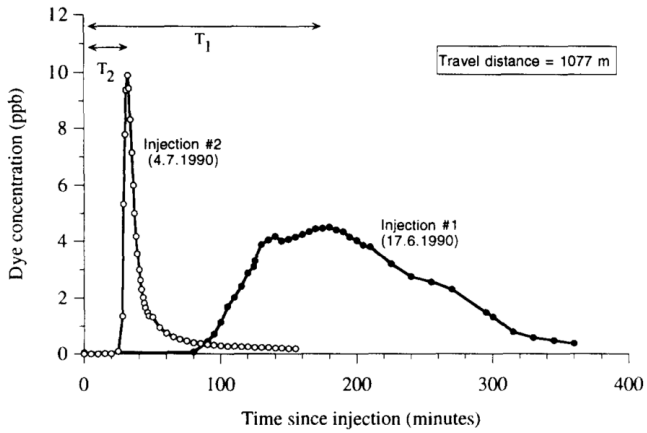

FIGURE 2.3: An example of two curves of dye concentration versus time measured in an outlet stream near the terminus of a glacier (Hubbard, 1998). The plots show radioactive dye concentration with time. The peak on the left demonstrates a subglacial drainage system that is in an "efficient" mode as the dye is quickly transported through the glacier and arrives over a small time window. The peak on the right suggests an "inefficient" subglacial drainage system in which the dye arrive much later and over a longer time period which suggests a slow, indirect flow.

These larger channels are referred to as R-channels, after Röthlisberger (1972) who provided a physical mechanism for how these natural tunnels could be sustained. An R-channel grows from the flow of water dissipating heat against the sides causing melting. Simultaneously, the walls of the channel are closing in on itself as the glacial ice deforms under it's own weight. A balance between melting and creep closure keep an R-channel open.

Because R-channels are thought to provide efficient and direct pathways for subglacial water, they reduce water pressure. By creating a localised zone of low water pressure, R-channels can draw water from nearby cavities (Andrews et al., 2015; Werder et al., 2013). The resulting increase in water flow causes further wall melting and decreasing water pressure (Fountain and Walder, 1998; Röthlisberger, 1972). Effective pressure N can then increase over a significant portion of the bed and, in this way, the development of channels can provide a control on limiting sliding speed in glaciers and ice sheets (Andrews et al., 2015).

Slow or "distributed" drainage

Slow water transit speeds are thought to represent water flow through a series of poorly-connected cavities that exist in the lee-side of bedrock obstacles (Figure 2.6). In this state, water flow is "distributed" in a cavity network across a large region of the bed (as opposed to converging in discrete channels)(Fountain and Walder, 1998). Subglacial Water is thought to follow indirect paths to the terminus through confined channels that are much smaller in cross-sectional area compared to R-channels (Figure 2.4, 2.6). Cavity volume is unable to be sustained by wall melting because of low

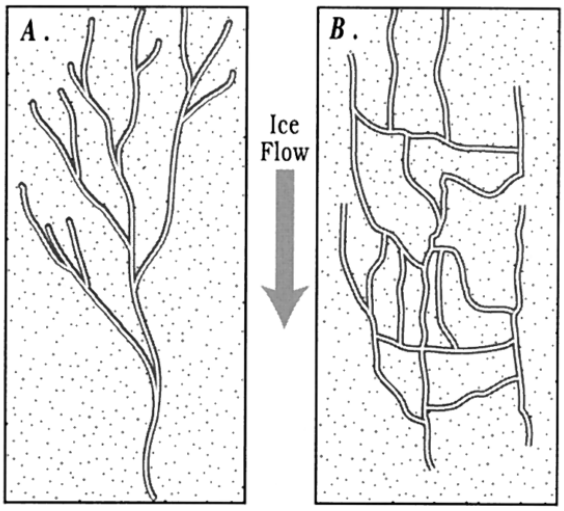

FIGURE 2.4: An idealised plan view of (A) a channelised and (B) a distributed subglacial drainage system (Fountain and Walder, 1998).

flow rates in a distributed drainage system. However, due to inefficient flow, water pressures are generally high and can provide enough support to balance closure under creep deformation, eliminating the need for opening by wall melting.

Distributed drainage has the opposite effective pressure response to changes in water flux compared to channelised drainage. Because the cavities and interconnecting channels are smaller in volume than R-channels, and water flow is indirect, water volume builds up instead of being drained away. Hence, if water rapidly enters a cavity network, water pressures can rise and faster sliding occurs (Cuffey and Paterson, 2010). However, sliding speeds are ultimately limited by cavity opening: faster sliding opens cavities and the conduits between them, increasing drainage and ultimately alleviating water pressure (Mair, Sharp, and Willis, 2002; Schoof, 2010). Instances of low effective pressure in a distributed drainage system could explain rapid sliding observed in Haupapa/Tasman Glacierduring episodes of high rainfall (Horgan et al., 2015)(Section 1.3.2)

Effective Pressure

In the study of glacial hydromechanics, the relationship between water flow and the forces that govern the motion of sliding are thought to be greatly affected by the competition between surface runoff and the capacity of the drainage system (Flowers, 2011). When there is more water than the subglacial drainage system has room to accommodate water pressure increases. Elevated water pressures result in a greater supporting pressure balancing the overlying weight of the ice and decreased ice–bed contact due to cavity growth (both of which lead to a reduction in basal stress) (Cuffey and Paterson, 2010; Lliboutry, 1986). Hence, the link between water flow and sliding is often considered to be the effective pressure (N) of ice against bedrock, i.e

FIGURE 2.5: A large subglacial channel (or R-channel after Röthlisberger, 1972) exposed at Pastaruri, Peru. Image sourced from Cuffey and Paterson (2010)

the balance between the pressure due to the overlying weight of ice P_i and the water pressure P_w:

$$N = P_i - P_w \tag{2.2}$$

Ideally, the sliding velocity response across a glacier bed would be known if the effective pressure could be mapped across its entirety. However, sampling subglacial water pressure to produce such a map is made difficult by the challenge of drilling boreholes through glacial ice to sample water pressure. Moreover, existing studies of water pressure in borehole arrays can produce significantly different water pressure readings even when sampled at proximity to each other (Hubbard et al., 1995; Rada and Schoof, 2018).

The mechanical behaviour of channelised and distributed systems

Channelised and distributed drainage systems have opposite effective pressure responses to increased surface water flux. In the case of the distributed system, when water discharge through the conduits increases, the effective pressure drops. This equates to an increase in water pressure because more water is entering the cavity volume than it can drain. The result is that the water pressure provides a greater support force normal to the cavity roof, reducing the rate that ice deforms. The rate of change of channel area $\frac{dS}{dt}$ (a cavity formed alongside a step in the bedrock as in Figure 2.7) can be described by:

$$\frac{dS}{dt} = c_1 Q\Psi + u_b h - c_2 N^n S \tag{2.3}$$

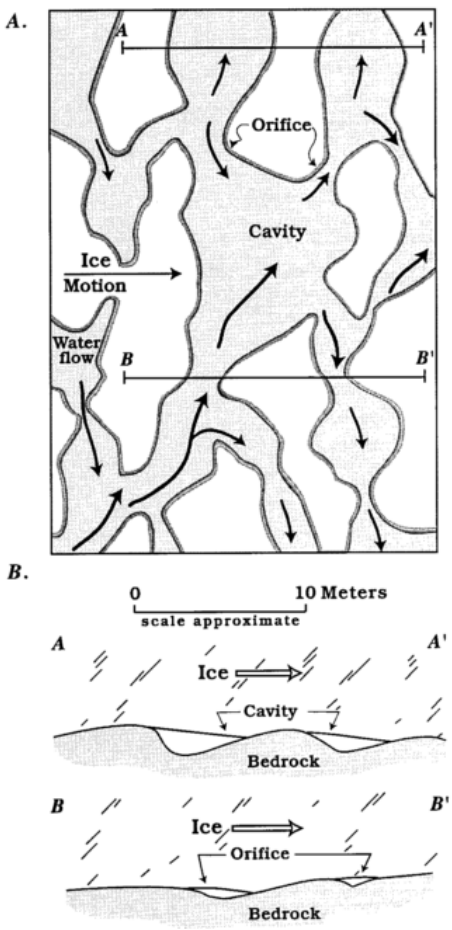

FIGURE 2.6: A close-up plan view of a cavity network where orifices (cavities) are interconnected by small channels (conduits) that weak around bedrock obstacles (Fountain and Walder, 1998).

which is a balance between the opening rate due to wall melting, opening due to sliding (i.e. by ice sliding over bumps in the bedrock), and the closure due to the creep behaviour of ice (Schoof, 2010). Q is the discharge of water in the subglacial drainage system, Ψ is the hydropotential gradient, u_b is the sliding speed, N is the effective pressure, and n is Glen's flow law exponent. The constants c_1 and c_2 are related to the latent heat of fusion and rate factor of ice respectively (Schoof, 2010). The cross-sectional area of a cavity is sustained when the opening by sliding term balances creep closure. Because discharge rates are low in cavity networks, the melting term is usually insignificant.

Channels have the opposite effective pressure effect: an increase in discharge lowers water pressure in the conduit. This is because channels are sustained by the balance between wall melting and creep closure – where sliding speed has less of an effect on channel size. An increase in discharge Q increases channel area by causing more wall melting via heat transfer and friction from the increased water flow. Hence, adding water can increase the capacity of a channelised drainage system, resulting in a decrease in water pressure.

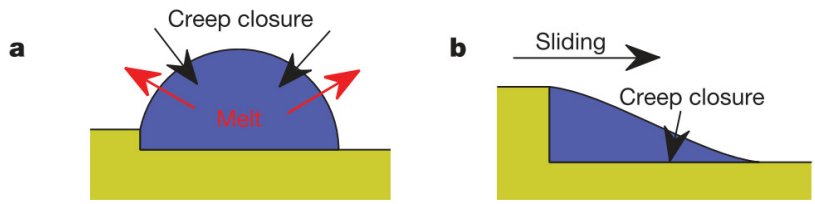

FIGURE 2.7: A diagram from Schoof (2010) that demonstrates a) the balance in melting and creep closure that sustains R-channel size, b) the balance between sliding and creep closure that sustains cavity size

Water pressure behaviour across the glacier can vary with time. The distribution of water pressure depends on the state of the drainage system and the rate of water input. For instance, a steady high input of water into the drainage system develops channels and keeps the hydraulic capacity and the discharge rate of the system high, which suppresses velocity as effective pressure cannot build up (Schoof, 2010). Such as is observed in outlet glaciers of the Greenland ice sheet where consistently high melt rates are thought to establish efficient drainage (Sundal et al., 2011). It is the variability in the surface water supply that is important in creating feedback between surface melt or precipitation and ice velocity. Large accelerations require a build-up of effective pressure, which requires a distributed or "slow" drainage system which has a relatively lower volume and connectivity, meaning water pressure can rise significantly and cause speed-ups.

A distributed system can form into a more efficient system; in glacier models when a critical flux is reached and cavities spontaneously form into channels (Schoof, 2010). It the evolution of the hydrological system that is of interest in explaining the hourly-seasonal velocity variations in land-terminating glaciers (Bartholomew et al., 2012; Sole et al., 2013). It is such that rapid fluctuations of runoff that enter a drainage system, that is slowly adapting to longer-term temperature and runoff signals, and provide a mechanism through which velocity peaks following enhanced melt can be explained — even during instances of channelised drainage (Bartholomaus, Anderson, and Anderson, 2008; Bartholomew et al., 2012; Kamb et al., 1994). The means of linking the water pressure behaviour at the bed to the resulting ice motion is then achieved through a sliding law.

2.5 Glacier Sliding

Our ability to model accelerated glacier sliding in response to water at the base depends on our knowledge of how ice flows around obstacles in the glacier bed. To assess the degree to which accelerated ice flow contributes to mass on an individual, regional, or global scale we require an understanding of what processes are important in limiting and enhancing glacier motion. In the context of enhanced surface melting and precipitation in future climates, the question of hydromechanical processes becomes important: how does the change of water flow beneath a glacier over time affect the friction of ice against bedrock? Addressing this question requires a means of quantifying the physical deformation of ice unique to the base-ice boundary and how much pressure of ice upon bedrock is alleviated by changes in basal water pressure. We then require an equation that represents the physical processes that ice undergoes as it pushes against and traverses these bed obstacles. This equation is referred to as a sliding law. An overarching goal for improving ice flow models is to employ a sliding law that can re-create how basal ice flow varies across space and time (Stearns and Veen, 2018).

An easily implementable sliding law with as few parameters as possible is ideal in a numerical model of ice flow (Gagliardini et al., 2007). However, the simple nature of existing sliding laws may not be capturing the complexity of the subglacial drainage system that is important in controlling rapid sliding acceleration. This section will review the generally accepted mechanisms for describing glacier sliding, the commonly applied sliding laws and their various advantages and shortfalls. Sliding laws can be successful in reproducing motion in some instances, but this section will deal with the complexities of glacial hydrology that touch on important assumptions on which these sliding laws are defined.

Weertman's theory of hard bed sliding

Before direct observations of the glacier bed through tunnelling or borehole experiments, the first descriptions of sliding over bedrock were theorised by Weertman (1957). His work addressed the problem of how basal ice, assumed to be at the melting temperature and thus forming a thin film of water across its base, is able to slide at a constant speed. Using a simple "tombstone model", Weertman demonstrated that basal friction is the product of normal forces σ_{nn} supplied by bumps and undulations in an undeformable glacier bed.

To maintain a steady velocity, the pressure on the upstream side of obstacles must be higher than the downstream side (Cuffey and Paterson, 2010; Fowler, 2011; Iken, 1981). The vertical stress upon the bed due to gravity is balanced by the total stress over the bed. For a flat bed, the pressure normal to the bed would be uniform. However, if parts of the bed protrude, as is observed in exposed glacier beds, then some stress opposing ice flow is generated. The upstream side of obstacles face the oncoming glacier flow and so ice compresses against it, resulting in a greater normal

force compared to the downstream parts of the obstacle. Hence, the normal stresses over a bed obstacle are non-uniform. The total basal stress is then the sum of all normal stresses across the size of a bed obstacle (given by λ):

$$\tau_b = \int_0^{\lambda} \sigma_{nn} d\lambda \tag{2.4}$$

In Weertman's model, to maintain a steady sliding speed, forces must be in balance at the bed and hence the increase in pressure on the upstream side of a bed obstacle must be balanced by an equal decrease in pressure on the downstream side ΔP (assuming symmetry). The compressive normal stress imparted on the bed obstacles can be written as:

$$P_o(x) = P_i + \Delta P(x) \tag{2.5}$$

where ΔP is positive on the upstream face and negative downstream side.

Weertman (1957) first presented the two now generally accepted sliding mechanisms for an impermeable, undeformable bed based on the difference in stress between downstream and upstream sides of bed obstacles. Firstly, *regelation* is invoked to describe the movement of ice due to pressure melting. Under greater pressures, the melting point of ice is reduced, meaning that ice more readily melts on the upstream side of obstacles. Basal meltwater then flows to the other side of the obstacle and refreezes where pressures and the melting point is lower, resulting in a net movement of material around the obstacle. Secondly, *enhanced creep* describes how elevated compressive stresses cause ice to deforms at a greater rate – a process described by Glen's flow law (Glen, 1955). Because compressive stress is higher upstream of obstacles, ice deformation is quicker around obstacles compared to the rest of the ice.

The goal of a friction law is to treat the problem as a contact problem — to provide an equation that describes the flow relative motion of two bodies in contact. In classical problems of friction, we treat two surfaces as flat without describing the exact interaction with asperities that eventually rise as friction between two surfaces on the macro scale. As such, we parameterise the small-scale flow of ice around bed obstacles and describes its effect on the large-scale flow of the glacier over a "smoothed" bedrock (Fowler, 1979). In this case, using these processes, Weertman defined a sliding law: a function that links basal velocity to the average basal stress imparted by the basal ice flow normal to the bed (Fowler, 2011).

2.5.1 The influence of subglacial hydrology on basal sliding

Sliding enhanced by low effective pressures

The Budd-type sliding law derived from lab experiments that sliding velocity is strongly dependent on effective normal stress in addition to basal stress and roughness (Budd, Jenssen, and Smith, 1984; Budd, Keage, and Blundy, 1979). The introduction of an effective pressure term in sliding laws was of particular interest

for studies investigating the fast flow of Antarctic ice streams towards the terminus (Budd, Jenssen, and Smith, 1984; Gladstone et al., 2017). The Budd-type law can essentially be thought of as a Weertman law corrected for the effect of elevated water pressure at the bed (Cuffey and Paterson, 2010). The idea is that the sliding speed scales with the degree of bed separation, termed the *bed separation index*:

$$u_b \sim \frac{\tau_b}{N} \tag{2.6}$$

where the degree of cavitation scales with basal stress (e.g. Equation 2.9) and the closure of cavities scale with the effective pressure (Bindschadler, 1983; Cuffey and Paterson, 2010). This approach includes the same power-law relationship based off of enhanced creep and aims to provide a simple theoretical approach to capture the broad behaviour of enhanced water pressures. While the Budd-type sliding law (Equation 2.6) has been used to model the sliding component of glacier flow in a number of cases (e.g Bindschadler, 1983; Jansson, 1995; Raymond and Harrison, 1987), the sliding law generally works in matching larger-scale seasonal patterns but breaks down in explaining short-term variations in surface velocity. Stearns and Veen (2018) use a comparable sliding law of the form

$$u_b = A_s \tau_b^n N^{-q} \tag{2.7}$$

where A_s is a tunable sliding parameter that represents a friction coefficient in the absence of cavitation. In place of of basal water pressure data, and assuming a strong connection with the ocean, the effective pressure beneath the ice can be estimated by the height above buoyancy H_{ab}:

$$N \approx H_{ab} = H - \frac{\rho_w}{\rho_i} D \tag{2.8}$$

where H is the ice thickness at any point along the bed, D is the water depth, ρ_w is the density of water, and ρ_i is the density of ice. The effective pressure behaviour of current and future state of Greenlandic outlet glaciers have been estimated using this method (Nick et al., 2009, 2013; Stearns and Veen, 2018). However, if water pressure varies due to processes other than buoyancy, it is likely that this sort of sliding law does not accurately represent the water pressure behaviour of the basal hydrology system. Basal drainage is observed to be a fast-changing system with a significant effect on basal sliding (Bartholomew et al., 2010; Stearns and Veen, 2018; Sundal et al., 2011).

Studies that compare surface velocity with effective pressure data from boreholes can demonstrate that Equation 1.4 and 2.7 generally hold (e.g. Bindschadler, 1983; Iken and Bindschadler, 1986; Jansson, 1995)(Figure 1.6); however, there are issues with the "Budd-type" sliding law that prevent it from being used as a general sliding law – i.e one that can be applied to many glaciers and is consistent over time.

2.5.2 Issues with the empirical sliding law

The basal drag — velocity relationship suggested by the Budd-type law implies that basal stress is unbounded; equation 2.6 implies that sliding velocity and basal stress can increase indefinitely. Furthermore, under this sliding law, if effective pressures tend to zero (for $P_w \rightarrow P_i$) then an infinitely fast sliding velocity would occur. This is physically impossible and, for computer models of sliding, numerically unstable. The leap from an empirical- to a process-based sliding law is then based on defining what qualities of the ice-bed interface limits sliding speed. These limits have been resolved by investigating additional processes related to water flow and water pressure affecting basal friction. A key process is cavity growth and the resulting separation of ice from the underlying bedrock (Lliboutry, 1986).

Iken's Bound

Iken (1981) using a simple tilted staircase model (Figure 2.8) to demonstrate that basal stress and sliding speed do not increase indefinitely (as suggested by Equation 1.4, 2.7). Iken's study provides upper and lower bounds on basal stress that depend on the size of cavities. As sliding speed increases under low effective pressure, basal stress is limited due to the associated cavity growth, which in turn depend on the size and shape of bed obstacles.

Iken uses a "tombstone" model similar to Weertman's where the downstream sides of the bed obstacles experience less stress from the overlying ice. In the case of increasing water pressure where water is added to the base by rainfall or surface melt, water pressure increases across the bed. Ice on the downstream face applies less normal stress against the bed and so less water pressure is needed to push the ice up. Hence, the downstream face is then the first place ice separates from the bed. Consequentially, the water pressure needed to produce separation is equal to the lowest normal stress on the downstream face of the ice — referred to as the *separation pressure* P_s:

$$P_s = P_i - \frac{\lambda \tau_b}{h\pi} \tag{2.9}$$

where $\frac{h}{\lambda}$ is the roughness of the bed (Cuffey and Paterson, 2010). Cavity growth is more favourable when the difference in compressive stress ΔP across bed obstacles is larger (see Section 2.5), which is true for either rougher beds or for lower basal stresses. This condition provides the lower bound for which cavitation develops and begins to increase sliding velocity.

Iken also argues that there should be a critical water pressure P_c after which unstable sliding occurs. Sliding is "unstable" when the bed is unable to apply enough normal force to support the overlying weight of the glacier, and so the ice accelerates downslope. Such would be the case where cavities become large enough to "drown" the bedrock topography (Gagliardini et al., 2007). Even if the sliding speed increases

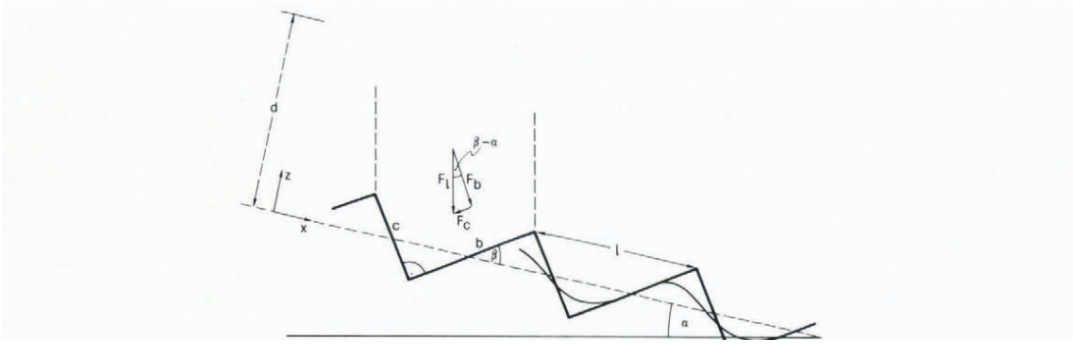

FIGURE 2.8: The tilted staircase model used by Iken (1981) to derive the separation pressure and limiting pressure for cavity development

indefinitely, the frictional strength of the glacier base cannot. For an idealised, tilted staircase bed (as in Figure 2.8), Iken (1981) defines the separation pressure by :

$$P_c \approx P_i - \frac{\tau_b}{\tan \beta} \tag{2.10}$$

which results in some critical effective pressure $N_c = P_i - P_c$. Hence, a limit to the basal stress is set up that depends only upon the bedrock geometry where:

$$\tau_b < N_c \tan \beta \tag{2.11}$$

Equation 2.11 is comparable to the Coulomb friction criteria used to describe the failure of rock due to elevated pore fluid pressures (Cuffey and Paterson, 2010). An analogous process in the case of glacier sliding may be heavy rainfall prior to a landslide which saturates shallow soil and rock layers, raising water pressure, weakens the frictional strength of the rock, causes failure and runaway sliding(Cuffey and Paterson, 2010).

The lower bound on sliding speed should result from the combination of ice deformation, regelation, and enhanced creep. The upper limit should involve complete flotation where bed obstacles are no longer able to support normal stresses. Approaching flotation, the gravitational driving stress of the glacier is instead balanced by the stretching of the glacier and friction against the margin walls (Cuffey and Paterson, 2010; Horgan et al., 2015)

Sliding in the presence of subglacial cavities

Modelling the velocity response of a glacier to large changes in water pressure requires that the sliding law complies with the lower and upper limits of basal stress that the glacier bed can impart. A sliding law that obeys Iken's bound was derived for a general glacier bed by Schoof (2005) (Equation 1.5). This type of relationship was validated for non-linear ice rheology by Gagliardini et al. (2007) and the general

relationship for sliding is written as:

$$\frac{\tau_b}{N} = C_{max}\left(\frac{\chi}{1+\alpha\chi^q}\right)^{1/n} \tag{2.12}$$

where

$$\chi = \frac{u_b}{C_{max}^n N^n A_s} \tag{2.13}$$

where $\alpha = \frac{(q-1)^{q-1}}{q^q}$. This sliding law captures the main feature of sliding in the presence of cavities. Figure 2.9 shows the relationship between basal stress and sliding velocity for a range of flow exponents n. In general, the relationship suggested by Schoof (2005) (the black line in Figure 2.9) provides an adequate sliding relationship when n is between 1 and 4. Moreover, Figure 2.9 demonstrates that basal stresses have approximately the same limit (the maximum value of τ_b/N which is set by the C_{max} parameter) for each n used. In other words, the limit in basal stress suggested by Iken (1981) can be demonstrated using a numerical model and the limit is independent of the rate at which ice deforms (i.e. for greater n ice deforms faster under a given stress).

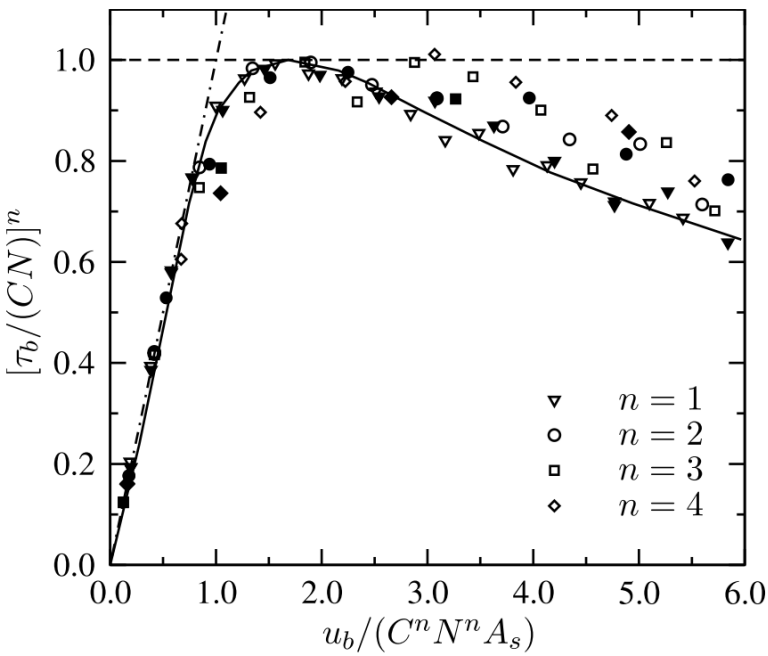

FIGURE 2.9: The basal stress versus sliding speed relationship from a finite-element simulation of ice sliding over an idealised glacier bed. Figure is taken from Gagliardini et al. (2007)

The Coulomb-type law demonstrates two end-member cases of effective pressure (Brondex et al., 2017). Firstly, for low water pressures and thus high effective pressures ($N \to \sigma_{nn}$), Equations 1.5 & 2.9 reduce to a Weertman-type law ($\tau_b \sim C_s u_b$). This gives the initial linear relationship in Figure 2.9. For the case when water pressure approaches overburden ($N \to 0$), the cavities are large enough to effectively

"drown" the bedrock topography. This tends towards the case were Iken's bound is exceeded, activating a Coulomb-type friction regime where $\tau_b \sim C_{max}N$ (Brondex et al., 2017). Coulomb friction laws in fault mechanics typically refer to sliding which is either "on" or "off" depending on some failure criteria – in glacier sliding the 'Coulomb-type" sliding law represents a sliding relationship that transitions between a Weertman-style sliding regime and plastic deformation. As effective pressures approach zero, the base of the glacier loses its ability to apply frictional resistance as a means of balancing the glacier's gravitational driving stress. As a result, the weight of the glacier is instead balanced by friction against the sides or stretching within the glacier itself, meaning that sliding velocity becomes limited by processes outside of the glacier's base (Cuffey and Paterson, 2010). Processes acting outside of the subglacial environment that limit ice velocity are referred to as "global controls" (Cuffey and Paterson, 2010).

A summary of the behaviour of sliding laws

The sliding velocity responses to effective pressure for each sliding law are summarised in Figure 2.10 (Brondex et al., 2017). The Weertman-type law cannot model rapid changes in basal sliding because it is independent of water pressure. When $P_w = 0$, the Budd-type sliding law is equivalent to the Weertman-type; however, the sliding speed from Budd-type law increases with lower effective pressure by a power-law relationship, resulting in a straight line in the logarithmic plot below. This runs into the issue of an infinite sliding speed when $N \rightarrow 0$, so may lead to unreasonably high sliding velocities if modelling basal sliding events where water pressures are likely to be very high and cause extensive cavitation, which is thought to be the case at Haupapa/Tasman Glacier (Horgan et al., 2015). The Coulomb-type law (sometimes referred to as "Schoof law") is synonymous with Weertman-type sliding at zero water pressure. As water pressure approaches flotation, however, the Coulomb-type sliding law becomes more sensitive and will result in a large change in velocity for a small change in water pressure (Jay-Allemand et al., 2011).

2.5.3 Transient Cavity Growth

Because the Budd- and Coulomb-type sliding laws imply that sliding velocity is only a function of basal stress and effective pressure (for a given glacial bed), they are unable explain inconsistencies in basal water pressure versus sliding speed relationships (Cowton et al., 2016)(Section 1.4). For instance, sliding speed can vary depending on whether water pressures are increasing or decreasing (Sugiyama and Gudmundsson, 2004) and, in some case, can have no apparent relationship to water pressure at all (Fudge et al., 2009; Harper et al., 2007). One process that is suggested to alter the relationship between sliding speed and effective pressure is cavity growth (Cowton et al., 2016; Cuffey and Paterson, 2010; Howat et al., 2008). As

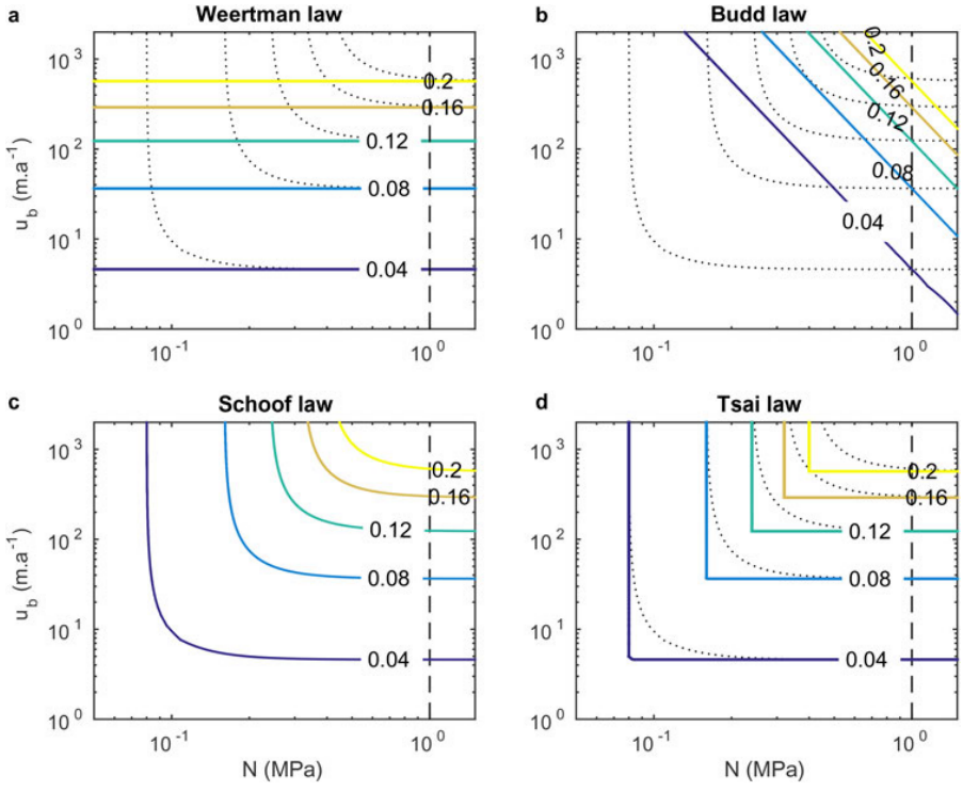

FIGURE 2.10: A comparison of the sliding laws presented in Brondex et al. (2017). Each plot shows the relationship between effective pressure N and sliding speed u_b for a range of basal stresses (basal stresses are shown by the contour lines and are in units of MPa). The Tsai law effectively incurs a switch between Weertman and perfectly plastic deformation beyond a threshold effective pressure. This law is applicable for models with soft-bed deformation and, hence, is not investigated in this study (Brondex et al., 2017; Tsai, Stewart, and Thompson, 2015).

discussed in Section 1.4.1, Iken (1981) demonstrated that the physical growth of cavities could result in temporarily enhanced sliding speed through "hydraulic jacking" (Cowton et al., 2016; Sole et al., 2011; Werder et al., 2013). Essentially, if basal water pressure changes faster than cavities can grow, then the elevated pressure pushes (or "jacks") basal ice upwards and downstream. As a result, sliding speed is elevated until the cavity reaches a steady size where opening by sliding speed balances creep closure (e.g. Section 2.4.2, Equation 2.3).

Figure 2.11 illustrates the "hydraulic jacking" process by showing how forces are redistributed across an idealised glacier bed in response to applied water pressure. Initially, the normal stress on the crests P_0, troughs P_0, downstream P_1, and upstream P_3 sides of obstacles balance the weight of the overlying ice. However, this balance can be upset if one of the forces upon any of these parts of the bed change, causing the glacial base to accelerate. For instance, if water pressure suddenly increases on the lee side (image B in Figure 2.11), this increases the net force

in the downstream direction. In response, the pressure on the upstream side of the bed obstacle increases to $P_3' = (P_w - P_1) + P_3$. Because the stresses in the trough are largest when the cavity is not formed, the flow of the glacier over obstacles is closer to being parallel to the bed, resulting in more rigid basal ice motion and greater velocities (Iken, 1981). The cavity then grows to its new size (image C in Figure 2.11) and the pressure in the crest drops from P_0 to P_w (as water pressure is equal in all directions). This is compensated by an increase in the pressure on the crests of the obstacles $P_4'' = \frac{(P_0 a_4 + (P_0 - P_w) a2)}{a4}$ (Iken, 1981). Finally, the net forces acting on the crests, troughs, downstream, and upstream P_3 sides of obstacles (P_4'',P_w,P_w,P_3 respectively) again balance the overlying weight of the ice.

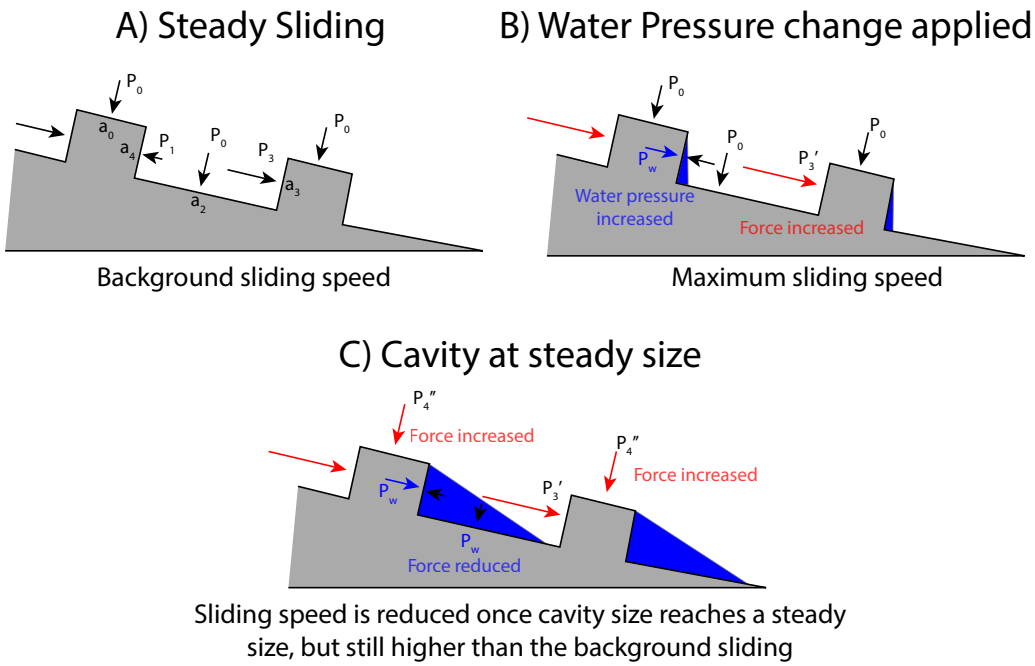

FIGURE 2.11: An idealised glacier bed from a tombstone model akin to the original model used by Weertman (1957) (figure adapted from Iken (1981)). A) demonstrates the force balance prior to a rapid water pressure change. B) shows the redistribution of forces the moment a water pressure change is applied resulting in enhanced sliding speed. C) shows the final state where the cavity is in steady-state.

2.5.4 Calculating bed separation

The vertical velocity of a point on the glacier surface is a combination of the vertical component of sliding $u_b \tan\beta$, the vertical deformation rate $\langle \dot{\epsilon_{zz}} \rangle$, and the bed separation $\frac{dB}{dt}$:

$$u_z = u_b \tan\beta + \langle \dot{\epsilon_{zz}} \rangle H + \frac{dB}{dt} \tag{2.14}$$

(Hooke et al., 1989). Vertical displacement during speed-up events are often attributed to the growth of subglacial cavities in response to elevated water pressures

(Bartholomaus, Anderson, and Anderson, 2008; Iken et al., 1983; Iken and Bindschadler, 1986; Kamb et al., 1985; Sole et al., 2011). Rapid changes in vertical displacement can indicate regions of the bed where subglacial water flux is great enough to overwhelm a cavity system and possibly develop subglacial channels (Section 2.4.2). Horgan et al. (2015) for instance use Equation 2.14 to calculate the bed separation B during speed-up events at Haupapa/Tasman Glacier (Figure 1.13). While bed separation rates are not calculated in this study, based on the limited extent of vertical deformation and vertical component of sliding, the total vertical GNSS motion is assumed to estimate the degree of bed separation (Section 1.6.4).

2.6 Summary

While basal processes involving subglacial drainage and basal sliding are not often observed directly, a strong theoretical background exists to describe the causes of rapid surface-water induced accelerations. Both the evolution of drainage, whether it is inefficient, efficient, or transitions between the two, are important for controlling the relationship between effective pressure and sliding speed. The Coulomb-type sliding law offers a relationship between effective pressure and sliding speed that obeys the physical limit of basal stress that depends on the maximum slope of bedrock topography. However, in cases where water pressure changes faster than cavities can grow, the steady-state assumption of the Coulomb-type law is challenged. This poses a potential challenge for modelling speed-ups at Haupapa/Tasman Glacierwhere transient cavity grow this thought to occur. The following chapter will detail the use of GNSS data and finite-element modelling to observe and recreate Haupapa/Tasman Glacier's rain-induced sliding events. The Coulomb-type sliding law described in this Chapter will be tested using the finite-element model in its applicability for modelling speed-ups induced by the rapid introduction of rainwater beneath Haupapa/Tasman Glacier.

Chapter 3

Methods

Episodes of heavy rainfall over Haupapa/Tasman Glacier and its surrounding valley catchment provide a repeatable natural experiment in which investigate the processes that govern variation in sliding speeds. High rainfall rates rapidly add water to the glacier's base, increasing basal water pressure and triggering accelerated sliding (Horgan et al., 2015). Due to the inaccessibility of the glacier bed, the results of this natural experiment are only observed as changes in surface elevation and horizontal position. This chapter presents a year-long record of surface position and velocity recorded by a network of GNSS (Global Navigation System Satellites) instruments installed across Haupapa/Tasman Glacier. Six speed-up events are isolated from the annual record to investigate the relationship between horizontal and vertical displacement during rapid accelerations.

3.1 Surface position measurements

The change in glacier surface position with time records the combined effect of internal deformation, sediment deformation, and basal sliding (Equation 2.1). Using a network of GNSS units, surface position data is presented in this study to investigate the processes driving variability in Haupapa/Tasman Glacier's motion (Figure 3.1). While GNSS measurements only provide point measurements of the surface (i.e. have a low spatial resolution), their high precision, accuracy, and temporal sampling are ideal for documenting surface velocity changes that occur over hourly-daily scales. The interest of this study is to detail changes in horizontal and vertical displacement that occur over the scale of a few hours that other methods, such as remote sensing, would miss out on. A high sampling rate of glacier velocity provides more precise motion for numerical models to capture, which is likely to challenge sliding laws which assume a steady cavity size.

3.1.1 GNSS Network

A network of seven Global Satellite System (GNSS) receivers units were installed on the glacier surface over 2016 (Figure 3.1). The primary objective of this network was to record spatial and temporal variability in Haupapa/Tasman Glacier's surface motion. This network expands on the three GNSS sites installed along the flowline

of Haupapa/Tasman Glacier presented in Horgan et al. (2015). An additional flow-line site and four off-centre sites are introduced in this study. The centre-line sites are chosen where the greatest surface velocity of the glacier is present and the off-centre sites monitor how velocity decreases towards the lateral glacier margins. Lobes in the surface of the glacier indicate that side friction is important in the background field of Haupapa/Tasman Glacier's flow (Figure 3.1). The naming of the sites are made by their position left (L) or right (R) relative to the flow direction or along the centre-line (C). Each site is numbered based on its position upstream (where 1 is the most downstream station). A base station to process GNSS positions against is installed on a rocky outcrop on Annette Plateau ∼10 km from the lower glacier located at (1363418.35 m E,5151015.09 m N,2251.688 m) in NZTM (New Zealand Transverse Mercator) coordinates.

3.1.2 GNSS instruments

Each GNSS instrument had a solar power unit, battery, receiver, antennae, and tripod for mounting the unit to the glacier surface. The position of each unit is recorded at 15-second intervals. Not all sites recorded simultaneously throughout 2016 with a maximum of five sites available at any given moment (Figure 3.2).

3.1.3 GNSS Processing

A record of surface position with time is derived from kinematic processing of GNSS data. In this process, the position of the GNSS at any given time is the product of the lag between the carrier wave and the returning wave signal of GNSS satellites, where at least four satellites are required to form a solution (Chen, 1998). Positions are processed with respect to the Annette Plateau station some 10 km to the southeast of the glacier. Over the ∼10-15km scale between the base station and the GNSS instruments, it is assumed that tropospheric and ionospheric corrections for each of the on-glacier GNSS units are consistent with the Annette Plateau base station. The kinematic GNSS solutions produce latitude, longitude, and elevation in the WGS84 coordinate system. To record displacements in units of metres as opposed to azimuths, the processed latitude-longitude coordinates are projected into the New Zealand Transverse Mercator (NZTM) coordinate system. GNSS position solutions were calculated by Huw Horgan following the processing outlined in (Horgan et al., 2015). Some data loss resulted due to instances of heavy rain and snow blocking the solar panels which caused temporary power loss. Noise is generally present as a result of when units have difficulty locating enough satellites.

3.1.4 GNSS Velocities

Surface velocity is calculated as the gradient of a weighted linear regression of GNSS position. Regression weightings are given by the inverse square of processing uncertainties, which mostly result from satellite geometry (Horgan et al., 2015). Gradients

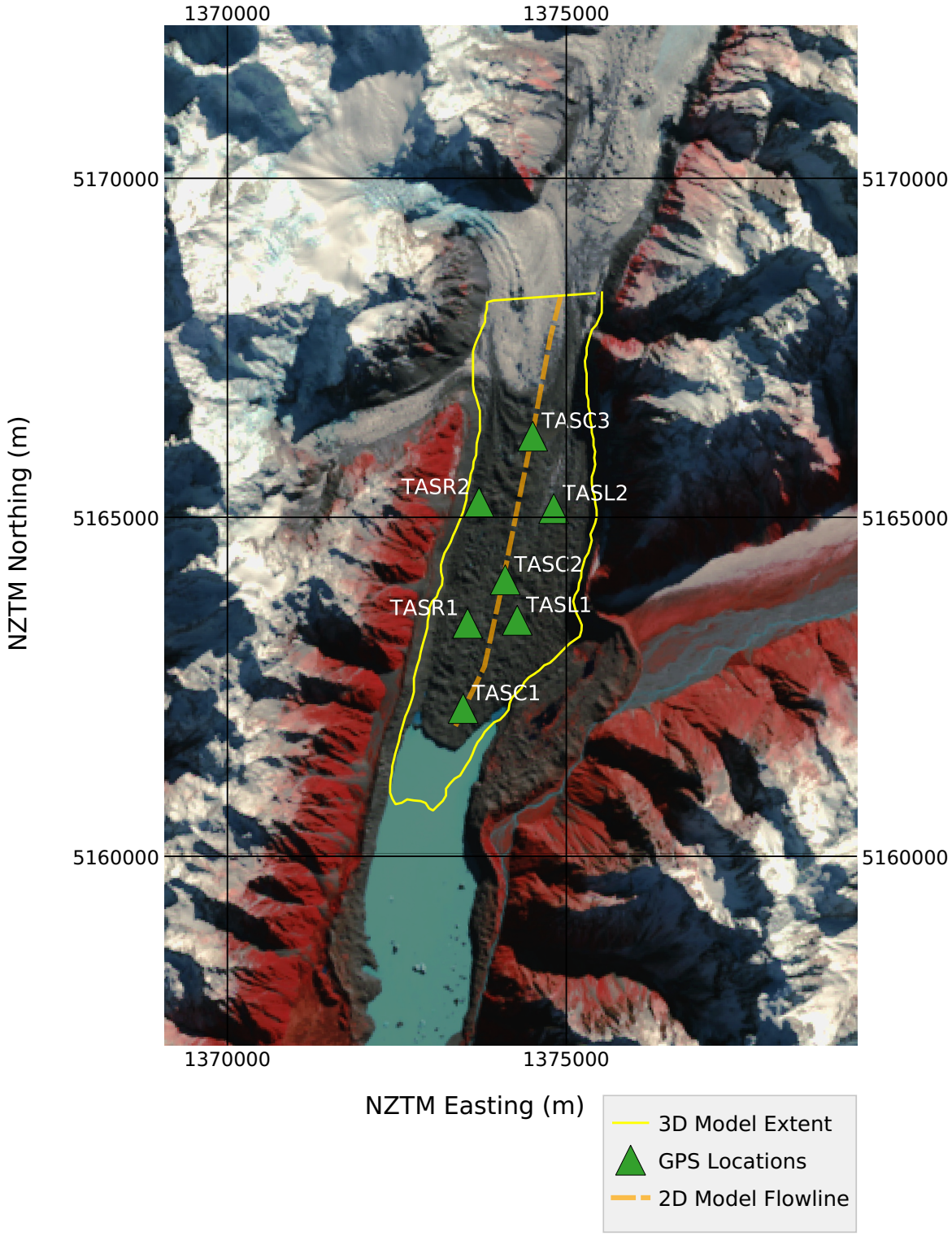

FIGURE 3.1: Site map of of the 2016 GNSS network installed on Haupapa/Tasman Glacier's surface. GNSS units are shown by green triangles. The glacier outline used to define the extent of the 3D model is shown by the yellow line. The points used to sample the surface and bed elevations for the 2D model lie along the orange dotted line.

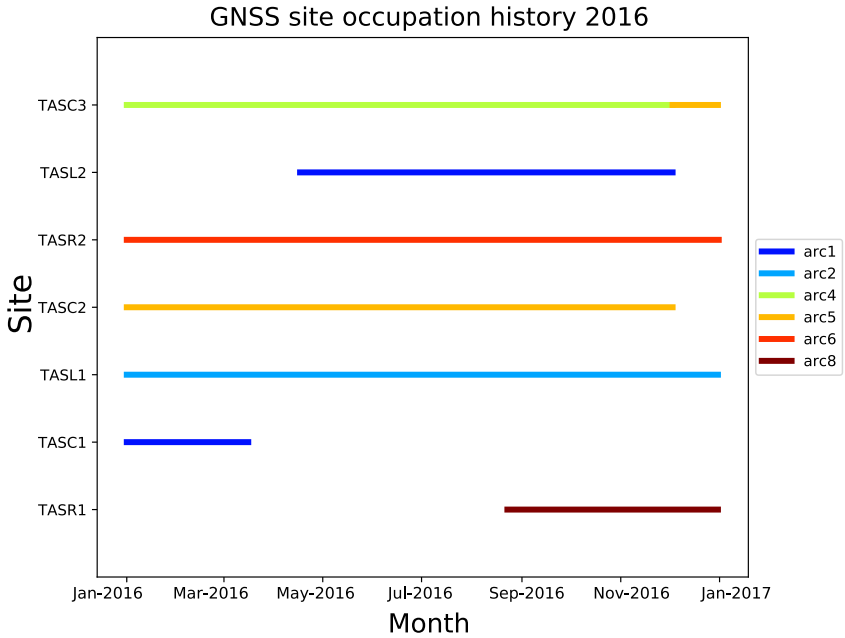

FIGURE 3.2: This figure displays the occupation history of GNSS sites over 2016 and the movement of GNSS units between sites. Over 2016, up to six sites are available to extract surface position data from. Each colour refers to an individual GNSS unit which is numbered from arc1 to arc8.

are calculated at the centre of a moving time window. The position data is divided into each component (x,y,z) which results in three components of motion u_x, u_y, u_z where the horizontal velocity is calculated as $u = \sqrt{u_x^2 + u_y^2}$. Horizontal velocities are calculated every five minutes for documenting the change in surface motion (Chapter 4) and every hour for comparing finite-element model output to surface velocity (since model timesteps are 1 hour) (Chapter 5).

Tweaking the window size over which velocity is calculated effectively changes the degree of smoothing in the processed velocity data. Window sizes of 3-hours and 24-hours are used in this study. The 24-hour window fits GNSS positions over an entire day and so averages or "smooths out" sub-hourly—hourly variation or noise. As a result, the 24-hour window best demonstrates the daily—weekly signals in glacier motion. On the contrary, the 3-hour window is more sensitive to shorter changes in surface position and therefore gives the closest representation to the instantaneous speed of the glacier surface while still reducing noise introduced by GNSS errors. Horgan et al. (2015) note that the increase in peak velocity due to a decreasing window size does not appear to have a limit. Consequently, any reported peak velocities may potentially by underestimates of true maximum surface velocity (Horgan et al., 2015).

Before sampling the velocity, anomalous peaks in GNSS velocity are removed. These peaks are associated with moving the instrument or adjusting antennae height during site checks, or from loss of satellite coverage. Satellite errors are spotted from the lack of the characteristic rise and decay of speed-up events or the surrounding

loss of data or the excess of physically reasonable glacier speeds. Furthermore, any data point with a standard deviation of greater than 10cm in vertical or greater than 5 cm in the horizontal components is removed prior to velocity processing. During the linear regression, the maximum and minimum velocities ($u_{x_{min}}$ and $u_{y_{min}}$) are given as 95% confidence intervals from the coefficients of the minimum error linear fit (linear least squares approach). The horizontal errors are calculated as $u_{max} = \sqrt{u_{x_{min}}^2 + u_{y_{min}}^2}$.

Finding seasonal signal

Horgan et al. (2015) demonstrated that the background velocity of Haupapa/Tasman Glacier, i.e. the horizontal velocity data with speed-up events removed, contains a seasonal signal. The seasonal variation in velocity is likely due to changes in water inputs and subglacial hydrology (e.g. greater melt rates in summer provide more water drainage to the bed, creating larger cavities and decreasing basal drag). At the two GNSS sites with continuous records over 2013-2014, horizontal velocity was elevated the summer months and suppressed in the winter. The total variability of this signal (peak$-$trough) is 10.27 ± 0.13 ma^{-1} and 8.85 ± 0.15 ma^{-1} for the downstream and upstream sites respectively (Horgan et al., 2015). A linear trend from year to year is superimposed over the sinusoidal variation, which is expected to be the movement of the GNSS site over faster regions of the glacier.

Following Horgan et al. (2015), the seasonal variability and linear trend in horizontal velocity are here modelled in the 2016 data using a sinusoidal function:

$$u_{seasonal}(t) = a \sin(\omega t + \phi) + bt + c \tag{3.1}$$

where a is the seasonal variability, ω is the frequency locked in at a year, ϕ is the phase shift, b is the gradient of a linear trend, and c is a constant. Using a weighted least-squares approach, the parameters in this equation are optimised to fit the velocities calculated over a 24-hour window (which most closely represent the average/background ice flow). To remove the effect of speed-up events, which create significant perturbations from the average horizontal velocity throughout the year, data that exceeds 146 m yr^{-1} (a threshold velocity suggested by Horgan et al. (2015)) is cut before finding a best-fit for Equation 3.1. Once the best fit is found, the minimum in the curve (the trough) is assumed to indicate the slowest basal sliding when basal water pressures are at a minimum.

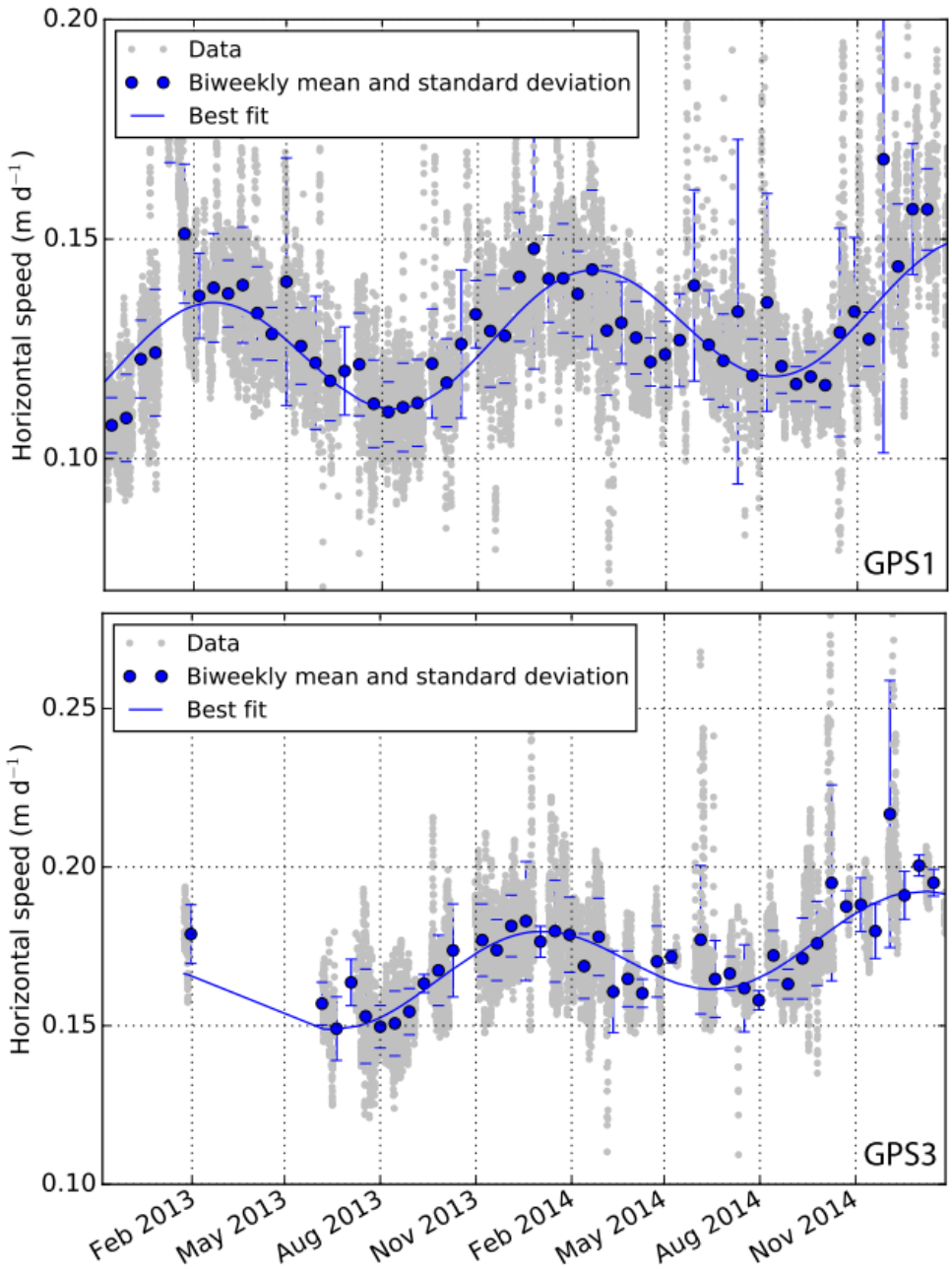

FIGURE 3.3: Seasonal horizontal velocity signal of Haupapa/Tasman Glacier from Horgan et al. (2015). A sinusoidal with a linear trend is fit to horizontal velocity over 2013-2014 (see Figure 5 in Horgan et al. (2015)). The grey dots show the 24-hour window velocities after speed-up events have been removed.

Uplift record

To get the magnitude of surface uplift during speed-up events, the elevation record has the background signal removed. The detrended uplift time-series is calculated by removing the background trend in elevation that occurs over the year. A sinusoidal curve with a superimposed linear trend is used to model seasonal variation

and the change in seasonal velocity as a GNSS site moves into a faster or slower part of the glacier. The same approach to data fitting as the seasonal velocity is applied. Seasonal variations in surface elevation are thought to reflect the amount of water storage within the glacier's subglacial drainage system (e.g. (Iken et al., 1983)).

$$z_{seasonal}(t) = a \sin(\omega t + \phi) + bt + c \tag{3.2}$$

Rainfall data

Rainfall data is collected from the Mt. Cook village weather station ∼11 km to the southwest of the glacier terminus (1366140.390 m E,5153348.661 m N, 765 m) (Horgan et al., 2015). Due to the widespread nature of storm events over the Southern Alps, it is assumed to represent rainfall over the glacier (Henderson and Thompson, 1999). Rainfall is measured in hourly bins where the measurement is made at the end of each hour. The timing of the rainfall data is shifted to UTC (Coordinated Universal Time) to align with time used in the position and velocity record.

3.2 Finite-element model of Haupapa/Tasman Glacier

A finite-element model of Haupapa/Tasman Glacier is constructed to explore the link between evolving water pressure and the resulting flow of the glacier. Glacial ice flows under viscous deformation (Section 2.2); hence, the finite-element model solves equations that dictate how velocity and pressure vary through a viscous fluid (Section 3.2.1). An open-sourced finite-element solver, Elmer/Ice, is used to solve these equations (Section 3.2.2). The solution for velocity and pressure depends on boundary condition of the model; these include how fast ice is flowing at the terminus or the upper limit of our model space (given by the yellow border in Figure 3.1) and how fast the glacier slides along its base. Because friction is reduced by the presence of water, the basal boundary of the layer undergoes a change in force balance that results in a rapid speed-up (Cuffey and Paterson, 2010; Iken, 1981). The reduction in friction and resulting increase in sliding speed is accounted for using a Coulomb-type sliding law (Section 1.3.2, 2.5.2). Here, by imposing an evolving water pressure along the basal boundary of a glacier model (Section 3.2.4), a forward modelling approach is taken with the aim of reproducing observed peaks in surface velocity and vertical displacement. For a full description of how Elmer/Ice is implemented in solving glaciological problems, see Gagliardini et al. (2013). Likewise, a broad overview of the finite-element method is presented by Zienkiewicz, Taylor, and Zhu (2013).

3.2.1 The equations of ice flow

The finite-element model of Haupapa/Tasman Glacier solves for the flow of ice under gravity — i.e. the velocity due to the viscous deformation of ice u_{def} (Section 2.2).

Gravity drives the glacier down its bed, where, for a constant glacier velocity, the weight of the glacier is balanced by friction against the base and its side walls. The force balance at any point in the ice then depends on the thickness (and therefore mass) of the ice, the steepness of the bed slope and surface slope, internal stresses in the ice due to the resistance to its own flow (i.e. its viscosity), and basal stress against the underlying glacial bed (Cuffey and Paterson, 2010). The force balance and resulting motion in a viscous fluid are described by the Navier-Stokes equation:

$$\nabla \cdot \boldsymbol{\sigma} + \rho \vec{g} = 0 \tag{3.3}$$

where $\boldsymbol{\sigma}$ is the stress tensor, ρ is the density of ice, and $\vec{g}$ is gravitational acceleration. The inertia terms are neglected in the Navier-Stokes equations in solving for glacier flow due to the high viscosity of ice that resists any significant acceleration (Gagliardini et al., 2013).

In solving the Navier-Stokes equation for glaciers flow, ice is treated as an incompressible fluid. This greatly simplifies the equations by restricting deformation such that density remains constant. The result being that if a portion glacial ice is compressed along one axis, the material will expand along the other two axes to ensure the original volume of the material remains constant (Cuffey and Paterson, 2010):

$$\nabla \cdot \vec{u}_{def} = 0 \tag{3.4}$$

The compression or stretching of a viscous, incompressible fluid such as ice is governed by deviations from the average stress state in a fluid (Cuffey and Paterson, 2010). In other words, deformation does not occur when stresses are equal in all directions, so, by subtracting the mean stress σ_{mean} from the stress tensor we attain the deviatoric stress τ that contribute to deformation:

$$\boldsymbol{\tau} = \boldsymbol{\sigma} - \sigma_{mean} \tag{3.5}$$

Deformation is measured by the strain along each axis. The rate of deformation, or strain rate, in ice flow models is typically described by Glen's Flow law (Glen, 1955):

$$\dot{\boldsymbol{\epsilon}} = A\tau_e^{n-1}\boldsymbol{\tau} \tag{3.6}$$

where A is a flow parameter that depends on temperature (via a Arrhenius relationship), ice fabric, hydrostatic pressure, crystal orientation, and englacial water content. The flow exponent n is typically set to 3 based on the results of field and laboratory experiments (Cuffey and Paterson, 2010). τ_e is the second invariant of the deviatoric stress tensor:

$$\tau_e^2 = \frac{\boldsymbol{\tau}_{ij}\boldsymbol{\tau}_{ij}}{2} \tag{3.7}$$

To solve for the resulting strain rate field (Equation 3.6), which is analogous to u_{def},

in response to the pressure gradients and gravitational forces acting on the ice, the Navier-Stokes equations (Equation 3.3) are rewritten as:

$$\nabla \cdot \boldsymbol{\tau} - \nabla p + \vec{\rho} g = 0 \tag{3.8}$$

Where $\boldsymbol{\tau}$ is the deviatoric stress tensor, ∇p is the pressure gradient and $\rho \vec{g}$ is the gravitational force. This gives the set of partial differential equations in a form where the pressure and deviatoric stress can be solved for using a finite-element solver (Section 3.2.2).

3.2.2 Elmer/Ice

A widely used method for solving Equation 3.8 for models of glacier flow is the finite-element approach. Elmer/Ice is an open-sourced finite-element solver associated with the multi-physics code Elmer (Gagliardini et al., 2013). One of the main advantages of using Elmer/Ice to model ice flow is that it solves the full set of Stokes equations (i.e. it does not make any further approximations to simplify the equations). Hence, it is appropriate for dealing with complex stress regimes.

Tests in Elmer/Ice are run from "Solver Input Files" (SIF) which contain the list of equations that need to be solved (e.g. the Navier-Stokes equation), the constants important to these equations (e.g. gravity), the boundary conditions that control the solution (e.g. water pressure along the base), the geometry object these equations are to be solved over (Tasman Glacier), and the material properties of this object (e.g. the density of ice). An example SIF file is displayed in Appendix E. The following sections will detail how the geometry Haupapa/Tasman Glacier is reworked into a form that Elmer/Ice can solve equations over (Section 3.2.3), how boundary conditions in the model are varied to recreate rapid sliding (Section 3.2.4, 3.2.4, 3.2.4), and the parameters required to solve the equations that dictate ice flow and sliding of ice across bedrock (Section 3.2.6).

3.2.3 Tasman Glacier Mesh Generation

In a finite-element glacier model, the glacier is recreated as a grid of points called a "mesh". At each point on the mesh, the equations of motion are solved (Equation 3.8) to produce velocities and pressure throughout the grid and, ideally, replicate similar motion to that observed by GNSS units (Section 3.1.4). This section describes how Digital Elevation Models (DEMs) are used to construct 2D and 3D meshes of Haupapa/Tasman Glacier.

Building a bed Digital Elevation Model

The bed DEM for Haupapa/Tasman Glacierused in this study is sourced from the results of the Ice Thickness Models Intercomparison eXperiment (ITMIX) (Farinotti et al., 2017). The project compared various methods by which the thickness of glaciers

can be estimated from surface observations. The glacier bed used in this study is produced by the method of Huss and Farinotti (2012), which uses surface mass balance distributions and surface DEMs to calculate the flux of ice and convert it to thickness via a flow law for ice (Glen, 1955). For a full description of the method, the reader is referred to Huss and Farinotti (2012). This was the first mass-conservation approach to estimating glacier ice thickness applied on a global scale (thickness maps for 171,000 glaciers were calculated using this method) (Farinotti et al., 2017; Huss and Farinotti, 2012).

The thickness map produced for Haupapa/Tasman Glacier is generally too thin compared to ground truth measurements (Figure 3.4). The over-deepening measured from a seismic survey by Anderton (1975) is deeper than the Huss and Farinotti (2012) method (Section 1.6.2), or almost all of the methods in the ITMIX project, predicts across the centre of Haupapa/Tasman Glacier (Farinotti et al., 2017). If the bed DEM is too thin compared to Haupapa/Tasman Glacier's true thickness, then smaller water pressure changes would be required to get to flotation and possibly causing an underestimate of water pressures needed to cause large speed-up events. Furthermore, the inversion used to produce glacier thickness (see Huss and Farinotti, 2012) naturally smooths the bed geometry and only resolves the longer wavelength features of the bed (i.e. much larger topographical variation than the bed obstacles which generate basal friction). In lieu of a detailed image of basal topography, the basal roughness controlling sliding can be inferred from a friction coefficient (or "sliding parameter") through finite-element modelling (Gagliardini et al., 2007)(Section 2.5.1, 2.5.2).

Digital Elevation models of Haupapa/Tasman Glacier

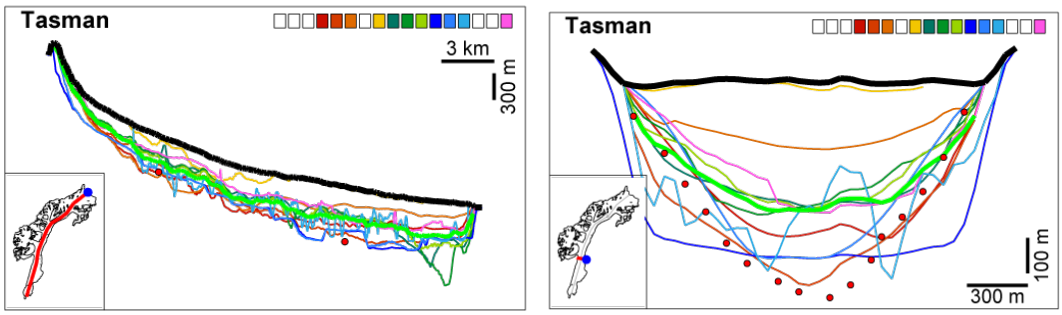

(A) Flowline view of DEMS for Haupapa/Tasman Glacier

(B) A cross section through different bed models of Haupapa/Tasman Glacier

FIGURE 3.4: A comparison of all glacier bed DEMs created for Haupapa/Tasman Glacier as part of ITMIX(figures are taken directly from Farinotti et al. (2017)). Measured bed thicknesses from seismic observations made by Anderton (1975) are shown by red dots. The light orange line corresponds to the solution using the method of Huss and Farinotti (2012). The red line in the inset maps show where the bed DEMs are sampled to produce A) and B)

Compiling 2D and 3D meshes

The geometry of 2D and 3D meshes representing Haupapa/Tasman Glacier are confined by a surface DEM (Digital Elevation Model), a thickness map from Farinotti et al. (2017) using the method of Huss and Farinotti (2012), and an outline of the glacier. The bed DEM is created by subtracting the thickness map from the surface DEM. The outline is taken from the Randolph Glacier Index (RGI) which contains a worldwide inventory of digitised glacier outlines (Pfeffer et al., 2014).

A 2D flowline mesh and a 3D mesh are created to represent the lower ∼8 km of Haupapa/Tasman Glacier (Figure 3.1). In both cases, the meshes terminate where the Hochstetter Ice Fall enters the main trunk. This is to avoid the large change in ice velocity apparent across the intersection with the icefall (Figure 1.12) (Redpath et al., 2013). The up-stream limit should also not be placed too close to the GNSS network, as the velocity boundary condition placed here could influence the modelled surface velocities at GNSS sites (the sensitivity of sliding speed due to the velocity of the upper boundary condition is presented in Section 5.2.3).

To define the surface of the 2D mesh, the surface and bed DEMs are sampled manually with a spacing of approximately 100 m up the centre of Haupapa/Tasman Glacier's main trunk. The two DEMs define the upper and lower boundaries in which a rectangular grid of points is fit into (Figure 3.5). The squares of the grid define the "elements" of the model, and the points of the grid define the "nodes" where the equations that give the stress, velocity, and pressure are solved (using the Navier-Stokes equations) (Equation 3.8; Section 3.2.1).

2D mesh of Haupapa/Tasman Glacier

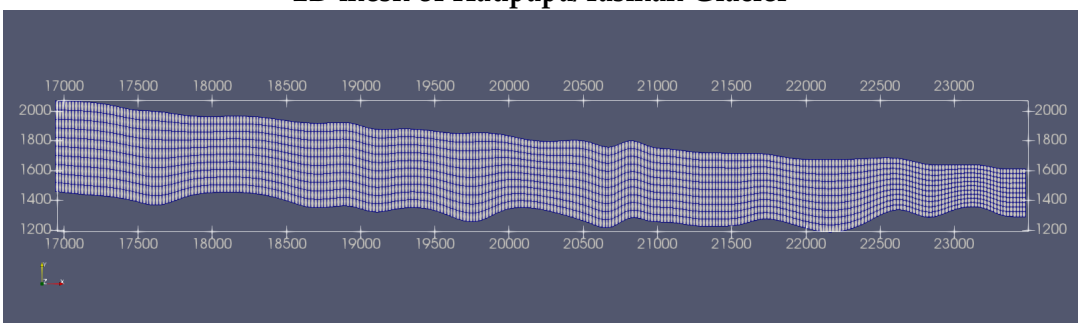

FIGURE 3.5: A 2D mesh of Haupapa/Tasman Glacier where the terminus is on the right and upstream is towards the left. Y axis of grid is elevation above sea level in (m). X axis is distance from upper most limit of Haupapa/Tasman Glacier in metres. A vertical exaggeration of 2× is used to better view variation in bed topography.

The 3D Mesh is created by first creating a "footprint" of the glacier i.e. a flat surface defined by the outline of the glacier and divided into many individual triangular elements (Figure 3.6). The footprint is made into a 3D object by stacking similar 2D layers onto each other (i.e. layers which have the same set of triangular elements) until it forms a 3D grid within the glacier outline contour. The top and bottom layers of the mesh are defined by the surface and bed DEMs – both of which

are re-sampled using a 100m grid to be consistent with each other. The resolution of the mesh is controlled by the number of points in the outline file. An outline with points spaced at 100 m is chosen to run all experiments with. A high resolution is needed to capture the changes in strain that occur over small distances during a glacier that does not accelerate uniformly – which is suggested in the observations of (Horgan et al., 2015). A 100 m resolution gives a trade-off between capturing the changes in strain over short distances and using manageable model run times which get significantly longer for higher resolutions.

3D mesh of Haupapa/Tasman Glacier

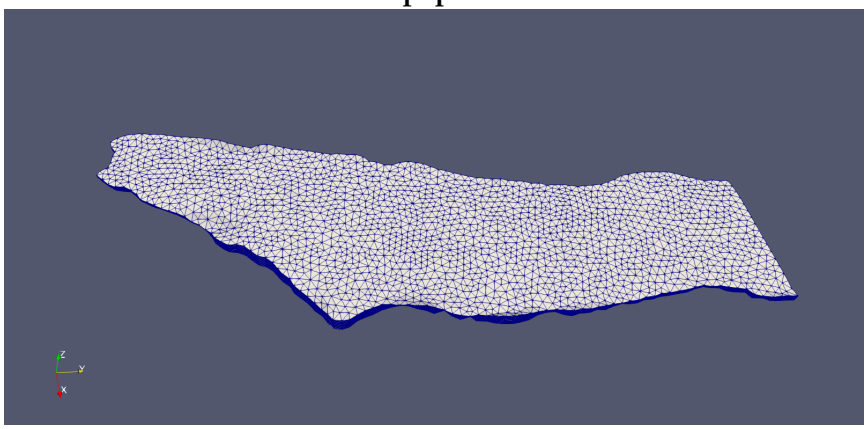

(A) View of 3D mesh from above. Terminus on left

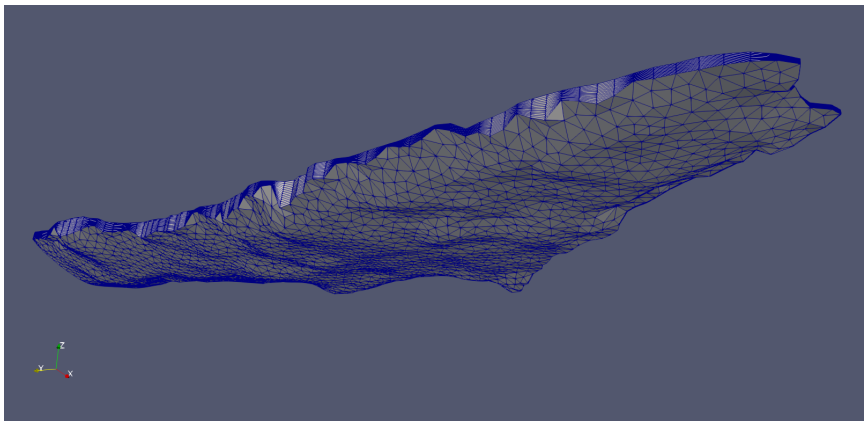

(B) View of 3D mesh from below. Terminus on right.

FIGURE 3.6: The mesh used to run finite-element model simulations of Haupapa/Tasman Glacier. An outline file with a point spacing of 100 m was used in constructing the mesh.

Manual edits to 3D mesh

Near the meeting point between the terminus and the Murchison Valley is a depression in the surface where the thickness map also tends towards very low values (Figure 1.11, 3.1). This region is troublesome in that some of the bed DEM values greater than the surface DEM which create points with negative thickness). To fix

this, a minimum height of 1.0 m is imposed on all points so that if a negative thickness arises the 3D mesh will not attain any tangled nodes.

3.2.4 Sliding laws in Elmer/Ice

A goal of this study is to evaluate the use of a Coulomb-type sliding law in recreating rapid sliding at Haupapa/Tasman Glacier (i.e. Research Question 2 in Section 1.7). Here, a finite-element model of ice flow solves for the deformational velocity $\vec{u}_{def}$ and the sliding velocity $\vec{u}_b$ simultaneously which combine to give a modelled velocity field for Haupapa/Tasman Glacier (Equation 3.8, Section 2.2). The Coulomb-type sliding law can produce a significant velocity response under low effective pressures (Section 2.5.2). To make use of this behaviour, both 2D and 3D models are run with a varying basal water pressure to decrease basal stress and trigger large sliding speeds (to be discussed fully in Sections 3.2.4 & 3.2.4).

Modelled sliding speed and basal stress in an Elmer/Ice simulation are constrained by a simple linear equation:

$$\vec{\tau}_b = \beta \vec{u}_b \tag{3.9}$$

where β is the slip coefficient that links basal stress to sliding velocity (Gagliardini et al., 2013). In order to implement a sliding law that causes sliding speed to vary with effective pressure, β must be defined such that it becomes a function of position, sliding speed, and basal water pressure (i.e. $\beta(\vec{x}, \vec{u}_b, N, t)$). The Coulomb-type law given by Equation 2.12 is reworked into the form of Equation 3.9:

$$\beta(\vec{x}, \vec{u}_b, N, t) = C_s N \left[\frac{\chi \vec{u}_b^{-n}}{1 + a\chi^q} \right]^{1/n} \tag{3.10}$$

where

$$\chi = \frac{\vec{u}_b}{C_{max}^n N^n A_s} \tag{3.11}$$

C_s is a friction coefficient tweaked to fit observations and represents basal roughness and mechanical properties of ice (Cuffey and Paterson, 2010). C_{max} is the maximum slope of the bedrock topography (used in Iken's bound for basal stress which is explained in Section 2.5.2). A_s is a friction parameter that represents a friction coefficient for sliding in the absence of cavitation (e.g. Equation 2.7).

Boundary conditions in simulations of speed up events

Solving the Navier-Stokes equations (i.e. Equation 3.8) to produce solutions for velocity, stress, and pressure over a finite-element mesh requires boundary conditions along the model's sides. The boundary conditions common to each model are summarised in Table 3.1. The Coulomb-type sliding law (Section 2.5.2) is used in each experiment to govern sliding velocity and basal stress along the lower boundary.

The velocity boundary condition for the upstream limit and glacier terminus are uniform horizontal velocities in the downstream direction. For instance, the terminus velocity is locked at 45 m yr^{-1} which is taken as a lower limit of background velocity based on the surface velocity field presented by Redpath et al. (2013). The horizontal velocity of the upstream limit is varied in model experiments to test for the sensitivity of this boundary condition upon the surface velocity solution (Section 5.2.3). In all future experiments, this is achieved by the parameter u_{side}. In 3D models, the u_{side} parameter is also set to vary the velocity of the glacier sides. The upper surface of the model is a stress-free surface. This allows the surface to deform vertically due to compression or extension of the glacier — thus allowing a calculation of vertical displacement of strain (Section 2.14).

TABLE 3.1: A Summary of boundary conditions for finite-element models in this study. The velocity and stress boundary conditions presented here are for both 2D and 3D modelling, though additional boundary conditions for 3D are described in Section 3.2.4 & 5.4. Velocity conditions for the terminus and upper limit are uniform horizontal velocities in the downstream direction

Boundary	**Velocity Condition**	**Stress Condition**
Terminus	45 m yr^{-1}	-
Upper surface	-	$\vec{\sigma} \cdot n = 0$
Upper limit	Variable in model u_{side}	-
Glacier Sides (3D only)	Variable in model u_{side}	
Glacier Bed	Coulomb-type sliding law	Coulomb-type sliding law

Water Pressure Function

The most crucial function of this model is to link rainfall to accelerated sliding, a process which is facilitated by including an effective pressure variable that varies with time (i.e. $N(x,t)$) in the COulomb-type sliding law. The most obvious means of assessing whether the Coulomb-type sliding law produces a physically reasonable solution of basal sliding in reproducing observed surface velocities is whether effective pressure stays below flotation. Effective pressure is calculated in Elmer/Ice by

$$N = -\sigma_{nn} - P_w \tag{3.12}$$

where σ_{nn} is the normal stress to the bed. Instead of using P_i as in Equation 2.2, normal stress is more accurate for describing the force balance where bed topography is sloped (Figure 3.5, 3.6; Section 1.3.1). Here, a rapid increase in basal water pressures P_w is mimicked in finite-element models using a simple exponential rise and decay:

$$P_w(x,t) = \begin{cases} \Delta P e^{t - t_{peak}/c_{rise}} + P_0, & t < t_{peak} \\ \Delta P e^{-(t - t_{peak})/c_{decay}} + P_0, & t \geq t_{peak} \end{cases} \tag{3.13}$$

where $\Delta P = P_{peak} - P_0$ is the difference between the maximum and background (i.e. prior to the speed-up) water pressures. t_{peak} is set to the same time as observed peak velocities in the GNSS record, which assumes basal water pressure peaks with velocity (which should be true if Haupapa/Tasman Glacier undergoes sliding that can be described by the Coulomb-type sliding law) (Iken and Bindschadler, 1986; Jansson, 1995). The parameter c_{rise} defines the shape of the rising phase of the water pressure curve and essentially controls how rapidly the rise occurs. Similarly, the c_{decay} parameter controls the timescale over which water pressure decays from peak to background levels. In modelling water pressure, it is assumed that these constants are related to the total time it takes for the water pressure signal to rise and fall by $t_{rise} = c_{rise}$ and $t_{decay} = 5c_{decay}$. In other words, after a time t_{decay}, the peak change in pressure signal ΔP has decayed to zero such that

$$P(t_{peak} + t_{decay}) = \Delta P e^{1/5} + P_0 \approx P_0 \tag{3.14}$$

Hence, the parameters varied to model water pressures in this study are: P_0, P_{peak}, t_{peak}, t_{rise}, and t_{decay}.

Horgan et al. (2015) notes that their upstream GNSS site accelerates before the downstream site during speed-up events, suggesting that peak velocity propagates downstream. To model this observation, the time of peak water pressure is set to vary with position downstream. Assuming the glacier is roughly aligned north-south, position downstream is given in terms of the northing coordinate (in the New Zealand Trans Mercator coordinate system)(Figure 3.1):

$$t_{peak}(y, t) = t_{TASC3} + \frac{\partial dt_{peak}}{\partial dy} \Delta y \tag{3.15}$$

where y is position in northings. t_{TASC3} is the time of peak velocity at the northernmost GNSS site TASC3, $\frac{\partial dt_{peak}}{\partial dy}$ is the speed of the wave-front southwards (which is assumed to be constant) and $\Delta y = y_{TASC3} - y_{site}$ is the downstream distance of each station from the reference site TASC3. The speed of the wave front is found by a linear fit to the time of peak velocity versus distance north-south (Figure 4.13, 4.14).

The basal water pressure function aims to capture the fact that speed-up events tend to show a rapid initial phase of acceleration, before a more prolonged decay (Horgan et al., 2015). Allowing the water pressure to peak at the same value across the bed and increase uniformly in the east-west direction is likely an oversimplification of the true subglacial drainage system beneath Haupapa/Tasman. However, this water pressure model would be most comparable to a distributed subglacial drainage system in which a cavity network extends over the entire bed and is connected enough, or develops enough connectivity, to cause water pressure variations over a large enough scale to control the overall sliding speed of the glacier (Jansson, 1995; Kamb and Echelmeyer, 1986; Mair et al., 2001). The treatment of subglacial hydrology in the finite-element models is discussed further in Section 6.2.3.

3.2.5 Time-evolving velocity boundaries in 3D

For the Coulomb-type sliding law, as water pressures approach flotation, longitudinal stress and friction against the sides become increasingly important in supporting a glacier's driving stress. Ideally, a test of how significant side friction is on limiting a glacier's peak velocity would include a sliding law applied along the side walls of the 3D mesh. In this way, a sliding law and a unique friction coefficient could be tweaked to investigate the balance of side friction upon peak velocity. However, in this study, issues were encountered involving the 3D mesh where the bed DEM meets the vertical sides (Figure 3.6). Where the slope of the bed is close to being flat or negative there is a sharp corner in the mesh where it joins the side walls. In these zones, the model results are unstable, resulting in anomalously high spots of velocity in the angular corners. These corners are unlikely to be a natural feature of the bed as glacier valleys tend to be rounded from erosion.

A simpler approach is instead applied, in which a time-evolving velocity boundary condition is applied to the upstream limit and, in 3D models, the sides of the glacier model. For simplicity and continuity in the velocity field, a single parameter u_{side} is chosen to represent the peak boundary velocity $u_{boundary}$ that varies at a similar rate as the basal water pressure:

$$u_{boundary}(t) = \begin{cases} \Delta u_{side} e^{t - t_{peak}/c_{rise}} + u_0, & t < t_{peak} \\ \Delta u_{side} e^{-(t - t_{peak})/c_{decay}} + u_0, & t \geq t_{peak} \end{cases} \tag{3.16}$$

where u_0 is the inital background speed of the sides and/or upstream limit and $\Delta u_{side} = u_{side} - u_0$.

3.2.6 Other parameters in ice flow model

In addition to basal water pressure, parameters that control the rate of ice deformation and the dependence of sliding speed on bedrock topography need to be defined. These parameters are summarised in (Table 3.2). Elmer/Ice calculates velocities and pressure in a m-MPa-yr (metres-Megapascals-year) unit system as opposed to the standard m-Pa-s (meters-pascals-seconds) system because velocities and pressures in glaciological problems are typically quoted in meters per year and Megapascals.

Values for the Glen's flow exponent n, creep parameter A, and enhancement factor E are recommended values taken from Paterson (1994) which have been adopted in Elmer/Ice simulations in Gagliardini and Werder (2018). Iken's bound parameter C_{max} gives the maximum slope of bedrock topography and controls the maximum τ_b/N ratio in the Coulomb-type sliding law. This parameter is not well constrained as there is limited information of Haupapa/Tasman Glacier's bed (Section 1.6.2). C_{max} is, however, likely to exists in a range between 0.18-0.84 based on limited laboratory and field experiments (Cuffey and Paterson, 2010).

TABLE 3.2: A list of parameters used for modelling ice deformation and basal sliding in this study. Parameters in the standard unit system and the m-MPa-yr system, for use in Elmer/Ice, are displayed.

Glen's flow law parameter	n	3	3
Creep parameter	A	6.8×10^{-24} s^{-1} Pa^{-3}	1.258×10^{13} yr^{-1}MPa^{-3}
Enhancement factor	E	1.0	1.0
Ice density	ρ_i	900 kg m^{-3}	9.05×10^{-19} MPa yr^{-2} s^{-2} m^{-2}
Gravity	g	9.81 m s^{-1}	9.756×10^{15} m yr^{-2}
Average ice temperature	T_{ice}	-3.0 °C	-3.0 °C
Young's modulus	Y	1.0	1.0
Poisson ratio	ν	0.3	0.3
Iken's bound parameter	C_{max}	0.5	0.5
Post-peak exponent	q	1	1

3.2.7 Finite-element modelling process

The 2D and 3D models generally follow the same process in recreating Haupapa/-Tasman Glacier's speed-up events. This section details the methods of attaining unknown parameters and what parameter space is explored in each experiment. In general, there are two types of experiments: steady-state (where forces are balanced) and transient (where forces evolve with time). Steady-state tests are used for recreating Haupapa/Tasman Glacier's background velocity field and transient tests are used when modelling speed-up events. A full summary of the modelling process is represented diagrammatically in Figure 3.7.

The 2D flowline model of Haupapa/Tasman Glacier acts as a preliminary test for the magnitude of basal water pressure changes during rapid acceleration. Before developing the 3D model, which is constrained by the GNSS network (Figure 3.1), the 2D model aims to replicate the motion of only the centre-line units. Essentially, the flowline model treats the sides of the glacier as having a negligible effect upon the velocity at the glacier's centre.

Seven variables are tweaked in the process of recreating a speed-up event using a finite-element model: C_s, P_0, P_{peak}, t_{peak}, t_{rise}, t_{decay} u_{side}. Each test (described below) is aiming to constrain one or more of these parameters. A test is set up by creating a range for each variable and creating a parameter sweep: this is where a solver file for every combination of every variable is created and run in Elmer/Ice. The output of each model is compared to either GNSS velocities or vertical displacements. Parameters are tweaked to minimise misfit between the motion at each GNSS site and the nearest nodes on the mesh to each GNSS site by a least-squares approach. The general modelling process is described in the following section.

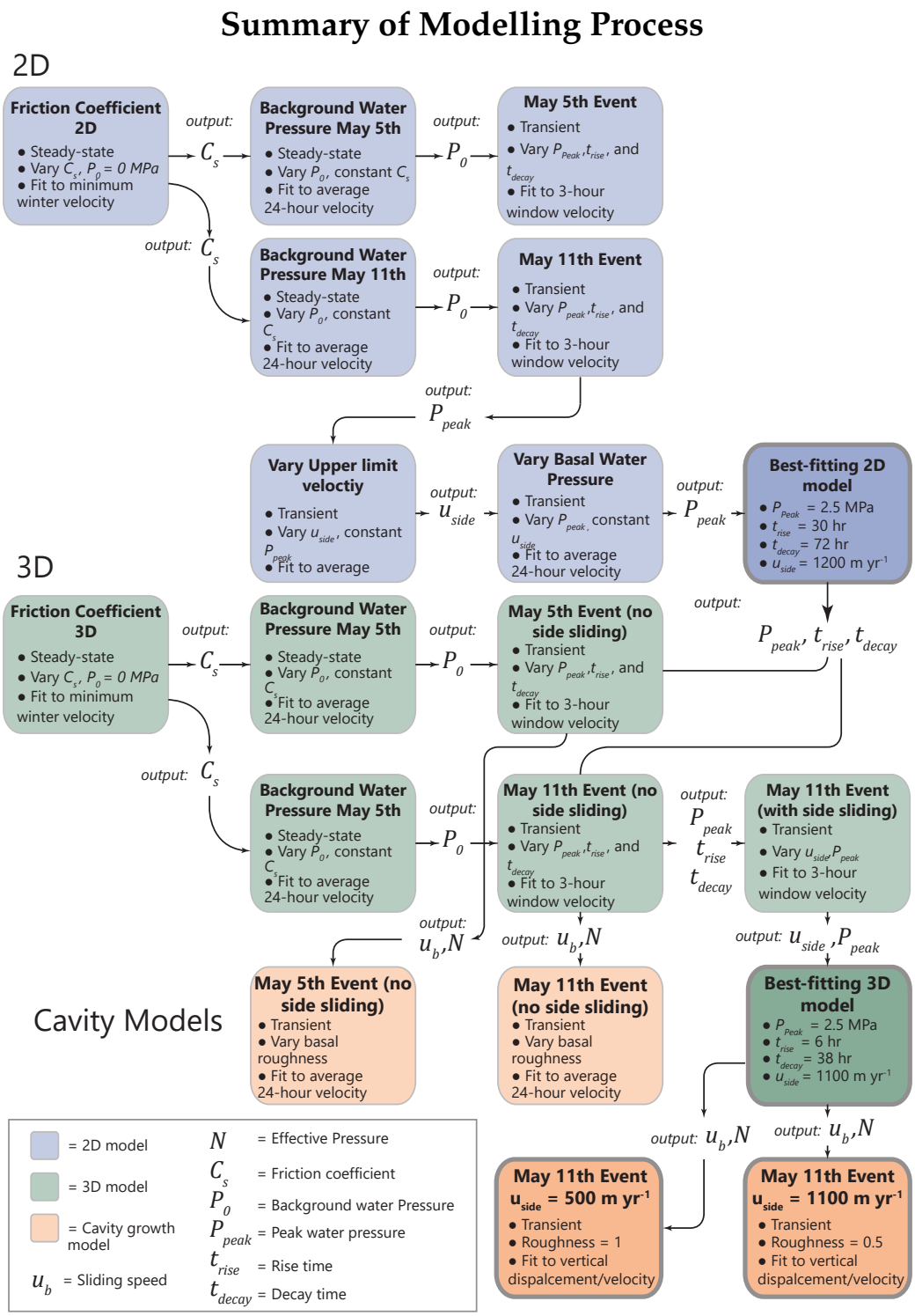

FIGURE 3.7: A flowchart showing the modelling process for all results presented in Chapter 5.

Stage 1: Find friction coefficient C_s

Firstly, a group of steady-state tests are run which vary the friction coefficient C_s. The surface velocity of each model is compared to the minimum winter velocity calculated from the seasonal fit in using Equation 3.1 (Section 3.1.4).The background

seasonal signal gives the long-term, background velocity signal that smooths small-wavelength variation such as diurnal variation, speed-up events, and GNSS noise. The minimum velocity from each GNSS should then indicate when water pressure is at its minimum (Table 4.2). Due to a lack of basal water pressure measurements at Haupapa/Tasman Glacier, the water pressure is assumed to be $P_w = 0$ following, Flowers et al. (2011). Of course, this assumption is easily challenged by the fact that there a constant background flow due to high annual rainfall and background surface melting (Horgan et al., 2015; Purdie and Fitzharris, 1999). So while absolute water pressures may not be resolved in this study, it is the change in basal water pressure and proximity of peak water pressure to overburden pressure that is important in assessing the Coulomb-type sliding law in modelling Haupapa/Tasman Glacier's speed-up events (i.e. Research Question 2 in Section 1.7) (Jay-Allemand et al., 2011).

Stage 2: Find background water pressure P_0

Using the friction coefficient found from the experiment described in the previous step, a second experiment is run to solve for the background water pressure P_0 leading up to the May 5th and May 11th speed-up events (Figures 5.2.2, 5.9). A steady-state model is run and the basal water pressure parameter is varied to match surface velocities. The surface velocities being matched are the average background horizontal velocity leading up to the event. These background velocities are calculated by taking an average of the GNSS derived velocities calculated over a 24-hour time window in the 3 days leading up to an event. The basal water pressure that provides the best match to the average background horizontal velocities defines the initial water pressure P_0 used in the transient models.

Stage 3: Transient test with constant side velocity boundary conditions

Using the friction coefficient and background water pressure from the previous two tests, a transient test is undertaken that varies P_{peak}, t_{rise}, and t_{decay} in order to match surface observations during speed-up events. Horizontal and vertical velocity records over a three-day window around speed-up events (defined by the green boxes in Figure 4.1, 4.2, 4.4) are extracted. For 2D models the upstream boundary velocity is locked at $u_{side} = 70\,\mathrm{m\,yr^{-1}}$ (Figure 5.4). For 3D models, the sides are kept static $u_{side} = 0\,\mathrm{m\,yr^{-1}}$ (i.e. a "no-side-slip" model) for model stability.

Stage 4: Transient test that varies water pressure and side boundary conditions

A second transient test is run which varies P_{peak} and u_{side} in order to test the effect of the velocity boundary condition on the resulting modelled surface velocity field (e.g. Figure 5.6, 5.13).

Stage 5: Test the effect of the C_{max} parameter on sliding velocity

Run a test that varies C_{max} over its likely range (see Section 3.2.6) to test the sensitivity on the modelled surface (Section 5.5.1).

Stage 6: Cavity model

Use the modelled sliding speed u_b, effective pressure N, and vertical strain ϵ_{zz} from the previous transient tests to run a cavity model that models vertical displacement during speed-ups (explained in Section 3.3).

3.3 Cavity Modelling

Because the Coulomb-type sliding law is restricted to motion parallel to the bed (i.e. a no penetration into the bedrock or basal uplift is applied), some additional mechanism is required to reproduce vertical displacements in models of ice flow. Vertical displacement at the surface can be the product of either vertical deformation or bed separation due to cavity growth (Section 2.5.4) (Hooke et al., 1989; Sugiyama and Gudmundsson, 2004). Here, 2D and 3D finite-element models calculate vertical deformation (ϵ_{zz}) as part of the solution for velocity and pressure as the upper boundary is a free surface (Section 3.2.1). However, vertical deformation is only a small part of observed vertical displacement ($\sim$ 0.04m out of up to $\sim$0.5 m) from previous observations of Haupapa/Tasman Glacier (Horgan et al., 2015). Hence, the vertical strain output from the 3D finite-element models and a separate model of cavity growth are combined to reproduce vertical displacements during speed-up events at Haupapa/Tasman Glacier.

Following Anderson (2004), the rate of bed separation $\frac{dB}{dt}$ is defined as the rate of change of cavity volume V_{cavity} per area of bed:

$$\frac{dB}{dt} = \frac{1}{\lambda_L \lambda_T} \frac{dV_{cavity}}{dt} \tag{3.17}$$

where λ_L and λ_T define the separation of bed obstacles in the longitudinal and transverse directions (i.e. downstream and across-stream) that house the space for a cavity to grow in. In the simplest case, the volume of the cavity can be described by the cross-sectional area of box-shaped cavity S multiplied by its width $V_{cavity} = SW$ (Figure 3.8). Where, assuming no wall melting occurs during speed-up, then bed separation rate is given by:

$$\frac{dB}{dt} = \frac{W}{\lambda_L \lambda_T} \frac{dS}{dt} = \frac{W}{\lambda_L \lambda_T} \left[\frac{l u_b}{\cos(\alpha + \beta)} - SAN^n \right] \tag{3.18}$$

where, assuming that the sliding velocity is parallel to the bedrock, α is the mean bed slope from the horizontal and β is the slope of the obstacle in a tilted staircase (Figure 3.8)(Anderson, 2004). In this model, the rate in which cavity volume is produced can be controlled by the angle of the obstacles β, which is influenced the step

height h (assuming a staircase geometry in which the upstream and downstream sides remain perpendicular). The rate of change of cavity volume is dependent on the sliding rate that opens cavity space and the rate of creep closure. The rate of creep closure of cavity volume is dependent on effective pressure. Bed separation rates are also dependent on the bed roughness, which are the ratio of obstacle size to obstacle separation — i.e. $\frac{W}{\lambda_T}$ in the across-stream and $\frac{h}{\lambda_L}$ in the downstream, direction. Higher bed roughness results in greater separation rates. To vary separation rates so that vertical displacements are matched, the downstream roughness $\frac{h}{\lambda_L}$ is varied. The across stream roughness is locked at $\frac{W}{\lambda_T} = 0.8$, which is a suggested upper limit used for modelling basal water pressures in Anderson (2004).

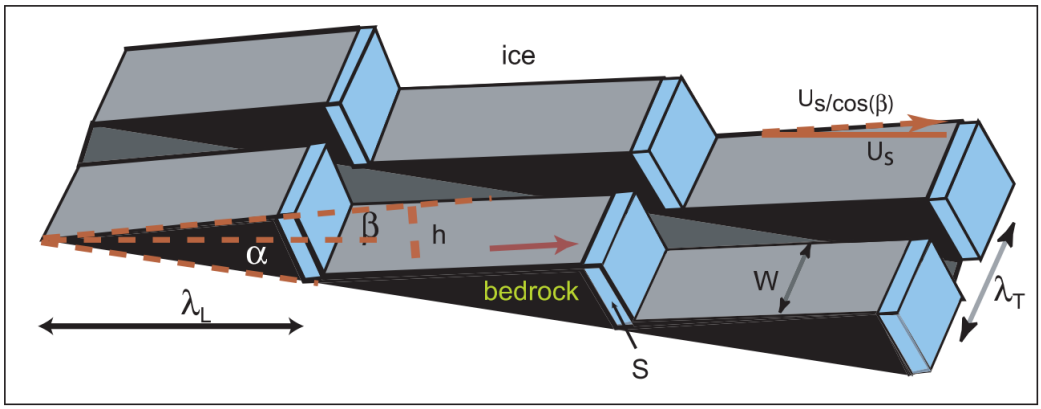

FIGURE 3.8: A simple 3D tilted staircase model of cavity growth on an idealised be used by Anderson (2004) to model subglacial water pressure based on bed separation data

3.4 Summary

The surface motion during speed-up events at Haupapa/Tasman Glacier is monitored using GNSS instruments installed across the surface. Off-centre stations (i.e. TASL1, TASL2, TASR2) allow the investigation of spatial variability of surface displacement during episodes of rain-induced acceleration (see Research Question 1 in Section 1.7). Secondly, the method of recreating these events using a finite-element approach is described in this chapter. A finite-element model is used to help assess the ability of a Coulomb-type sliding law (an effective pressure dependent sliding law) in recreating observed rapid accelerations at Haupapa/Tasman Glacierusing a downstream-propagating wave of high water pressure (see Research Question 2 in Section 1.7). The surface motion constraints for these models are presented in Chapter 4.

Chapter 4

GNSS Results

Here, I present a record of surface position and velocities of Haupapa/Tasman Glacier over 2016 from the TAS2016 deployment (see the description of GNSS network in Section 3.1). Within this year-long record are six speed-up events of interest in which the glacier accelerates significantly above background velocities. The speed-up events resemble those presented in Horgan et al. (2015) (Figure 1.13), though the expansion of the GNSS network in this study provides a more complete spatial pattern of glacial acceleration.

4.1 Horizontal and Vertical Surface Position

GNSS position data provides the cleanest record of surface displacement; surface velocity smooths out finer variations during the linear regression fit to surface position (Section 3.1.4). Offsets in both the annual vertical (Section 4.1.1) and horizontal displacement (Section 4.1.2) correspond to speed-up events. Comparing horizontal and vertical displacement during individual speed-up events shows that Haupapa/Tasman Glacier's surface is displaced in an arc-like trajectory as GNSS sites are uplifted and displaced downstream (Section 4.1.3).

4.1.1 Annual horizontal position record

Offsets in the annual record for horizontal position correspond to instances in which the GNSS sites are rapidly displaced downstream (Figure 4.1). The record is presented at each site in term of distance from the northing (i.e position on the north–south axis of the site map in Figure 3.1) of the Haupapa/Tasman Glacier's terminus. Because the glacier is roughly north–south, the northing coordinate shows the strongest signal in terms of displacement over both the annual record and individual speed-up events. The approximate terminus location is taken from the 2015 terminus presented in Purdie et al. (2016).

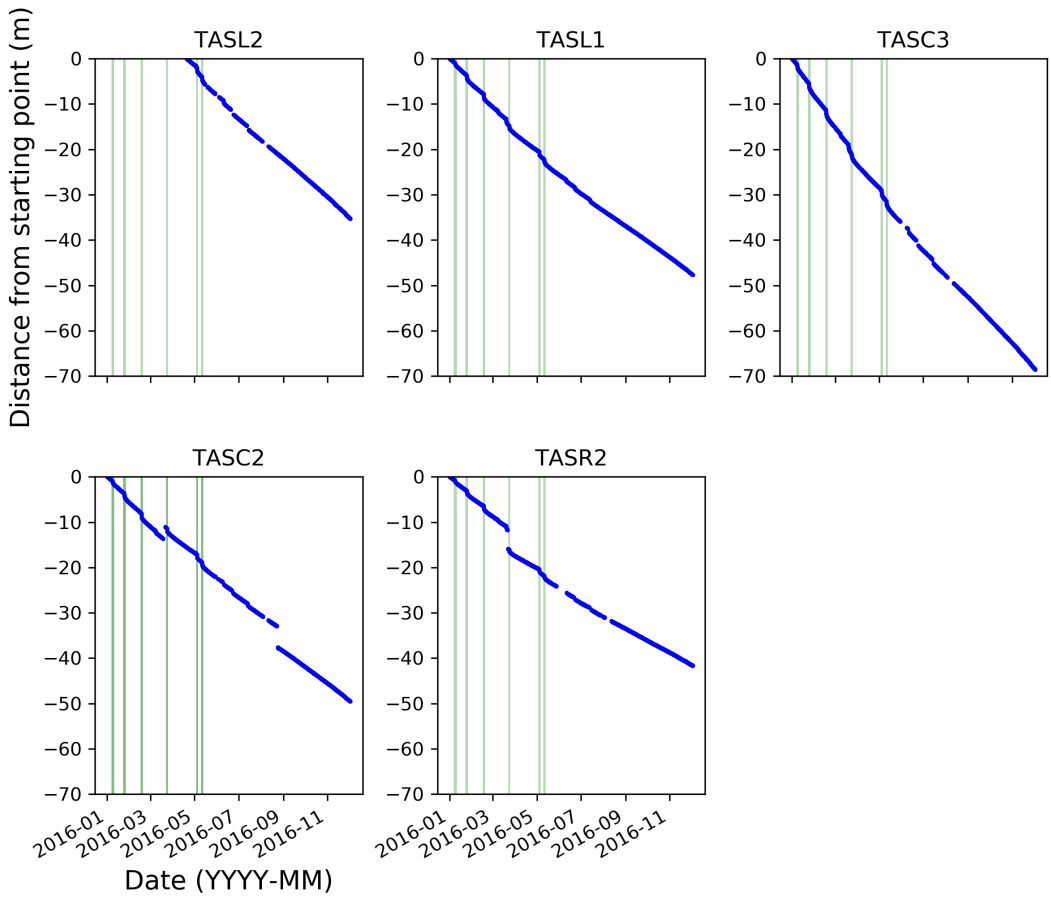

FIGURE 4.1: The downstream migration of GNSS units at each site in TAS2016 network. Only the component of southward displacement (with respect to its starting point) is displayed, which roughly aligns with the direction of Haupapa/Tasman Glacier's flow. The green bars highlight the offsets in horizontal distance that correspond to speed-up events. Following Horgan et al. (2015), the threshold for a speed-up event is $145\,\mathrm{m\,yr^{-1}}$. Events were not selected in the winter or spring months due to noise in the data introduced by poor satellite coverage and issues with GNSS station power.

4.1.2 Annual surface elevation record

The elevation of the GNSS follows a gradual rise and fall with the seasons. During winter, elevations are subdued before rising in the summer. For the sites that have a complete year-long record, the total elevation decrease over the year ($\frac{\Delta \mathrm{m}}{\Delta \mathrm{yr}}$ is always greater than the seasonal variability a (Figure 4.2). This total elevation decrease is due to a combination of the movement of the GNSS site downstream and surface melting (Table 4.1). Over 2016, several steps up to $\sim 50\,\mathrm{cm}$ in the vertical displacement record are present where the surface elevation rapidly increases during speed-ups (seen in detail in Figure 4.3).

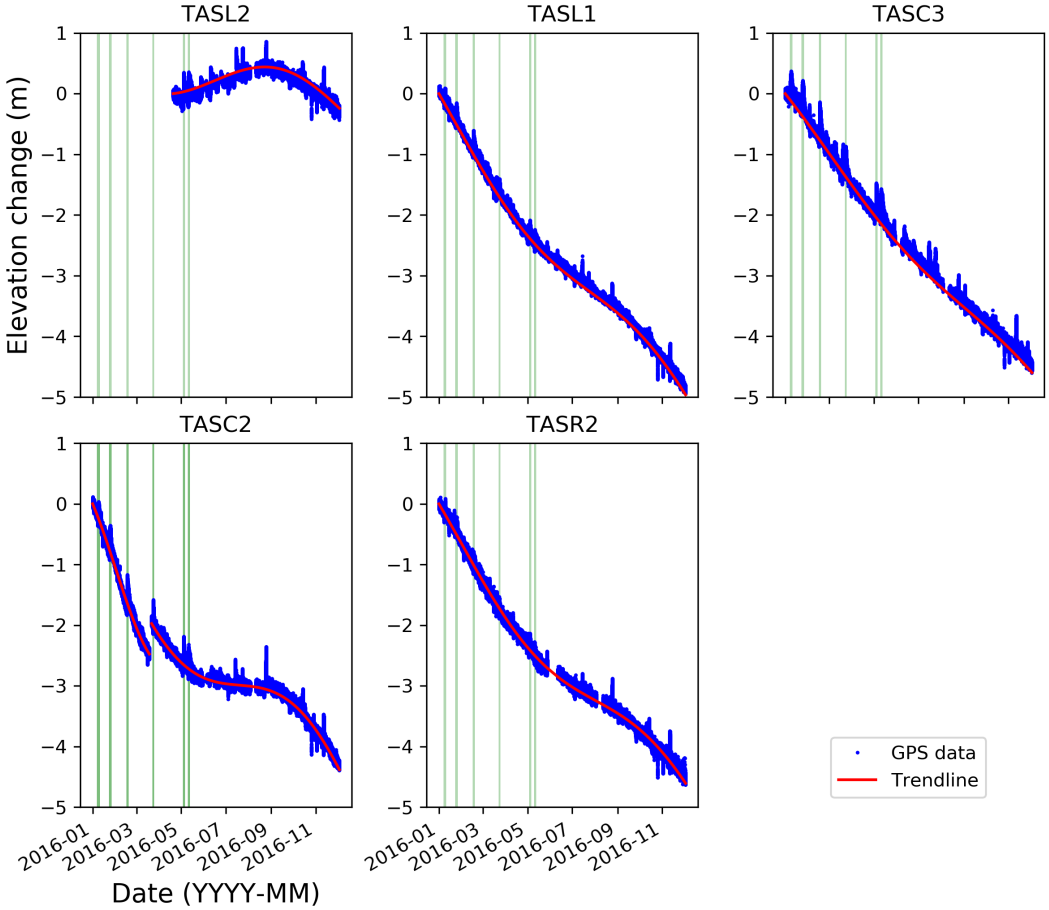

FIGURE 4.2: A year-long elevation record for TAS2016 network with best-fit trendline plotted in red. Elevation is plotted with respect to each GNSS site's initial elevation. A record of detrended elevation (used in future plots such as Figure 4.8) is achieved by subtracting the best-fit line function from the raw elevation data. The green bars are the same as plotted in Figure 4.1

TABLE 4.1: Annual variability in elevation (peak–trough) and the total decrease in elevation over the year for each GNSS site

Site	a (m)	$\frac{\Delta m}{\Delta yr}$ (m yr^{-1})
TASC3	0.39	-5.01
TASR2	0.87	-5.15
TASL2	0.97	-1.21
TASC2	1.52	-5.15
TASL1	0.73	-5.53

4.1.3 Horizontal and vertical displacement during speed-up events

Over a 72-hour period, speed-up events tend to cause Haupapa/Tasman Glacier's surface to displace downstream by ∼1–2 m and vertically up to 0.53 m (maximum uplift occurs at TASC3 site of February 17th) (Figure 4.3). Vertical displacement provides a record of vertical deformation and bed separation due to an increase in cavity volume at the base (background theory discussed in Sections 2.5.4 & 3.3). The Vertical displacement is used to constrain a model for cavity growth and is presented in Section 5.5. While the magnitude of displacement varies between each event, the behaviour of at each GNSS site is similar. TASC3 is always displaced furthest, followed by TASL2, TASC2, TASL1, and TASR2. Broadly speaking, the sites with greater vertical displacement experience greater downstream displacement (Figure 4.3). Although, TASL1 and TASC2 have almost the same degree of displacement in every event despite TASL1 undergoing roughly half of the maximum vertical displacement. TASR2 does not experience any significant vertical displacement apart from briefly peaking at 0.16 m on the January 24th event.

During the main phase of acceleration the relationship between vertical and horizontal surface displacement results in an arc-like trajectory (Figure 4.3). As the glacier begins to accelerate, both the vertical and horizontal displacements increase together. Then, vertical displacement peaks and the glacier surface begins a slow decline towards its original elevation over several days. The concentration of markers in Figure 4.3 is much higher during the decay stage meaning the surface experiences a slow return to the background elevation. Even after three-days, the centre-line sites tend to remain ∼10–20 cm above the original elevation (with the exceptions of the Jan 8th and March 23rd events and TASC2 during the Jan 24th event).

4.2 Surface velocity record

Surface displacements displayed in Figure 4.3 occur at a much greater rate than the average background velocity throughout the year. Average velocities over the course of 2016 range from 34.8–61.3 m yr^{-1} compared to the peak velocity of 1543 m yr^{-1} observed at TASC2 on February 17th (Figure 4.7) (Appendix A.3). This section provides a record of both the annual velocity record over 2016, in which speed-up events clearly stand out from the background flow. Also shown is the background flow with speed-up events removed (Section 3.1.4).

4.2.1 Yearly horizontal velocity record

During 2016, Haupapa/Tasman Glacier underwent several speed-up events that correlate with episodes of heavy rainfall (Figure 4.4). Rainfall rates of over 50 mm $day^{-}1$ result in a glacier-wide acceleration, represented by distinct peaks in the horizontal velocity record (highlighted in green in Figure 4.4) that are coincident for every available GNSS site. The maximum velocity of these peaks range between

430–1543 m yr^{-1} for velocity averaged over a 3-hour window, which gives the closest representation of instantaneous velocity (see Section 3.1.4).

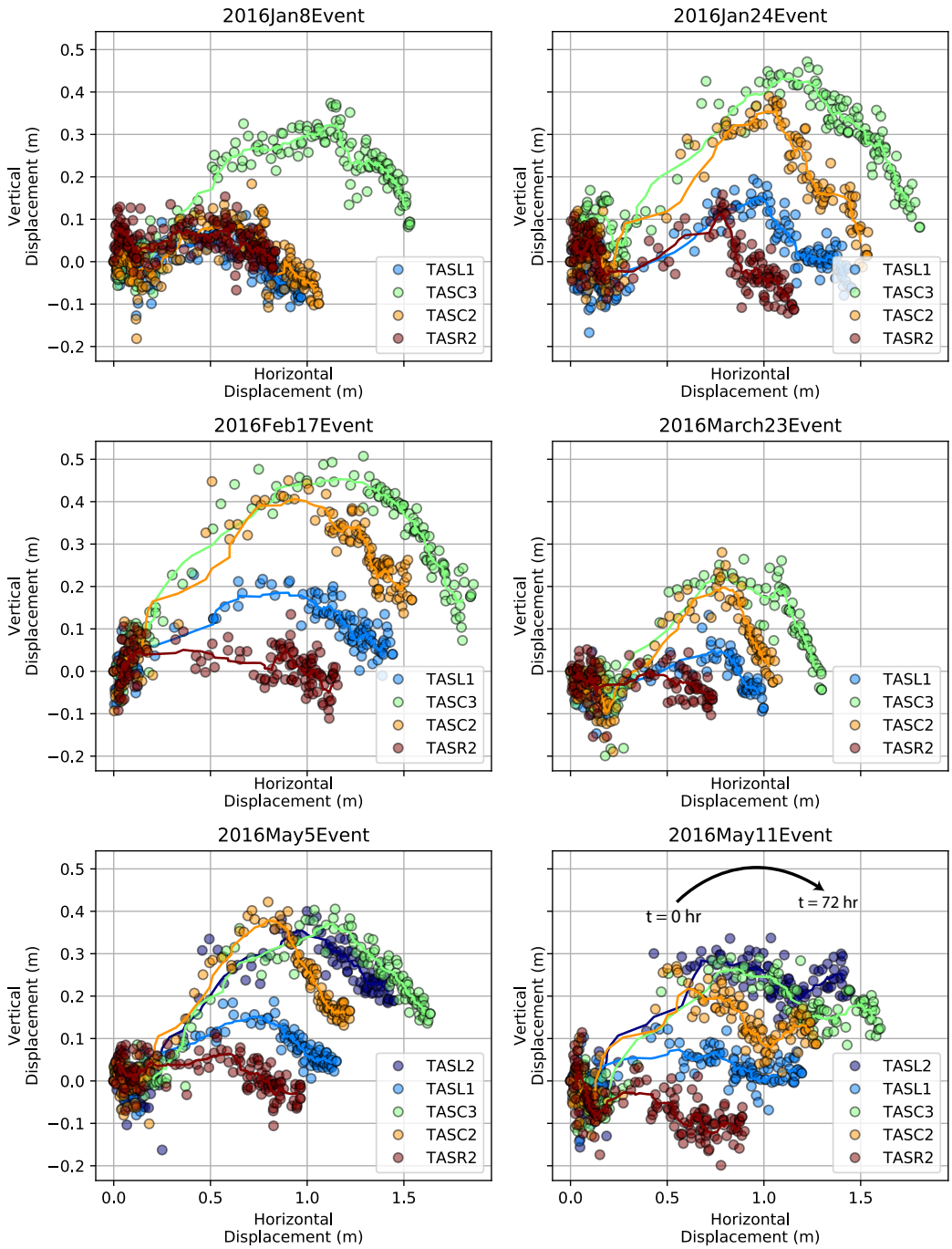

FIGURE 4.3: The vertical and horizontal positions during each speed-up event for each GNSS site. The black arrow displayed in the May 11th plot demonstrates the temporal progression of the "arc" that the glacial surface follows over the 72-hour time window. Markers are plotted every 15 minutes and cover a total of three days. A running mean with (a window size of 13 data points) is also plotted. Each plot begins at 0,0 at the start of the three-day window.

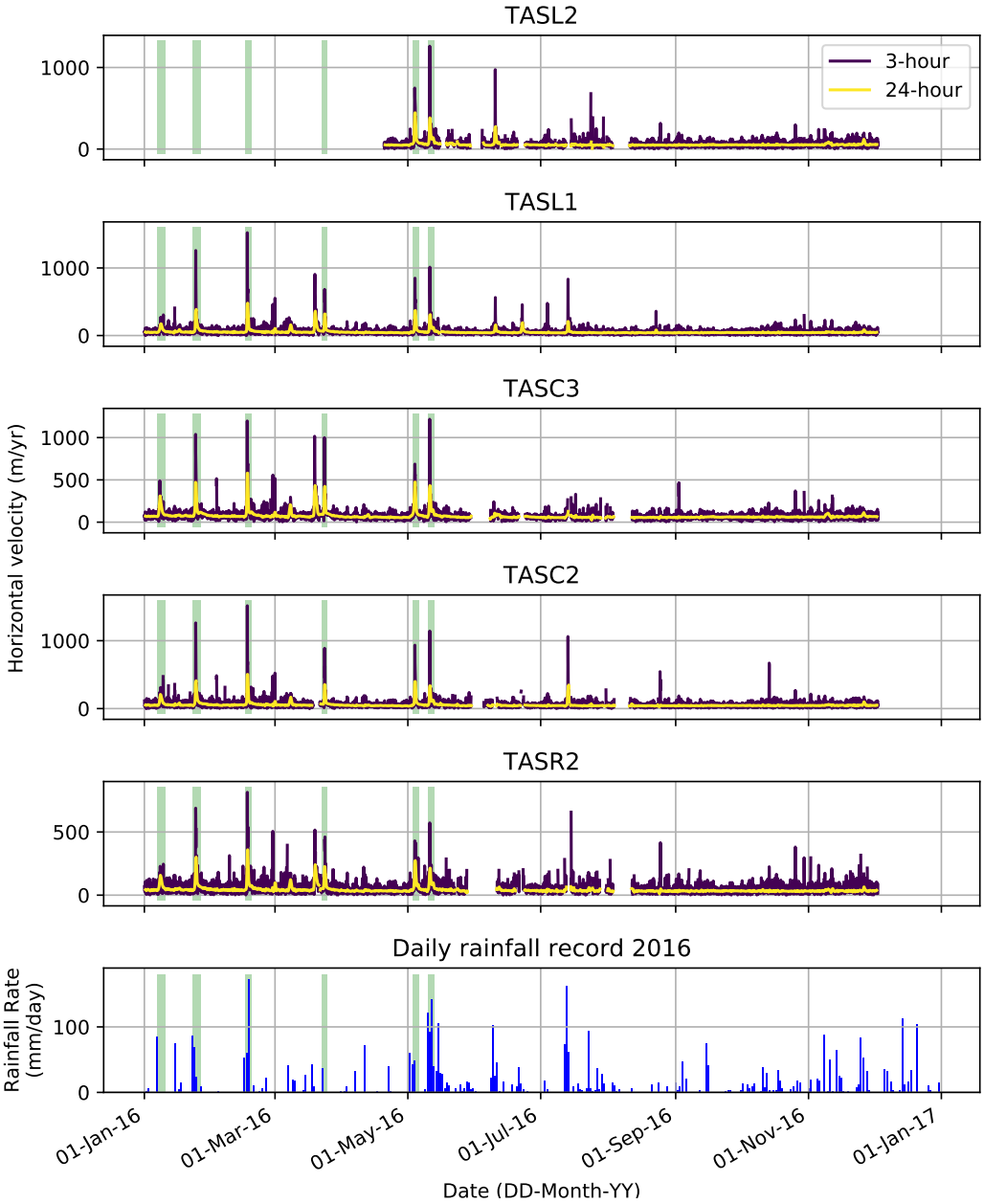

FIGURE 4.4: A plot of horizontal velocity u over 2016 for each GNSS site and the corresponding rainfall rate data (shown in the bottom plot). This shows the entirety of the velocity record considered in this study. Following Horgan et al. (2015), the threshold for a speed-up event is 145 m yr^{-1}; however, apparent speed-ups from July onwards were not selected for further study due to the higher noise in the data during winter and spring. Furthermore, some of the velocity spikes during this time are not seen at all sites and hence do not provide as strong a spatial coverage or surface velocity constrain for finite-element modelling in this study.

4.2.2 Seasonal signal in horizontal velocity

Over 2016, Haupapa/Tasman Glacier's background velocity field varies with the seasons. During summer months, the background velocities are slightly elevated, before becoming subdued in winter months (Figure 4.5). The sinusoidal variation is strongest at the TASC2 and TASC3 sites which show that a minimum velocity occurs during July (Table 4.2). Except where data gaps exist, the sinusoidal function is within the standard deviation of bi-weekly means of horizontal velocity. The minimum velocities at each site are used in the test to find the friction coefficient (see full description in Section 3.2.7). This background velocity record provides a reference velocity field prior to speed up events and is used to constrain the background water pressure (P_0) before speed-up begins (Section 3.2.7). Figure 4.5 illustrates "unperturbed" glacier flow where sliding rates are steady, water pressures are relatively low, and diurnal variation is averaged out.

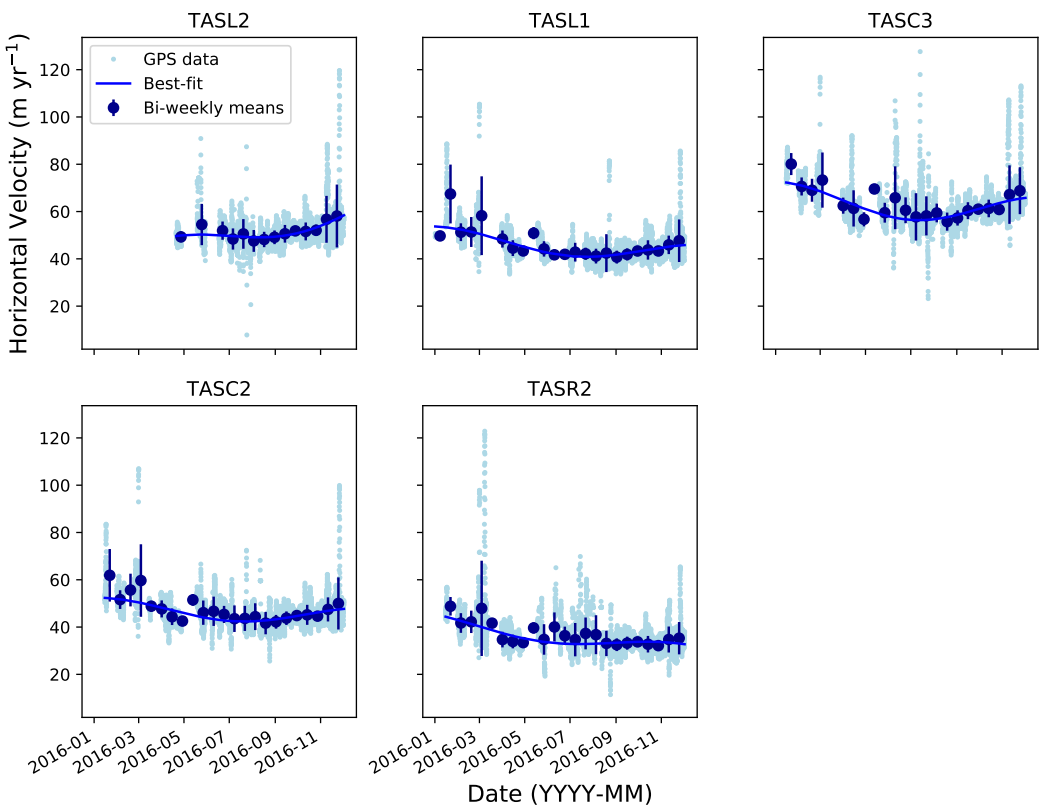

FIGURE 4.5: Best fit for a sinusoidal curve to velocity data calculated using a 24-hour velocity window. Data gaps show where speed-up events have been removed before fitting the sinusoidal function.

TABLE 4.2: Parameters for sinusoidal curves that best fit horizontal velocity data)calculated using a 24-hour velocity window) for each GNSS site over 2016. The average velocity u_{av}, seasonal variation $a_{seasonal}$, uncertainty in seasonal variation $\sigma_{a_{seasonal}}$, minimum velocity u_{min}, and date of minimum velocity for the best-fit function to background velocities over 2016.

GNSS site	u_{av} (m yr^{-1})	$a_{seasonal}$ (m yr^{-1})	$\sigma_{a_{seasonal}}$ (m yr^{-1})	u_{min} (m yr^{-1})	date of min
TASL2	51.3	11.1	0.7	49	Aug 10
TASL1	44.2	8.7	0.2	41	Jul 23
TASC3	61.3	12.9	0.2	56	Jul 12
TASC2	45.4	7.8	0.2	42	Jul 21
TASR2	34.8	6.5	0.3	32	Dec 2

4.2.3 GNSS Velocity Uncertainty

Uncertainty in horizontal velocities calculated over a three-hour window (processing explained in Section 3.1.4) are small compared to peak velocity during speed-ups (Table 4.3). 95% of uncertainties in the 3-hour window velocities are lower than 18 ± 2 m yr^{-1} across the network, which is $< 0.03\%$ of the maximum peak speeds displayed in Table 4.3 (894 m yr^{-1} at TASR2 on February 17th). Using a 24-hour window greatly reduces uncertainties. In this case, 95% of uncertainties are less than 1.4 ± 0.4 m yr^{-1}, which is $< 0.06\%$ of the lowest average velocity in Table 4.2 (see histograms for 24-hour window velocities in Appendix C).

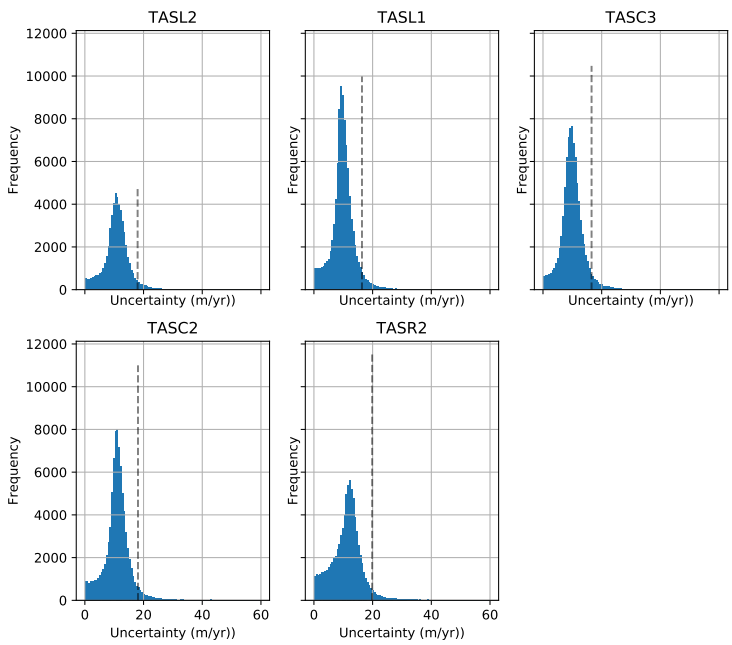

FIGURE 4.6: Histograms for uncertainties in horizontal velocities (3-hour window) over 2016. The uncertainties are 95% confidence limits of the slope of GNSS positions calculated over a three-hour window.

TABLE 4.3: 95% confidence limits for horizontal velocity distributions shown in Figure 4.6. Peak velocities and date of occurrence are also shown for comparison.

GNSS site	95% limit (3-hour)	95% limit (24-hour)	Max horizontal velocity
TASL2	18 m yr^{-1}	1.7 m yr^{-1}	1317 m yr^{-1} (May 11th)
TASL1	16 m yr^{-1}	1.0 m yr^{-1}	1541 m yr^{-1} (Feb 17th)
TASC3	16 m yr^{-1}	1.3 m yr^{-1}	1216 m yr^{-1} (May 11th)
TASC2	18 m yr^{-1}	1.5 m yr^{-1}	1543 m yr^{-1} (Feb 17th)
TASR2	20 m yr^{-1}	1.8 m yr^{-1}	894 m yr^{-1} (Feb 17th)

4.3 Surface motion during speed-up events

4.3.1 Vertical and horizontal velocity relationship during speed-up events

In general, the accelerating and decelerating phases of the speed-up show different relationships between the velocity components (Figure 4.7). The vertical and horizontal velocities increase together, peak within an hour of each other before decaying. Initially, horizontal velocities increase with vertical velocities — which is typically attributed to the temporary enhancement of sliding speed due to cavity growth (Cowton et al., 2016; Iken et al., 1983). For each event, vertical velocity always decays to background levels first. This forms a "loop" in a plot of vertical versus horizontal velocity, which is most evident in the May 11th event (Figure 4.7). However, the faster decrease in vertical velocity is not always evident for each GNSS site in each event. The TASC2 site, in particular, appears to follow a similar path between both accelerating and decelerating phases during the February 17th, March 23rd, and May 11th events.

Furthermore, the relationship between horizontal velocity and vertical displacement can be noticeably different between sites. For the centre-line sites (TASC2 and TASC3) and TASL2, the vertical velocities generally peak with similar magnitude and timing to the horizontal component (Figure 4.7). A greater peak horizontal velocity is associated with a greater rate of vertical motion. This trend, however, doesn't hold for the off-centre-line site TASL1 which has a similar horizontal velocity record to TASC2, but around half of the peak vertical velocity. Because the vertical velocity record is noisy (Section 3.1.4), the "loops" of vertical and horizontal velocity are often disrupted when vertical velocities a few hundred m yr^{-1}. Plots of horizontal velocity versus detrended elevation demonstrates a more consistent relationship (see Section 4.3.2).

The January 8th event is not well resolved by the GNSS network as it is only detected at the TASC3 site. The event is anomalous in that no other event shows only a single centre-line site accelerating in the 2016 record or in Horgan et al. (2015)'s record. In the remainder of this study, only events which demonstrate characteristic speed-up behaviour will be discussed.

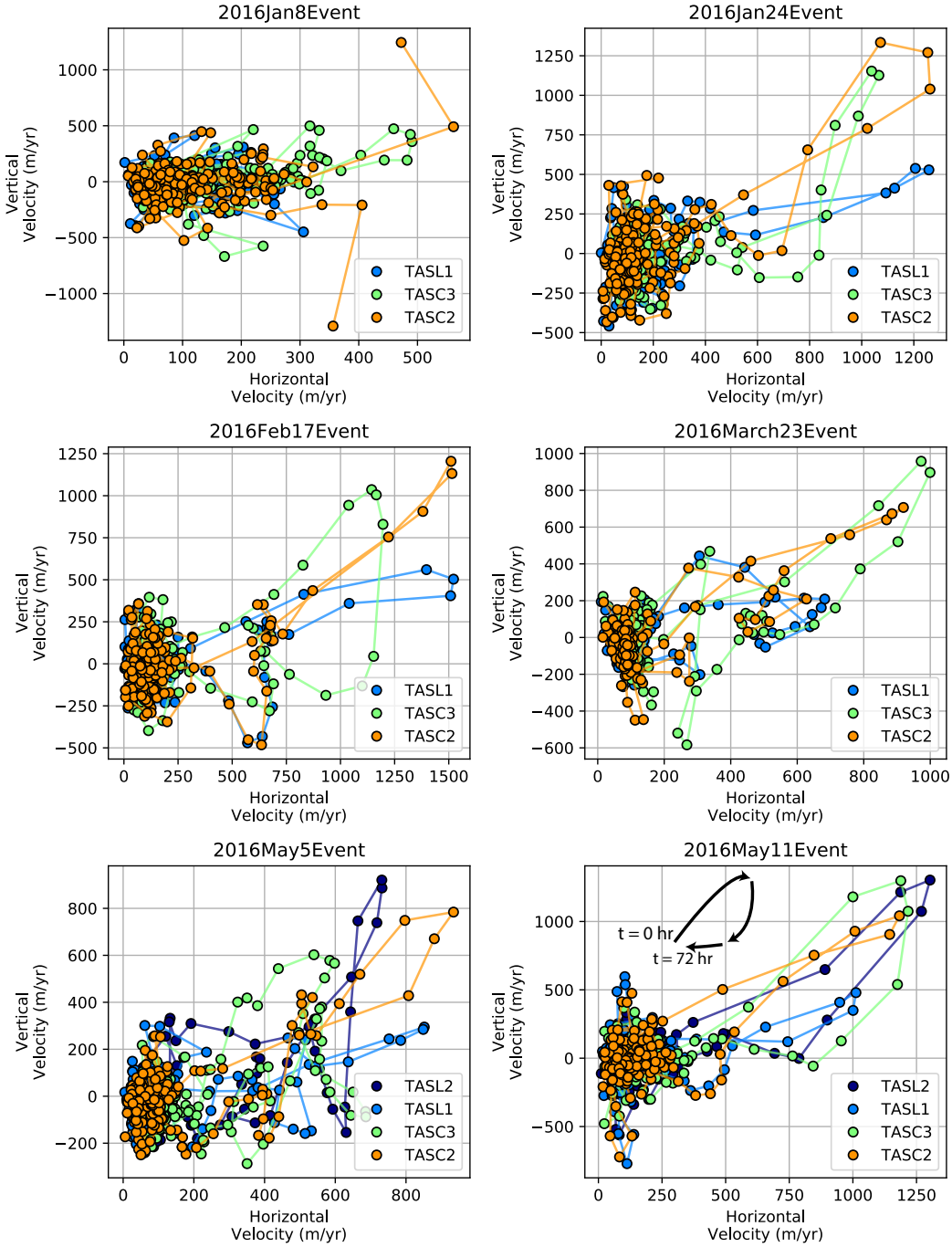

FIGURE 4.7: Horizontal and vertical velocities plotted against each other for each event for each GNSS site. Each marker is one hour apart for a total time of three days. The black arrows displayed in the May 11th plot demonstrate the temporal progression of the "loops" in the velocity relationship over the 72-hour time window.

4.3.2 Horizontal velocity versus detrended elevation

A key field observation for demonstrating the temporary enhancement of glacier sliding velocity due to cavity growth is the lag between horizontal velocity and vertical displacement measured at the surface (Cowton et al., 2016; Howat et al., 2008; Iken et al., 1983). In this study, vertical offsets in the detrended elevation record during speed-up are assumed to be primarily the result of bed separation (Cowton et al., 2016; Horgan et al., 2015; Section 1.6.4). For each GNSS site, changes in elevation lag changes in horizontal velocity (Figure 4.8), forming "loops" which are described schematically in Figure 4.9. During the first two stages, significant changes in detrended elevation occur after horizontal velocity has been increasing for ∼1–10 hours. This observed lag tends to increases as the glacier slows down; the TASC3 site during the May 11th event, for example, remain uplifted by over 30cm for at least 7 hours while horizontal velocity drops from $\sim 1200\,\mathrm{m\,yr^{-1}}$ to $\sim 300\,\mathrm{m\,yr^{-1}}$.

The simultaneous increase in horizontal and vertical velocity is less evident in Figure 4.8 because the raw detrended elevation record is combined with the horizontal velocity that is smoothed by the 3-hour time window over which it is calculated. The speed-up events can be described to occur in four stages (as in Figure 4.9):

1. The horizontal velocity increases with, but faster than, the vertical velocity (Figure 4.7). The detrended elevation shows little movement or begins to increase subtly.

2. Horizontal velocity plateaus while the surface elevation increases most rapidly (i.e. maximum vertical and horizontal velocities occur within a few hours of each other).

3. The horizontal velocity drops towards background levels while the surface remains elevated.

4. The surface elevation slowly decreases towards its original value before the speed-up event.

This relationship between horizontal velocity and detrended elevation suggests a similar hysteresis relationship between horizontal velocity and bed separation presented in Horgan et al. (2015). (Figure 4.8, 6.2). The hysteresis in surface motion observations is an argument for cavity growth in other studies (e.g Howat et al., 2008) and its implications on recreating speed-up events with the Coulomb-type sliding law are discussed in Sections 6.1.2 and 6.2.1 respectively.

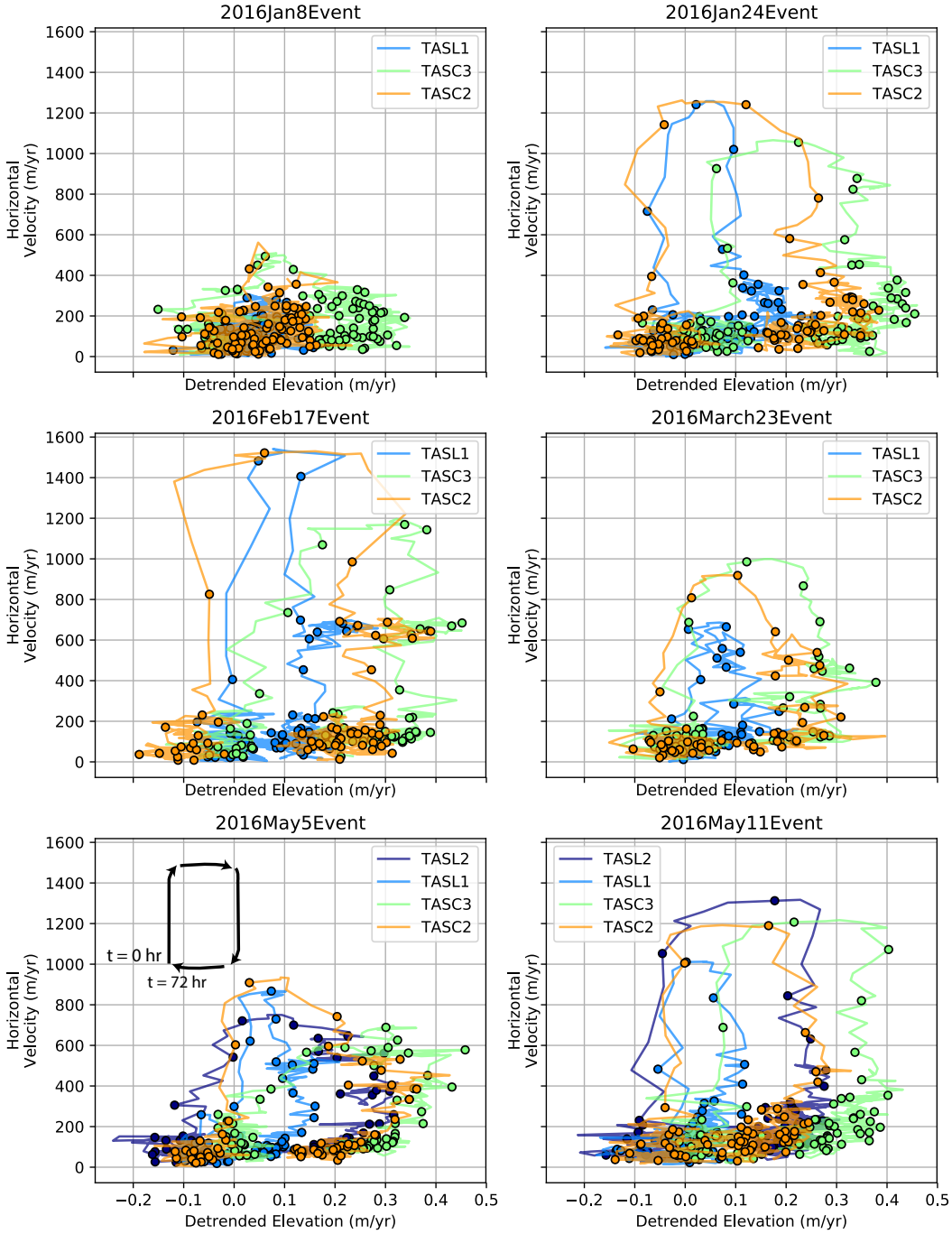

FIGURE 4.8: The relationship between horizontal velocity versus detrended elevation during six speed-up events at Haupapa/Tasman Glacier. The events displayed show a similar hysteresis relationship to Horgan et al. (2015) where the relationship follows clock-wise around each loop. The black arrows displayed in the May 5th plot demonstrate the temporal progression of the "loops" over the 72-hour time window. Velocity and detrended elevation are interpolated every 15 minutes. The markers in each loop are one hour apart.

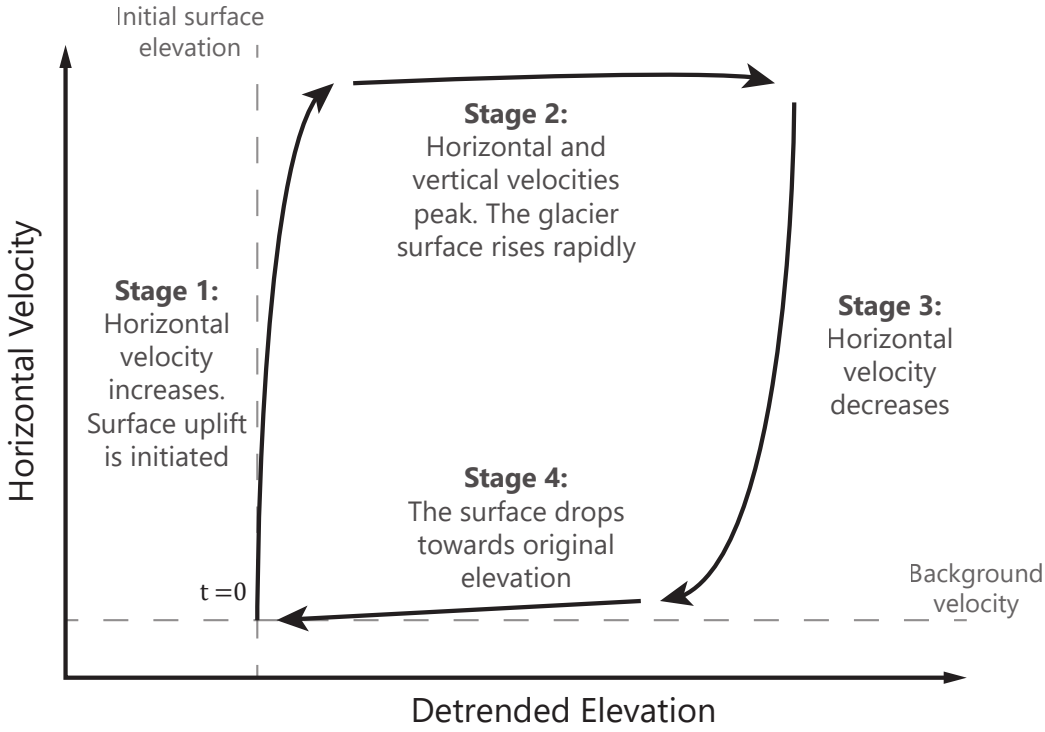

FIGURE 4.9: A schematic diagram of the apparent four-stage relationship between horizontal velocity and detrended elevation observed during speed-up events at Haupapa/Tasman Glacier.

4.4 Velocity and rainfall during speed-up events

Time series of horizontal and vertical velocities over individual speed-up events demonstrate the surface response to rainfall events. Speed-up events in the GNSS record are distinguished by both their magnitude (compared to the background velocity) and asymmetric rise and decay of horizontal velocity and vertical position. Two significant events occurred in quick succession on May 5th and May 11th (Figure 4.10, 4.11). These events will be presented in this section as exemplars of speed-up events and are the two events finite-element models in this study aim to replicate (Chapter 5). Following heavy rainfall, the initial acceleration of horizontal velocity is rapid (over the course of ∼6-12 hours) before decaying over $\sim 12 - 24$ hours to a longer-term elevated horizontal velocity that lasts up to several weeks (Figure 4.10, 4.11, 4.12). Likewise, the surface elevation increases rapidly over ∼12 hours before relaxing back to its original position over several days (Figure 4.10, 4.11, 4.3). The horizontal accelerations are large; for instance, during the May 5th event, the horizontal velocity at the TASC2 site accelerates from 42 m yr^{-1} to 935 m yr^{-1} (a 2220 % increase). The acceleration during the May 11th event is even larger at the TASC2 site, rising from 50 m yr^{-1} to 1192 m yr^{-1} in under 12 hours (a 2400 % increase). The greatest velocity from any event is 1543 m yr^{-1} recorded at the TASC2 site during the February 17th event (Appendix A). Other speed-up events presented in this study occurred on January 8th, January 24th, February 17th, and March 23rd — all of which

are plotted in Appendix A.

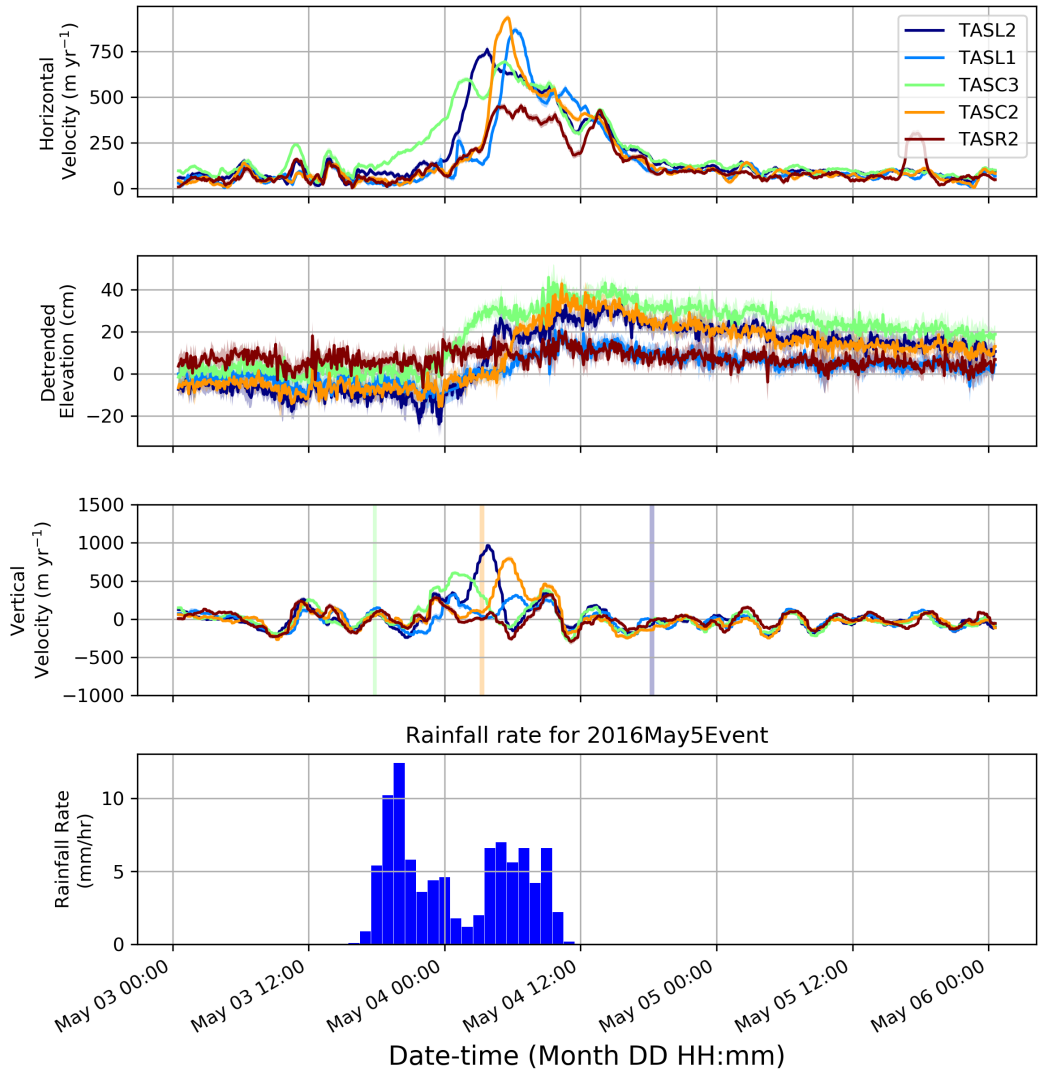

FIGURE 4.10: Horizontal velocity, detrended elevation, vertical velocity and rainfall record during the May 5th, 2016 speed-up event at Haupapa/Tasman Glacier. The horizontal velocity, vertical velocity, and detrended elevation data are interpolated to 15 minute intervals.

Spatial variability in peak velocity and surface uplift is apparent in Figures 4.10 and 4.11. Typically, the centre-line sites have the greatest peak velocities and surface uplift. The site closest to the margin, TASR2, is consistently slower and shows more of a plateau in horizontal velocity as opposed to a peak. However, the two off-centre sites TASL1 and TASL2 attain comparable, if not higher velocities than the centre-line sites. The GNSS sites in closest proximity to each other are TASC2 and TASL1 which show closely matching horizontal records (most notably during the May 5th and February 17th events). However, TASL1 has only around half the uplift of the nearby TASC2 site (Figure 4.10,Appendix A.3.

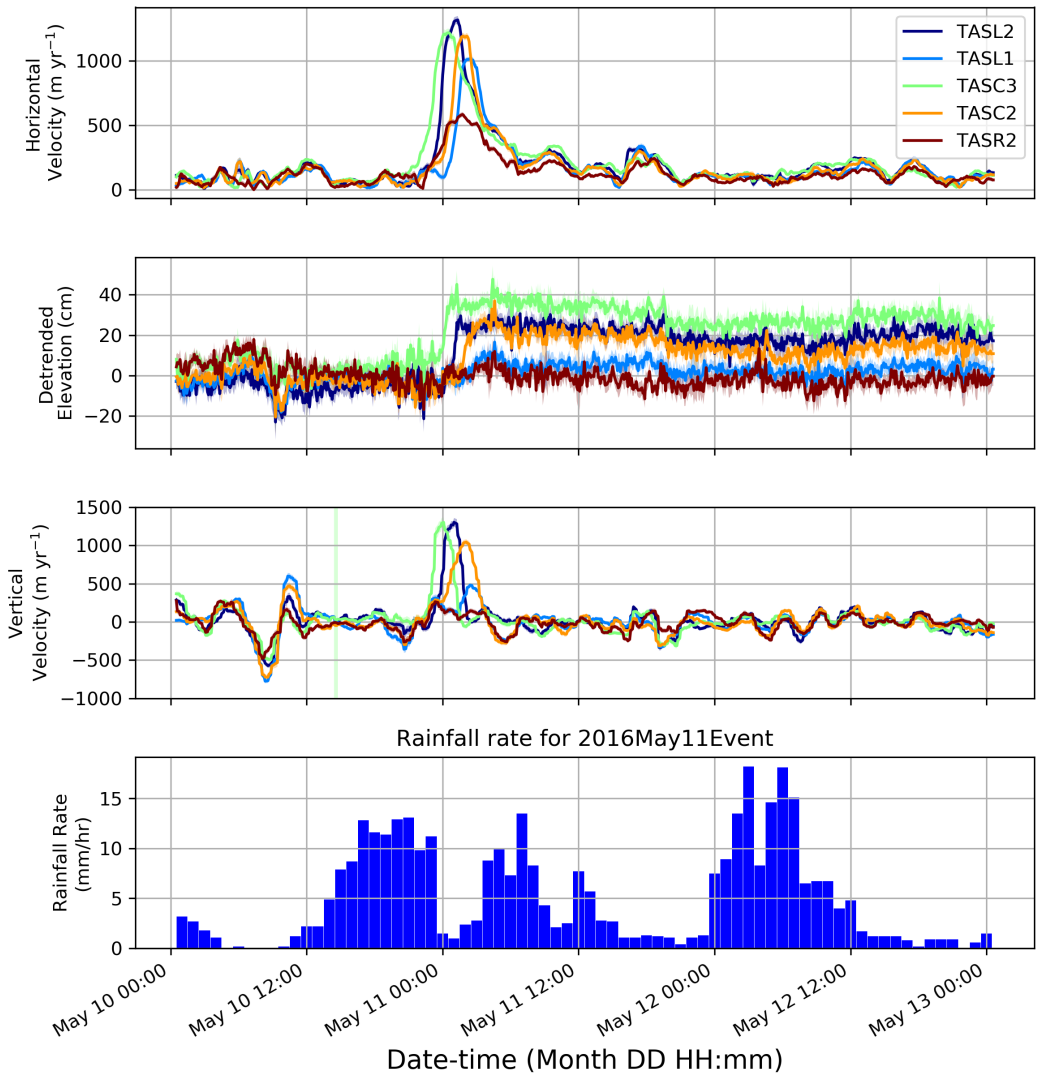

FIGURE 4.11: Horizontal velocity, detrended elevation, vertical velocity and rainfall record during the May 11th, 2016 speed-up event at Haupapa/Tasman Glacier. A significant rainfall event occurs on May 12th which shows almost no response in the velocity record. This apparent lack of response is discussed in Section 4.4.3

.

4.4.1 Elevated horizontal velocity following peak velocity

Horizontal velocities remain higher than background speeds for several days following peak velocity and vertical displacement. Figure 4.12 demonstrates that horizontal velocity returns to background levels over the same timescale as surface elevation. During the January 24th event, the peak returns at a higher velocity. The May 5th event shows a gentle decay until May 11th where the glacier spikes rapidly in response to a rainfall event. The elevated horizontal velocity embodies the second phase of the speed-up event described in Horgan et al. (2015), where the sliding speed is significantly lower than that which occurs during peak velocity but is still higher than the average velocity prior than speed-up. The horizontal velocity and surface elevation then decay over similar timescales (Figure 4.12).

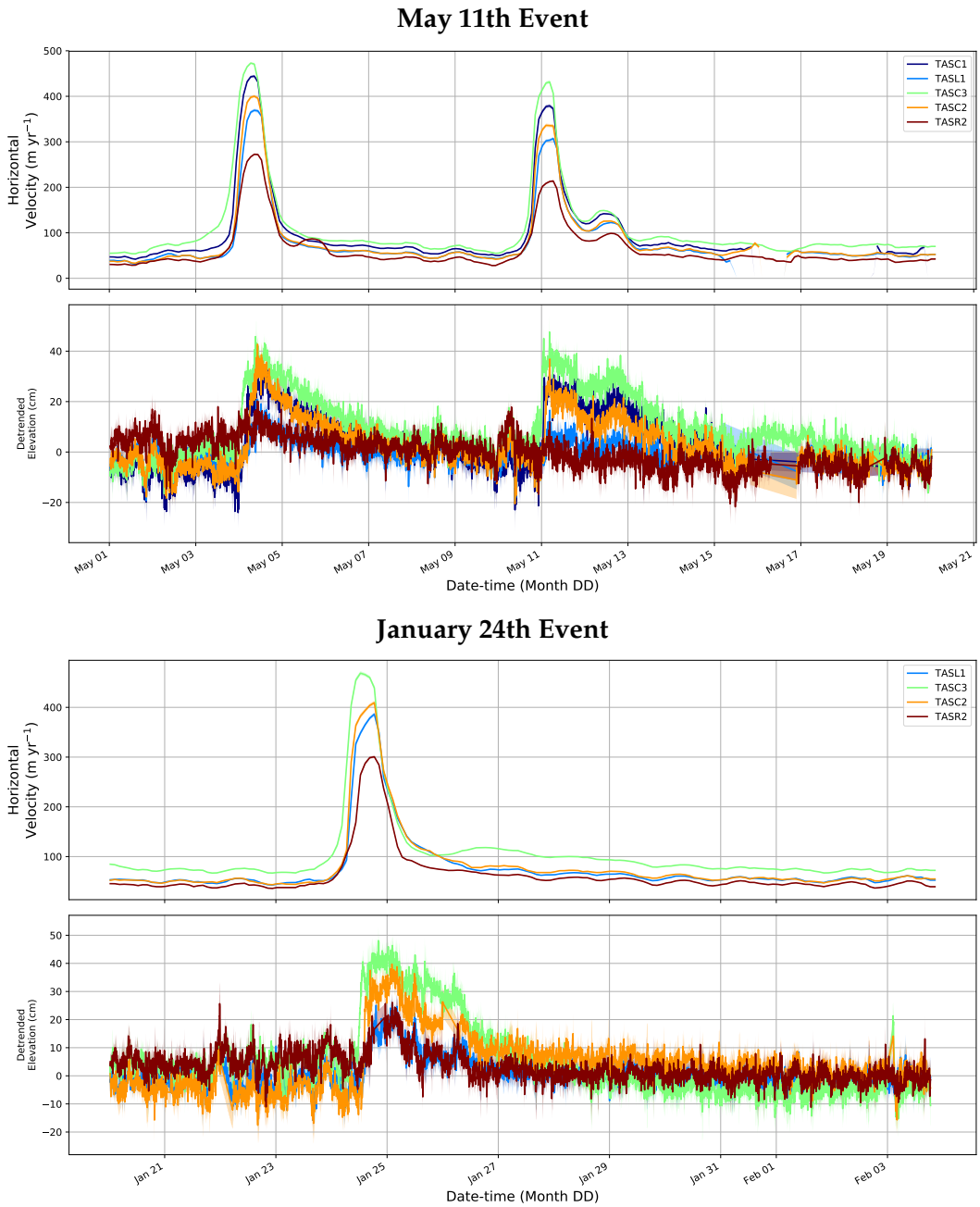

FIGURE 4.12: Elevated horizontal velocities and surface elevations following speed-up events. Velocities calculated over a 24-hour window are displayed over a two-week time frame around speed up events

4.4.2 The down-glacier propagation of velocity during speed-up

During speed-up events, a wave of peak velocity propagates down-glacier. The site furthest up-glacier is always the first to accelerate and reach peak velocity, followed by each site sequentially moving downstream (Figure 4.13, 4.14). The TASL1 and TASL2 sites follow a similar trend to the centre-line sites, which is also what is seen in terms of the magnitude of the horizontal acceleration and surface uplift for the TASL1 site. The site closest to the margin (TASR2) does not follow the downstream migration of velocity with the other sites and is excluded from the linear fit in Figures 4.13 and 4.14. TASR2 is likely influenced by the effect of shear friction at the margin. Wave speeds of the "velocity waves" propagating downstream during each event are displayed in Table 4.4.

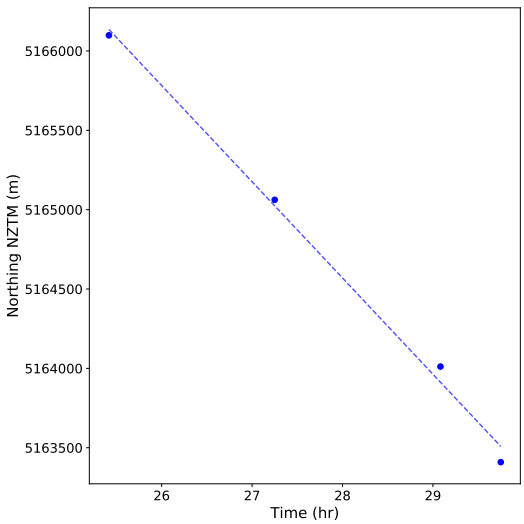

FIGURE 4.13: Time of peak velocity versus distance down-glacier for May 5th event

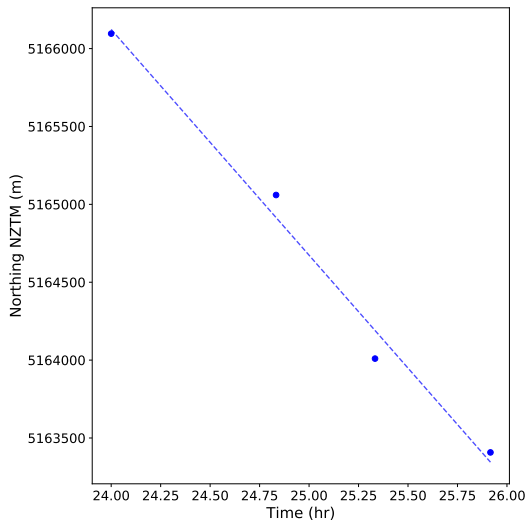

FIGURE 4.14: Time of peak velocity versus distance down-glacier for May 11th event

TABLE 4.4: Speeds of downstream propagating "velocity wave" during each speed-up event

Event	Jan 24th	Feb 17th	March 23th	May 5th	May 11th
Wave speed (m yr^{-1})	967	2303	1209	606	1449

4.4.3 Rainfall—Speed-up relationship

The magnitude of Haupapa/Tasman Glacier's acceleration in response to high rainfall rates likely depends on both rainfall rate and the state of the subglacial system. Speed-up events follow episodes of heavy rainfall between ∼6-24 hours in length, all of which demonstrate a peak daily rainfall rate exceeding 50 mm/day. Asymmetry in the horizontal velocity is a general feature of speed-up events, but the shape of the horizontal velocity curve varies between events. For example, the May 5th

event has a broader horizontal velocity curve that plateaus near peak velocity for a greater time compared to May 11th (Figure 4.10, 4.11). In general, peak velocity scales with rain-rate (Iken and Bindschadler, 1986; Jansson, 1995); however, the duration of a rainfall event and the efficiency of the subglacial drainage system – which is inherited from how the subglacial systems have evolved in the past – should both influence the size and duration of speed-up events (to be discussed in Section 6.1) (Kamb, 1987; Schoof, 2010; Tedstone et al., 2013).

Peaks in rainfall rate did not, however, always result in glacier speed-ups. For instance, the May 11 event is followed by a second, larger peak in rainfall ∼1.5 days following the initial rainfall event that triggered the speed-up (Figure 4.11). The same is true for the February 17th speed-up events (Figure 4.15,Appendix A). No obvious velocity peak or offset in vertical displacement is present. This too can be explained by a shift in the subglacial drainage system, though in this case, the lack of velocity response suggests an increase in drainage efficiency (Section 6.1.2).

4.5 Summary

GNSS position and velocity data over 2016 contain six rain-induced speed-up events where large horizontal accelerations (up to 24 times background speeds) and vertical uplifts (up to 0.53 m) occur. Near the centre-line (i.e. TASC3, TASC2, and TASL2), horizontal and velocities rise and peak together, reaching similar maximum velocities. However, near the margin (TASR2) the total speed-up is much lesser and vertical displacement is negligible. The TASL1 site shows large horizontal accelerations, but limited vertical displacements. In the following chapter, the surface motion during two closely-spaced speed-up events (May 5th, 2016, and May 11th, 2016) are recreated using a finite-element model that uses a Coulomb-type sliding law and water pressure function to vary sliding speed.

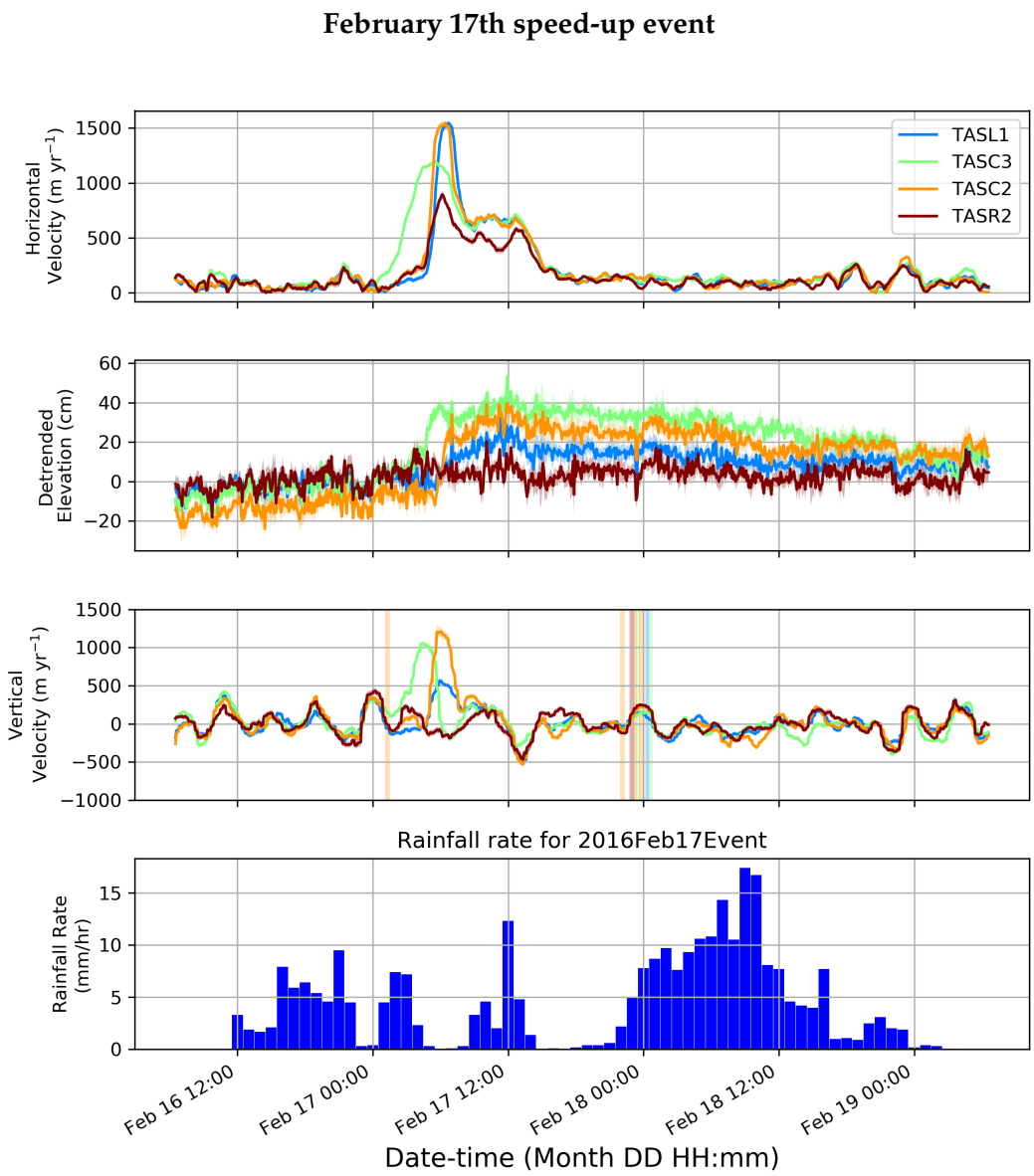

FIGURE 4.15: The GNSS and rainfall record during the February 17th, 2016 speed-up event at Haupapa/Tasman Glacier

Chapter 5

Finite-Element Modelling Results

Rapid sliding events that occurred on May 5th, 2016 and May 11th, 2016, are recreated in this study using 2D and 3D finite-element models. Transient models are run to mimic the processes leading to a speed-up event by imposing an evolving basal water pressure and using the Coulomb-type sliding law to produce a sliding velocity response (Section 3.2). The sliding speed and basal water pressure output of the model is used to estimate the bed separation, which can be used to explain the magnitude of vertical displacement during the May 11th event.

5.1 Modelling Process

The overall modelling process is summarised in (Figure 3.7). In general, because the 2D models were faster to run and included less complicating factors than 3D models (e.g. friction against sides) and have fewer nodes to calculate the equations of motion for ice over (see Section 3.2.1, 3.2.3), more models can be run in less time. Hence, 2D models provide a more efficient means of sweep through a range for parameters for peak water pressure $P_{w_{max}}$, rise time t_r, and decay time t_d for the basal water pressure function described in Section 3.2.4. Results from 2D models help define a likely range of water pressures, decay times, and rise times for 3D results. The sliding speed u_b and N output of the 3D models are then the input used for cavity models. The cavity models explore their own parameter space of basal roughness h/λ_L (ratio of obstacle height to obstacle separation) described in Section 3.3.

5.2 2D Flowline models

2D flowline models of Haupapa/Tasman Glacier provide a preliminary insight into the magnitude of water pressure changes during speed-up events. A range of peak water pressures, rise times, and decay times are tested to fit surface velocity observations (Section 3.2.7). Before a model with a time-evolving water pressure boundary condition is run, the unknown friction coefficient C_s and background water pressure P_0 are required.

5.2.1 Friction Coefficient Test

The friction coefficient for the Schoof law C_s is calculated using the values for the minimum winter velocities of $42\,\mathrm{m\,yr^{-1}}$ and $56\,\mathrm{m\,yr^{-1}}$ for the TASC2 and TASC3 sites respectively. A minimum error with respect to the two available flowline units was achieved for $C_s = 0.0205\,\mathrm{MPa\,m^{-1/2}\,yr^{1/3}}$ (Figure 5.1). This is a comparable value to Kehrl (2012)'s flowline model for Franz Josef Glacier, Southern Alps, New Zealand, which required C_s =0.03 $\mathrm{MPa\,m^{-1/2}\,yr^{1/3}}$ to fit winter minimum velocities.

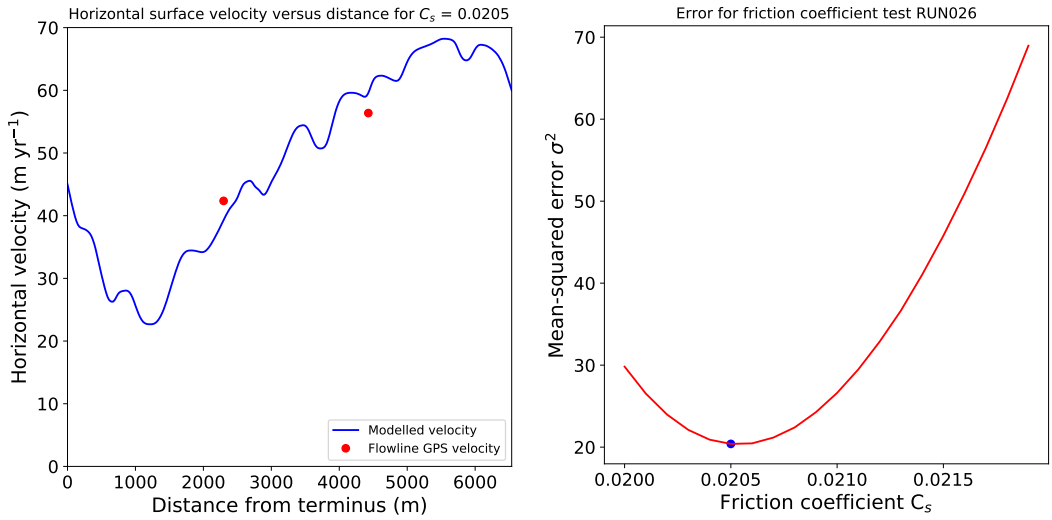

(A) Surface velocity (B) Mean-squared error

FIGURE 5.1: Horizontal surface velocity versus distance from terminus (A) for a friction coefficient of $C_s = 0.0205\,\mathrm{MPa\,m^{-1/2}\,yr^{1/3}}$which gives the minimum error solution (B). Mean-squared error is calculated as the difference between modelled surface velocity at the nodes on the 2D mesh closest to the TASC2 and TASC3 sites and minimum winter velocities for TASC2 and TASC3

5.2.2 Water pressure test (May 11 event)

A uniform background water pressure of $P_0 = 1.82\,\mathrm{MPa}$ provided the best fit to the starting velocities for the centre-line units (Figure 5.2). This is not likely to be an accurate measurement of absolute water pressure since several parameters are poorly constrained (C_{max}, for instance, is not informed by any roughness data)(Section 3.2.6), but provides a base value for water pressure such that the total change in water pressure is in the range the Coulomb-type law is sensitive to (Section 2.5.2). The sliding speed given by the Coulomb-type sliding law is relatively insensitive to changes in water pressure below $\sim 1.7\,\mathrm{MPa}$ for the flowline model of Haupapa/Tasman Glacier (Figure 5.3). Even at $P_0 = 1.7\,\mathrm{MPa}$, a section of the bed ($\sim 10 - 15\%$) near the terminus is at flotation — though the terminus remains at a stable due to the velocity boundary condition of $u_{terminus} = 45\,\mathrm{m\,yr^{-1}}$ set here (Section 3.2.4). The resulting

value of water pressure in the transient tests can be used to assess the change in water pressure needed to cause the observed acceleration in horizontal velocity (Section 3.2.7).

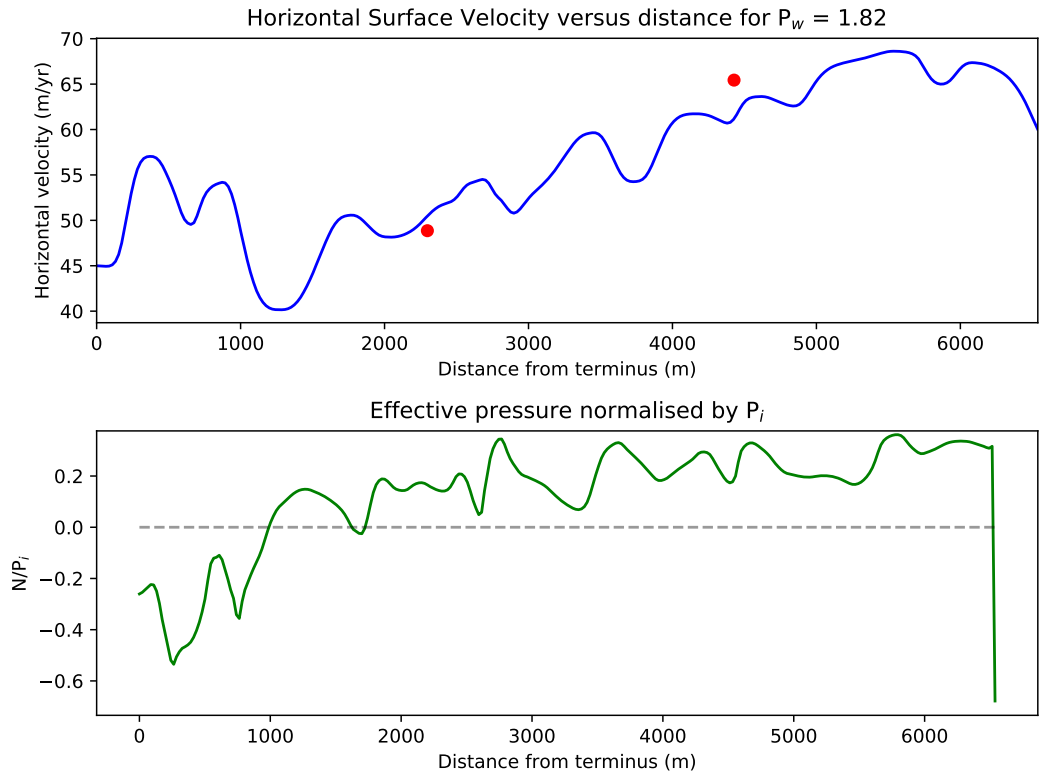

FIGURE 5.2: Best fitting 2D flowline model for $P_0 = 1.82$ MPa. Surface velocity of the 2D model is compared to average 24-hour window velocities prior to the May 11th event.

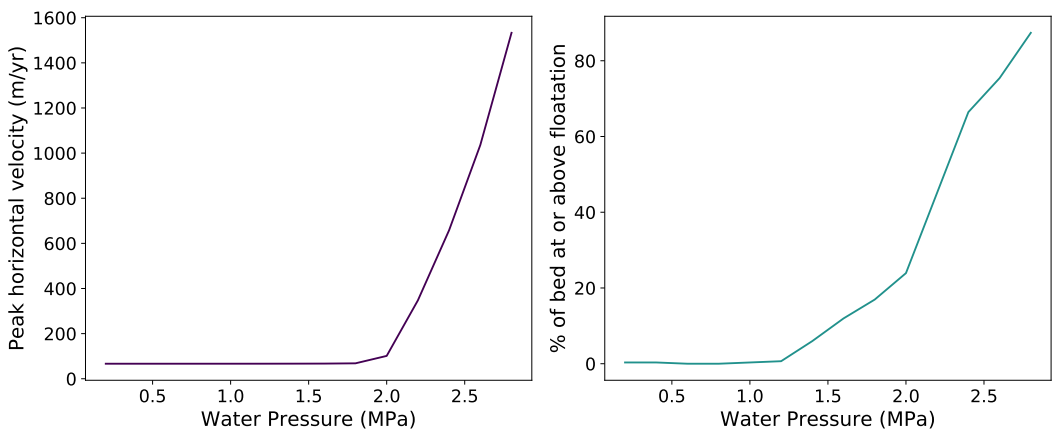

FIGURE 5.3: Peak Horizontal Velocity and % of Bed at Flotation For 2D P_0 test. This plot indicates how the sensitivity of peak surface velocity to water pressure for Coulomb-type sliding law changes as water pressure increases.

5.2.3 Transient test May 11

Surface velocities that occur on May 11th, 2016 at centre-line GNSS sites are not matched unless water pressures exceed the weight of the overlying ice. For a transient flowline model where the upper limit is set to $u_{upper} = 70.0\,\mathrm{m\,yr^{-1}}$, the best-fitting peak water pressure is $P_{peak} = 2.85\,\mathrm{MPa}$, suggesting a change in water pressure of $\Delta P_w = 1.03\,\mathrm{MPa}$ from background levels (Figure 5.4). For this result, the effective pressure at TASC3 is 15% greater than overburden, and 5% greater than overburden at TASC2. However, the solution is sensitive to the upper limit velocity boundary condition, defined by the u_{side} parameter in this test (Section 3.2.4). A time-evolving velocity boundary condition is applied to the upper limit of the glacier which rises and falls at the same rate as the water pressure function (in this case $t_{rise} = 30\,\mathrm{hr}$ and $t_{decay} = 72\,\mathrm{hr}$) and peaks at $u_{side} = 1200\,\mathrm{m\,yr^{-1}}$ (which is roughly the same speed as the TASC3 unit) (Figure 5.5). With this boundary condition, the peak water pressure required to match the surface velocity data is reduced to $P_{peak} = 2.5\,\mathrm{MPa}$. The fit to the data is improved and the effective pressure is reduced 5% and 3% at TASC3 and TASC2 respectively.

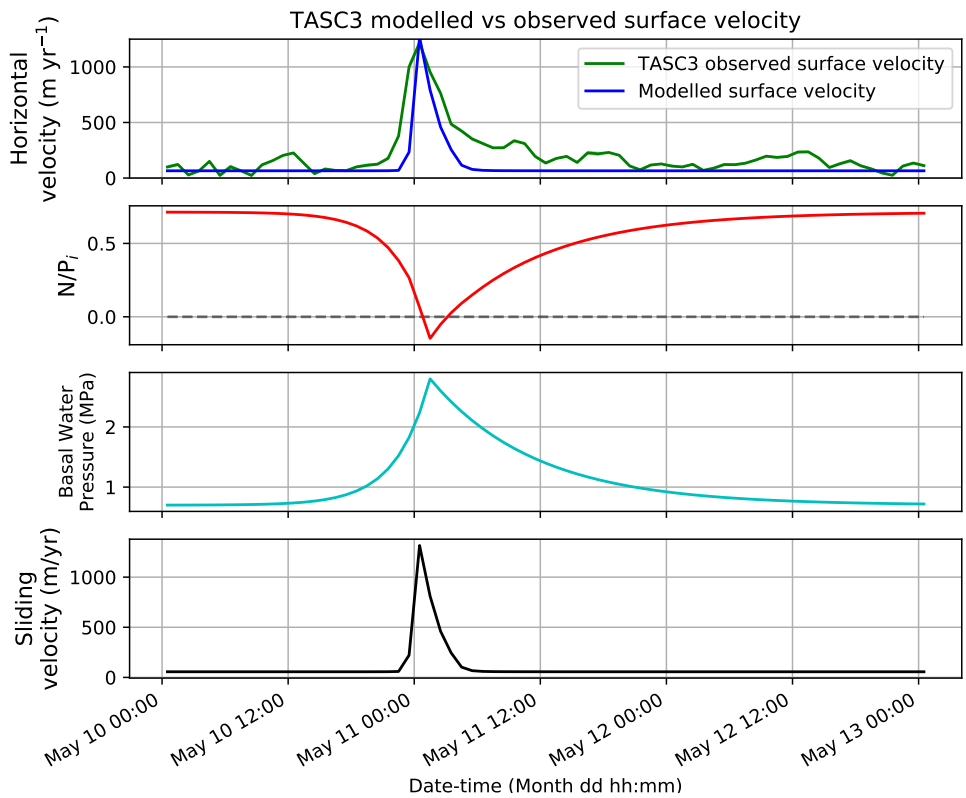

FIGURE 5.4: Best-fitting peak velocity for 2D flowline with static upper limit velocity. For this model, $P_{peak} = 2.85\,\mathrm{MPa}$ and $u_{side} = 70\,\mathrm{m\,yr^{-1}}$

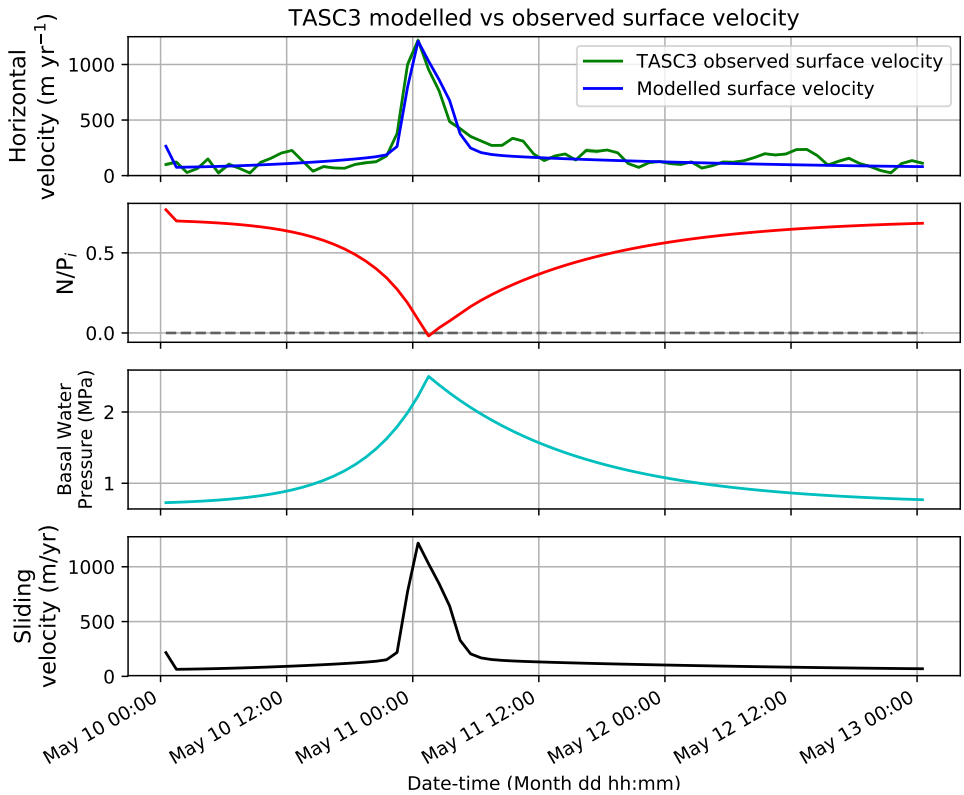

FIGURE 5.5: Best-fitting 2D Flowline model with Time-Evolving Velocity Boundary. For this model, $P_{peak} = 2.5\,\text{MPa}$ and $u_{side} = 1200\,\text{m}\,\text{yr}^{-1}$

Ultimately, both negative effective pressures and peak upstream boundary velocities on the same order as peak GNSS velocities need to be invoked to recreate the May 11th speed-up event. The sensitivity to both the peak water pressure and peak upper limit velocity are shown in Figures 5.6 and 5.7. The upper limit velocity can be high (i.e. u_{side}), but if effective pressures are over 20% of ice overburden, then the surface modelled surface velocity peaks at $\sim 300\,\text{m}\,\text{yr}^{-1}$. Hence, both the reduction in basal friction and limiting velocity gradients within the ice are important in recreating observed speed-up events at centre-line sites (Figure 5.7)(Section 6.1).

2D Surface Velocity Profiles for Range of Upper Limit Peak Velocities for $P_{peak} = 2.4\,\mathrm{MPa}$

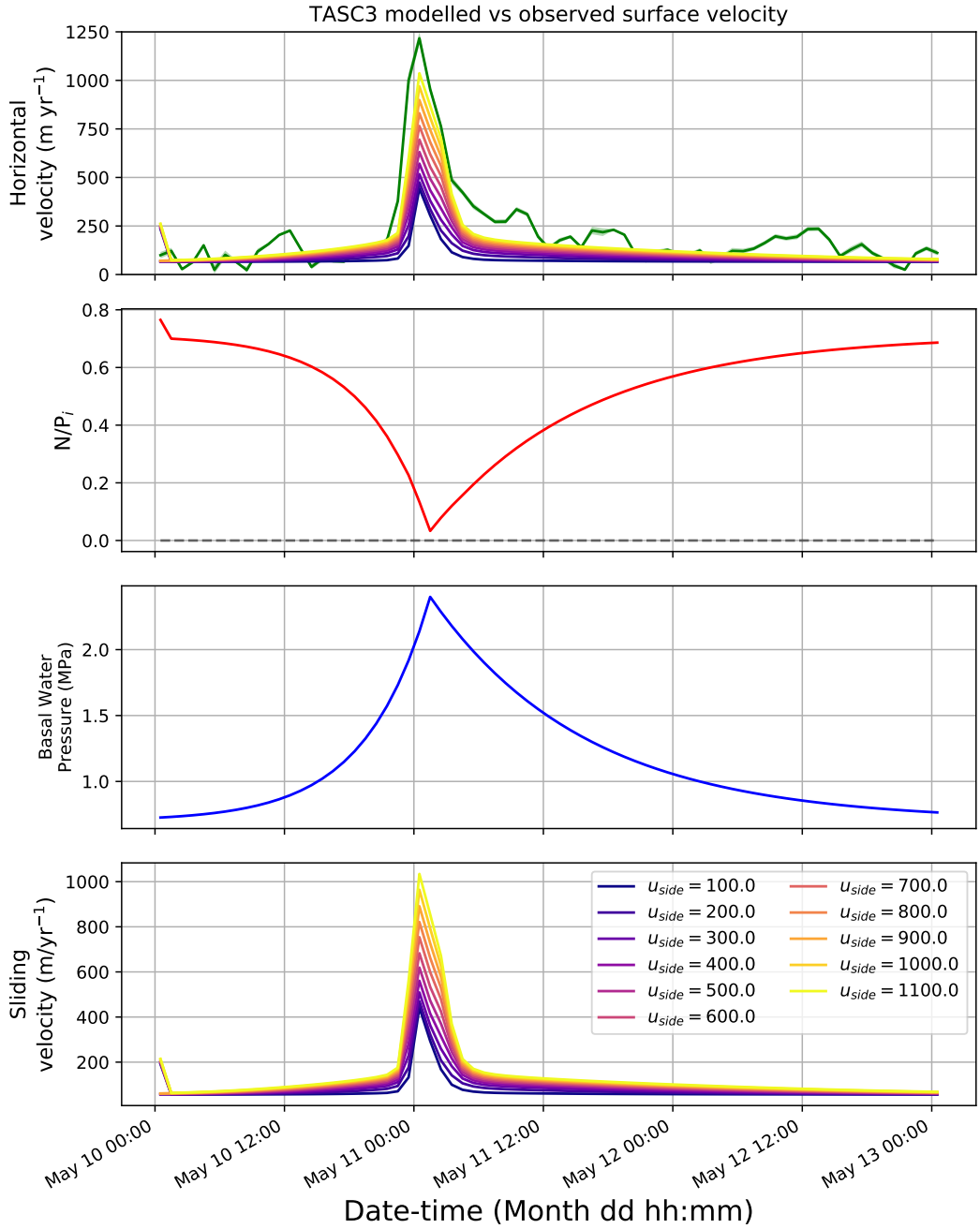

FIGURE 5.6: The velocity boundary condition causes the velocity at both stations to vary by several hundred m yr^{-1} at a given water pressure where both stations just about reach flotation ($P_{peak} = 2.4\,\mathrm{MPa}$).

2D Surface Velocity Profiles for Range of Water Pressures for $u_{side} = 1200\,\mathrm{m\,yr^{-1}}$

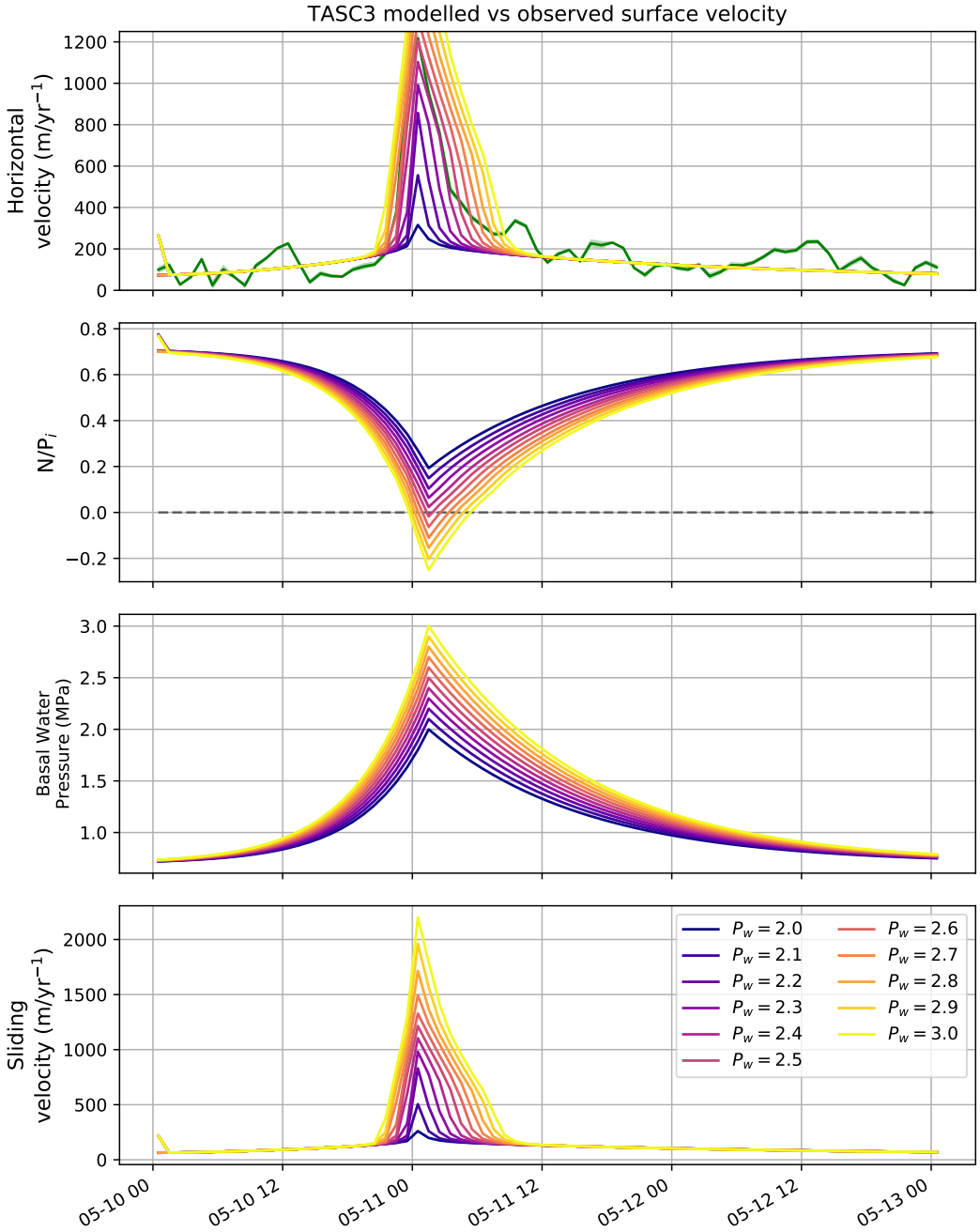

FIGURE 5.7: A model run that locks the upper terminus at $u_{side} = 1200\,\mathrm{m\,yr^{-1}}$ and sweeps between $P_{peak} = 2.0\,\mathrm{MPa}$ and $P_{peak} = 3.0\,\mathrm{MPa}$ shows that a spike in water pressure that approaches flotation is still needed to match observed surface velocities.

5.3 3D models

To make use of all available GNSS stations during the May 5th and May 11th events as a surface velocity constraint, a three-dimensional model is introduced. The modelling process is akin to the 2D case: a set of experiments are run to determine the friction coefficient, background water pressure, peak water pressure, and the velocity of the model boundaries. The 3D models highlight the strong control the velocity of the glacier sides has upon the glaciers sliding velocity.

5.3.1 Friction Coefficient

Using a Coulomb-type sliding law, a friction coefficient of $C_s = 0.0102\,\mathrm{MPa\,m^{-1/2}\,yr^{1/3}}$ provides the best fitting steady-state velocity field to match the minimum winter velocities. TASR2, the site closest to the margin, shows the largest discrepancy between the observed and modelled velocity, suggesting the surface velocity decays too fast towards the boundaries in this region.

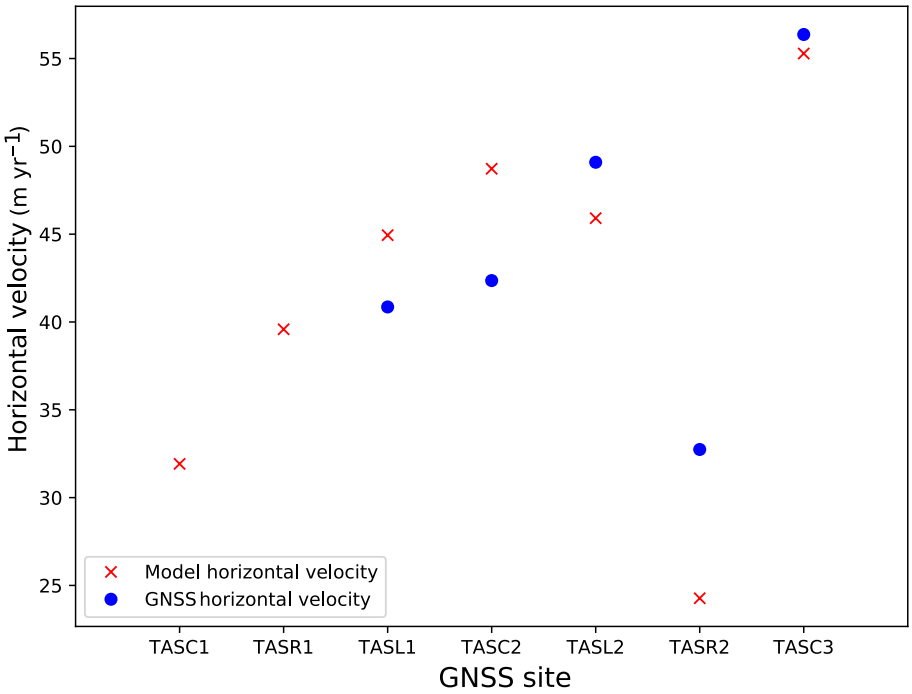

FIGURE 5.8: Result of best-fitting 3D model for friction coefficient. In this model, $C_s = 0.0102\,\mathrm{MPa\,m^{-1/2}\,yr^{1/3}}$

5.3.2 Starting Water Pressure

For the May 5th and May 11th events, background water pressures of $P_w = 0.7$ MPa and $P_w = 0.9$ MPa provide the best fit to the average background velocity in the days leading up to the event (Figure 5.9). Each station is within 10 m yr^{-1} of the average precursor velocity for each site, which is inside the range of likely uncertainty. The starting water pressure needed to cause basal sliding to be fast enough to help match surface GNSS data is 0.95 MPa less than the 2D model. Effective pressures are mostly between 60-80% of overburden along the central trunk of the model under the imposed uniform water pressure in this model. Areas of negative effective pressure are confined to the edges of the model where the glacier mesh is thinner and overburden pressure is much lower than the rest of the glacier. Likewise, effective pressured falls beneath 40% and tends to negative values at the glacier terminus.

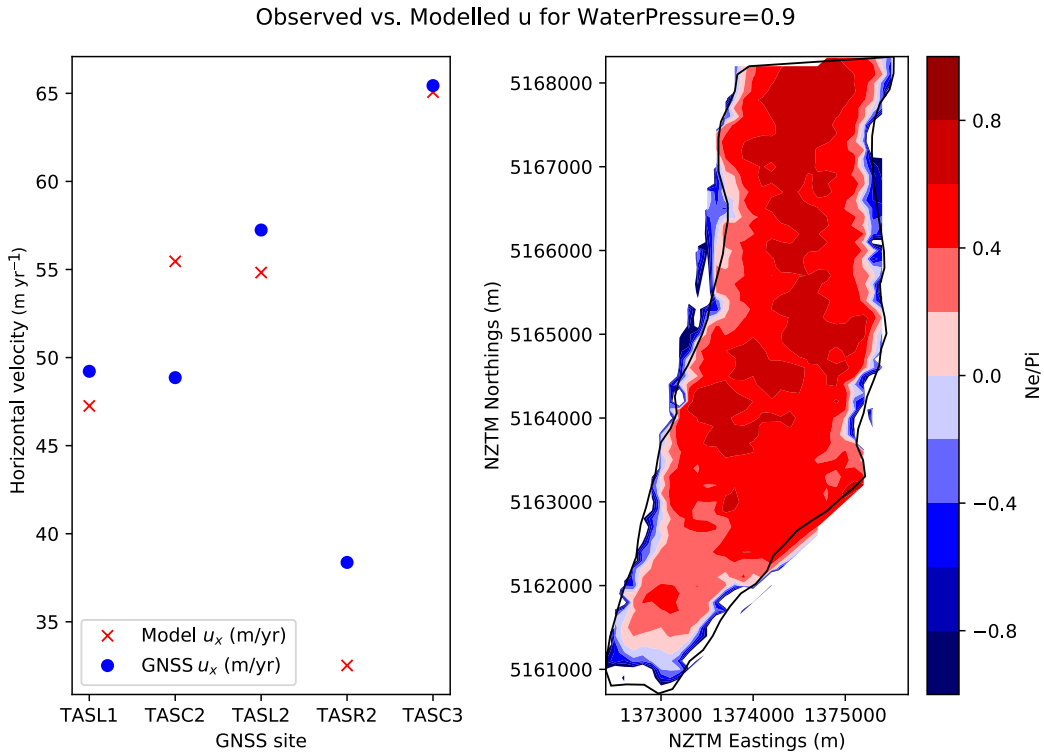

FIGURE 5.9: Result of best-fitting 3D model for background water pressure where $P_w = 0.9$ MPa. The colour scale is plotted as the ratio of effective pressure to ice overburden $Pi = \rho_i g H$ where H is ice thickness, ρ_i is ice densityn and g is gravitational acceleration.

5.3.3 Transient tests with a no-slip condition along glacier margins

When using a Coulomb-type sliding law, friction against the glacier walls can help limit sliding velocity as negative pressures approach flotation and basal stresses tend to zero (Cuffey and Paterson, 2010; Schoof, 2005). A no-slip boundary condition defines a case where the friction against the glacier walls is significant. To see the effect

side friction has on limiting the model's peak velocity, a spike in basal water pressure that exceeds flotation is imposed. Under this model setup, the peak modelled velocity at the surface is less than the observed velocity by $\sim$700 m yr^{-1} for May 5th and $\sim$920 m yr^{-1} for May 11 (Figure 5.10, 5.11). Even when water pressures are increased to excessive levels peak observed velocity cannot be matched; for instance, the TASC2 site exceeds overburden by 41.2% and 31% for the May 5th and May 11th cases respectively. Likewise, when the flotation condition is significantly exceeded at TASR2 (water pressure is over twice overburden), sliding velocity peaks at $\sim$140 m/yr. This is the expected behaviour for the Coulomb-type sliding law: beyond flotation, basal stress is negligible and basal motion essentially becomes decoupled from the base. Consequently, while the pressure function spikes, the sliding speed rounds off towards its upper limit (which is best exemplified in Appendix B.1). This upper limit is then the result of the motion along the sides and the internal viscosity of ice.

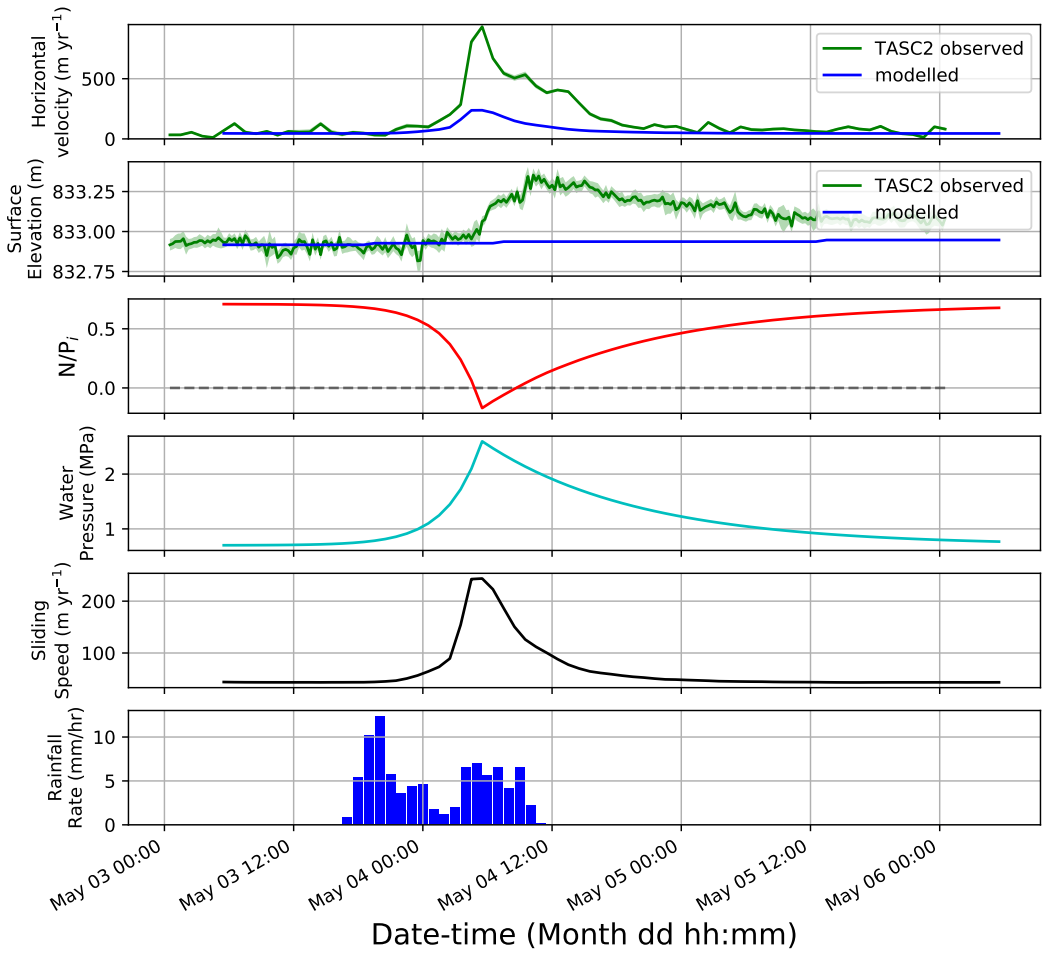

FIGURE 5.10: 3D transient model result for May 5th event where a no-slip condition is imparted along the lateral margins of the glacier model. These results compare observed and modelled velocity at the centre-line position TASC2 and closest surface node in the 3D model.

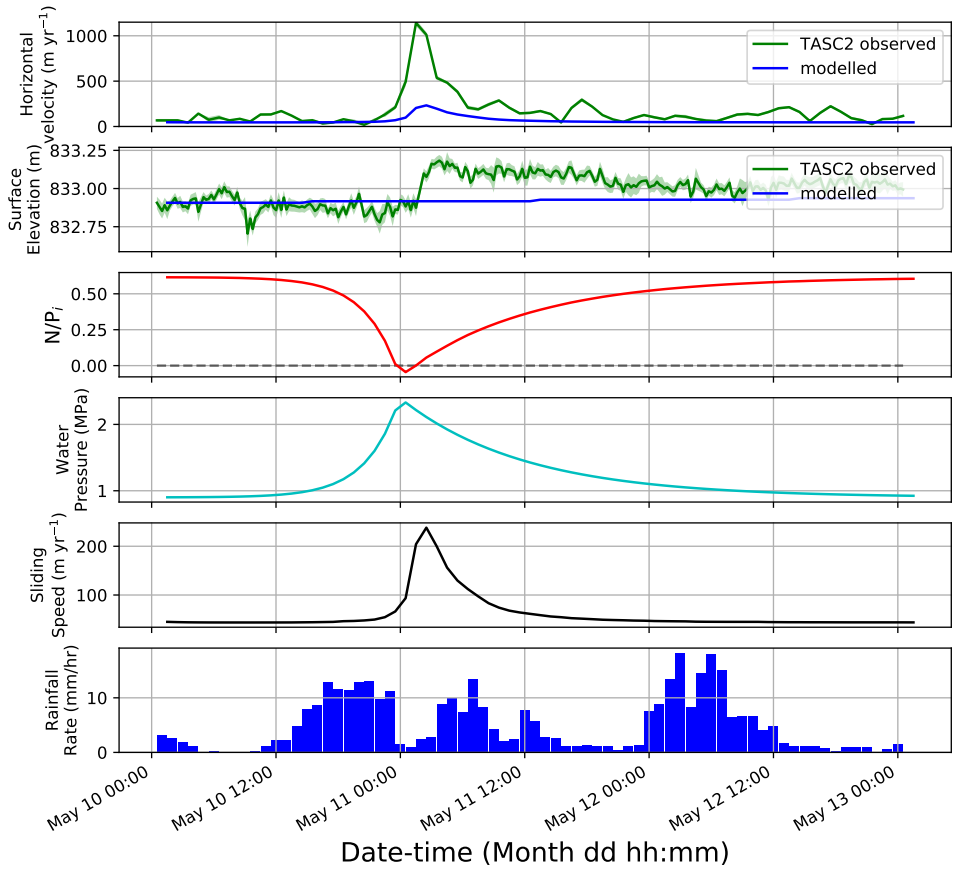

FIGURE 5.11: Another model run for the May 1tth event is conducted where a no-slip condition is imparted along the lateral margins of the glacier model. These results compare observed and modelled velocity at the centre-line position TASC2 and closest surface node in the 3D model.

For the case where water pressures are above flotation at all GNSS sites, the sliding velocity curve rounds off towards its peak, showing that it has ceased to become as sensitive to the changes in water pressure (Figure B.1). In this case, it represents lateral friction as being the dominant control on sliding velocity where, for zero effective pressure, the Coulomb-type law tends towards applying negligible basal stress (Section 2.5.2). The sliding velocity at any point on the bed, then, maxes out at a limit that depends on the viscosity of ice and the distance from the sides.

5.4 Time-evolving velocity boundary condition

As side motion limits the basal sliding velocity in 3D models, a time-evolving side velocity boundary condition is applied to reduce the restriction on the resulting surface speeds. The velocity along the sides of the model is set to evolve with the same time of rise, decay, and peak as the water pressure function (see description in Section 3.2.5). This mimics the effect of having a slip condition along the edges; though, instead of varying the degree of slip based on friction, this approach acts to answer the question: at what speed should the sides be moving in order to allow peak velocities near the centre of the glacier model to match the GNSS velocities?

Peak velocities can be achieved if the glacier walls in this model are allowed to move during speed-up, but the sides need to be moving faster than the TASR2 site which sits near the glacier margins. A best-fitting model is produced for $P_{peak} = 2.5\,\mathrm{MPa}$, $t_{rise} = 6\,\mathrm{hr}$, $t_{decay} = 38\,\mathrm{hr}$, and $u_{side} = 900\,\mathrm{m\,yr^{-1}}$. This exceeds the expected limit of 584 m/yr suggested by the TASR2 unit. The GNSS positions have a range of effective pressures that are both well under and in great excess of overburden (Table 5.1).

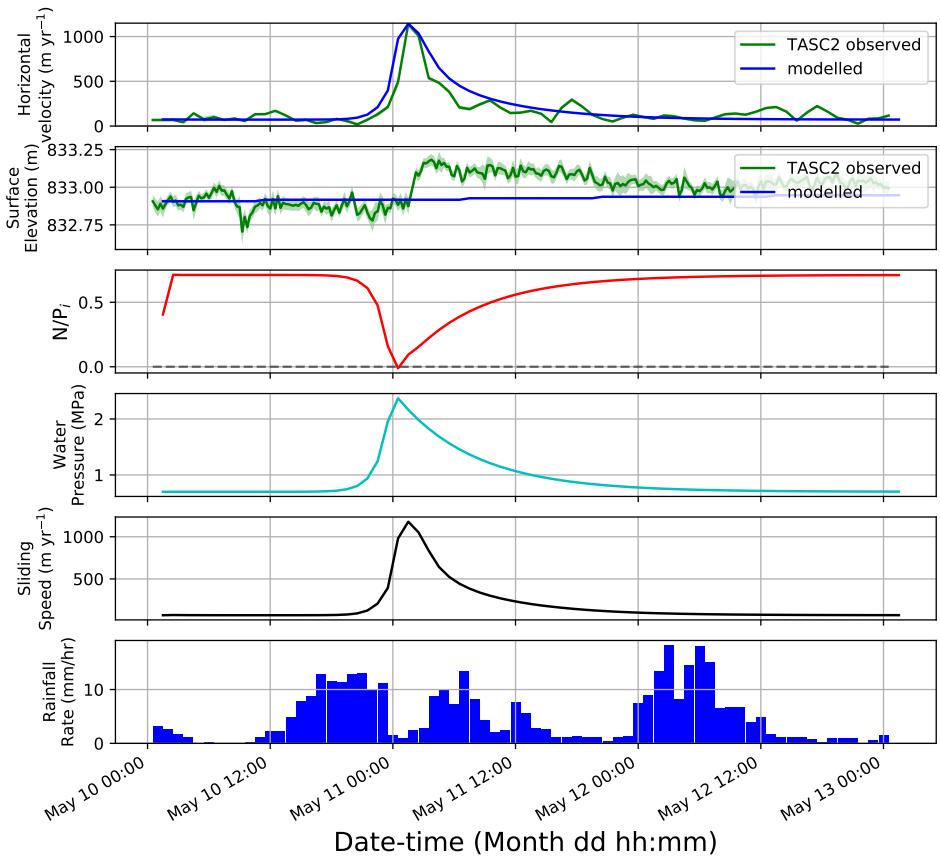

FIGURE 5.12: Observed versus modelled surface velocity for best-fitting transient 3D model at TASC2 site for P_{peak} 2.5 MPA and $u_{side} = 1100\,\mathrm{m\,yr^{-1}}$

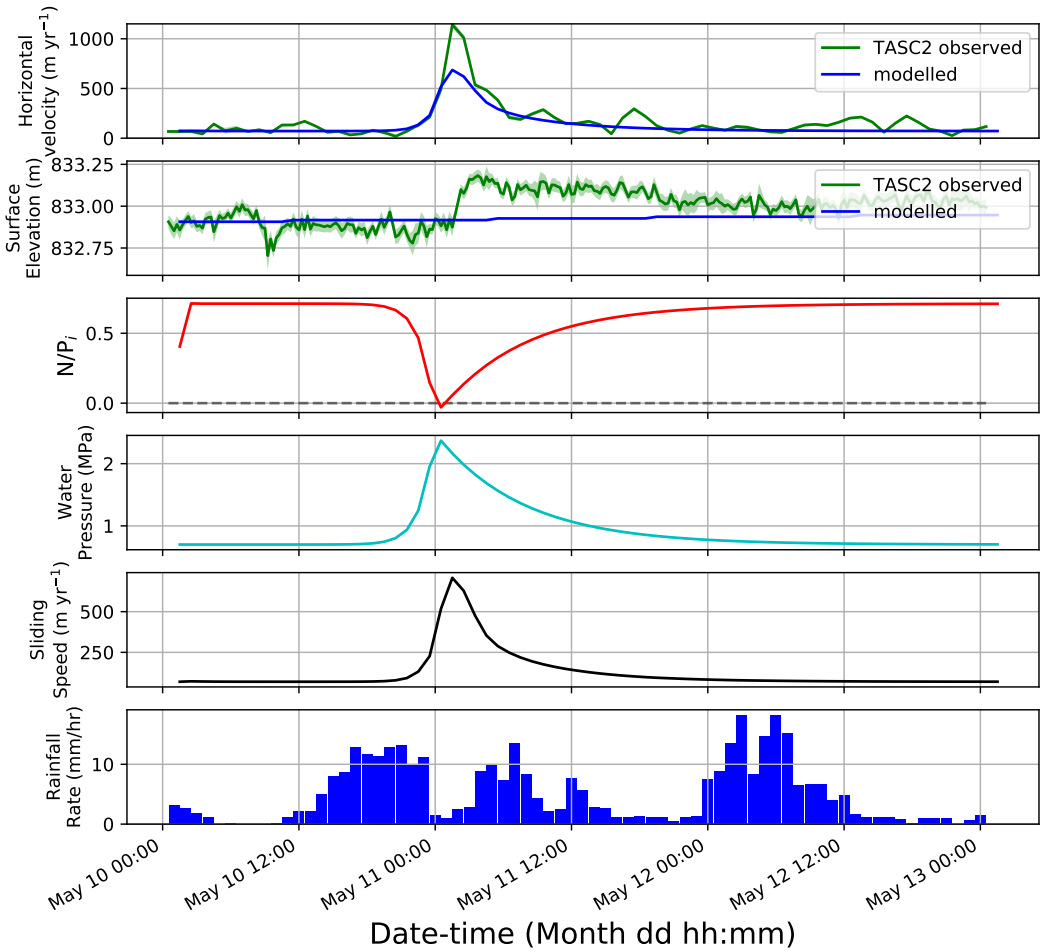

FIGURE 5.13: Best fitting transient 3D model at TASC2 site for $P_{peak} =$ 2.5 MPA and $u_{side} = 500$ m/yr. The model is unable to achieve the peak velocity at every site when the sides are only able to move at a maximum of 500 m yr^{-1}

TABLE 5.1: Peak surface velocity and percentage exceeding overburden for the 3D model which most closely fits the observed GNSS velocities during May 11th. In this model, $P_{peak} = 2.5$ MPa

Sitename	TASC3	TASR2	TASL2	TASC2	TASL1
Peak u	1022	1088	997 m yr^{-}1	1130 m yr^{-}1	1122 m yr^{-}1
% of P_i	13.3%	-78%	3.5%	-2.0%	-39.0%

5.5 Cavity growth model

In the no-slip 3D model, the resulting horizontal velocity is so low, compared to observations, that the cavity model velocities are several hundred m yr^{-1} short of observations. The parameters for roughness in the across-stream (W/λ_T) and downstream directions (h and λ_L) have strong control on the rate of cavity growth. In general, the rougher the bed, the greater the cavity volume per area of the bed, and the greater the separation rate. Even if downstream roughness $\frac{h}{\lambda_L}$ is raised to 1 (which is assumed to be a reasonable upper limit in lieu of basal roughness data), the resulting separation rates max out at ~200 m yr^{-1}, which is still several hundreds of metres per year short of matching the vertical velocity record (Figure 5.14, 5.15).

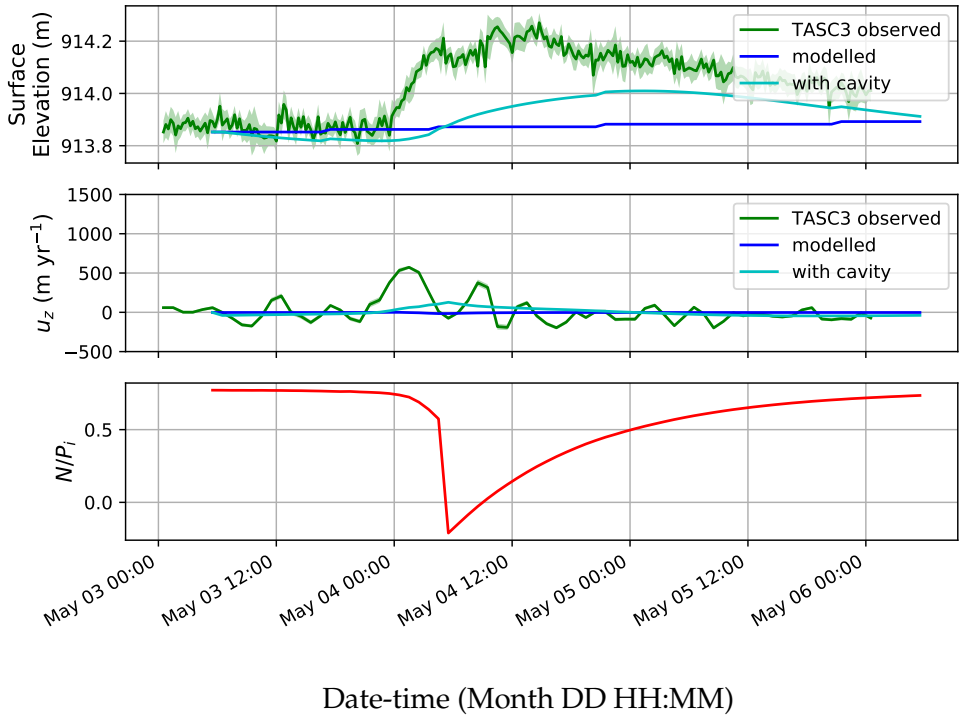

FIGURE 5.14: Cavity growth model result for May 5th event with a no-slip condition imparted along the glacier model's lateral margins. In this cavity model, a basal roughness of $h/\lambda_L = 1$ is used.

Vertical displacement can, however, be matched when using the output of models which have a time-evolving velocity along the sides. Here, two models are presented to show the non-uniqueness of the solution. One is a model with a side velocity in excess of the TASR2 site (u_{side}=1100 m yr^{-1}) and basal roughness $h/\lambda_L = 1$. The other has a side velocity of u_{side}=500 m yr^{-1} which is below (and close to) the peak TASR2 site velocity during May 11th, 2016, and a basal roughness $h/\lambda_L = 0.5$. In each of these cavity models, the TASL2 is generally the best fit in terms of the magnitude of vertical displacement and the initial rate of surface lowering — though, the model and observations begin to diverge towards over the last 24 hours of the speed-up event (Figure 5.17, 5.16). The change in surface elevation at TASC3 is also reasonably represented by the cavity model (discussed in Section 6.2.2), though is

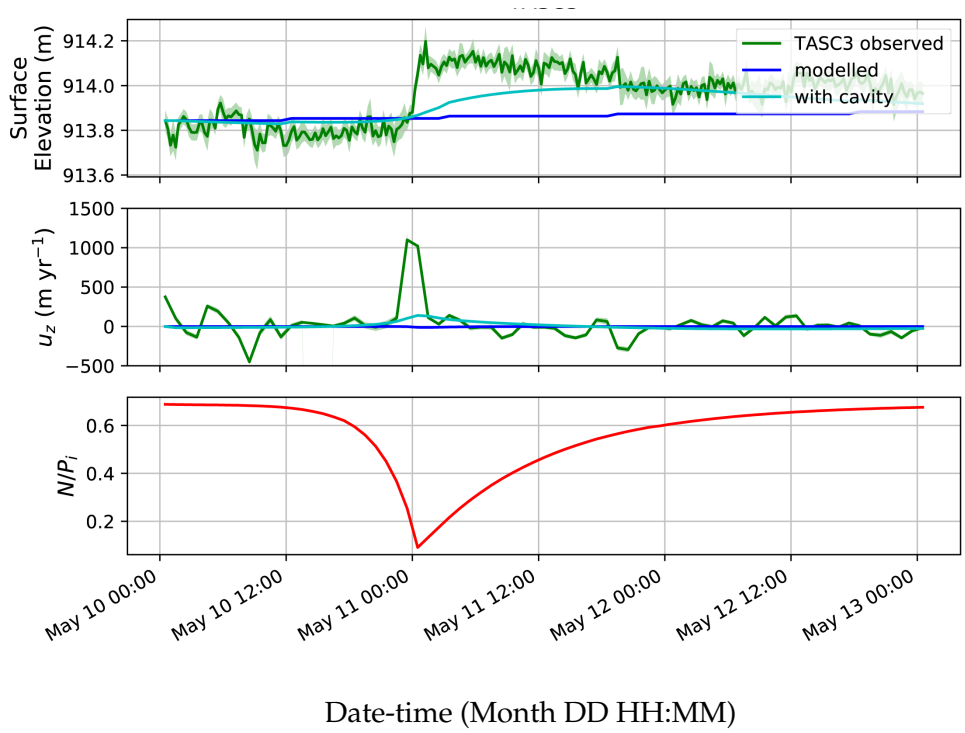

FIGURE 5.15: Cavity growth model result for May 11th event with a no-slip condition imparted along the glacier model's lateral margins. In this cavity model, a basal roughness of $h/\lambda_L = 1$ is used.

slightly overestimated — perhaps aided by the positive vertical strain calculated in this region of the glacier. The vertical displacement of the other centre-line site, TASC2, is significantly over-estimated, which may be aided by the negative effective pressures over this area of the bed. For the intermediate site TASL1, both the vertical velocity and displacement are wildly overestimated. It is possible that either cavity growth is not a primary cause of sliding at this site or that water pressures are far too high in this area, causing a lack of creep closure (this is discussed fully in Sections 1.6.4, 6.1.2, & 6.2.3). For the margin TASR2, the cavity model is not applicable as no significant uplift is observed. Lastly, for all the centre-line sites, the vertical velocities are underestimated; the model does not adequately capture the "jump" in the vertical position of GNSS units during speed-ups. It is noted that in this model there is no feedback between cavity size and sliding speed. Cavity growth can both limit water pressure and temporarily enhance sliding velocity (Anderson, 2004; Iken, 1981) which is a potential limitation in modelling sliding velocities in response to surface water inputs (e.g. Hewitt, 2013) to be discussed in detail in Section 6.2.3.

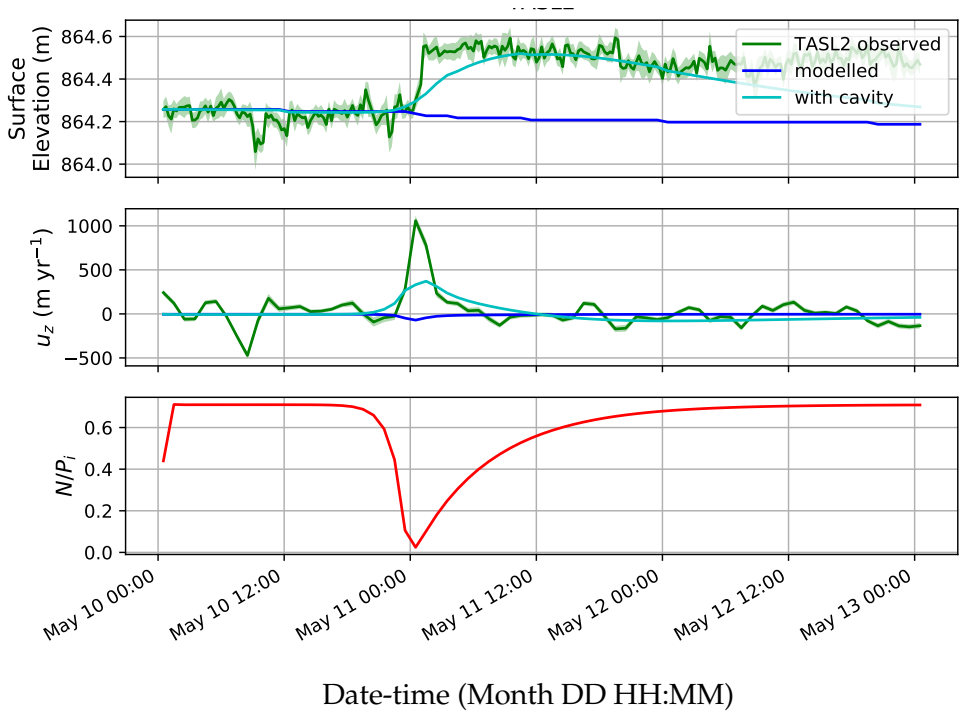

FIGURE 5.16: Model run with very high side sliding speed and moderate basal roughness (u_{side}=1100 m yr^{-1} and $h/\lambda_L = 0.5$). The model best fits the TASL2 site.

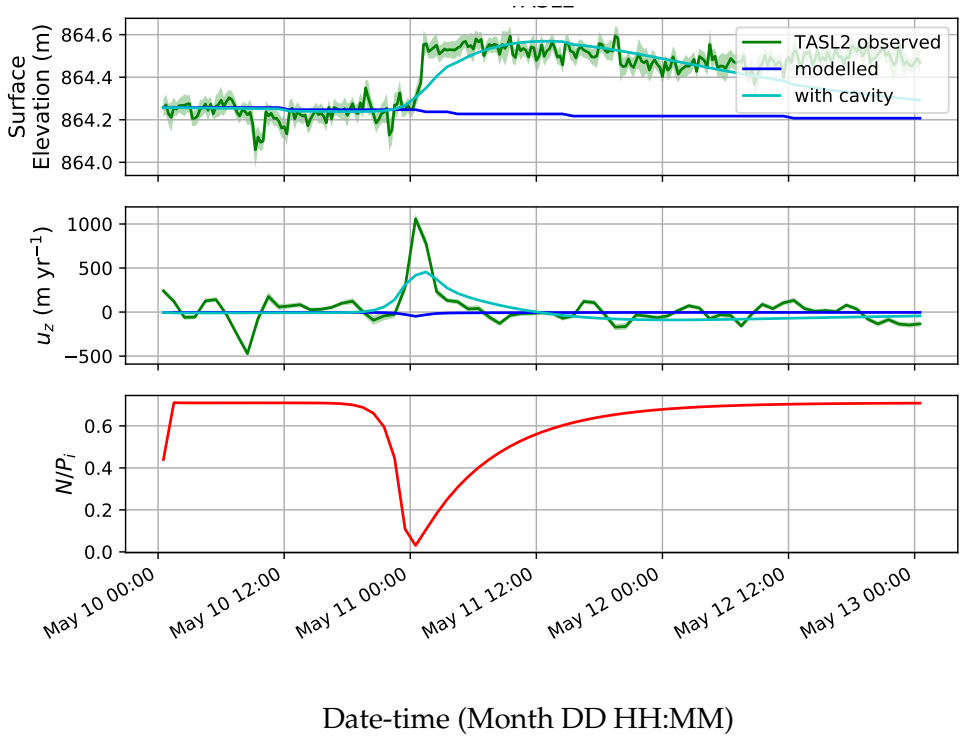

FIGURE 5.17: This figure displays cavity growth results from a model run with reasonable side sliding speed and high basal roughness (u_{side}=500 m yr^{-1} and $h/\lambda_L = 1$). Again, the fit for the TASL2 site is shown to provide a comparison to Figure 5.16

The lower downstream half of the 3D model runs into issues with excessive water pressures and bed separation. Firstly, in the best-fitting model during the timestep when the uniform water pressure of $P_w = 2.5\,\text{MPa}$ covers most of the bed, the whole lower half temporarily experiences effective pressures of over twice the ice overburden (Figure 5.18). The upper half generally remains stable due to the thicker mesh in this area. The significant negative effective pressures in the lower downstream half of the model are an artefact of using a basal water pressure model which has the same peak water pressure everywhere (Section 5.2) – water pressure fluctuations that are less than the overlying weight of the upstream half of glacier are significantly greater for the thinner downstream half (the implications of this are discussed in Section 6.2.3). One hour following the peak water pressure, most of the bed has negative effective pressures, apart from the central trunk. Ten hours following the peak water pressure, the bed separation remains high but exceeds 50 cm (roughly the maximum uplift observed in the GNSS record) over most of the lower trunk.

5.5.1 Iken's bound parameter

Varying the poorly constrained C_{max} parameter makes no difference in terms of being able to fit the observed velocities during the May 11th speed-up event for the model where $u_{side} = 500\,\text{m}\,\text{yr}^{-1}$. Even in the full range of likely values of the C_{max} parameter, the peak velocity only ranges between 563-665m yr^{-1}. This means that, due to the size of the observed accelerations, the maximum slope of the bedrock is not a sensitive enough parameter to attain the peak velocity during this event (Figure 5.19).

5.6 Summary

2D and 3D finite-element models with evolving basal water pressures and velocity boundary conditions suggest a peak water pressure of $P_{peak} = 2.5\,\text{MPa}$ is required to fit surface observations. The peak velocity of the glacier sides and upstream limit in transient tests need to be $1100\,\text{m}\,\text{yr}^{-1}$ or above to match results. In the following the chapter, the GNSS observations and finite-element modelling results will be discussed in terms of the subglacial drainage system (Section 6.1, 6.2.3) which highlight potential limitations in using the Coulomb-type sliding law.

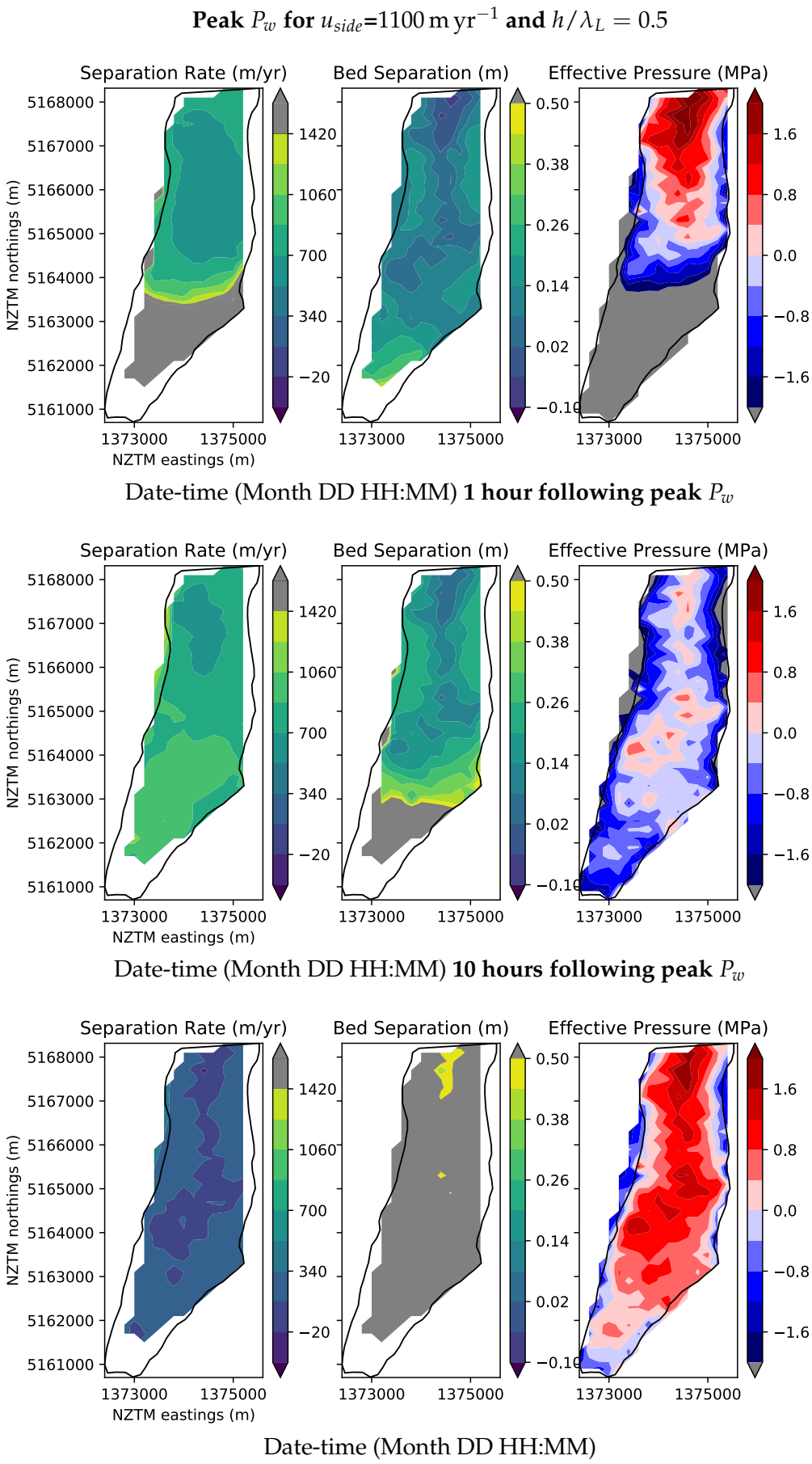

FIGURE 5.18: A map of bed separation rate (m yr^{-1}), bed separation (m), and effective pressure (MPa) during peak water pressure P_w , 1 hour and 10 hours following peak P_w for u_{side}=1100 m yr^{-1} and $h/\lambda_L = 0.5$

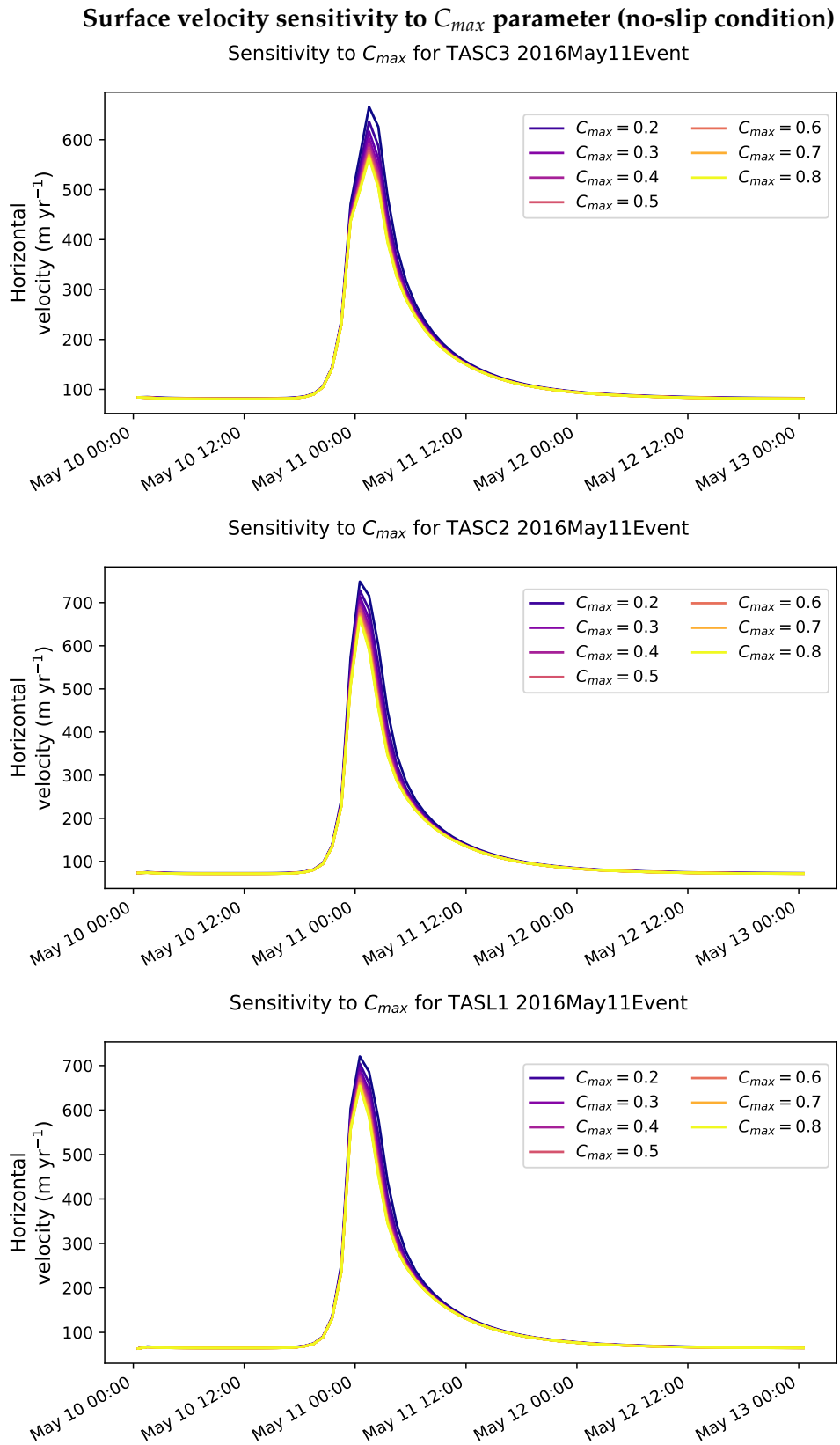

FIGURE 5.19: Range of surface velocities as TASC3 site for full range of possible C_{max} values

Chapter 6

Discussion

Haupapa/Tasman Glacier provides a case study for a glacier whose motion is regularly influenced by the rapid drainage of surface water. Large storms over the Southern Alps occur several times a year (e.g Henderson and Thompson, 1999) providing a repeatable natural experiment. During rainfall events, large volumes of water rapidly enter Haupapa/Tasman Glacier's subglacial drainage system and cause basal water pressure to rise. A transient increase in basal water pressure can explain the speed-up events observed at Haupapa/Tasman Glacier, of which six are presented in this study (Figure 4.10, 4.11; Appendix A). These speed-up events continue the 26-month record of Horgan et al. (2015) that is interspersed by similar episodes of enhanced surface velocity (Figure 4.4).

In this chapter, I discuss the surface displacement from the GNSS record in terms of glacier dynamics and the evolution of the subglacial system (Section 2.4.2). In general, the relationships between horizontal and vertical motion concur with previous studies that argue cavity growth provides a significant portion of the surface displacement during speed-ups (e.g Cowton et al., 2016). Rapid cavity growth is not described in the commonly-applied Coulomb sliding law (Section 1.4.1), and so, to test its ability in recreating accelerated sliding at Haupapa/Tasman Glacier, a finite-element model is developed (Section 3.2). The May 11th speed-up (an exemplary event) could be recreated using a Coulomb-type sliding law; however, it required side motion to be much higher than the observed TASR2 site and overburden pressures needed to be exceeded (Section 5.4).

6.1 Surface displacement during speed-up events

Rapid rain-induced acceleration is a recurring phenomenon at Haupapa/Tasman Glacier. Large rainfall events regularly provide a sufficiently large water input rate to trigger spikes in glacier velocity (Figure 4.4). Velocity peaks are large compared to a relatively stable background seasonal velocity: speeds of up to 1543 m yr^{-1} are observed while the average velocity of GNSS units vary between 34-61 m yr^{-1} with seasonal variation in the range of 6-13 m yr^{-1}(Section 4.2; Table 4.2). The accelerations documented at Haupapa/Tasman Glacier are at the upper end of those reported for

speed-ups of alpine glaciers in terms of a percentage of background velocity (Table 6.1). The obvious exception is the episodic lake-drainage reported in Das et al. (2008b), which involves concentrated drainage of a large water quantity to the bed of Greenland Ice Sheet. If Haupapa/Tasman Glacier is demonstrating speed-ups that are near the upper limit in terms of percentage increase from background velocity for alpine glaciers, then it provides an excellent test for inquiring what basal processes allow such large accelerations. GNSS units record the motion occurring within and beneath a glacier and thus provide a constraint on what mechanisms involving basal water are influencing basal motion. This section discusses the GNSS results of this study in terms of what the basal mechanisms could be involved in order to explain surface motion.

Haupapa/Tasman Glacier's speed-up events are generally consistent in terms of how the glacier's surface is displaced in response to rainfall, supporting the conclusion that common set of processes is influencing basal motion at each site (Figure 4.3, 4.7) (Section 4.1). The style of surface displacement varies between the centre and the glacier towards its margins. Based on the relationship between horizontal and vertical motion, GNSS sites in the TAS2016 network can be classed into three groups: centre-line sites (TASC2, TASC3, TASL2), glacier margin sites (TASR2), and intermediate sites (TASL1). While TASL2 is not a centre-line site, it's surface displacement closely resembles the TASC3 and TASC2 units. Centre-line sites regularly undergo the greatest amount of vertical displacement during speed-up events, reaching up to 50 cm at TASC3 during the February 17th event (Figure 4.3). Trajectories for these centre-line sites – and, to a lesser extent, TASL1 – generally follow an "arc" shape (Figure 4.3). The glacier surface is initially displaced upwards while the glacier accelerates downslope, followed by a slow descent to the original surface elevation. When ranking the GNSS sites from greatest to least horizontal displacement during speed-up, the order is always the same: the TASC3 unit always travels the furthest downstream (up to $\sim$1.8 m), followed by TASC2, TASL2, TASL1, and TASR2 (Figure 4.3). As a general rule, greater vertical displacement is associated with greater horizontal displacement — though, the TASL2 site challenges this as is it travels a comparable distance to TASC2 for each speed-up event despite often undergoing less than half of TASC2's vertical displacement (Section 4.1.3). Surface displacement records suggest consistency in the basal mechanism driving speed-up, though some limiting factors to both horizontal and vertical displacement towards the margin are likely to exist. For instance, horizontal velocities could be limited by friction against the glacier's sides (i.e. "global controls" described in Section 2.5.2) and vertical displacement limited by reasonably inactive subglacial hydrology system near the margins (Section 2.4.2, 2.5.4).

Examples of speed-up events

Glacier	% Speed up	Mechanism	Notes
Haupapa/Tasman Glacier, New Zealand (Horgan et al., 2015)	3600 %	Rain-induced sliding	When measured over a three-hour window
Frans Joseph Glacier, New Zealand (Kerhl, 2012)	30–60 %	Surface melt variability	
Breiðamerkurjö kull, Iceland (Howat et al., 2008)	400–500 %	Enhanced surface melt, Rain-induced sliding	Compared to background velocities prior to speed-up
Leverett Glacier, Greenland (Cowton et al., 2016)	< 1000 %	Surface melt variability	Typical speeds range between 0.1-1.0 m day^{-1}
Bench Glacier, Alaska (Anderson et al., 2004)	430–750 %	Warm up-valley wind triggering surface melting	
Haut Glacier d'Arolla, Switzerland (Mair et al., 2002)	∼500 %	Enhanced surface melting	An example of a "spring event"
Columbia Glacier, Alaska (Kamb et al., 1994)	15–30 %	Changes in water storage/ spontaneous reorganisation of basal drainage system	Small "speed-up events" on a surging glacier
Storglaciaren, Sweden (Jansson et al., 1995)	∼200 %	Enhanced surface melt, Rain-induced sliding	Compared to winter velocities
Greenland Ice Sheet Western Margin (Das et al., 2008)	∼8,000 %	Surface lake drainage	93 m/yr to ∼8000 m/yr

TABLE 6.1: Examples of speed-up events documents on alpine glaciers, outlet glaciers, and the margin of the Greenland Ice Sheet

The processes through which subglacial water influences basal motion need to explain why sliding speed is more sensitive to the initial input of rainfall before undergoing a slower return to the background state (Section 4.4). The main observations that require explaining are:

1. At each GNSS site, horizontal motion increases more rapidly than it decays (Figure 4.10, 4.11; Appendix A). The only exception being the TASR2 site which, while having a rapid acceleration, appears to plateau before decaying on the same timescale as the other sites (e.g. Figure 4.11, 4.15). Hence, sliding speed is likely to be accelerating during the greatest rate of water pressure rise following high rainfall, as expected from models of subglacial hydrology (e.g Schoof, 2010). The subsequent drop in rainfall does not appear to translate to a rapid decrease in horizontal velocity. The March 23rd event, for instance, shows a particularly dramatic rise and fall in rainfall rate that still results in the same asymmetry in horizontal velocity as other events (Figure A.4). It should be noted that there is likely to be some unknown degree of smoothing between rainfall and the resulting flux of water into the bed due to the time it takes for water to traverse catchment valleys or the englacial system. Furthermore, the water pressure response at each point on the bed also depends on the efficiency of the drainage system (Schoof, 2010; Werder et al., 2013; Section 6.1.1).

2. Where vertical displacement is significant, the initial offset occurs over a few hours, whereas the drop to background elevation occurs over several days (Figure 4.12). Likewise, the horizontal velocity is elevated in the days after peaking (Figure 4.12). This elevated velocity is much lower than peak velocity, but still noticeably higher than the original background speed. The process driving basal motion should explain the asymmetry in both the vertical displacement and horizontal velocity during speed-ups.

3. Horizontal and vertical velocities peak together during speed-up events (Figure 4.7). During a brief ($<$ 4 hours) plateau in horizontal velocity, significant offsets in surface elevation are observed. The process driving basal motion during speed-ups should also explain why changes in vertical displacement lag behind horizontal velocity — an observation referred to as a "hysteresis" relationship in other studies (Horgan et al., 2015; Howat et al., 2008; Sugiyama and Gudmundsson, 2004). (Figure 4.8, 4.9). Ultimately, horizontal velocity is better correlated with vertical velocity during speed-ups, not vertical displacement (which would be predicted by a sliding law that depends on cavity size, not growth rate) (Cowton et al., 2016).

4. On a few occasions, the TASL1 site achieves the same horizontal velocity as the centre-line units despite incurring around half of the observed vertical displacement and vertical velocity (Figure 4.7). It is possible that vertical motion is not fully indicative of the basal mechanism causing significant sliding at Haupapa/Tasman Glacier, or that basal acceleration is not completely controlled locally at the bed and hydrological connections along the bed (e.g. pathways between cavities or subglacial tunnels) or stress gradients within the ice are important factors (Section 2.4.2, 2.5.2).

It should also be noted that while the broad features of surface displacement during speed-ups at Haupapa/Tasman Glacier are consistent, the finer variation in surface motion that differentiate individual events from each other is a combination of how the rain rate evolves (which controls the rate of water entering the glacier) and the efficiency and layout of the sub-glacial drainage system which governs the sliding response (Figure 4.10, 4.11, A.2, 4.15, A.4). In other words, the resulting basal motion is the result of a rain input filtered through the drainage system which can amplify or suppress the response to rain input based on its spatial distribution and drainage efficiency (e.g. size and layout of subglacial channels or cavities) (Andrews et al., 2018; Iken and Bindschadler, 1986; Tedstone et al., 2013). A given response of a glacier to rainfall is then dictated by a subglacial drainage system it has inherited from how drainage has evolved in the past.

6.1.1 The role of cavity growth in speed-up events

Cavity expansion and collapse is a basal process that can provide a qualitative model to explain surface displacements of Haupapa/Tasman Glacier during rain-induced accelerations. Several parallels exist between GNSS observations presented in this study and surface motion of other glaciers that undergo significant acceleration (e.g. Cowton et al., 2016; Howat et al., 2008; Sugiyama and Gudmundsson, 2004). Most notably, the offset in surface elevation (i.e. Observation 1 described in Section 6.1) associated with speed-up events is common and involves a rapid increase before returning to background levels over several days (Anderson, 2004; Howat et al., 2008; Iken et al., 1983). Surface uplift is often attributed to the temporary storage of water in cavities at the base (Copland, Sharp, and Nienow, 2003; Howat et al., 2008; Iken et al., 1983; Iken and Bindschadler, 1986; Kamb et al., 1985; Mair, Sharp, and Willis, 2002). The link between surface uplift and subglacial water storage can be demonstrated by recording the discrepancy between water input and glacial discharge at the terminus (Anderson, 2004; Bartholomaus, Anderson, and Anderson, 2008; Copland, Sharp, and Nienow, 2003; Kamb et al., 1985). However, no discharge record exists for Haupapa/Tasman Glacier as it drains directly into a proglacial lake — lake-level data is available but is tied into subglacial water pressure due to direct connection at the glacier's terminus so does not allow a direct calculation for the volume of water leaving the glacier (Horgan et al., 2015; Figure 1.13). Following studies which document surface-water induced speed-ups (e.g. Howat et al., 2008; Iken et al., 1983), vertical displacement during rapid acceleration at Haupapa/Tasman Glacier is interpreted to reflect the average cavity growth over the glacier bed in response to elevated water pressures. This interpretation implies that large water input during rainfall events both exceed the initial volume of the subglacial system and allow cavities to remain water-filled as they expand. Cavity growth in the lee (downstream) side of obstacles accommodate water added to the subglacial system and promote faster sliding on the stoss (upstream) sides of bed obstacles. The result is bed separation which contributes to surface uplift (Anderson, 2004; Harper

et al., 2007; Mair, Sharp, and Willis, 2002; Section 2.5.4). Hence, cavity growth is a favourable process for explaining the deficit between vertical strain, the vertical component of mean downslope flow, and the vertical GNSS displacement (Horgan et al., 2015).

The slow decrease in surface elevation following speed-ups (Observation 2 in Section 6.1) can be explained by the subsequent collapse of cavities that form during the initial acceleration of a speed-up event (Section 4.4.1). As example, Anderson (2004) interpret the decrease in bed separation after a speed-up event ("Event 2" in Figure 6.1a) as the decrease in cavity volume under creep closure (which is modelled by Equation 3.18). The decrease in elevation approximately follows exponential decay, which is expected for creep closure where the rate of change in cavity area is proportional to cavity area itself (i.e. $\frac{dS}{dt} \propto S$). The increase in bed separation is joined by a greater discharge at the terminus that contains a greater degree of suspended sediment, demonstrating that drainage efficiency has increased (Figure 6.1a). The post-speed-up decay of surface elevation at Haupapa/Tasman Glacier is similarly exponential in shape, though occurs over a faster timescale than the example of Bench Glacier in Figure 6.1a. Also, the rise in surface elevation occurs over a shorter timescale at Haupapa/Tasman Glacier, suggesting a more rapid water input, cavity growth, and efficient drainage development which contribute to faster peak sliding speeds and shorter events.

The observed lag between horizontal velocity and vertical displacement (Observation 3) can be explained by cavity growth temporarily providing a significant contribution to basal motion. During rapid glacial acceleration, hysteresis has been demonstrated between water pressure and horizontal velocity (e.g. e.g. Sugiyama and Gudmundsson, 2004 and bed separation and horizontal velocity (Horgan et al., 2015; Howat et al., 2008; Figure 6.2) – both are evidence that cavity growth temporarily accelerates basal ice. In the first stage of the hysteresis loop presented in this study (Figure 4.8, 4.9), horizontal acceleration is large while vertical displacement is initiating. Horgan et al. (2015) also provide observations of hysteresis during speed-ups of Haupapa/Tasman Glacier (Figure 6.2), though in their results, horizontal velocity and bed separation increase together during the initial stage of acceleration. This first stage is interpreted to be a rapid acceleration of sliding speed due to an initially poorly connected cavity network under a sudden influx of rainwater. It is likely that, following this influx, water pressures grow faster than the cavity volume can accommodate by expanding. Iken (1981) demonstrated that faster sliding velocities occur the instance a water pressure change is applied and, if this water pressure remains high, sliding velocity decreases until a steady cavity size is achieved. A steady cavity size occurs when opening by sliding (which depends on sliding speed) balances creep closure (Equation 2.3). The sliding speed which achieves that balance would be calculated by Coulomb-type sliding law for a given effective pressure N. However, if sliding during Haupapa/Tasman Glacier's speed-up events followed Coulomb-type sliding law, then horizontal velocity would better correlate to vertical

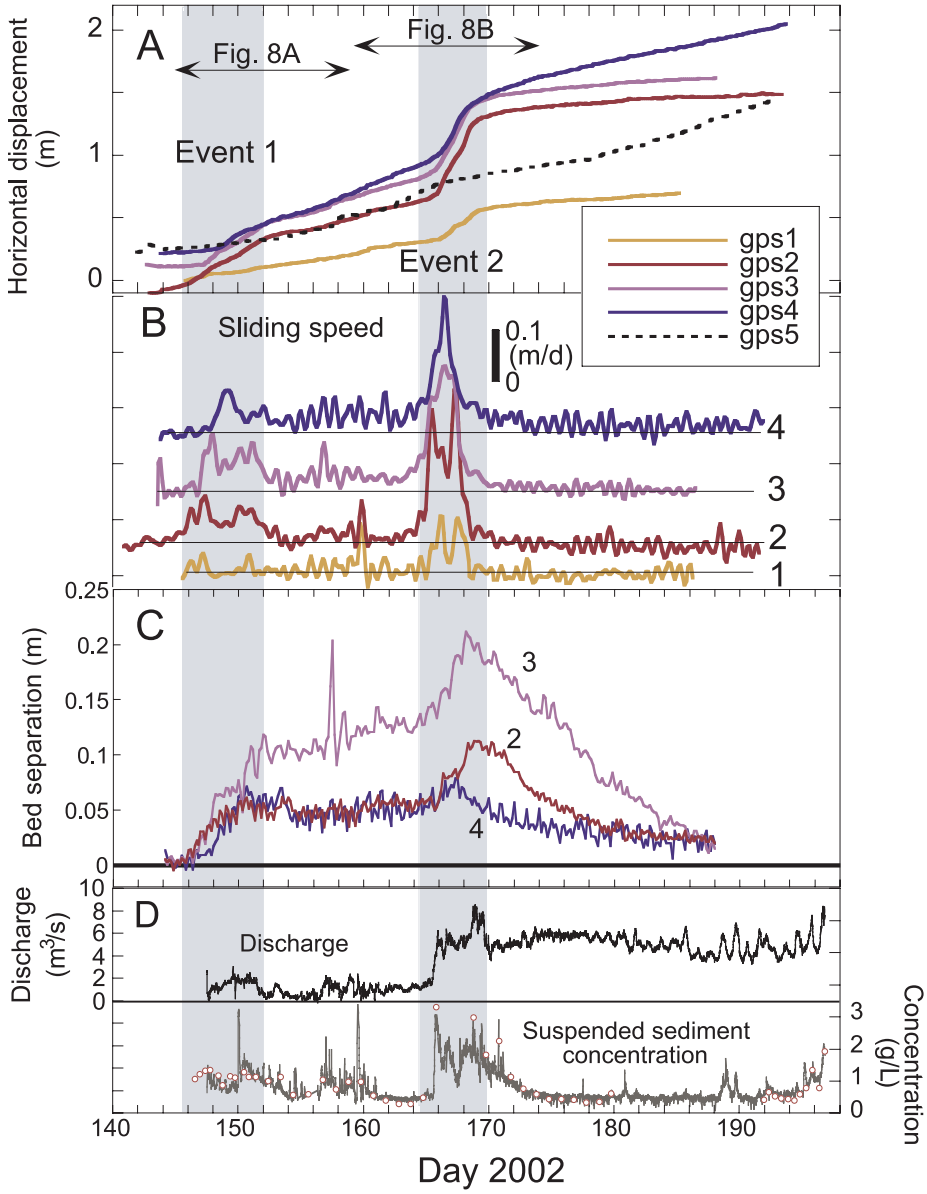

(A) that involves significant bed separation. The decay in bed separation occurs over about two weeks in response to more efficient drainage developing, alleviating basal water pressure.

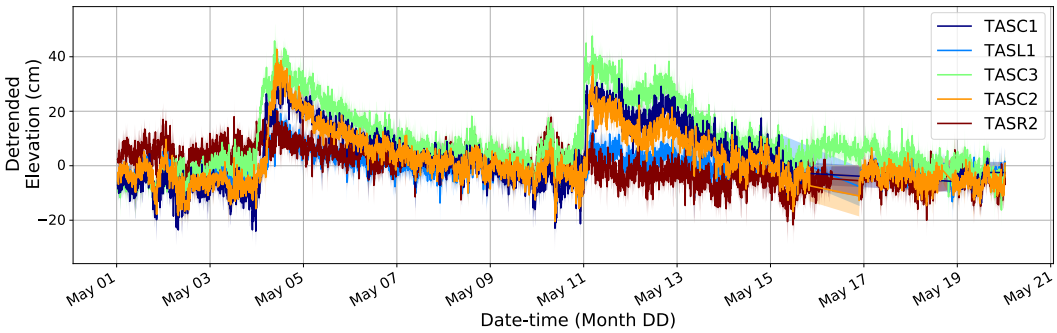

(B) The surface elevation decreases after the May 5th and May 11th speed-up events following an approximately exponential decay, similar to bed separation in (Figure 6.1a)

FIGURE 6.1: A) A figure from Anderson (2004) displaying an episode of enhanced sliding at Bench Glacier and B) Surface elevation decay from two speed-up events in this study

displacement, not vertical velocity Cowton et al. (2016). Instead we observe that the highest horizontal velocities occur during the greatest rates of surface uplift, which is used to assert that cavity growth is the primary control on sliding speed during rapid water input in accordance with the findings of Iken (1981)(Cowton et al., 2016; Howat et al., 2008; Iken et al., 1983; Iken and Bindschadler, 1986; Figure 4.7, 4.8, 4.9; Section 2.5.3)

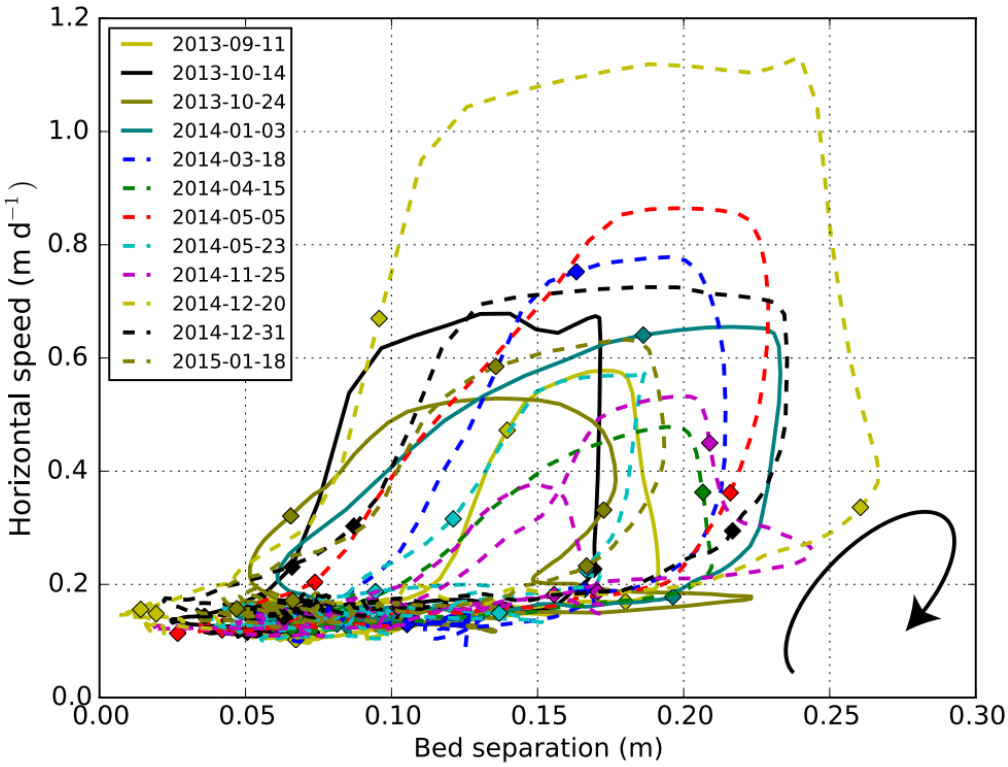

FIGURE 6.2: A figure of bed separation versus horizontal velocity relationship from Horgan et al. (2015). Velocity and bed separation data are taken from two-week intervals around speed-up events. Diamond markers are plotted every 24-hour. The clockwise trajectories are shown by the arrow.

An increase in the volume of subglacial cavities during speed-ups also explains the slow return of the glacier's horizontal speed to its background state over several days. Once surface displacement peaks and remains elevated, the horizontal velocity falls back towards its original value (i.e. Stage 3 of hysteresis relationship in Figures 4.8 & 4.9). This represents the cessation of cavity growth rates, limiting their contribution to sliding speed and resulting in the observed decrease in horizontal velocity while bed elevation remains high. Moreover, sliding speeds should also decrease as the drainage of water from the glacier bed eventually lowers water pressures and increasing the cavities to close under viscous creep (Equation 2.3). Horizontal velocities do, however, remain above background speeds for days to weeks after the peak velocity (Horgan et al., 2015; Figure 4.12), which can be explained by the persisting cavity volume. Some degree of bed separation and residual water

content in the subglacial drainage system are likely sustaining relatively lower basal stress compared to the background state. During this second phase of the speed up, as cavity growth rates continue to diminish, the glacier is tending towards a steady-state, meaning that the sliding velocity is more likely to follow the type of relationship between sliding speed and effective pressure suggested by the Coulomb-type law sliding (Schoof, 2005).

Areas of Haupapa/Tasman Glacier's bed where cavity growth is significant are problematic for sliding laws. The Coulomb-type sliding law, for example, assumes that forces balance: the stress applied by the overlying ice is balanced by water pressure and normal stress against bedrock obstacles so no acceleration occurs (Fowler, 1986; Schoof, 2005). However, if the greatest sliding speeds occur during rapid cavity growth, then this assumption is unlikely to hold. Because cavities require a certain time to grow, highly variable water pressure changes can cause an imbalanced force downstream that temporarily enhances (or hinders) sliding speed (Iken, 1981; Section 2.5.3). Hence, in terms of modelling the response of Haupapa/Tasman Glacier's motion to Haupapa/Tasman Glacier's rain events, the Coulomb-type may not predict the correct sliding velocity: for a given water pressure, the sliding velocity will be greater if cavities are expanding and slower when cavities are contracting (Howat et al., 2008; Sugiyama and Gudmundsson, 2004). Similar conclusions have been asserted in studies of Greenlandic glaciers where the Coulomb-type sliding law is thought to be inappropriate for explaining sliding speeds where strong diurnal melt variability causes significant water pressure fluctuations in a channelised subglacial drainage system (Andrews et al., 2015; Cowton et al., 2016). Cowton et al. (2016) suggest that areas of the more extensive cavity network (Section 2.4.2) that are distant from channels and moulins are likely to be in steady-state or show a greater correlation between horizontal velocity and vertical displacement and hence more appropriate for the use of the Coulomb-type sliding law. Similarly, this sliding law is likely to be more appropriate for modelling the seasonal variability in Haupapa/Tasman Glacier where horizontal velocity and surface elevation follow a similar sinusoidal variation (Figure 4.5, 4.2). During speed-ups, cavity growth is significant for the centre-line sites (TASC2, TASC3, TASL2) and likely to define a region where water pressure fluctuations are large. Though, an outstanding question is whether strong water pressure fluctuations are confined to this limited region of the bed or not. The TASL1 site, for instance, shows a weaker vertical displacement signal (implying lesser cavity growth), but similar horizontal velocities to TASC2. Furthermore, the TASR2 site shows no obvious cavity growth-like signal; however, the site records a maximum horizontal velocity of $894\,\mathrm{m\,yr^{-1}}$ (Table 4.3) on February 17th which is twenty-eight times larger than its mean background velocity (Table 4.2). It is possible that the acceleration in sliding speed is not forced locally, and some coupling exists between TASL1 and TASR2 sites to the central region of the glacier (where water pressure variation is strong)(e.g. Cowton et al., 2016). An analysis of surface

strain from comparing relative GNSS velocities would be a useful future investigation to how longitudinal and transverse stresses in the glacier influence speed-up at each site. Additionally, sliding speeds at TASR2 are likely influenced by friction against the sides, which should act to limit the observed speed-up at this site.

6.1.2 Subglacial hydrology during speed-up

Considering cavity growth likely provides a significant control on basal motion over much of the glacier, understanding how the subglacial hydrology system at Haupapa/Tasman Glacier evolves is important for evaluating a numerical model that represents speed-ups. While individual GNSS sites provide an approximation of bed separation rates per area of the bed beneath a point on the glacier surface (see Section 2.5.4), the network of sites illustrates how the subglacial drainage system acts over a larger spatial scale. Recording how surface displacement varies across the glacier aids in constraining how the effective pressure across the bed is likely to vary due to variability in surface water inputs (i.e. Section 2.1). Models of "distributed" or "channelised" drainage (discussed in Section 2.4.2) are often invoked to describe changes in the basal friction behaviour at the bed in response to water inputs (Iken and Bindschadler, 1986; Kamb et al., 1994; Mair, Sharp, and Willis, 2002). For instance, glacier speed-ups associated with the transition to spring, during which surface melt rates rapidly increase, are often explained by water entering an inefficient, distributed cavity network that is largely closed under creep and low melt rates during winter (Mair, Sharp, and Willis, 2002; Werder et al., 2013). Even with limited constraints on the subglacial drainage system, the large accelerations observed in the GNSS record can only be explained a significant rise in water pressure – i.e. sliding is the only component of the velocity field able to change fast enough and the deluge of rainwater is the most likely trigger of reduced friction (discussed in Sections 2.2 and 2.3 respectively). Hence, because a strong effective pressure response is expected to an increased influx of water, the drainage system is likely to be in a largely inefficient configuration (Schoof, 2010; Section 2.4.2) – or rather, Haupapa/-Tasman Glacier has a drainage system that is typically efficient enough to handle the flow of water from background melt rates, but is overwhelmed by the significantly larger quantities of water entering the glacier during rainfall events (Horgan et al., 2015; Purdie and Fitzharris, 1999).

However, it is observed that large rainfall events that shortly follow speed-ups on February 17th and May 11th yield no significant change in surface velocity (Figure 4.11, A.3). The absence of a surface motion response to large surface water inputs can be explained by the previous development of efficient/channelised drainage. This is exemplified in studies of Greenlandic outlet glaciers where sustained high melt rates have been shown not to produce a continued high velocity (Bartholomaus, Anderson, and Anderson, 2008; Sundal et al., 2011; Tedstone et al., 2013). Instead, these glaciers develop channelised drainage that better evacuates incoming surface water as opposed to confining and thus increasing water pressure. Channels

have the opposite effective pressure response to increases in water flux compared to cavity networks in greater discharges result in stronger wall melting, which further decrease water pressure (Röthlisberger, 1972; Schoof, 2010; Section 2.4.2). It is possible that, at the termination of each speed-up event at Haupapa/Tasman Glacier, the connectivity of the drainage system has developed efficient enough drainage that the input of additional rainfall is drained without inducing a significant speed-up response (Macgregor, Riihimaki, and Anderson, 2005; Figure 4.11; Appendix A.3). Though, it is noted that a small peak on May 12th is evident in the 24-hour velocity record and surface elevation results in response to a large rainfall peak ($> 15\,\mathrm{mm\,hr^{-1}}$) following the May 11th speed-up event (Figure 4.12, 4.11). This more subtle velocity response can be attributed to a drainage system efficient enough to drain the water added by a $\sim> 13\,\mathrm{mm\,hr^{-1}}$ event that has only partially closed over a couple of days. Hence, the even larger event exceeds the drainage capacity enough to temporarily increase horizontal velocities. The regularity of events at Haupapa/Tasman Glacier suggests that cavities and channels must continually collapse back into a more restricted state, becoming re-primed for speed-up during the next rainfall event. From the two most closely-spaced events (May 5th, 2016 and May 11th, 2016), it is suggested that an apparent lower limit of $\sim$6 days is needed before creep closure has sufficiently closed cavities to an original background state that cannot accommodate rapid water surface water input (Figure 4.12).

The down-glacier migration of peak velocity suggests that the rainwater input and the development of more efficient drainage is not uniform across the bed during speed-ups (Figure 4.13, 4.14). During all speed-up events, the onset of acceleration at GNSS sites persistently follows a downstream trend (Figure 4.10, 4.11, A.2, 4.15, A.4). The timing of peak velocity moves downstream at an approximately constant rate (Figure 4.13, 4.14). Similar "waves" of peak velocity have been observed in glaciers that undergo speed-ups where a propagation of horizontal motion is often joined with surface uplift (e.g Iken et al., 1983) and/or peaks in water pressure (e.g. Iken and Bindschadler, 1986) – which parallels the observations at Haupapa/Tasman Glacier (Figure 4.10, 4.11). The propagation of a velocity and/or water pressure signal across the glacier bed can be explained in term of the a "switch" between inefficient and efficient subglacial drainage (Bartholomaus, Anderson, and Anderson, 2008; Kamb et al., 1985; Kamb and Engelhardt, 1987; Macgregor, Riihimaki, and Anderson, 2005). Some areas of the glacial bed may be more primed for large effective pressure variation and the development of efficient drainage than others; for instance, ice near the terminus experiences the highest melt rates (though this is not necessarily the case for the debris-covered region of Haupapa/Tasman Glacier) and is typically where downstream subglacial water flow converges, meaning it is easiest to sustain subglacial channels (Cowton et al., 2016). As an example, Anderson (2004) explain the upstream propagation of sliding speed by $\sim$600 m d^{-1} (or $\sim$25 m hr^{-1}) during a speed-up of Bench Glacier, Alaska, as being due to thinner ice nearer to the terminus experiencing greater melt rates (Event 1 in Figure 6.1a).

Lower overburden pressure and greater surface meltwater input rates contribute to a stronger effective pressure response to induce rapid sliding — the sensitivity decreasing upstream as ice thickens and temperatures are generally cooler. Secondly, the termination of a second speed-up event (Event 2 in Figure 6.1a) is attributed to an upstream propagation of efficient drainage development. Near the terminus upstream flow converges and experiences lower creep closure rates meaning channels are easier to sustain here. Faster sliding promotes cavity opening across the glacier bed, providing more space for water to evacuate through the subglacial environment in up-glacier regions (Anderson, 2004; Schoof, 2010). Cavity growth can then limit sliding when high enough water flux causes unstable wall melting and cavities form into subglacial tunnels, resulting in water discharging as opposed to being stored and building water pressures (Kamb, 1987; Schoof, 2010).

In contrast to Anderson (2004), Haupapa/Tasman Glacier demonstrates a downstream propagating velocity peak. A likely explanation for this behaviour is that water pressure fluctuations are primed to trigger acceleration upstream. Potentially, the delivery of water to the bed occurs upstream either earlier or more rapidly, causing water pressures and cavity growth then develop (resulting in upstream GNSS sites increasing in elevation first) (Figure 4.10, 4.11). This relatively higher water pressures upstream compared to downstream contribute to a greater downstream flow, aided by cavity growth increasing connectivity — the result being a run-on effect where acceleration propagates downstream. Horizontal and vertical velocity also decelerate downstream, meaning that efficient drainage is likely associated with rapid cavity growth also. Water flow is likely to be most prevalent along the centreline (units TASC2, TASC3) where the greatest vertical displacement and horizontal acceleration is observed (Figure 4.8). The water pressure changes propagating down glacier causing rapid cavity growth are likely to cover a large enough area to have significant control on the overall sliding speed of the glacier (Jansson, 1995; Kamb and Echelmeyer, 1986; Mair et al., 2001).

The wave of velocity observed at Hauapapa/Tasman Glacier is faster than those reported in other examples of speed-up events. Kamb et al. (1985) report peak velocities during a "mini-surge" of Variegated Glacier, Alaska, U.S.A., that propagate at $\sim 300\,\mathrm{m\,yr^{-1}}$. Iken and Bindschadler (1986) report the downstream propagation of peak water pressure in boreholes during speed-ups of Findelengletscher, Switzerland between 87-158 $\mathrm{m\,hr^{-1}}$. However, wavefront speeds on the order of 600-2300 $\mathrm{m\,hr^{-1}}$ are observed at Haupapa/Tasman Glacier during speed-ups (Table 4.4), which is higher than other examples but demonstrates significant variability. The speed of the waves should reflect the balance of water storage (i.e. cavity volume) and discharge at the wavefront – i.e. how easily the water in a zone of cavity growth conveys water downstream (Iken and Bindschadler, 1986). At Haupapa/Tasman Glacier, pressure signals appear to be conveyed quickly relative to other examples which are likely to be due of the size of its accelerations: the rapid cavity growth induced by significant changes in sliding speed is developing connectivity

faster. This interpretation requires that rainwater input rates remain high enough to sustain high water pressures to quickly drive water flow across the bed. The limit to bed separation depends on whether drainage is efficient enough to transport water to lower parts of the glacier without building water pressures. Models of speed-up that involve subglacial flooding or a sudden change in the connectivity of the bed (e.g. Harper et al., 2007) are unlikely to apply to Haupapa/Tasman which exhibits significant uplift which requires the confinement and subsequent pressurisation of water and resulting cavity growth to explain surface observations.

6.2 Finite-element modelling of basal water pressure and sliding speed

An outstanding issue for modelling glacier acceleration in response to enhanced surface melting or rainfall is whether commonly-applied sliding laws are always applicable for linking changes in subglacial hydrology to changes in basal motion. During rapid surface water input, such as rainfall, lake drainage, or surface melt during the onset of the melt season, the subglacial drainage system can evolve rapidly. In section 6.1.2, the switch from inefficient to efficient drainage offers an explanation for the downstream propagating rise and fall in horizontal velocity and surface elevation (Section 2.4.2). The rapid cavity growth associated with a transition from an inefficient to an efficient drainage system over several hours directly challenges the underlying assumption in the Coulomb-type sliding law that forces are balanced at the glacier's base (Schoof, 2005). Despite the apparent contradiction, the Coulomb-type sliding law is often used to in numerical models to produce sliding velocities in response to variable surface water inputs Flowers et al. (e.g. 2011), Hewitt (2013), Jay-Allemand et al. (2011), Pimentel, Flowers, and Schoof (2010), and Pimentel and Flowers (2011). Finite-element models are used in this study to test the consequences of using a sliding law that implies a sliding speed for a given water pressure (and hence a stable cavity size). The models negative effective pressures and high side velocities (u_{side}) needed to match surface observations for the May 11th event in particular (e.g. Figure 5.5, 5.13) demonstrate the limitations of the potential limitations of the Coulomb-type sliding laws where basal motion changes significantly over hourly timescales.

6.2.1 Modelling rapid sliding using a Coulomb-type sliding law

Finite-element models using a Coulomb-type sliding law for replicating transient acceleration of Haupapa/Tasman Glacier results in basal water pressures that exceed overburden pressure and velocity boundary conditions that are required at greater speeds than nearby GNSS units (Figure 5.4, 5.5, 5.13). While water pressures greater than the weight of the overlying ice are observed in some borehole observations (e.g. Andrews et al., 2015; Copland, Sharp, and Nienow, 2003; Cowton et al., 2016; Rada

and Schoof, 2018), they typically only exceed flotation by a few percent and may only be observed in poorly connected areas of the bed (Fudge et al., 2009; Rada and Schoof, 2018). In order to fit observed peak velocities in both 2D and 3D models, the basal water pressure imposed as a "pressure wave" travelling downstream, along the basal boundary peaks at $P_{peak} = 2.5\,\mathrm{MPa}$ (Figure 5.5, 5.13). In the 2D case, basal water pressure exceeds flotation between 5-10% to recreate the motion of the centre-line GNSS units (Figure 5.4). This is even more extreme for the 3D model: where overburden is exceeded, modelled water pressures are between 2-79% greater than overburden (Figure 5.13, Section 5.2.3, Table 5.1). The greater range in effective pressures is the result of including all available GNSS sites in a model where P_{peak} is uniform across the entire bed. For the bed model used in this study (Farinotti et al., 2017; Huss and Farinotti, 2012), some sites reside over thinner ice that is more sensitive to water pressure fluctuations. If the same water pressure is required to meet surface observations in both 2D and 3D models, and this water pressure exceeds overburden in both cases, then this implies that the Coulomb-type sliding law requires much of glacier model's basal boundary to lose its ability to apply basal stress. As effective pressures tend to zero, the sliding law both tends to $\tau_b \sim C_s N$ which then tends to $\tau_b = 0$ for $N \rightarrow 0$ (Brondex et al., 2017). Figure 5.18 demonstrates that most of the bed is above flotation pressure at least an hour after peak speed-up. Therefore, it is not simply the mechanism of enhanced sliding velocity under greater cavity size that is required to match surface observations, but an increasingly large portion of the bed loses basal stress for negative effective pressures.

Recreating observed peak velocities of Haupapa/Tasman Glacier's speed-up events requires a significant loss of both basal stress and imposed peak velocity along the glacier's sides. Essentially, high peak water pressures prime the glacier bed for rapid acceleration, but the influence of "global controls" (e.g. sidewall friction and longitudinal stresses as discussed in Section 2.5.2) outside of the glacier's base ultimately limit the total velocity the glacier can achieve. Here, finite-element models of Haupapa/Tasman Glacier mimic a decrease in sidewall friction as the increase in peak velocity of a time-evolving velocity boundary condition (Section 3.2.7). Faster motion along the sides implies reduced side friction, resulting in lower velocity gradients and therefore lower stress gradients across the glacier to balance the gravitational driving stress of ice (Cuffey and Paterson, 2010). In both 2D and 3D models, the velocity boundary conditions impart a strong control on the peak velocity of the glacier. For instance, in the 2D model varying the u_{side} parameter between 100-1100 $\mathrm{m\,yr^{-1}}$ produces a peak sliding velocity at TASC3 between 400-1000 $\mathrm{m\,yr^{-1}}$ (Figure 5.6). However, a fit to horizontal velocity at TASC3 also requires a peak water pressure of $P_{peak} = 2.5\,\mathrm{MPa}$ as lower water pressures produce too much drag locally to allow fast enough sliding (see sensitivity to varying P_{peak} in Figure 5.7). Likewise, in the 3D model, the "rounding-off" of the sliding velocity at high water pressures demonstrates that the sliding velocity can no longer increase due to a loss of basal stress (Figure B.1). To bridge the deficit of $\sim$900 $\mathrm{m\,yr^{-1}}$ between the model with no

slip along the sides and observations (Figure 5.11), a peak side velocity of $u_{side} = 1100\,\mathrm{m\,yr^{-1}}$ is required (Figure 5.13). This result implies that surface velocity does not change significantly upstream, which is likely to be true during speed-up. However, it does also result in velocities that are relatively uniform across the width of the glacier, which is unlikely. The TASR2 unit demonstrates that the glacier decreases in velocity the sides glacier and hence a model for ice flow should retain some decay in peak velocity towards the margins (e.g Figure 4.11).

A peak side velocity of $u_{side} = 1100\,\mathrm{m\,yr^{-1}}$ may be an unreasonable parameter choice for representing side motion at Haupapa/Tasman Glacier during speed-up, but lower values of u_{side} aren't able to match observations. Presuming the TASR2 site is the best constraint on side sliding speed, we would expect some peak side velocity to be less than this GNSS site's observed peak horizontal speed ($584\,\mathrm{m\,yr^{-1}}$). Despite following this constraint, a model with $u_{side} = 500\,\mathrm{m\,yr^{-1}}$ still falls short of surface observations: the TASC2 site for instance requires an extra $\sim 500\,\mathrm{m\,yr^{-1}}$ to meet peak velocity. Even if the only other major unconstrained variable, C_{max}, is varied across its entire range of expected values, it only varies the result in a range of $\sim 100\,\mathrm{m\,yr^{-1}}$ (563-665$\mathrm{m\,yr^{-1}}$) — this is not enough to explain the gap between modelled and observed velocities. Overall, the Coulomb-type sliding law is not able to achieve peak velocities by the response to basal water pressures on its own and needs a combination of a) a significant portion of the bed to lose cohesion and b) to display greater slip (implying reduced side friction) than the velocity of the TASR2 site suggests.

To recreate speed-up events with lower water pressures and more reasonable velocity boundary conditions, the model of Haupapa/Tasman Glacier would need to incur a greater acceleration in the central portion of the glacier (where TASC2, TASC1, TASL2, and TASL1 are located). This would require some additional mechanism to be introduced into the sliding law. Because GNSS observations in the centre of the glacier show evidence of subglacial cavity growth as providing a significant influence of basal displacement during speed-ups (Section 6.1.1), and cavity size appears to become negligible towards the margins, implementing transient cavity growth into the basal sliding law could provide the necessary mechanism to provide a more physically reasonable fit to data. Hence, the large events observed at Haupapa/Tasman Glacier could provide an additional modelling experiment that would benefit from a sliding law of the type suggested by Howat et al. (2008) — i.e. a sliding law which includes the both effective pressure and cavity size in calculating sliding speed (Equation 1.6) (Cowton et al., 2016; Hewitt, 2013).

6.2.2 Modelling cavity size based on speed-up event model output

A simple model for bed separation rate (i.e. the change in cavity volume per area of bed described by Equation 3.18) can be used to reproduce the magnitude of surface uplift during the May 11th, 2016 speed up event, but it fails to match the rate

of vertical displacement (Anderson, 2004; Figure 5.14, 5.15, 5.17, 5.17). In the cavity models presented in Section 5.5, cavity opening via sliding largely controls the initial $\sim$ 40 cm of vertical displacement during the initial acceleration; even in the presence of negative pressures, opening via creep deformation would still occur of several days (Anderson, 2004). Instead, creep deformation controls the lowering of the surface after modelled sliding velocities lower to their background level P_0. When sliding velocities are great enough to match surface velocities, such as in the 3D model with $u_{side} = 1200\,\mathrm{m\,yr^{-1}}$ (Figure 5.13), the cavity model can achieve the observed uplift. Using the sliding speed, effective pressure, and vertical strain output of this model in combination with a basal roughness of $h/\lambda_L = 0.5$ provides a similar record of displacement to GNSS sites — namely for TASL2 (Figure 5.17)(see methodology in Sections 3.2.7 & 3.3). A basal roughness of $h/\lambda_L \leq 1$ is considered physically reasonable. An advantage of the cavity growth model is that it helps loosely constrain basal geometry, which may be useful in subglacial hydrology models. The cavity model is highly non-unique, however, as the considerably slower $u_{side} = 500\,\mathrm{m\,yr^{-1}}$ model can provides an almost identical vertical displacement record for a basal roughness of $h/\lambda_L = 1$ (Figure 5.17). Hence, cavity the model must also be constrained by the horizontal velocity record.

A major limitation to the bed separation model (Section 3.3) is that the Coulomb-type sliding law does not account for the interaction of cavity growth and sliding velocity (Equation 3.18). Cavity growth is a used to explain surface uplift (Cowton et al., 2016; Iken et al., 1983; Iken and Bindschadler, 1986; Kamb, 1987; Mair, Sharp, and Willis, 2002) and temporarily enhanced sliding velocity during speed-up events (Cuffey and Paterson, 2010; Howat et al., 2008; Iken, 1981; Mair, Sharp, and Willis, 2002). In general, the cavity model works better in areas where cavity growth is likely to be taking place (i.e. TASC3, TASC2, TASL2) (Figure 5.16, 6.3, 6.3) and less well where the relationship between horizontal and vertical displacement is more subdued (TASL1, TASR2)(Figure 6.4, D.2). However, it is unlikely that a robust relationship exists between u_b and N through which to calculate cavity size due to significant bed separation rates being calculated from model output in this study. For instance, bed separation rates $\frac{dB}{dt}$ of around $400\,\mathrm{m\,yr^{-1}}$ are calculated at the TASC2 site during the peak water pressure in the May 11th model with $u_{side} = 1200\,\mathrm{m\,yr^{-1}}$ and a basal roughness of $h/\lambda_L = 0.5$. Iken (1981)'s "hydraulic jacking" mechanism, where sliding velocity is elevated as a cavity expands towards its steady size after a water increase is applied (Section 2.5.3), is likely applicable when describing basal displacement at Haupapa/Tasman Glacier during speed-ups. The hysteresis relationship between horizontal velocity and vertical displacement evident in GNSS records have already suggested the need to include cavity growth to explain observations (Section 6.1). Moreover, to improve models that investigate the role of subgalcial drainage in vertical displacement during speed-up, a sliding law that varies with cavity growth would be valuable.

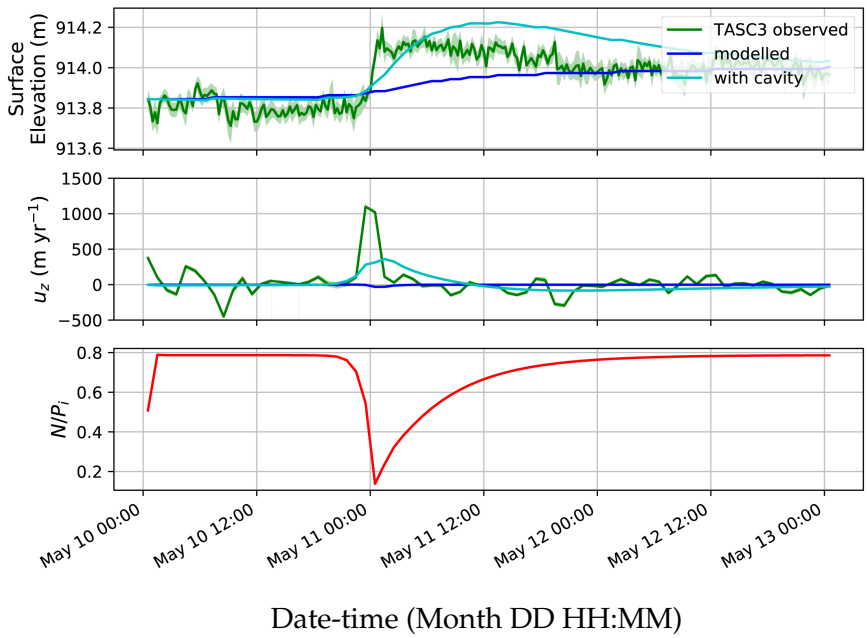

FIGURE 6.3: Cavity model run result with high side sliding speed and moderate basal roughness (u_{side}=1100 m yr^{-1} and $h/\lambda_L = 0.5$). Modelled and observed results are compared at the TASC3 site. The magnitude of vertical displacements are reasonably well calculated by the cavity growth model; however, the surface uplift rates are poorly matched.

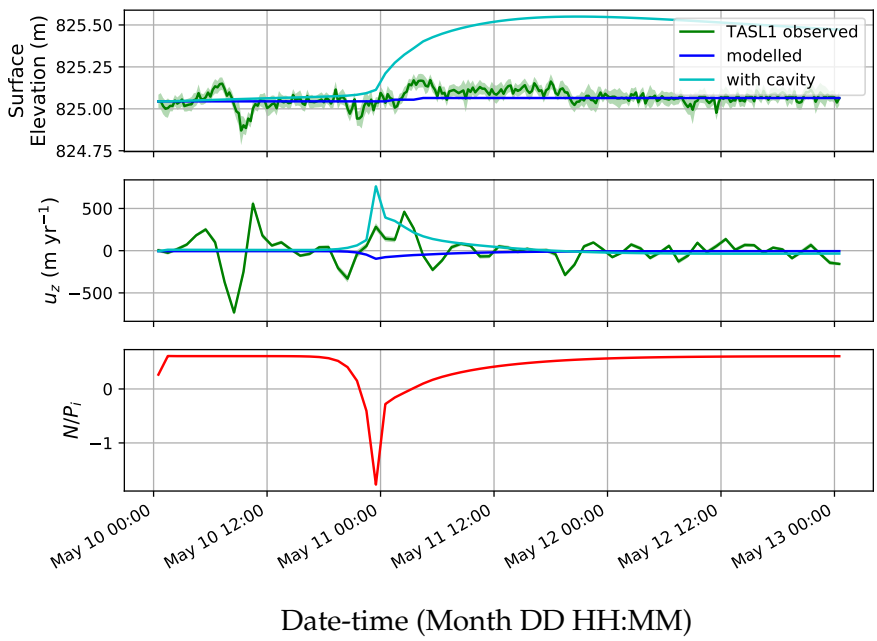

FIGURE 6.4: Significant misfit in cavity model for TASL1 site. In this model run, a high sliding speed along the lateral margins of the glacier model and moderate basal roughness are imposed (u_{side}=1100 m yr^{-1} and $h/\lambda_L = 0.5$). Modelled and observed surface elevation, vertical velocity, and effective pressure are compared at the TASL1 site. Opening rates are too great and cause excessively high vertical displacements.

6.2.3 The treatment of subglacial hydrology in finite-element models of Haupapa/Tasman Glacier

The simple model for water pressure used in this study is able to capture the broad behaviour of surface motion in conjunction with the Coulomb-type sliding law; although, the simplified water pressure model may only offer a limited picture of how the subglacial drainage system evolves during speed-ups (see description of water pressure models in Section 3.2.4). By creating a downstream moving "wave" of basal water pressure that rises and decays exponentially, the model aims to capture the essential behaviour of the hydrological system used to explain the surface displacement of GNSS sites in Section 6.1.2. Enforcing an exponential rise in water pressure following a rainfall event assumes a distributed cavity system that is largely undeveloped, has poor conductivity and is overwhelmed by a rapid rainwater input. The downstream propagation of peak water pressure emulates cavity growth being triggered upstream first, rapidly opening connections between cavities, and thus promoting water transport downstream (Mair, Sharp, and Willis, 2002). Peak water pressure P_{peak} is only a function of distance downstream and so water pressure rises uniformly across the width of the glacier as the wave passes downstream; though, it should be noted that a uniform water pressure across-stream is a condition applied for simplicity in the modelling process and is unlikely to represent water pressure evolution nearer to the margins. Likely, a lack of elevated water pressures driving cavity growth near the glacier margins could explain the lack of vertical displacement observed at TASR2 (Iken et al., 1983). Furthermore, in 3D transient models, while the exponential rise in water pressure mimics surface velocities reasonably well for centre-line sites (Figure 5.4, 5.16), the water pressures and resulting sliding velocities of the TASR2 and TASL1 sites tend to be grossly over-predicted (Figure 6.5, 6.5b). Ultimately, the 3D transient models are better suited to the GNSS sites that are thought to undergo the most significant cavitation during speed-up (i.e. TASC3, TASC2, and TASL2). Some areas of the model are constantly under negative effective pressure during the transient model runs, such as near the glacier terminus and sides (Figure 5.9). A more realistic model could limit significant water pressure variation to where vertical uplift is detected and limit water pressures to ice overburden where the glacier is thinner or where drainage is likely to already be more efficient (i.e. near the terminus)(Section 6.1.2).

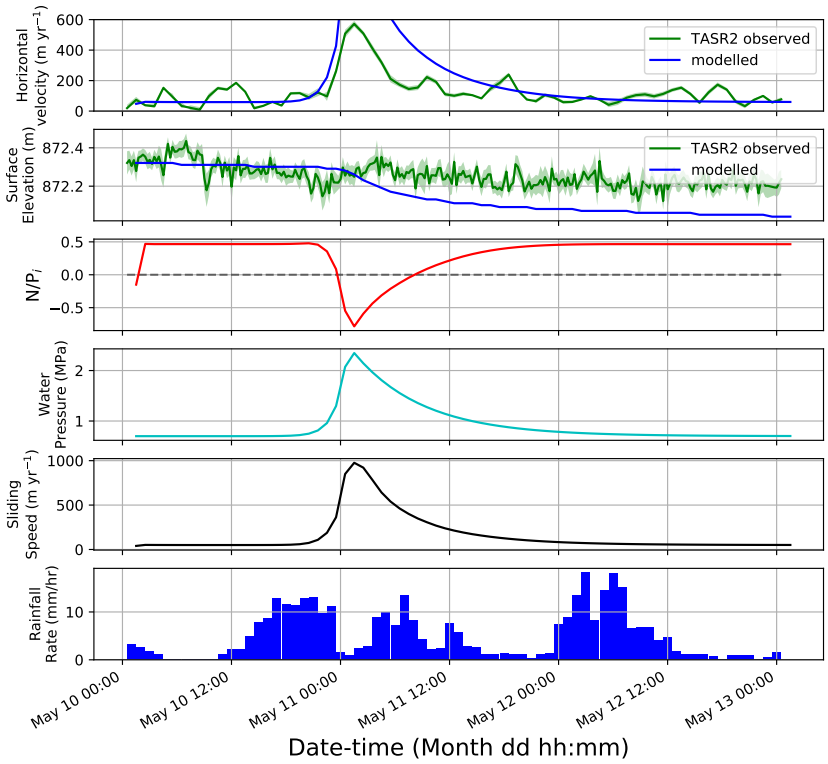

(A) TASR1 result

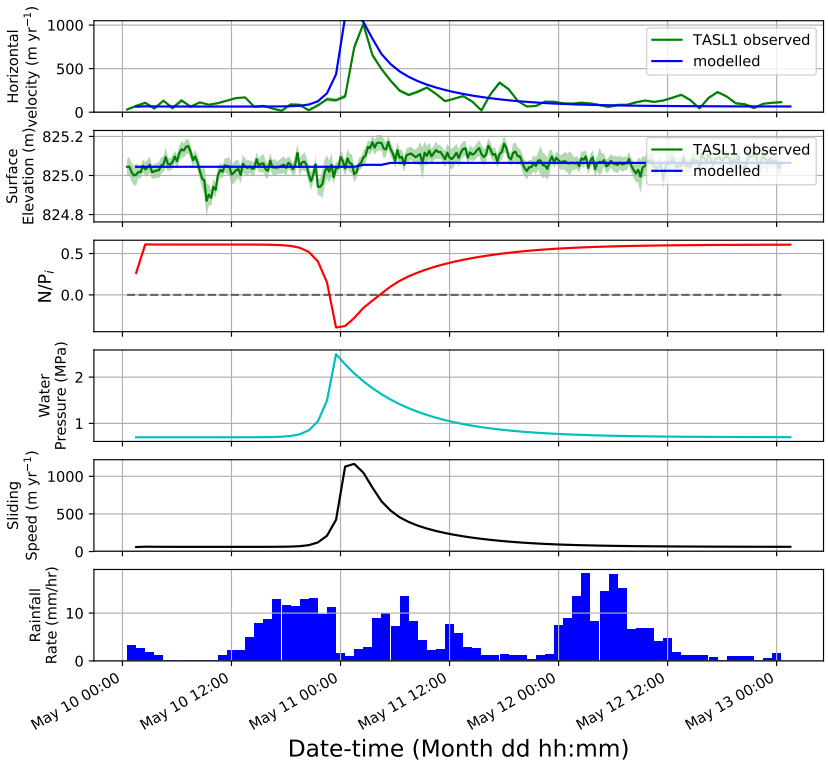

(B) TASL1 result

FIGURE 6.5: Fit at TASL2 (A) and TASR2 (B) to for 3D model for May 11th, 2016 with $u_{side} = 1100\,\mathrm{m\,yr^{-1}}$. At both sites, modelled horizontal velocities greatly exceed observations and effective pressures are negative.

The decay in horizontal velocity following a speed-up is matched by a water pressure function in 2D and 3D models that also decays more slowly than it rose – which agrees with the interpretation of how subglacial drainage evolves at Haupapa/Tasman Glacier during speed-up (Section 6.1.2), but does not necessarily quantify the degree of efficiency or change in discharge. To match the observed asymmetry in horizontal velocities (Figure 4.10, 4.11; Section 4.4), modelled basal function water pressure, naturally, required a greater decay time t_{decay} than rise time t_{rise} (e.g. Section 5.2.3, 5.4, 3.2.4). This broadly represents the behaviour of the subglacial system following speed-up. After rapid uplift associated with cavity development, cavity enlargement should eventually develop the efficiency of the drainage system to the point where water is able to flow at lower pressures — i.e. lower compared to the high water pressures experienced during cavity growth when cavity volume is smallest and rainwater input at the bed is highest (Iken, 1981; Mair, Sharp, and Willis, 2002). Areas of the bed with increased cavity size and connectivity – or areas which develop into a subglacial R-channels – flow at lower pressures which draws water from nearby cavities and conveys it downstream. Because horizontal velocity, vertical displacement, and lake level and remain elevated for several days after speed-up events (e.g. Figure 4.12, 1.13) it is likely that water pressures also experiences a slower return to background levels due to residual water in the system. It is noted that water pressures do decrease faster than surface elevation, which also indicates more efficient drainage developing (Anderson, 2004). In addition, the cavity model in this study poorly captures the decay in surface elevation over the scale of several days, which could mean the final water pressures are too low causing higher than expected creep rates. This suggests that drainage should not be efficient enough to completely evacuate the rainwater that causes the speed-up event over the time it takes for horizontal speeds to decay. Overall, the simple water pressure model agrees with the general qualities of subglacial drainage evolution. However, a more complete picture on the discharge rate and the extent of channelised drainage will possibly require a process-based hydrological model of the Haupapa/Tasman Glacier bed (e.g. Werder et al., 2013).

Another possibility for describing the cause of speed-ups is the Harper et al., 2007 model where the glacial bed becomes flooded and connectivity over a large area of the bed controls rapid sliding (Section 1.4). However, the velocity response at Haupapa/Tasman Glacier is consistent between events, provided they are separated by enough time (Section 4.4), and the lack of speed-up due to rainfall in the days after an event suggests a mechanism based on increased drainage efficiency as opposed to changes in connectivity. However, it remains to be validated whether there is enough time for channels to develop. This would require either high melt rates (which have been neglected in this study) or high water fluxes to sustained for long enough to allow the subglacial tunnel to remain open while conveying large quantities of water.

Here, the basal water pressure solutions of finite-element models likely represent the general behaviour of the subglacial drainage system during speed-up, but the forward-modelling approach used to produce these solutions is non-unique. One issue is that the velocity boundaries have a strong effect on the final solution (Section 5.3.3, 5.3.3). For instance, by introducing a time-evolving velocity boundary condition to the 3D models, a deficit of $\sim 900\,\mathrm{m\,yr^{-1}}$ between modelled and observed surface velocity could be accounted for (Figure 5.11, 5.13). Side friction, then, plays an important role in modelled sliding speed; however, the artificial implementation of a velocity boundary does not offer a process-level understanding of how side friction controls velocity at Haupapa/Tasman Glacier. Ideally, a sliding law would be introduced along the side boundaries where slip would depend on stresses within and applied by the ice instead of being artificially imposed (e.g. Pimentel, Flowers, and Schoof, 2010; Schoof, 2006). However, this would likely require additional GNSS units along the margin to constrain friction parameters for the glacial walls.

A further outcome of the forward-modelling process in this study is that the basal water pressure evolution is imposed instead of being calculated using physical processes involving basal water flow and sliding speed. An exponential basal water pressure function naturally suits the approximately exponential rise and decay of horizontal velocity during speed-ups (e.g. Figure 4.11, Section 3.2.4). Because the sliding speed increases monotonically with decreasing effective pressure through the Coulomb-type sliding law (until water pressure approaches flotation), the sliding law naturally works to mimic observations (Brondex et al., 2017; Figure 2.10). However, GNSS results of this study challenge the use of a sliding law where sliding speed increases as a function of effective pressure and basal stress alone (Section 1.6.4). Hysteresis between horizontal velocity and vertical displacement at GNSS sites give rise to the possibility that changes in sliding velocity lag behind water pressure. For instance, Sugiyama and Gudmundsson (2004) use water pressure and ice flow records during a speed-up of Lauteraargletscher, Switzerland, to demonstrate that flow speed can increase after a change in water pressure is applied (Figure 6.6). Hence, if cavity growth is included in a basal water pressure model for Haupapa/Tasman Glacier (i.e. the "hydraulic jacking" mechanism described in Section 2.5.3), the timing of water pressure peaks be earlier than that predicted by the models in this study (e.g Figure 5.13). Furthermore, forward-modelling with an imposed basal water pressure does not necessarily test how the basal drainage is behaving during rapid surface water input. Because records of discharge at the glacier terminus records are lacking, numerical modelling and conceptual models, in conjunction with surface observations, are the most readily available tools for investigating the basal hydrology of Haupapa/Tasman Glacier. The switch between "efficient" and "inefficient" drainage is a useful – and widely used – conceptual model to explain the processes underlying speed-ups (Section 2.4.2, 6.1.2). However, the basal water pressure functions in the finite-element models presented

in Chapter 5 do not directly calculate the processes of cavity volume change, water flux, or wall melting. Therefore, further modelling development is needed to understand the subglacial water storage and effective pressure response in a quantitative, process-based approach.

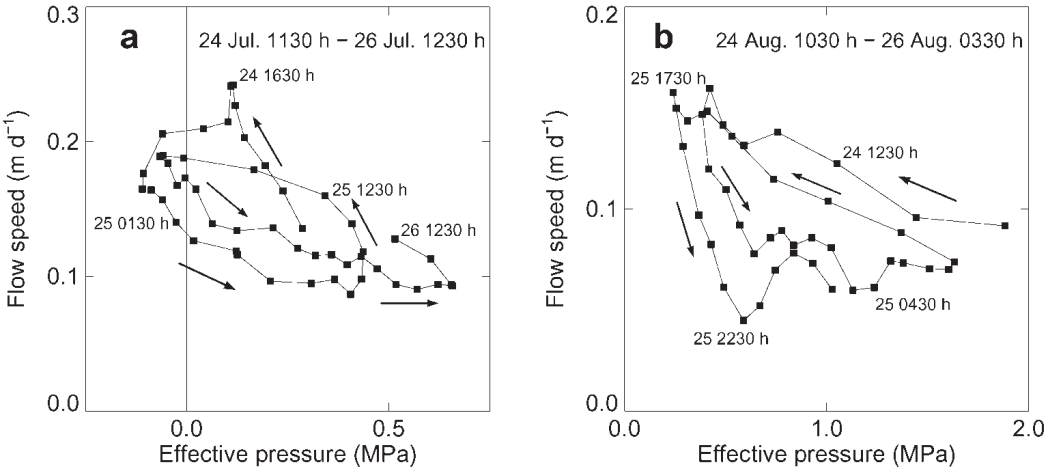

FIGURE 6.6: Hysteresis between effective pressure and flow speed observed by Sugiyama and Gudmundsson (2004). Observations of borehole water pressure and surface velocity during speed-up events at Lauteraargletscher, Bernese Alps, Switzerland demonstrated that peak water pressure occurred before peak velocity.

Incorporating a drainage system model into the ice flow model could be a means of validating the basal processes involving water that influence basal ice motion. Firstly, a model of subglacial hydrology could better define the background water pressure distribution and average cavity size of Haupapa/Tasman Glacier in response to its background melt rate and high annual rainfall (Henderson and Thompson, 1999; Horgan et al., 2015; Purdie and Fitzharris, 1999). Subglacial drainage models calculate water pressure and discharge of water across the bed by solving for hydropotential ϕ due to ice thickness H and bed elevation B:

$$\phi = \rho_w g B + P_w \tag{6.1}$$

where ρ_w is water density, g is gravitational acceleration, B is the height of the glacier bed above some datum (typically sea-level) and P_w is water pressure. Water flows from high hydropotential to low, meaning that both the pull of gravity and distribution of basal water pressure drive flow. Also, a hydrological model would provide a test for whether the input of water during episodes of heavy rainfall is enough to develop channelised drainage or whether an increase in cavity volume is enough to discharge the surface water and limit basal water pressures. Ideally, to test the hypothesis that the evolution of subglacial drainage has a strong control on the surface displacement observed in the GNSS record of this study (Section 6.1.2), a model which can account for the switch between a distributed and channel model would

be incorporated. Currently, only two hydrology models can be coupled with models of ice flow in Elmer/Ice. One option models efficient and inefficient drainage by the diffusion of water through either a high or low porosity layer (De Fleurian et al., 2014). Another option is a coupled distributed and channelised finite-element model presented in Werder et al. (2013). The advantage of the Werder et al. (2013) model is that it calculates the cavity opening rate directly by:

$$\frac{\partial h}{\partial t} = u_b(h_r - h)/l_r - Ah|N|^{n-1}N \tag{6.2}$$

where h gives the height of a "water sheet" representing the average cavity volume, u_b is sliding speed, h_r is the height of bedrock obstacles, l_r is the obstacle spacing, A is the creep parameter, n is Glen's flow law exponent,and N is effective pressure. However, as Hewitt (2013) and Cowton et al. (2016) point out, the implementation of sliding speed in Equation 6.2 usually relies on a sliding law that does not take into account cavity growth. This poses a problem in modelling basal hydrology for glaciers like Haupapa/Tasman Glacier where the majority of the surface motion signal appears to represent cavity growth (Cowton et al., 2016; Howat et al., 2008). A sliding law that includes cavity growth could also help to bridge basal hydrology and ice flow models. Coupled models have already been developed in Elmer/Ice for testing the influence of meltwater variability addressing Greenland Ice Sheet's mass loss – but models which use a process-based hydrology model (i.e. Werder et al., 2013) in Elmer/Ice have not yet been fully explored for recreating observed velocity variation of valley glaciers like Haupapa/Tasman Glacier (De Fleurian et al., 2018; Gagliardini and Werder, 2018). Hence, a suggested path of future work in modelling speed-up events at Haupapa/Tasman Glacier involves quantifying discharge versus water storage in cavities using a hydrological model and implementing cavity growth in sliding laws to better capture the sliding–cavity opening feedback.

On a final note, the negative effective pressures required to match observed peak velocities at Haupapa/Tasman Glacier (Figure 5.4, 5.5, 5.13) is not a unique issue in modelling rapid surface water input using a Coulomb-type sliding law. Pimentel, Flowers, and Schoof (2010), for instance, attain water pressures that significantly exceed ice overburden when modelling the surface lake drainage event reported in Das et al. (2008b)(Section 2.3.2) using an ice flow model coupled to a hydrology model through the Coulomb-type sliding law (Figure 6.7). Large negative pressures (up to eight times overburden) occur during a lake drainage scenario unless a channelised drainage model is implemented to better alleviate water input. Peak water pressure is also reduced by including some background flow in the initial cavity network to maintain initial cavity volume and introducing channels to increase discharge ability (plots c and d in Figure 6.7). Adding more realistic hydrological processes could be a means of reducing effective pressure in the finite-element models of this study, as well as future hydrological modelling of Haupapa/Tasman Glacier that which will have to deal with large volumes of water entering the subglacial environment. Similarly, Werder et al. (2013) model the subglacial drainage system of

Gornergletscher, Switzerland over a melt season and find several instances where effective pressure is negative due to excessive rates of water input (Figure 6.8). They attribute a possible cause of excessive basal water pressure to the lack of a hydraulic jacking mechanism creating a rapid enough growth in cavity volume to evacuate the influx of water (and thereby alleviate water pressure). Hence, implementing cavity growth into finite-element modelling could help reduce the water pressures needed to recreate surface accelerations (e.g. Section 3.3), better couple basal hydrology to ice flow models, and help basal hydrology models to better accommodate rapid influxes of water. However, hydraulic jacking is currently not included in existing sliding laws (Howat et al., 2008). Schoof, Hewitt, and Werder (2012) suggested a possible mechanism of limiting effective pressures to zero by allowing bed separation at zero effective pressure to provide space to accommodate high water flux, but the process is numerically expensive (Hewitt, 2013). Providing a coupled calculation of cavity growth, drainage efficiency, and basal ice flow is likely to be taxing in terms of mathematical complexity and computation time, but is likely to be a likely avenue for better understanding the role of subglacial hydrology in increasing ice loss via accelerated sliding — and with computer power regularly increasing is becoming less of an issue.

Excessive effective pressure from surface lake drainage model

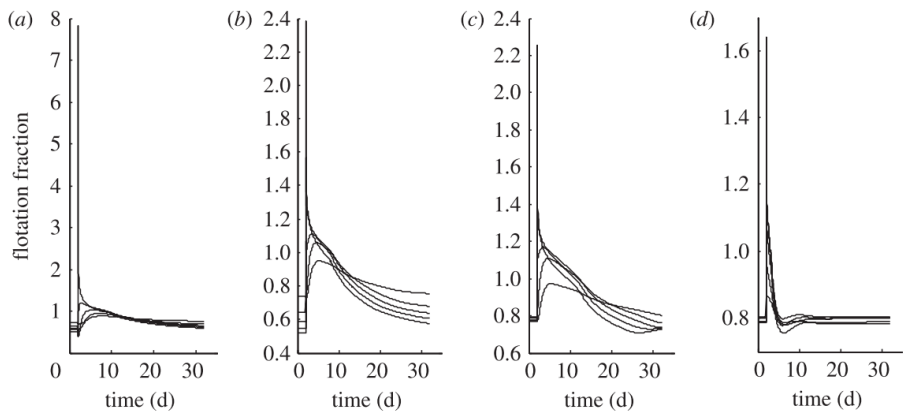

Figure 5. Evolution of modelled subglacial water pressures (given as a flotation fraction P_w^s/P_i) plotted at 5 km intervals (spike is closest to flood injection point). (*a*) Sheet drainage only, (*b*) mixed (sheet-conduit) drainage, (*c*) mixed drainage with a prescribed background discharge of $Q_{in}^c = 10\,m^3\,s^{-1}$ and (*d*) $Q_{in}^c = 100\,m^3\,s^{-1}$. Note the difference in vertical scales between the panels.

FIGURE 6.7: The evolution of water pressure with time at 5km intervals along a 2D ice flow model presented in Pimentel, Flowers, and Schoof (2010)

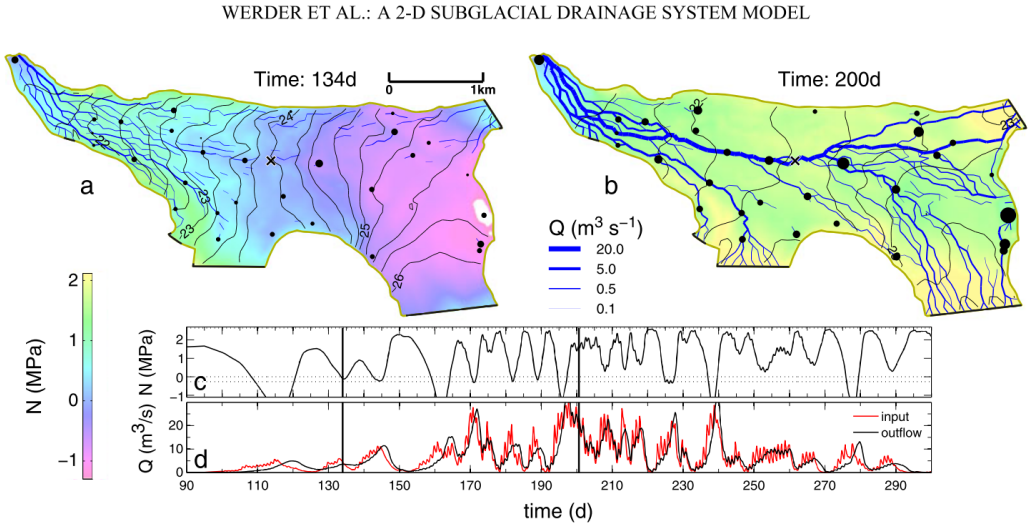

FIGURE 6.8: GlaDS Model output from Werder et al. (2013). Werder et al. model subglacial drainage of Gornergletscher, Switzerland over a melt season. The images show the glacier on (a) 14 May and (b) 19 July (which is approximately the time of peak input). Blue lines show the area of channelised drainage and the colour scale is the effective pressure at the bed. Large negative water pressures result from melt-water input at the start of the melt system into an inefficient system that has not had time to develop channels. The contours of hydraulic potential are lines of equal hydropotential ϕ (MPa).

Chapter 7

Conclusions

This study incorporates GNSS observations of Haupapa/Tasman Glacier into a finite-element modelling framework to investigate the basal processes that lead to rapid basal sliding. Episodes of high rainfall rate ($> 10\,\mathrm{mm\,hr^{-1}}$) resulted in significant accelerations from background velocity. For instance, horizontal velocities increased by 2220% and 2400% on May 5th and May 11th respectively at centre-line GNSS site TASC3 (see Figure 3.1 for site map)(Section 4.4). Cavity growth is likely to be the dominant signal in surface displacements of centre-line units (TASC2 and TASC3) and an off-centre unit (TASL2) based on the correlation between peak horizontal and vertical velocities during speed-up events (Figure 4.7, 4.8). An exemplary speed-up event which occurred on May 11th, 2016, is recreated using a finite-element model; however, peak velocities could only be achieved when basal water pressure exceeded flotation and, for 3D models, the velocity of the glacier sides exceeded observed velocity at the GNSS site nearest to the valley walls (Section 5.2, 5.3). Excessive water pressures and side velocities may be required because the acceleration of sliding speed in these models is not sensitive enough to rapid changes in water pressure. Therefore, a sliding law which produces accelerated sliding velocity during instances of cavity growth is required to reproduce surface velocities during speed-ups of Haupapa/Tasman Glacier.

The research questions motivating this study, as defined in Section 1.7, are now addressed:

1. *Is the relationship between horizontal and vertical displacement consistent across Haupapa/Tasman Glacier during speed-ups, or is spatial variability significant?*

   The relationship between vertical and horizontal velocity is not consistent across each GNSS site. During each speed-up event, centre-line sites (TASC2 and TASC3) and an off-centre site (TASL2) display a speed-up events where a) during the initial acceleration, horizontal and vertical velocities rise and peak together (Figure 4.7) and b) changes in vertical displacement lag behind horizontal velocity (Figure 4.8). These are interpreted as areas of high water pressure fluctuation where the resulting surface displacement is largely the result of cavity growth temporarily enhancing sliding speed. The observed relationship between horizontal and vertical displacement extends to the TASL2 site which can achieve similar, if not larger, displacements than TASC2 and TASC3.

At TASL1, however, while horizontal velocities are comparable to centre-line sites, the vertical displacement is significantly lower (Figure 4.3, 4.7). On the other hand, the margin at TASR2 still shows significant horizontal velocity peaks relative to its background speed, but the GNSS unit at this site does not record significant uplift (Figure 4.7, 4.10). Ice velocity at the TASR2 site is likely limited by a) friction against the side walls and b) a lack transient cavity growth temporarily enhancing velocity because there is little water storage beneath the site (assuming the lack of surface uplift represents low basal water storage in this area).

Lastly, peak horizontal velocity occurring at each site follows a strong downstream-propagating signal (Figure 4.13, 4.14). This is interpreted as a wave of water pressure moving downstream that triggers the rapid evolution of the subglacial drainage system (Section 6.1.2). The rapid sliding associated with cavity growth acts to also increases both cavity opening rates and the connectivity between cavity space — thus promoting water flow downstream. Sliding speed and cavity growth reach a limit when the glacial surface displacement is at a maximum, representing a state where drainage is efficient enough to evacuate rainwater downstream. The rapid rise and subsequent decline in horizontal speed and surface elevation move downstream at a rate determined by the balance between water storage capacity of cavities and the degree of connectivity between cavities and subglacial channels (if channels are present)(Iken and Bindschadler, 1986).

2. *If cavity growth causes enhanced basal motion during rapid water input at Haupapa/Tasman Glacier, what are the consequences of modelling speed-up events using a sliding law which assumes a steady-state cavity size?*

   Firstly, not only is rapid cavity growth able to explain surface displacements of Haupapa/Tasman Glacier, but models of cavity growth suggest bed separation rates of up to 570 m yr^{-1} at centre-line sites during peak water pressure, which is certainly not indicative of a cavity system in steady-state. The primary consequence on modelling sliding speed is that negative effective pressures are needed to reproduce surface velocities of Haupapa/Tasman Glacier. The commonly-used Coulomb-type law is not allowing sliding speed to respond in a fast enough way to changes in water pressure to reach peak velocities. Instead, surface velocities are matched by allowing an increasingly large portion of the bed to lose its capability of applying basal stress. In addition, the sides of the glacier need to be moving almost as fast as the centre-line sites during speed-ups — which exceeds the constraint of the near-margin site TASR2. The modelling framework in this study highlights the potential limitations of using a Coulomb-type sliding law which is used for modelling the glacial velocity response to time-evolving basal water pressures (e.g. Flowers

et al., 2011; Gagliardini and Werder, 2018; Hewitt, 2013; Jay-Allemand et al., 2011; Pimentel, Flowers, and Schoof, 2010).

Haupapa/Tasman Glacier is an example of a glacier that responds strongly to surface water inputs — meaning that it undergoes rapid changes in motion due to variability in the climate it is situated in. The modelling results of this study, in addressing Research Question 2, highlight the concern raised by Cowton et al. (2016) that regions where large water pressure fluctuations causing rapid cavity growth may not be well represented by a Coulomb-type sliding law. In other words, not all of the processes involved in connecting hydrology to sliding speed are being well implemented. This is a potential problem for the development of coupled models that aim to constrain the impacts of surface melt on the subglacial drainage system and the accompanying change in glacial flow speed (De Fleurian et al., 2018; Gagliardini and Werder, 2018). Part of the future work in developing models that link climate forcing to glacier dynamics should involve a better coupling of subglacial drainage and basal friction that can respond to cavity growth.

Appendix A

GNSS records of other speed-up events

A.1 January 8th event

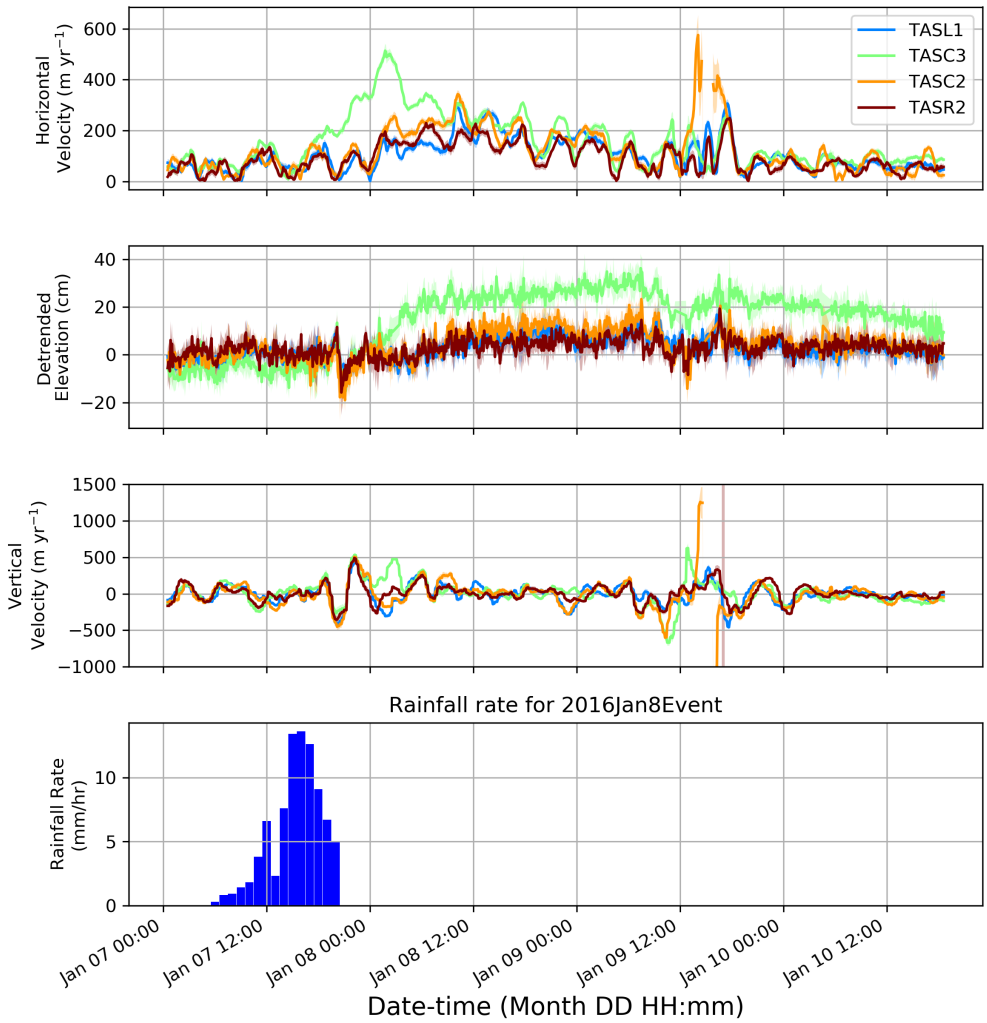

FIGURE A.1: The GNSS and rainfall record during the Jan 8th, 2016 speed-up event at Tasman Glacier

A.2 January 24th event

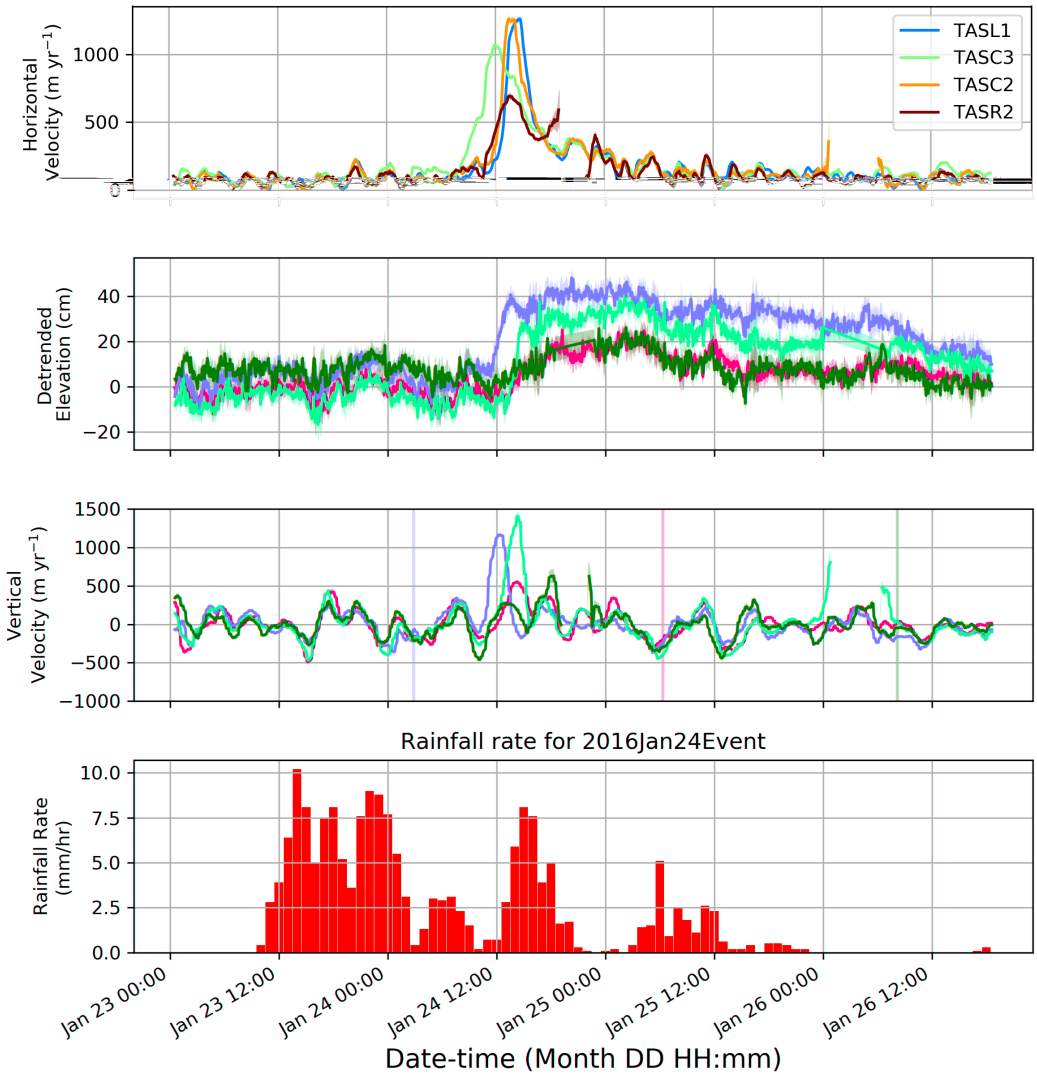

FIGURE A.2: The GNSS and rainfall record during the Jan 24th, 2016 speed-up event at Tasman Glacier

A.3 Febuary 17th speed-up event

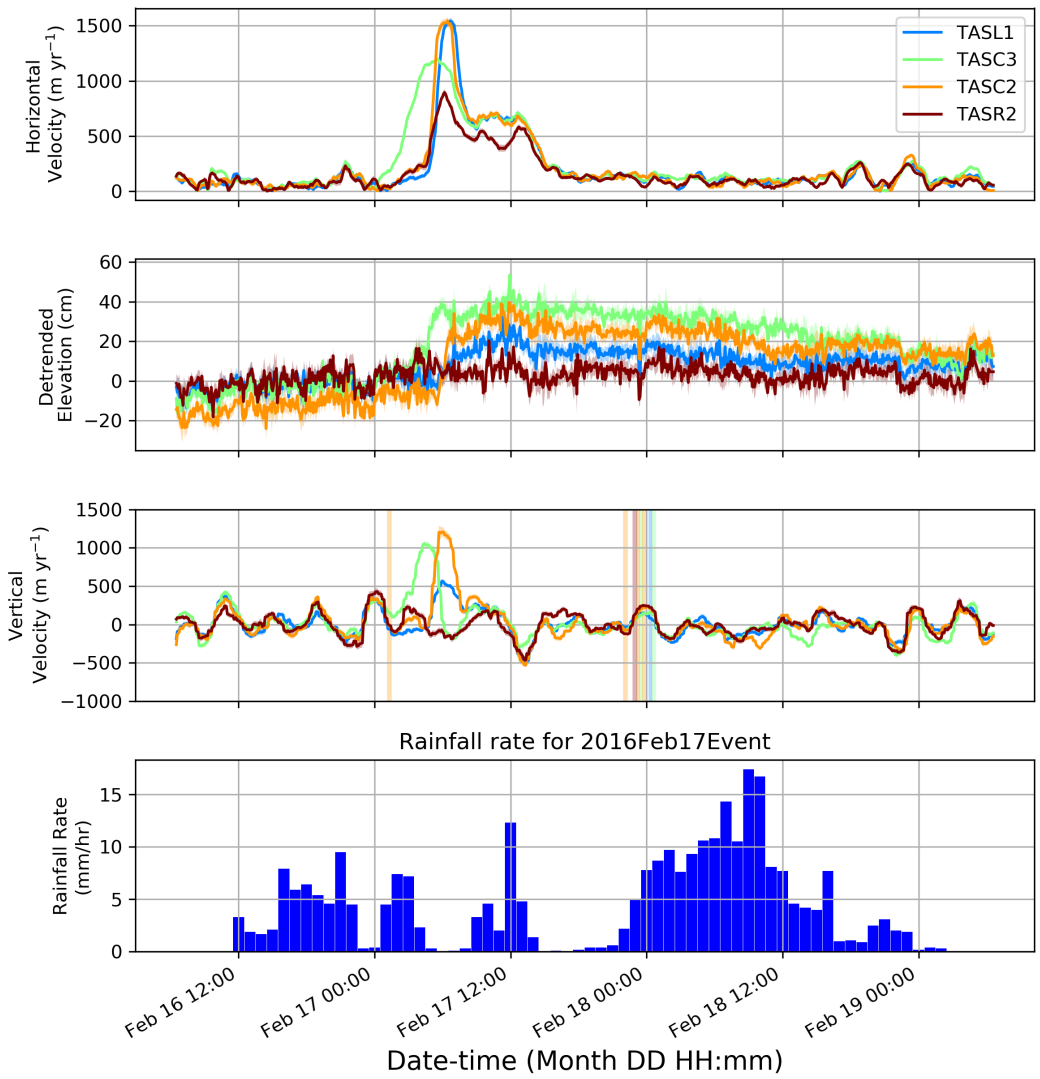

FIGURE A.3: The GNSS and rainfall record during the Febuary 17th, 2016 speed-up event at Tasman Glacier

A.4 March 23 speed-up event

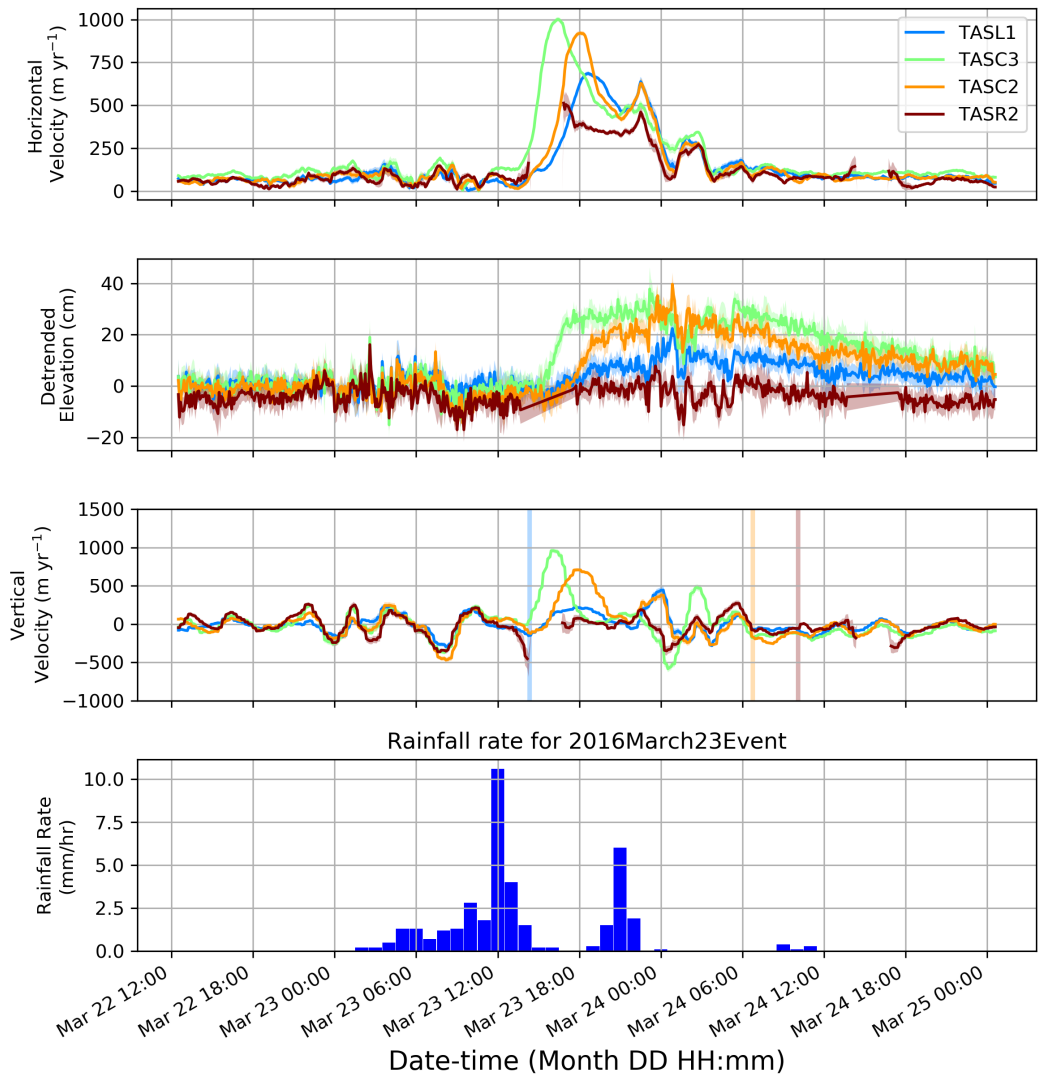

FIGURE A.4: The GNSS and rainfall record during the March 23rd, 2016 speed-up event at Tasman Glacier

Appendix B

Additional May 11 no side sliding 3D model results

B.1 Extreme Water Pressure Peak Scenario (TASC2)

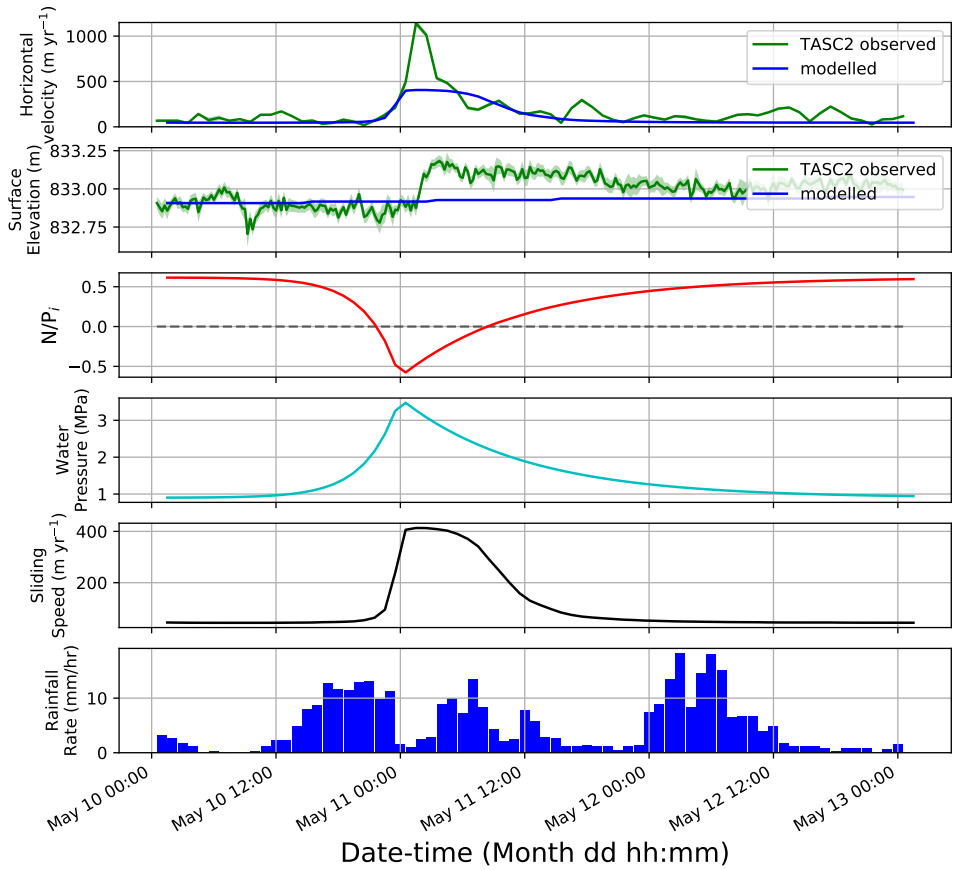

FIGURE B.1: Fit to TASC2 for 3D transient model for excessive water pressure variation. Extremely high water pressures do not result in a greater peak velocity, but instead cause sliding velocities to plateau. The Coulomb-Type sliding law causes basal stress to tend to zero and so side friction becomes an important process in limiting sliding velocity.

B.2 Low water pressure variation TASC3

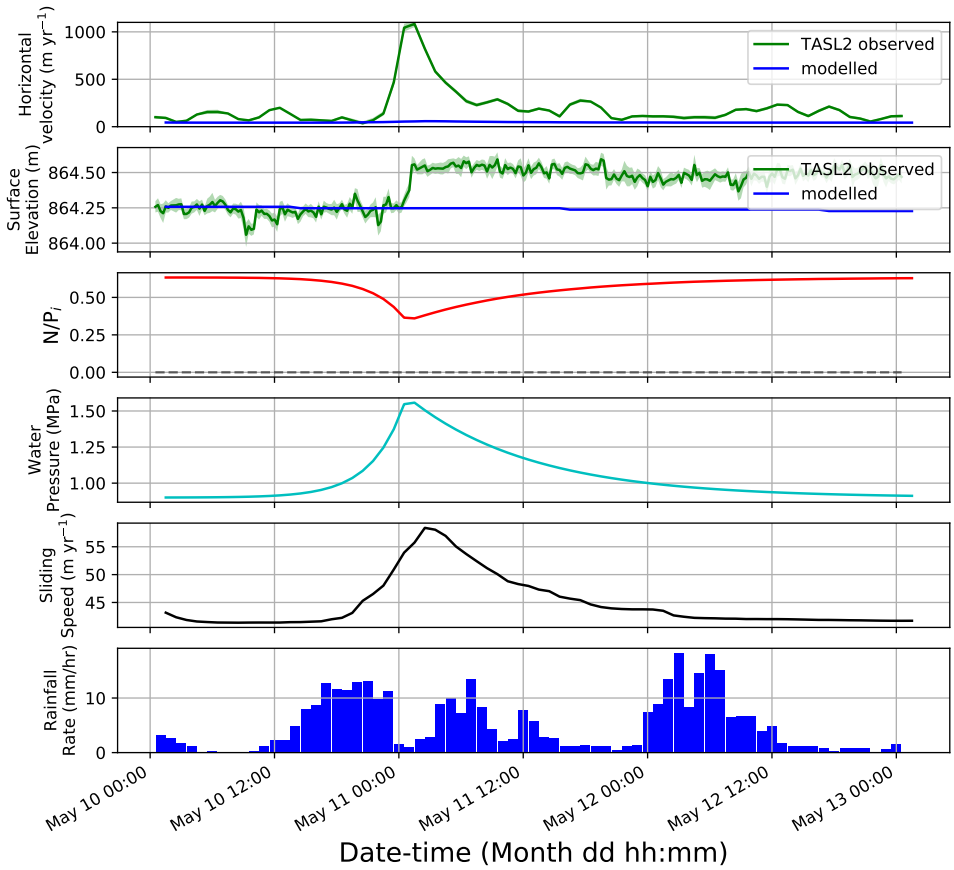

FIGURE B.2: Very little difference to velocity field results for $P_{peak} = 1.6MPa$

Appendix C

Uncertainty histograms for horizontal velocities (24-hour window)

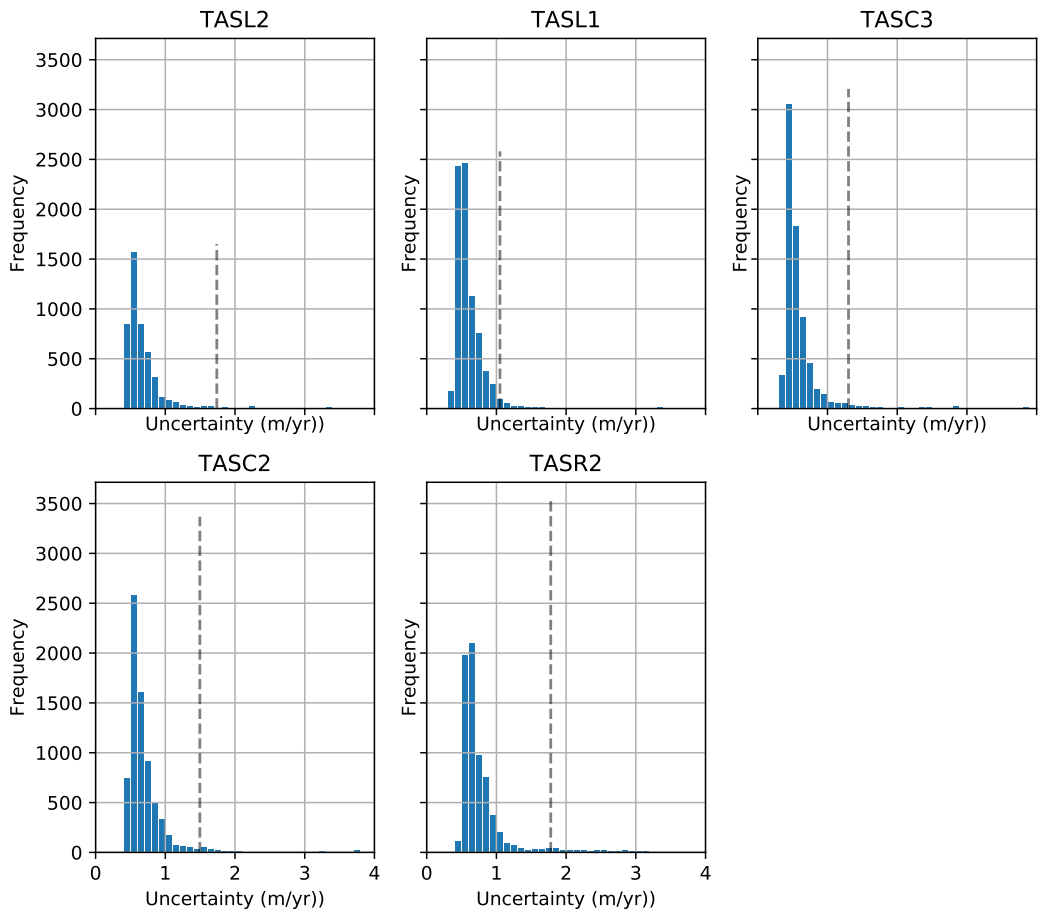

FIGURE C.1: Uncertainty histograms for horizontal velocities calculated with 24-hour window

Appendix D

Final cavity model for $u_{side} = 1100\,\mathrm{m\,yr^{-1}}$ and $h/\lambda_L = 0.5$

D.1 TASC2

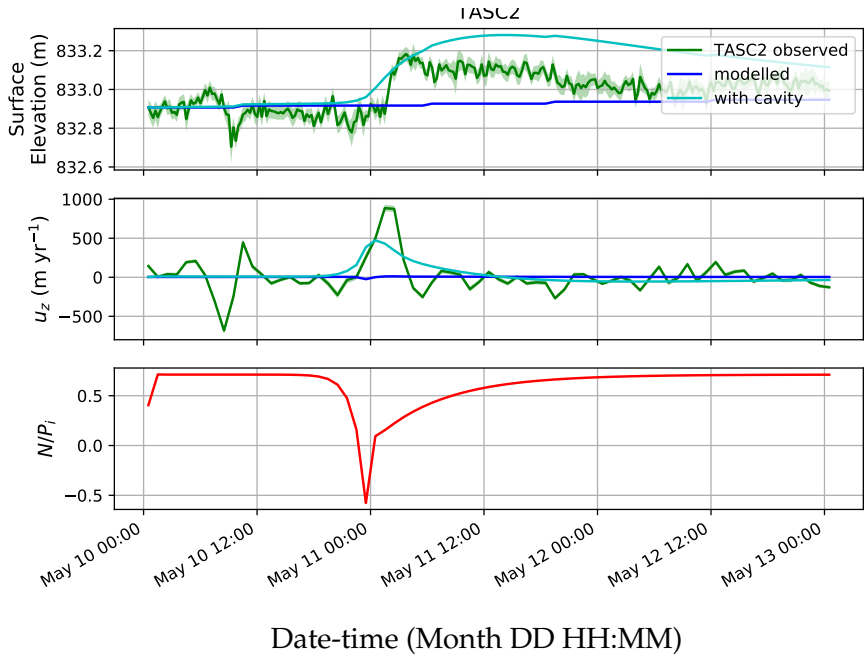

FIGURE D.1: Model run with high side sliding speed and moderate basal roughness (u_{side}=1100 m yr^{-1} and $h/\lambda_L = 0.5$) compared to TASC2 site.

D.2 TASR2

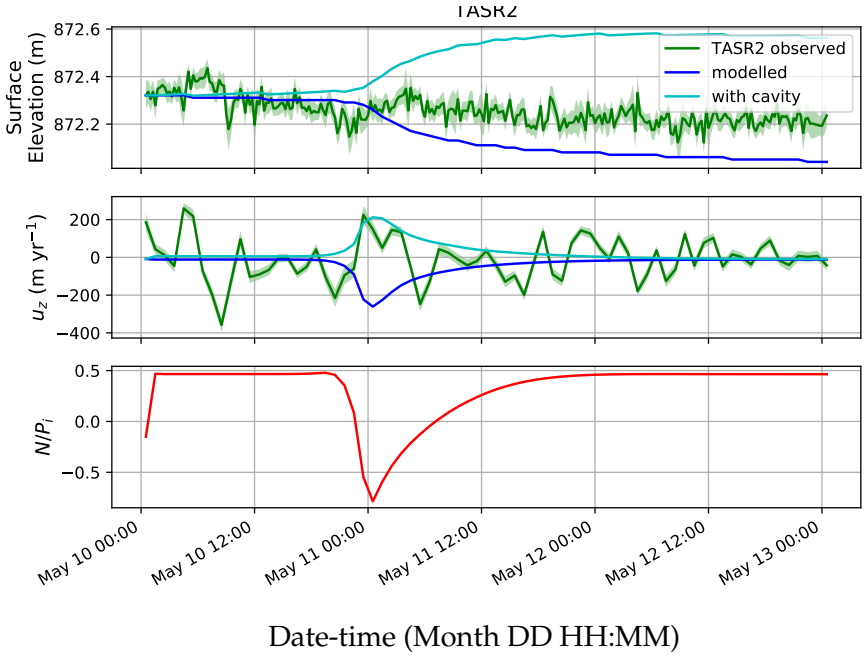

FIGURE D.2: Model run with high side sliding speed and moderate basal roughness (u_{side}=1100 m yr^{-1} and $h/\lambda_L = 0.5$) compared to TASR2 site.

Appendix E

Solver Input File for May 11th, 2016 simulation

```
!!!!!!!!!!!!!!!!!!!!!!!!!!!!!!!!!!!!!!!!
!      Sif file to run a test for Schoof law for 3D Tasman model
!
!!!!!!!!!!!!!!!!!!!!!!!!!!!!!!!!!!!!!!!!

!!!!!!!!!!!!!!!!!!!!!!!!!!!!!!!!!!!!!!!!
Header
  CHECK KEYWORDS Warn
   echo on
   Mesh DB "." "tas_lower_100m"
End



!!!!!! Name of test
$model="3D_TAS_"
$name="100m_tr_allsides_transientsideV"



$yearinsec = 365*24*60*60
$hourinyr = 24*365
$rhoi = 910.0/(1.0e6*yearinsec^2)
$rhow = 1000.0/(1.0e6*yearinsec^2)
$gravity = -1.0*9.81*yearinsec^2
$n = 3.0
$eta = (2.0*100.0)^(-1.0/n)

! Schoof parameters
$Cs=0.0102 !Schoof friction coefficient Cs = (1/As)^(1/n)
$As=Cs^(-n)
$WaterPressure=0.0 !
```

```
$Cmax=0.5

!Sides
$v_sides=-30.0
$v_upper=-70.0
$v_terminus=-50.0

! PEAK VSIDE PARAMETER
$Vside=300.0
! Set as a positive number --> USF makes this value negative

!!! Timesteps
$timestep=1.0/hourinyr

! decay parameter during rising phase
$Cr=(3*timestep)/5.0
! decay parameter during decaying phase
$Cd=(4*timestep)/5.0
! PEak Water Pressure
$Pk=3.0
! Time of peak water pressure
! Background water pressure
$Pbg=0.9

!!! Pressure wave
$dTp_dy=(1/1449.0)/hourinyr
$y0=5163407.421962204
!5164009.700447139
$PkT=24*timestep

$SL = 716.0


!!!!!!!!!!!!!!!!!!!!!!!!!!!!!!!!!!!!!!!!
Simulation
  Max Output Level = 10
  Coordinate System = "Cartesian 3D"
  Coordinate Mapping(3) = 1 2 3

  !!! simulation type
!  Simulation Type = Steady state
  Simulation Type = Transient
```

```
  !!! Ateady State Options
  Steady State Max Iterations = 3 !5
  Steady State Min Iterations = 1
  Output Intervals = 1

  !!! Transient options
  Timestepping Method = "bdf"
  BDF Order = 1
  ! 20 days of simulation with dt = 1 day
  TimeStep intervals = 73
  Timestep Sizes = $timestep
  Output Intervals = 1

  ! Restart file
  Restart File = "../RESTART_FILES/3DSCHOOF_001_DEM100m_test.
  result"
  Restart Position = 0
  Restart Before Initial Conditions = Logical True
  !Variable values given as initial or boundary conditions
  !and specified to depend on other variables are
  !initiated with those values from the restart file by
  !default if set to true
  Restart Time = Real 0.0


  ! Extrude Mesh
  Extruded Mesh Levels = Integer 14
!  Remesh Extruded Mesh Levels = Integer 14
  Stabilization Use Longest Element Edge = Logical True
  Set Dirichlet BCs By BC Numbering = Logical True
  Preserve Baseline = Integer 1
  Preserve Baseline = Integer 11
  Preserve Baseline = Integer 18

  !Extruded Mesh Name = String "Tasman Mesh"
  Post File = "$model name".vtu"
  Output File ="$model name".result"
End

!!!———————————————————— CONSTANTS ————————————————————!!!
Constants
```

```
  Stefan Boltzmann = 5.67e-08
  Gas Constant = Real 8.314

  Crise = Real $Cr
  Cdecay = Real $Cd
  PeakPw = Real $Pk
  !PeakT = Real $PkT
  Background Water Pressure = Real $Pbg

  Wavefront Speed = Real $dTp_dy
  Reference Peak time = Real $PkT
  Reference Co-ordinate = Real $y0

  Vside Peak time = Real $PkT
  Peak Vside = Real $Vside
  Initial Vside = Real $-1.0*v_sides  ! needs to positve
  !for input into the user function

  Bottom Surface Name = String "Zbed"

  Gravity = Real $gravity
  Water Density = Real $rhow
End

!!!------------------------------ BODIES ------------------------------!!!
! Tasman Glacier
Body 1
  Target Bodies(1) = 1
  Name = "Ice"
  Equation = 1
  Material = 1
  Body Force = 1
  Initial condition = 1
End

! Upper Surface
Body 2
  Equation = 2
  Body Force = 2
  Material = 1
  Initial Condition = 2
End
```

```
!!!------------------------- MATERIALS -------------------------!!!
Material 1
  Name = "Ice"

  !!!! Glen Law rheology
  Density = Real 9.150149e-19  ! MPa - a - m (910kg/m3)

  Viscosity = real 0.1 ! dummy value to avoid errors

  !!!!! Ice Rheology definition
  Viscosity Model = String "Glen"
  Critical Shear Rate = real $1.0E-03/31556926.0
  !Critical Shear Rate = real 1.0e-10
  Glen Exponent = Real 3.0

  !!! Rate factors (Paterson value in MPa^-3a^-1)
  Rate Factor 1 = Real 1.258e13
  Rate Factor 2 = Real 6.046e28

  ! these are in SI units - no problem, as long as
  ! the gas constant also is
  Activation Energy 1 = Real 60e3
  Activation Energy 2 = Real 139e3
  Glen Enhancement Factor = Real 1.0

  Limit Temperature = Real -10.0
  !!!! What variable to evalutae Arrhenius Law
  !Temperature Field Variable = String "Temp Homologous"
  ! HAS to be "Temp Homologous"

  Constant Temperature = Real -3.0
  !Temperature Field Variable = String "Temp Homologous"

  !!!! Calculate Cauchy tensor for Stress solver
  Cauchy = Logical True

  Youngs Modulus = Real 1.0
  Poisson Ratio = Real 0.3
```

```
  Sea level = Real $SL

End

!!!------------------------- BODY FORCES -------------------------!!!

Body Force 1
  Name = "Gravity"
  Flow Bodyforce 1 = 0.0
  Flow Bodyforce 2 = Real 0.0
  ! gravity = -9.81 in SI units
  Flow Bodyforce 3 = Real $gravity
End

Body Force 2
  Name = "Mass Balance"
  Zs Accumulation Flux 1 = Real 0.0e0
  Zs Accumulation Flux 2 = Real 0.0e0
  Zs Accumulation Flux 3= Real 0.0e0
End

!!!------------------------- EQUATION -------------------------!!!
Equation 1
  Name = "Ice Equation"
  Active Solvers(7) = 1 2 3 4 5 6 8
  Flow Solution Name = String "Flow Solution"
End


Equation 2
  Name = "Surface Equation"
  Active Solvers(1) = 7
  Flow Solution Name = String "Flow Solution"
  Convection = String "Computed"
End

!!!!!!!!!!!!!!!!!!!!!!!!!!!!!!!!!!!!!!!!!!
Solver 1
  Exec Solver = "Before Simulation"
  Equation = "Read DEMs"

  Procedure = "ElmerIceSolvers" "Grid2DInterpolator"
```

```
  ! Bedrock DEM
  Variable 1 = String "BedDEM"
  Variable 1 data file = File "./DEMS/tas_bed_100m_final.xyz"
  Variable 1 x0 = Real 1372060.0
  Variable 1 y0 = Real 5159430.0
  Variable 1 lx = Real 10000.0
  Variable 1 ly = Real 10000.0
  Variable 1 Nx = Integer 101
  Variable 1 Ny = Integer 101
  Variable 1 Invert = Logical False
  Variable 1 Fill = Logical False
  Variable 1 Position Tol = Real 1.0e-1
  Variable 1 No Data = Real -9999.0
  Variable 1 No Data Tol = Real 1.0

  ! Surface DEM
  Variable 2 = String "ZsDEM"
  Variable 2 data file = File "./DEMS/tas_sur_100m_final.xyz"
  Variable 2 x0 = Real 1372060.0
  Variable 2 y0 = Real 5159430.0
  Variable 2 lx = Real 10000.0
  Variable 2 ly = Real 10000.0
  Variable 2 Nx = Integer 101
  Variable 2 Ny = Integer 101
  Variable 2 Invert = Logical False
  Variable 2 Fill = Logical False
  Variable 2 Position Tol = Real 1.0e-1
  Variable 2 No Data = Real -9999.0
  Variable 2 No Data Tol = Real 1.0

End

Solver 2
!  Exec Solver = "Never"
  Equation = "MapCoordinate"
  Procedure = "StructuredMeshMapper" "StructuredMeshMapper"

  Active Coordinate = Integer 3
  !Mesh Velocity Variable = String "dSdt"
  !Mesh Update Variable = String "dS"
  Mesh Velocity First Zero = Logical True
```

```
  !Top Surface Variable Name = String "Zs"
  Bottom Surface Variable Name = String "Zbed"

  !Displacement Mode = Logical False
  Correct Surface = Logical True
  Minimum Height = Real 1.0

End

Solver 3
  ! Exec Solver = "Before Simulation"
   Equation = "Normal vector"
   Variable = "Normal Vector"
   ! in 3dimensional simulations we have 3 entries
   Variable DOFs = 3
   !NB: does not need to actually solve a matrix
   !     hence no BW optimization needed
   Optimize Bandwidth = Logical False
   Procedure = "ElmerIceSolvers" "ComputeNormalSolver"
   ! if set to True, all boundary normals would be
   ! computed by default
   ComputeAll = Logical False
End

Solver 4
 ! Exec Solver = "Never" !"Before Simulation"
  Equation = "HeightDepth"
  Procedure = "StructuredProjectToPlane"
     "StructuredProjectToPlane"
  Active Coordinate = Integer 3

  Operator 1 = depth
  Operator 2 = height
End

!!!! N-S solver from old Weertman law test
Solver 5
  Equation = "Navier-Stokes"

  Stabilization Method = String Stabilized
```

```
  Flow Model = Stokes

  Exported Variable 1 = -dofs 1 "Mesh Velocity"
  Exported Variable 2 = -dofs 1 "Mesh Update"
  Exported Variable 3 = -dofs 1 "BedDEM"
  Exported Variable 4 = -dofs 1 "ZsDEM"


  Linear System Solver = "Iterative"
  Linear System Iterative Method = "GCR"
  BiCGStabl Polynomial Degree = 4
  Linear System Max Iterations = 500
  Linear System Convergence Tolerance = Real 1.0E-5
  Linear System Abort Not Converged = False
  Linear System Preconditioning = "ILU0"
  Linear System Residual Output = 1

  Nonlinear System Max Iterations = 100
  Nonlinear System Convergence Tolerance = 1.0E-2
  Nonlinear System Newton After Iterations = 50
  Nonlinear System Newton After Tolerance = 1.0E-1 !never
  Nonlinear System Newton Max Tolerance = Real 1.0e-2
  Nonlinear System Newton Max Iterations = Integer 15
  !Give up newton
  Nonlinear System Reset Newton = Logical True

  Nonlinear System Relaxation Factor = 0.7

  Steady State Convergence Tolerance = Real 1.0e-6


End

Solver 6
  Equation = String "StressSolver"
  Procedure =  File "ElmerIceSolvers" "ComputeDevStress"
  ! this is just a dummy, hence no output is needed
  !-----------------------------------------------------------------
  Variable = -nooutput "Sij"
  Variable DOFs = 1
  ! the name of the variable containing
  ! the flow solution (U,V,W,Pressure)
```

```
  !-----------------------------------------------------------------
  Flow Solver Name = String "Flow Solution"
  ! no default value anymore for "Stress Variable Name"
  Stress Variable Name = String "Stress"
  !-----------------------------------------------------------------
  Exported Variable 1 = "Stress"
  ! [Sxx, Syy, Szz, Sxy] in 2D
  ! [Sxx, Syy, Szz, Sxy, Syz, Szx] in 3D

  Exported Variable 1 DOFs = 6   ! 4 in 2D, 6 in 3D
!  Linear System Solver = "Iterative"
!  Linear System Iterative Method = "BiCGStab"
!  Linear System Max Iterations = 300
!  Linear System Convergence Tolerance = 1.0E-09
!  Linear System Abort Not Converged = True
!  Linear System Preconditioning = "ILU0"
!  Linear System Residual Output = 1

  Linear System Solver = Direct
  Linear System Direct Method = umfpack


End


Solver 7
!! FREE SURFACE
  Equation = "Free Surface Top"
  Variable = "Zs"
  Exec Solver = "After Timestep"
  Variable DOFs =  1
  Procedure =  "FreeSurfaceSolver" "FreeSurfaceSolver"
  Solver Timing = Logical True

!  Before Linsolve = "EliminateDirichlet" "EliminateDirichlet"

  Linear System Solver = Iterative
  Linear System Max Iterations = 1000
  Linear System Iterative Method = BiCGStab
  Linear System Preconditioning = ILU1
  Linear System Convergence Tolerance = Real 1.0e-8
  Linear System Abort Not Converged = False
```

```
  Linear System Residual Output = 1

  Nonlinear System Max Iterations = 100
  Nonlinear System Min Iterations = 2
  !needed for dirichlet min fs condition
  Nonlinear System Convergence Tolerance  = 1.0e-6

  Steady State Convergence Tolerance = 1.0e-03
  Flow Solution Name = String "Flow Solution"


  Stabilization Method = Bubbles
  Apply Dirichlet = Logical True

  Exported Variable 1 = String "Zs Residual"
  Exported Variable 1 DOFS = 1

  Exported Variable 2 = String "Reference Zs"
  Exported Variable 2 DOFS = 1
End

!! EXPORT BED VERTICALLY
Solver 8
  Equation = "ExportVertically"
  Procedure = File "ElmerIceSolvers" "ExportVertically"
  Variable = String "Zbed"
  Variable DOFs = 1
  Linear System Solver = "Direct"
  Linear System Direct Method = umfpack
End
!!

!!!!!!!!!!!!!!!!!!!!! INITIAL CONDTIONS !!!!!!!!!!!!!!!!!!!!!

Initial Condition 1
  Name = "Ice IC"
!  Velocity 1 = Real 0.0
!  Velocity 2 = Real 0.0
!  Velocity 3 = Real 0.0
!  Pressure = Real 0.0
End
```

```
Initial Condition 2

  Zs = Equals ZsDEM

  Ref Zs = Equals ZsDEM

End



!!!!!!!!!!!!!!!!!!!!! BOUNDARY CONDTIONS !!!!!!!!!!!!!!!!!!!!!

Boundary Condition 1
  Target Boundaries = 1
  Name = "Sidewall Boundary Condition"
!  Noslip wall BC = True
 ! ComputeNormal = Logical False

  !!!! No sliding
  Velocity 1 = Real 0.0
  !Velocity 2 = Real $v_sides
  Velocity 2 = Variable Time
    Real Procedure "./USF/SideSlideFunc" "SideSlideFunc"

  Velocity 3 = Real 0.0

!  ! Coulomb sliding condition
!  ComputeNormal = Logical True
!  Normal-Tangential Velocity = Logical True
!  External Pressure = Variable Time, Coordinate 2,
!  Coordinate 3, BedDEM
!    Real Procedure "./USF/WaterPressureFunc"
!"WaterPressureSchoofSides"
!
!  ! No penetration into bedrock
!  Velocity 1 = Real 0.0
!
!   !!!! COULOMB LAW PARAMETERS
!  Slip Coefficient 2 =  Variable Coordinate 1
!    Real Procedure "ElmerIceUSF" "Friction_Coulomb"
!  Slip Coefficient 3 =  Variable Coordinate 1
```

```
!     Real Procedure "ElmerIceUSF" "Friction_Coulomb"
!
!!! Parameters needed for the Coulomb Friction Law
!  Friction Law Sliding Coefficient = Real $As
!  Friction Law Post-Peak Exponent  = Real 1.0
!  Friction Law Maximum Value = Real 0.5
!  Friction Law PowerLaw Exponent = Real $n
!  Friction Law Linear Velocity = Real 1.0e-4



End

Boundary Condition 2
  Name = "Terminus"

  Target Boundaries = 11

  ComputeNormal = Logical False

  Velocity 1 = Real 0.0
  Velocity 2 = Variable Time
    Real Procedure "./USF/SideSlideFunc" "SideSlideFunc"
  !Velocity 2 = Real $v_terminus
  Velocity 3 = Real 0.0
End
!
Boundary Condition 3
  Name = "Upper limit"

  Target Boundaries = 18
  ComputeNormal = Logical False

  !!!! No sliding
  Velocity 1 = Real 0.0
  !Velocity 2 = Real $v_upper
  Velocity 2 = Variable Time
    Real Procedure "./USF/SideSlideFunc" "SideSlideFunc"
  Velocity 3 = Real 0.0

End
```

```
!!!!!!!!!!!!!!!!!!!!! INITIAL CONDTIONS !!!!!!!!!!!!!!!!!!!!!

Initial Condition 1
  Name = "Ice IC"
!   Velocity 1 = Real 0.0
!   Velocity 2 = Real 0.0
!   Velocity 3 = Real 0.0
!   Pressure = Real 0.0
End


Initial Condition 2

  Zs = Equals ZsDEM

  Ref Zs = Equals ZsDEM

End



!!!!!!!!!!!!!!!!!!!!! BOUNDARY CONDTIONS !!!!!!!!!!!!!!!!!!!!!

Boundary Condition 1
  Target Boundaries = 1
  Name = "Sidewall Boundary Condition"
!   Noslip wall BC = True
 ! ComputeNormal = Logical False

  !!!! No sliding
  Velocity 1 = Real 0.0
  !Velocity 2 = Real $v_sides
  Velocity 2 = Variable Time
    Real Procedure "./USF/SideSlideFunc" "SideSlideFunc"

  Velocity 3 = Real 0.0

!   ! Coulomb sliding condition
!   ComputeNormal = Logical True
!   Normal-Tangential Velocity = Logical True
!   External Pressure = Variable Time, Coordinate 2,
!   Coordinate 3, BedDEM
```

```
!     Real Procedure "./USF/WaterPressureFunc"
!   "WaterPressureSchoofSides"
!
!   ! No penetration into bedrock
!   Velocity 1 = Real 0.0
!
!    !!!! COULOMB LAW PARAMETERS
!   Slip Coefficient 2 =  Variable Coordinate 1
!     Real Procedure "ElmerIceUSF" "Friction_Coulomb"
!   Slip Coefficient 3 =  Variable Coordinate 1
!     Real Procedure "ElmerIceUSF" "Friction_Coulomb"
!
!!! Parameters needed for the Coulomb Friction Law
!   Friction Law Sliding Coefficient = Real $As
!   Friction Law Post-Peak Exponent  = Real 1.0
!   Friction Law Maximum Value = Real 0.5
!   Friction Law PowerLaw Exponent = Real $n
!   Friction Law Linear Velocity = Real 1.0e-4



End

Boundary Condition 2
  Name = "Terminus"

  Target Boundaries = 11

  ComputeNormal = Logical False

  Velocity 1 = Real 0.0
  Velocity 2 = Variable Time
    Real Procedure "./USF/SideSlideFunc" "SideSlideFunc"
  !Velocity 2 = Real $v_terminus
  Velocity 3 = Real 0.0
End
!
Boundary Condition 3
  Name = "Upper limit"

  Target Boundaries = 18
  ComputeNormal = Logical False
```

```
  !!!! No sliding
  Velocity 1 = Real 0.0
  !Velocity 2 = Real $v_upper
  Velocity 2 = Variable Time
    Real Procedure "./USF/SideSlideFunc" "SideSlideFunc"
  Velocity 3 = Real 0.0

End
```

Bibliography

Anderson, Robert S. (2004). "Strong feedbacks between hydrology and sliding of a small alpine glacier". In: *Journal of Geophysical Research* 109.F3, F03005. ISSN: 0148-0227. DOI: 10.1029/2004jf000120. URL: http://doi.wiley.com/10.1029/2004JF000120.

Anderton, P. W. (1975). "Tasman Glacier 1971-73. Hydrological Research: Annual Report 33". In: *Wellington Ministry of Works and Development, National Soil and Water Conservation Organisation*.

Andrews, Lauren C. et al. (2015). "Direct observations of evolving subglacial drainage beneath the Greenland Ice Sheet". In: *Nature* 514.7520, pp. 80–83. ISSN: 14764687. DOI: 10.1038/nature13796. URL: http://www.nature.com/articles/nature13796.

Andrews, Lauren C. et al. (2018). "Seasonal Evolution of the Subglacial Hydrologic System Modified by Supraglacial Lake Drainage in Western Greenland". In: *Journal of Geophysical Research: Earth Surface* 123.6, pp. 1479–1496. ISSN: 21699003. DOI: 10.1029/2017jf004585. URL: http://doi.wiley.com/10.1029/2017JF004585.

Bartholomaus, Timothy C., Robert S. Anderson, and Suzanne P. Anderson (2008). "Response of glacier basal motion to transient water storage". In: *Nature Geoscience* 1.1, pp. 33–37. ISSN: 17520894. DOI: 10.1038/ngeo.2007.52.

Bartholomew, Ian et al. (2010). "Seasonal evolution of subglacial drainage and acceleration in a Greenland outlet glacier". In: *Nature Geoscience* 3.6, pp. 408–411. ISSN: 1752-0894. DOI: 10.1038/ngeo863. URL: http://www.nature.com/articles/ngeo863.

Bartholomew, Ian et al. (2012). "Short-term variability in Greenland Ice Sheet motion forced by time-varying meltwater drainage: Implications for the relationship between subglacial drainage system behavior and ice velocity". In: *Journal of Geophysical Research: Earth Surface* 117.3. ISSN: 21699011. DOI: 10.1029/2011JF002220. URL: http://doi.wiley.com/10.1029/2011JF002220.

Bindschadler, R. (1983). "The importance of pressurized subglacial water in separation and sliding at the glacier bed." In: *Journal of Glaciology* 29.101, pp. 3–19. ISSN: 00221430. DOI: 10.1017/S0022143000005104.

Bindschadler, Robert A. et al. (2013). "Ice-sheet model sensitivities to environmental forcing and their use in projecting future sea level (the SeaRISE project)". In: *Journal of Glaciology* 59.214, pp. 195–224. ISSN: 00221430. DOI: 10.3189/2013JoG12J125.

Bingham, Robert G., Peter W. Nienow, and Martin J. Sharp (2003). "Intra-annual and intra-seasonal flow dynamics of a High Arctic polythermal valley glacier". In: *Annals of Glaciology* 37, pp. 181–188. ISSN: 02603055. DOI: 10.3189/172756403781815762.

Blake, W. et al. (1994). "Instruments and Methods: Direct measurement of sliding at the glacier bed". In: *Journal of Glaciology* 40.136, pp. 595–599. ISSN: 0022-1430. DOI: 10.1017/s002214300001248x.

Box, Jason E. and Kathleen Ski (2007). "Remote sounding of Greenland supraglacial melt lakes: implications for subglacial hydraulics". In: *Journal of Glaciology* 53.181, pp. 257–265. ISSN: 0022-1430. DOI: 10.3189/172756507782202883.

Broadbent, M (1973). "A preliminary report on seismic and gravity surveys on the Tasman Glacier 1971–2". In: *Geophysics division, DSIR, Wellington, K/6/2/1*.

Broadbent, Michael (1974). *Seismic and gravity surveys on the Tasman Glacier: 1971-2*.

Broeke, Michiel van den et al. (2009). "Partitioning Recent Greenland Mass Loss". In: *Science* 326.5955, pp. 984–986. ISSN: 0036-8075. DOI: 10.1126/science.1178176. arXiv: arXiv:1011.1669v3. URL: http://www.sciencemag.org/cgi/doi/10.1126/science.1178176.

Broeke, Michiel R. van den et al. (2016). "On the recent contribution of the Greenland ice sheet to sea level change". In: *Cryosphere* 10.5, pp. 1933–1946. ISSN: 19940424. DOI: 10.5194/tc-10-1933-2016. arXiv: arXiv:1011.1669v3. URL: https://dspace.library.uu.nl/handle/1874/340841.

Brondex, Julien, Fabien Gillet-Chaulet, and Olivier Gagliardini (2019). "Sensitivity of centennial mass loss projections of the Amundsen basin to the friction law". In: *Cryosphere* 13.1, pp. 177–195. ISSN: 19940424. DOI: 10.5194/tc-13-177-2019. URL: https://www.the-cryosphere.net/13/177/2019/.

Brondex, Julien et al. (2017). "Sensitivity of grounding line dynamics to the choice of the friction law". In: *Journal of Glaciology* 63.241, pp. 854–866. ISSN: 0022-1430. DOI: 10.1017/jog.2017.51.

Budd, W. F., D. Jenssen, and I. N. Smith (1984). "A three-dimensional time-dependent model of the West Antarctic ice sheet." In: *Annals of Glaciology* 5, pp. 29–36. ISSN: 02603055. DOI: 10.3189/1984AoG5-1-29-36.

Budd, W. F., P. L. Keage, and N. A. Blundy (1979). "Empirical studies of ice sliding." In: *Journal of Glaciology* 23.89, pp. 157–170. ISSN: 00221430. DOI: 10.1017/S0022143000029804.

Chen, G. (1998). "GPS kinematics positioning for the Airborne Laser Altimetry at Long Valley, California". PhD. Massachusetts Institute of Technology.

Chinn, T. J. (1996). "New Zealand glacier responses to climate change of the past century". In: *New Zealand Journal of Geology and Geophysics* 39.3, pp. 415–428. ISSN: 11758791. DOI: 10.1080/00288306.1996.9514723.

— (2001). *Distribution of the glacial water resources of New Zealand*. DOI: 10.2307/43922047. URL: http://www.jstor.org/stable/43922047.

Chu, Vena W. (2013). "Greenland ice sheet hydrology". In: *Progress in Physical Geography* 38.1, pp. 19–54. ISSN: 0309-1333. DOI: 10.1177/0309133313507075. URL: http://journals.sagepub.com/doi/10.1177/0309133313507075.

Church, John A. et al. (2013). "2013: Sea level change". In: *Climate Change 2013: The Physical Science Basis. Contribution of Working Group I to the Fifth Assessment Report of the Intergovernmental Panel on Climate Change*. Ed. by Stocker T.F. et al. Cambridge, United Kingdom and New York, NY, USA: Cambridge University Press. Chap. 13, pp. 1137–1216. ISBN: ISBN 978-1-107-66182-0. DOI: 10.1017/CBO9781107415315.026.

Claridge, David (1983). "A geophysical study of the termini of the Mount Cook National Park glaciers." In: URL: https://researchspace.auckland.ac.nz/handle/2292/5961.

Clarke, Garry K.C. (2005). "Subglacial processes". In: *Encyclopedia of Earth Sciences Series* Part 3.1, pp. 1101–1105. ISSN: 1871756X. DOI: 10.1007/978-90-481-2642-2_547. URL: http://www.annualreviews.org/doi/10.1146/annurev.earth.33.092203.122621.

Collins, Matthew et al. (2013). "Long-term Climate Change: Projections, Commitments and Irreversibility". In: *Climate Change 2013: The Physical Science Basis. Contribution of Working Group I to the Fifth Assessment Report of the Intergovernmental Panel on Climate Change*. Ed. by T. F. Stocker et al. Cambridge: Cambridge University Press. Chap. 12, pp. 1029–1136. ISBN: 0019-9567 (Print). DOI: 10.1002/mds.26688. URL: http://pure.iiasa.ac.at/id/eprint/10551/.

Copland, Luke, Martin J. Sharp, and Peter W. Nienow (2003). "Links between short-term velocity variations and the subglacial hydrology of a predominantly cold polythermal glacier". In: *Journal of Glaciology* 49.166, pp. 337–348. ISSN: 00221430. DOI: 10.3189/172756503781830656.

Cowton, Tom et al. (2016). "Variability in ice motion at a land-terminating Greenlandic outlet glacier: the role of channelized and distributed drainage systems". In: *Journal of Glaciology* 62.233, pp. 451–466. ISSN: 0022-1430. DOI: 10.1017/jog.2016.36.

Cuffey, Kurt M and William Stanley Bryce Paterson (2010). *The physics of glaciers*. Academic Press.

Das, Sarah et al. (2008a). *Fracture propagation to the base of the GIS during Supraglacial lake drainage.* DOI: 10.2307/20054686.

Das, Sarah B. et al. (2008b). "Fracture propagation to the base of the Greenland ice sheet during supraglacial lake drainage". In: *Science* 320.5877, pp. 778–781. ISSN: 00368075. DOI: 10.1126/science.1153360.

De Fleurian, B. et al. (2014). "A double continuum hydrological model for glacier applications". In: *Cryosphere* 8.1, pp. 137–153. ISSN: 19940416. DOI: 10.5194/tc-8-137-2014. URL: www.the-cryosphere.net/8/137/2014/.

De Fleurian, Basile et al. (2018). "SHMIP the subglacial hydrology model intercomparison Project". In: *Journal of Glaciology* 64.248, pp. 897–916. ISSN: 00221430. DOI: 10.1017/jog.2018.78.

Enderlin, Ellyn M. et al. (2014). "An improved mass budget for the Greenland ice sheet". In: *Geophysical Research Letters* 41.3, pp. 866–872. ISSN: 19448007. DOI: 10.1002/2013GL059010. URL: http://doi.wiley.com/10.1002/2013GL059010.

Farinotti, Daniel et al. (2017). "How accurate are estimates of glacier ice thickness? Results from ITMIX, the Ice Thickness Models Intercomparison eXperiment". In: *Cryosphere* 11.2, pp. 949–970. ISSN: 19940424. DOI: 10.5194/tc-11-949-2017.

Flowers, G. E. et al. (2011). "Present dynamics and future prognosis of a slowly surging glacier". In: *Cryosphere* 5.1, pp. 299–313. ISSN: 19940416. DOI: 10.5194/tc-5-299-2011.

Flowers, Gwenn E. (2011). "Glacier hydromechanics: early insights and the lasting legacy of three works by Iken and colleagues". In: *Journal of Glaciology* 56.200, pp. 1069–1078. ISSN: 0022-1430. DOI: 10.3189/002214311796406103.

— (2015). "Modelling water flow under glaciers and ice sheets". In: *Proceedings of the Royal Society A: Mathematical, Physical and Engineering Sciences* 471.2176, p. 20140907. ISSN: 14712946. DOI: 10.1098/rspa.2014.0907.

— (2018). *Hydrology and the future of the Greenland Ice Sheet*. DOI: 10.1038/s41467-018-05002-0.

Fountain, Andrew G. and Joseph S. Walder (1998). "Water flow through temperate glaciers". In: *Reviews of Geophysics* 36.3, pp. 299–328. ISSN: 87551209. DOI: 10.1029/97RG03579. URL: http://doi.wiley.com/10.1029/97RG03579.

Fowler, A. C. (1979). "A mathematical approach to the theory of glacier sliding." In: *Journal of Glaciology* 23.89, pp. 131–141. ISSN: 00221430. DOI: 10.1017/S0022143000029786.

— (1986). "A sliding law for glaciers of constant viscosity in the presence of subglacial cavitation." In: *Proceedings - Royal Society of London, Series A* 407.1832, pp. 147–170. DOI: 10.1098/rspa.1986.0090.

Fowler, A.C. (2011). "Weertman, Lliboutry and the development of sliding theory". In: *Journal of Glaciology* 56.200, pp. 965–972. ISSN: 0022-1430. DOI: 10.3189/002214311796406112.

Fudge, T.J. et al. (2009). "Rapid glacier sliding, reverse ice motion and subglacial water pressure during an autumn rainstorm". In: *Annals of Glaciology* 50.52, pp. 101–108. ISSN: 0260-3055. DOI: 10.3189/172756409789624247.

Gagliardini, O. et al. (2007). "Finite-element modeling of subglacial cavities and related friction law". In: *Journal of Geophysical Research: Earth Surface* 112.2. ISSN: 21699011. DOI: 10.1029/2006JF000576.

Gagliardini, O. et al. (2013). "Capabilities and performance of Elmer/Ice, a new-generation ice sheet model". In: *Geoscientific Model Development* 6.4, pp. 1299–1318. ISSN: 1991959X. DOI: 10.5194/gmd-6-1299-2013. URL: https://www.geosci-model-dev.net/6/1299/2013/gmd-6-1299-2013.pdf.

Gagliardini, Olivier and Mauro A. Werder (2018). "Influence of increasing surface melt over decadal timescales on land-terminating Greenland-type outlet glaciers". In: *Journal of Glaciology* 64.247, pp. 700–710. ISSN: 0022-1430. DOI: 10.1017/jog.2018.59.

Gladstone, Rupert Michael et al. (2017). "Marine ice sheet model performance depends on basal sliding physics and sub-shelf melting". In: *Cryosphere* 11.1, pp. 319–329. ISSN: 19940424. DOI: 10.5194/tc-11-319-2017. URL: www.the-cryosphere.net/11/319/2017/.

Glen, J. W. (1955). "The creep of polycrystalline ice". In: *Proceedings of the Royal Society of London. Series A. Mathematical and Physical Sciences* 228.1175, pp. 519–538. DOI: 10.1098/rspa.1955.0066. URL: http://www.royalsocietypublishing.org/doi/10.1098/rspa.1955.0066.

Gregory, J. M. et al. (2012). "Twentieth-Century Global-Mean Sea Level Rise: Is the Whole Greater than the Sum of the Parts?" In: *Journal of Climate* 26.13, pp. 4476–4499. ISSN: 0894-8755. DOI: 10.1175/jcli-d-12-00319.1.

Harper, Joel T. et al. (2007). "Two modes of accelerated glacier sliding related to water". In: *Geophysical Research Letters* 34.12, p. L12503. ISSN: 00948276. DOI: 10.1029/2007GL030233. URL: http://doi.wiley.com/10.1029/2007GL030233.

Hart, R (2014). "The ice thickness distribution of a debris-covered glacier: Tasman Glacier, New Zealand." Master's Thesis. Victoria University of Wellington. URL: http://internal-pdf//Hart2014-1600110337/Hart2014.pdf.

Henderson, R. D. and S. M. Thompson (1999). "Extreme rainfalls in the Southern Alps of New Zealand". In: *Journal of Hydrology New Zealand* 38.2, pp. 309–330. ISSN: 00221708. URL: https://www.jstor.org/stable/43944824.

Herman, Frédéric, Brian Anderson, and Sébastien Leprince (2011). "Mountain glacier velocity variation during a retreat/advance cycle quantified using sub-pixel analysis of ASTER images". In: *Journal of Glaciology* 57.202, pp. 197–207. ISSN: 0022-1430. DOI: 10.3189/002214311796405942.

Hewitt, I. J. (2013). "Seasonal changes in ice sheet motion due to melt water lubrication". In: *Earth and Planetary Science Letters* 371-372, pp. 16–25. ISSN: 0012821X. DOI: 10.1016/j.epsl.2013.04.022. URL: https://www.sciencedirect.com/science/article/pii/S0012821X13002045.

Hoegh-Guldberg, O. et al. (2006). "Impacts of 1.5Â°C of Global Warming on Natural and Human Systems Coordinating". In: *Global warming of 1.5Â°C. An IPCC Special Report on the impacts of global warming of 1.5Â°C above pre-industrial levels and related global greenhouse gas emission pathways, in the context of strengthening the global response to the threat of climate change,* ed. by T. Waterfiel V. Masson-Delmotte, P. Zhai, H. O. Pörtner, D. Roberts, J. Skea, P.R. Shukla, A. Pirani, W. Moufouma-Okia, C. Péan, R. Pidcock, S. Connors, J. B. R. Matthews, Y. Chen, X. Zhou, M. I. Gomis, E. Lonnoy, T. Maycock, M. Tignor. Vol. 170. 11. Chap. 3. ISBN: 1570270597. DOI: 10.1093/aje/kwp410. arXiv: arXiv:1011.1669v3. URL: http://www.ncbi.nlm.nih.gov/pubmed/19943627.

Hooke, Roger LeB. et al. (1989). "A 3 Year Record of Seasonal Variations in Surface Velocity, StorglaciÄren, Sweden". In: *Journal of Glaciology* 35.120, pp. 235–247. ISSN: 0022-1430. DOI: 10.3189/s0022143000004561.

Horgan, Huw J. et al. (2015). "Glacier velocity variability due to rain-induced sliding and cavity formation". In: *Earth and Planetary Science Letters* 432, pp. 273–282. ISSN: 0012821X. DOI: 10.1016/j.epsl.2015.10.016.

Howat, Ian M., Ian Joughin, and Ted A. Scambos (2007). "Rapid changes in ice discharge from Greenland outlet glaciers". In: *Science* 315.5818, pp. 1559–1561. ISSN: 00368075. DOI: 10.1126/science.1138478. URL: http://www.ncbi.nlm.nih.gov/pubmed/17289940.

Howat, Ian M. et al. (2008). "Dynamic controls on glacier basal motion inferred from surface ice motion". In: *Journal of Geophysical Research: Earth Surface* 113.3. ISSN: 21699011. DOI: 10.1029/2007JF000925.

Hubbard, Alun (1998). "Comparison of a three-dimensional model for glacier flow with field data from Haut Glacier d'Arolla, Switzerland". In: *Journal of Glaciology* 44.147, pp. 368–378. ISSN: 00221430. DOI: 10.1017/S0022143000002690.

Hubbard, B P et al. (1995). "Borehole water-level variations and the structure of the subglacial hydrological systelll of Haut Glacier d' Arolla, Valais," in: *Journal of Glaciology* 139.139, pp. 572–583.

Huss, Matthias and Daniel Farinotti (2012). "Distributed ice thickness and volume of all glaciers around the globe". In: *Journal of Geophysical Research: Earth Surface* 117.4, pp. 1–10. ISSN: 21699011. DOI: 10.1029/2012JF002523. arXiv: arXiv:1011.1669v3.

Iken, A. and M. Truffer (1997). "The relationship between subglacial water pressure and velocity of Findelengletscher, Switzerland, during its advance and retreat". In: *Journal of Glaciology* 43.144, pp. 328–338. ISSN: 00221430. DOI: 10.1017/S0022143000003282. arXiv: arXiv:1011.1669v3.

Iken, A. et al. (1983). "The uplift of Unteraargletscher at the beginning of the melt season - a consequence of water storage at the bed?" In: *Journal of Glaciology* 29.101, pp. 28–47. ISSN: 00221430. DOI: 10.1017/S0022143000005128.

Iken, Almut (1972). "Measurements of Water Pressure in Moulins as Part of a Movement Study of the White Glacier, Axel Heiberg Island, Northwest Territories, Canada". In: *Journal of Glaciology* 11.61, pp. 53–58. ISSN: 0022-1430. DOI: 10.1017/s0022143000022486.

— (1981). "The Effect of the Subglacial Water Pressure on the Sliding Velocity of a Glacier in an Idealized Numerical Model". In: *Journal of Glaciology* 27.97.

Iken, Almut and Robert A. Bindschadler (1986). "Combined measurements of Subglacial Water Pressure and Surface Velocity of Findelengletscher, Switzerland: Conclusions about Drainage System and Sliding Mechanism". In: *Journal of Glaciology* 32.110, pp. 101–119. ISSN: 0022-1430. DOI: 10.1017/s0022143000006936.

Jansson, P. (1995). "Water pressure and basal sliding on Storglaciaren, northern Sweden". In: *Journal of Glaciology* 41.138, pp. 232–240. ISSN: 00221430. DOI: 10.1017/S0022143000016130.

Jay-Allemand, M. et al. (2011). "Investigating changes in basal conditions of Variegated Glacier prior to and during its 1982-1983 surge". In: *Cryosphere* 5.3, pp. 659–672. ISSN: 19940416. DOI: 10.5194/tc-5-659-2011.

Kaab, A (2002). "Monitoring high-mountain terrain deformation from repeated air- and spaceborne optical data: examples using digital aerial imagery and ASTER data RID A-3607-2012". In: *Isprs Journal of Photogrammetry and Remote Sensing* 57.1-2, pp. 39–52. DOI: 10.1016/S0924-2716(02)00114-4.

Kamb, B. (1987). "Glacier surge mechanism based on linked cavity configuration of the basal water conduit system". In: *Journal of Geophysical Research* 92.B9, pp. 9083–9100. ISSN: 01480227. DOI: 10.1029/JB092iB09p09083. URL: http://doi.wiley.com/10.1029/JB092iB09p09083.

Kamb, B., H. F. Engelhardt, and W. D. Harrison (1979). "The Ice-Rock Interface and Basal Sliding Process as Revealed by Direct Observation in Bore Holes and Tunnels". In: *Journal of Glaciology* 23.89, pp. 416–419. ISSN: 0022-1430. DOI: 10.1017/s0022143000030124.

Kamb, B. et al. (1985). "Glacier Surge Mechanism: 1982-1983 Surge of Variegated Glacier, Alaska". In: *Science* 227.4686, pp. 469–479. ISSN: 0036-8075. DOI: 10.1126/science.227.4686.469.

Kamb, Barclay and Keith A. Echelmeyer (1986). "Stress-Gradient Coupling in Glacier Flow: I. Longitudinal Averaging of the Influence of Ice Thickness and Surface Slope". In: *Journal of Glaciology* 32.111, pp. 267–284. DOI: 10.3189/S0022143000015604.

Kamb, Barclay and Hermann Engelhardt (1987). "Waves of Accelerated Motion in a Glacier Approaching Surge: the Mini-Surges of Variegated Glacier, Alaska, U.S.A." In: *Journal of Glaciology* 33.113, pp. 27–46. ISSN: 0022-1430. DOI: 10.1017/s0022143000005311.

Kamb, Barclay and E. LaChapelle (1964). "Direct Observation of the Mechanism of Glacier Sliding Over Bedrock". In: *Journal of Glaciology* 5.38, pp. 159–172. ISSN: 0022-1430. DOI: 10.1017/s0022143000028756.

Kamb, Barclay et al. (1994). "Mechanical and hydrologic basis for the rapid motion of a large tidewater glacier: 2. Interpretation". In: *Journal of Geophysical Research* 99.B8, pp. 15231–15234. ISSN: 0148-0227. DOI: 10.1029/94jb00467.

Kehrl, L M (2012). "Glacier Speed-Up Events and Subglacial Hydrology on the Lower Franz Josef Glacier, New Zealand". Master's. Victoria University ofWellington, p. 100.

Kirkbride, Martin P. and Charles R. Warren (1999). "Tasman Glacier, New Zealand: 20th-century thinning and predicted calving retreat". In: *Global and Planetary Change* 22.1-4, pp. 11–28. ISSN: 09218181. DOI: 10.1016/S0921-8181(99)00021-1. URL: www.elsevier.comrlocatergloplacha.

Kjeldsen, Kristian K. et al. (2015). "Spatial and temporal distribution of mass loss from the Greenland Ice Sheet since AD 1900". In: *Nature* 528.7582, pp. 396–400. ISSN: 0028-0836. DOI: 10.1038/nature16183.

Kleffmann, Stefan et al. (2010). "Crustal structure in the central South Island, New Zealand, from the Lake Pukaki seismic experiment". In: *New Zealand Journal of*

Geology and Geophysics 41.1, pp. 39–49. ISSN: 0028-8306. DOI: 10.1080/00288306.1998.9514789.

Lliboutry, L. (1986). "General Theory of Subglacial Cavitation and Sliding of Temperate Glaciers". In: *Journal of Glaciology* 7.49, pp. 21–58. ISSN: 0022-1430. DOI: 10.1017/s0022143000020396.

Lliboutry, Louis A. (1959). "Une théorie du frottement du glacier sur son lit". In: *Ann.Geophysics*. Vol. 15, pp. 250–265.

Lliboutry, Luis (1965). *Traité de glaciologie: Glaciers, variations du climat, sols gelés*. Vol. 2. Masson.

Macgregor, Kelly R., Catherine A. Riihimaki, and Robert S. Anderson (2005). "Spatial and temporal evolution of rapid basal sliding on Bench Glacier, Alaska, USA". In: *Journal of Glaciology* 51.172, pp. 49–63. ISSN: 00221430. DOI: 10.3189/172756505781829485.

Magnússon, E. et al. (2010). "Reduced glacier sliding caused by persistent drainage from a subglacial lake". In: *Cryosphere* 4.1, pp. 13–20. ISSN: 19940424. DOI: 10.5194/tc-4-13-2010. URL: http://www.the-cryosphere.net/4/13/2010/.

Mair, Douglas et al. (2001). "Spatial patterns of glacier motion during a high-velocity event: Haut Glacier d'Arolla, Switzerland". In: *Journal of Glaciology* 47.156, pp. 9–20. ISSN: 0022-1430. DOI: 10.3189/172756501781832412.

Mair, Douglas W.F., Martin J. Sharp, and Ian C. Willis (2002). "Evidence for basal cavity opening from analysis of surface uplift during a high-velocity event: Haut Glacier d'Arolla, Switzerland". In: *Journal of Glaciology* 48.161, pp. 208–216. ISSN: 00221430. DOI: 10.3189/172756502781831502.

Marzeion, B., A. H. Jarosch, and M. Hofer (2012). "Past and future sea-level change from the surface mass balance of glaciers". In: *Cryosphere* 6.6, pp. 1295–1322. ISSN: 19940416. DOI: 10.5194/tc-6-1295-2012. URL: www.the-cryosphere.net/6/1295/2012/.

Marzeion, Ben et al. (2018). "Limited influence of climate change mitigation on short-term glacier mass loss". In: *Nature Climate Change* 8.4, pp. 1–4. ISSN: 17586798. DOI: 10.1038/s41558-018-0093-1. URL: http://www.nature.com/articles/s41558-018-0093-1.

Ministry for the Environment (2010). *River Environment Classification: West Coast*. Web. URL: https://data.mfe.govt.nz/layer/1857-river-environment-classification-west-coast-2010/.

Nick, Faezeh M. et al. (2009). "Large-scale changes in Greenland outlet glacier dynamics triggered at the terminus". In: *Nature Geoscience* 2.2, pp. 110–114. ISSN: 17520894. DOI: 10.1038/ngeo394. URL: http://www.nature.com/articles/ngeo394.

Nick, Faezeh M. et al. (2013). "Future sea-level rise from Greenland's main outlet glaciers in a warming climate (Supplementary information)". In: *Nature* 497.7448, pp. 1–29. ISSN: 00085472. DOI: 10.1038/nature. arXiv: NIHMS150003.

Nienow, P. W. et al. (2005). "Hydrological controls on diurnal ice flow variability in valley glaciers". In: *Journal of Geophysical Research: Earth Surface* 110.4. ISSN:

21699011. DOI: 10.1029/2003JF000112. URL: http://doi.wiley.com/10.1029/2003JF000112.

Nienow, P. W. et al. (2017). "Recent Advances in Our Understanding of the Role of Meltwater in the Greenland Ice Sheet System". In: *Current Climate Change Reports* 3.4, pp. 330–344. ISSN: 21986061. DOI: 10.1007/s40641-017-0083-9. URL: http://link.springer.com/10.1007/s40641-017-0083-9.

Nobes, David C. et al. (2010). "Downwasting of the Tasman Glacier, South Island, New Zealand: Changes in the terminus region between 1971 and 1993". In: *New Zealand Journal of Geology and Geophysics* 38.1, pp. 1–16. ISSN: 0028-8306. DOI: 10.1080/00288306.1995.9514635.

Paterson, W S B (1994). *The Physics of Glaciers 3rd edition*. Elsevier Science. ISBN: 9781483287256.

Pattyn, F. et al. (2012). "Results of the marine ice sheet model intercomparison project, MISMIP". In: *Cryosphere* 6.3, pp. 573–588. ISSN: 19940416. DOI: 10.5194/tc-6-573-2012. arXiv: arXiv:1011.1669v3. URL: www.the-cryosphere.net/6/573/2012/.

Pelt, Ward J.J. van et al. (2018). "Dynamic Response of a High Arctic Glacier to Melt and Runoff Variations". In: *Geophysical Research Letters* 45.10, pp. 4917–4926. ISSN: 19448007. DOI: 10.1029/2018GL077252. URL: http://doi.wiley.com/10.1029/2018GL077252.

Pfeffer, W. Tad et al. (2014). "The randolph glacier inventory: A globally complete inventory of glaciers". In: *Journal of Glaciology* 60.221, pp. 537–552. ISSN: 00221430. DOI: 10.3189/2014JoG13J176. arXiv: Pfeffer2014.

Pimentel, S., G. E. Flowers, and C. G. Schoof (2010). "A hydrologically coupled higher-order flow-band model of ice dynamics with a Coulomb friction sliding law". In: *Journal of Geophysical Research: Earth Surface* 115.4, F04023. ISSN: 21699011. DOI: 10.1029/2009JF001621. URL: http://doi.wiley.com/10.1029/2009JF001621.

Pimentel, Sam and Gwenn E. Flowers (2011). "A numerical study of hydrologically driven glacier dynamics and subglacial flooding". In: *Proceedings of the Royal Society A: Mathematical, Physical and Engineering Sciences* 467.2126, pp. 537–558. ISSN: 14712946. DOI: 10.1098/rspa.2010.0211.

Purdie, Heather et al. (2016). "Bathymetric evolution of Tasman Glacier terminal lake, New Zealand, as determined by remote surveying techniques". In: *Global and Planetary Change* 147, pp. 1–11. ISSN: 09218181. DOI: 10.1016/j.gloplacha.2016.10.010. URL: https://www.sciencedirect.com/science/article/pii/S0921818115301533.

Purdie, Jennifer and Blair Fitzharris (1999). "Processes and rates of ice loss at the terminus of Tasman Glacier, New Zealand". In: *Global and Planetary Change* 22.1-4, pp. 79–91. ISSN: 09218181. DOI: 10.1016/S0921-8181(99)00027-2. URL: https://www.sciencedirect.com/science/article/pii/S0921818199000272.

Quincey, D. J. and N. F. Glasser (2009). "Morphological and ice-dynamical changes on the Tasman Glacier, New Zealand, 1990-2007". In: *Global and Planetary Change* 68.3, pp. 185–197. ISSN: 09218181. DOI: 10.1016/j.gloplacha.2009.05.003.

Rada, Camilo and Christian Schoof (2018). "Channelized, distributed, and disconnected: Subglacial drainage under a valley glacier in the Yukon". In: *Cryosphere* 12.8, pp. 2609–2636. ISSN: 19940424. DOI: 10.5194/tc-12-2609-2018.

Radić, Valentina and Regine Hock (2011). "Regionally differentiated contribution of mountain glaciers and ice caps to future sea-level rise". In: *Nature Geoscience* 4.2, pp. 91–94. ISSN: 17520894. DOI: 10.1038/ngeo1052. URL: http://www.nature.com/articles/ngeo1052.

Radić, Valentina et al. (2014). "Regional and global projections of twenty-first century glacier mass changes in response to climate scenarios from global climate models". In: *Climate Dynamics* 42.1-2, pp. 37–58. ISSN: 09307575. DOI: 10.1007/s00382-013-1719-7. arXiv: Radic2013.

Raymond, C and W D Harrison (1987). "Fit of ice motion models to observations from Variegated Glacier, Alaska". In: *The physical basis of ice sheet modelling International Association of Hydrological Sciences, Proc. of the Vancouver Symposium* 170, pp. 153–166.

Raymond, C. F. and W. D. Harrison (1988). "Evolution of Variegated Glacier, Alaska, USA, prior to its surge". In: *Journal of Glaciology* 34.117, pp. 154–169. ISSN: 00221430. DOI: 10.1017/S0022143000032184.

Raymond, C.F. et al. (1995). "Hydrological discharges and motion of Fels and Black Rapids Glaciers, Alaska, U.S.A.: implications for the structure of their drainage systems". In: *Journal of Glaciology* 41.138, pp. 290–304. ISSN: 0022-1430. DOI: 10.3189/s002214300001618x.

Redpath, T. A.N. et al. (2013). "Accuracy assessment for mapping glacier flow velocity and detecting flow dynamics from ASTER satellite imagery: Tasman Glacier, New Zealand". In: *Remote Sensing of Environment* 133, pp. 90–101. ISSN: 00344257. DOI: 10.1016/j.rse.2013.02.008.

Ridley, Jeff et al. (2010). "Thresholds for irreversible decline of the Greenland ice sheet". In: *Climate Dynamics* 35.6, pp. 1065–1073. ISSN: 09307575. DOI: 10.1007/s00382-009-0646-0. URL: http://link.springer.com/10.1007/s00382-009-0646-0.

Rignot, Eric (2009). "Changes in the Velocity Structure of the Greenland Ice Sheet Eric Rignot," in: *Science (New York, N.Y.)* 986.2006, pp. 986–991. DOI: 10.1126/science.1121381.

Rignot, Eric, Michele Koppes, and Isabella Velicogna (2010). "Rapid submarine melting of the calving faces of West Greenland glaciers". In: *Nature Geoscience* 3.3, pp. 187–191. ISSN: 17520894. DOI: 10.1038/ngeo765. URL: http://www.nature.com/articles/ngeo765.

Ritz, Catherine et al. (2015). "Potential sea-level rise from Antarctic ice-sheet instability constrained by observations". In: *Nature* 528.7580, pp. 115–118. ISSN:

14764687. DOI: 10.1038/nature16147. arXiv: NIHMS150003. URL: https://www.nature.com/articles/nature16147.pdf.

Röthlisberger, Hans (1972). "Water Pressure in Intra- and Subglacial Channels". In: *Journal of Glaciology* 11.62, pp. 177–203. ISSN: 0022-1430. DOI: 10.1017/s0022143000022188.

Roux, P-F et al. (2010). "Observation of surface seismic activity changes of an Alpine glacier during a glacier-dammed lake outburst". In: *Journal of Geophysical Research: Earth Surface* 115.F3.

Schoof, Christian (2005). "The effect of cavitation on glacier sliding". In: *Proceedings of the Royal Society A: Mathematical, Physical and Engineering Sciences* 461.2055, pp. 609–627. ISSN: 14712946. DOI: 10.1098/rspa.2004.1350. URL: http://rspa.royalsocietypublishing.org/cgi/doi/10.1098/rspa.2004.1350.

— (2006). "Variational methods for glacier flow over plastic till". In: *Journal of Fluid Mechanics* 555, pp. 299–320. ISSN: 00221120. DOI: 10.1017/S0022112006009104.

— (2010). "Ice-sheet acceleration driven by melt supply variability". In: *Nature* 468.7325, pp. 803–806. ISSN: 00280836. DOI: 10.1038/nature09618.

Schoof, Christian, Ian J. Hewitt, and Mauro A. Werder (2012). "Flotation and free surface flow in a model for subglacial drainage. Part 1. Distributed drainage". In: *Journal of Fluid Mechanics* 702, pp. 126–156. ISSN: 0022-1120. DOI: 10.1017/jfm.2012.165.

Schuenemann, Keah C. and John J. Cassano (2010). "Changes in synoptic weather patterns and Greenland precipitation in the 20th and 21st centuries: 2. Analysis of 21st century atmospheric changes using self-organizing maps". In: *Journal of Geophysical Research Atmospheres* 115.D5, p. D05108. ISSN: 21698996. DOI: 10.1029/2009JD011706. URL: http://doi.wiley.com/10.1029/2009JD011706.

Shepherd, Andrew et al. (2009). "Greenland ice sheet motion coupled with daily melting in late summer". In: *Geophysical Research Letters* 36.1, pp. 2–5. ISSN: 00948276. DOI: 10.1029/2008GL035758.

Sole, A. J. et al. (2011). "Seasonal speedup of a Greenland marine-terminating outlet glacier forced by surface melt-induced changes in subglacial hydrology". In: *Journal of Geophysical Research: Earth Surface* 116.3, F03014. ISSN: 21699011. DOI: 10.1029/2010JF001948. URL: http://doi.wiley.com/10.1029/2010JF001948.

Sole, Andrew et al. (2013). "Winter motion mediates dynamic response of the Greenland Ice Sheet to warmer summers". In: *Geophysical Research Letters* 40.15, pp. 3940–3944. ISSN: 00948276. DOI: 10.1002/grl.50764. URL: http://doi.wiley.com/10.1002/grl.50764.

Solomon, Susan et al., eds. (2007). *IPCC, 2007: Climate Change 2007: The Physical Science Basis. Contribution of Working Group I to the Fourth Assessment Report of the Intergovernmental Panel on Climate Change*. Cambridge, UK and New York, NY, USA: Cambridge University Press.

Stearns, L. A. and C. J. van der Veen (2018). "Friction at the bed does not control fast glacier flow". In: *Science* 361.6399, pp. 273–277. ISSN: 0036-8075. DOI: 10.1126/science.aat2217. URL: http://www.ncbi.nlm.nih.gov/pubmed/29880724.

Stenborg, T (1973). *Some viewpoints on the internal drainage of glaciers*. Tech. rep., pp. 117–129.

Stevens, Laura A. et al. (2015). "Greenland supraglacial lake drainages triggered by hydrologically induced basal slip". In: *Nature* 522.7554, pp. 73–76. ISSN: 14764687. DOI: 10.1038/nature14480.

Sugiyama, Shin and G. Hilmar Gudmundsson (2004). "Short-term variations in glacier flow controlled by subglacial water pressure at Lauteraargletscher, Bernese Alps, Switzerland". In: *Journal of Glaciology* 50.170, pp. 353–362. ISSN: 00221430. DOI: 10.3189/172756504781829846.

Sundal, Aud Venke et al. (2011). "Melt-induced speed-up of Greenland ice sheet offset by efficient subglacial drainage". In: *Nature* 469.7331, pp. 521–524. ISSN: 00280836. DOI: 10.1038/nature09740.

Tedstone, Andrew J. et al. (2013). "Greenland ice sheet motion insensitive to exceptional meltwater forcing". In: *Proceedings of the National Academy of Sciences* 110.49, pp. 19719–19724. ISSN: 0027-8424. DOI: 10.1073/pnas.1315843110.

Tedstone, Andrew J. et al. (2015). "Decadal slowdown of a land-terminating sector of the Greenland Ice Sheet despite warming". In: *Nature* 526.7575, pp. 692–695. ISSN: 0028-0836. DOI: 10.1038/nature15722. URL: http://www.nature.com/articles/nature15722.

Thomas, Robert H. (2004). "Force-perturbation analysis of recent thinning and acceleration of Jakobshavn Isbræ, Greenland". In: *Journal of Glaciology* 50.168, pp. 57–66. ISSN: 00221430. DOI: 10.3189/172756504781830321.

Tsai, Victor C., Andrew L. Stewart, and Andrew F. Thompson (2015). "Marine ice-sheet profiles and stability under Coulomb basal conditions". In: *Journal of Glaciology* 61.226, pp. 205–215. ISSN: 0022-1430. DOI: 10.3189/2015jog14j221.

Vallot, Dorothée et al. (2017). "Basal dynamics of Kronebreen, a fast-flowing tidewater glacier in Svalbard: Non-local spatio-Temporal response to water input". In: *Journal of Glaciology* 63.242, pp. 1012–1024. ISSN: 00221430. DOI: 10.1017/jog.2017.69.

Van De Wal, R. S.W. et al. (2008). "Large and rapid melt-induced velocity changes in the ablation zone of the Greenland Ice Sheet". In: *Science* 321.5885, pp. 111–113. ISSN: 00368075. DOI: 10.1126/science.1158540. arXiv: arXiv:1011.1669v3.

Vaughan, David G. et al. (2013). "Observations: Cryosphere". In: *Climate Change 2013 - The Physical Science Basis*. Ed. by T.F. Stocker et al. Vol. 9781107057. Cambridge, United Kingdom and New York, NY, USA: Cambridge University Press. Chap. 4, pp. 317–382. ISBN: 9781107415324. DOI: 10.1017/CBO9781107415324.012. URL: http://ebooks.cambridge.org/ref/id/CBO9781107415324A020.

Veen, CJ Van der (1998). "Fracture mechanics approach to penetration of surface crevasses on glaciers". In: *Cold Regions Science and Technology* 27.1, pp. 31–47.

Walder, J. and B. Hallet (1979). "Geometry of former subglacial water channels and cavities." In: *Journal of Glaciology* 23.89, pp. 335–346. ISSN: 00221430. DOI: 10.1017/S0022143000029944.

Weertman, J. (1957). "On the Sliding of Glaciers". In: *Journal of Glaciology* 3.21, pp. 33–38. ISSN: 0022-1430. DOI: 10.1017/s0022143000024709.

Werder, M. A., T. V. Schuler, and M. Funk (2010). "Short term variations of tracer transit speed on alpine glaciers". In: *Cryosphere* 4.3, pp. 381–396. ISSN: 19940416. DOI: 10.5194/tc-4-381-2010.

Werder, Mauro A. et al. (2013). "Modeling channelized and distributed subglacial drainage in two dimensions". In: *Journal of Geophysical Research: Earth Surface* 118.4, pp. 2140–2158. ISSN: 21699011. DOI: 10.1002/jgrf.20146.

Zemp, Michael et al. (2015). "Historically unprecedented global glacier decline in the early 21st century". In: *Journal of Glaciology* 61.228, pp. 745–762. ISSN: 00221430. DOI: 10.3189/2015JoG15J017.

Zienkiewicz, O.C., R.L. Taylor, and J.Z. Zhu (2013). "Problems in Linear Elasticity and Fields". In: *The Finite Element Method: its Basis and Fundamentals*, pp. 21–45. ISBN: 9781856176330. DOI: 10.1016/b978-1-85617-633-0.00002-2. URL: http://linkinghub.elsevier.com/retrieve/pii/B9781856176330000022.

Zwally, H. Jay et al. (2002). "Surface melt-induced acceleration of Greenland ice-sheet flow". In: *Science* 297.5579, pp. 218–222. ISSN: 00368075. DOI: 10.1126/science.1072708. arXiv: arXiv:1011.1669v3.